U.S. DEPARTMENT OF COMMERCE
National Oceanic and Atmospheric Administration
Environmental Research Laboratories

NOAA Technical Memorandum ERL NSSL-70

LIFE CYCLE OF FLORIDA KEYS' WATERSPOUTS

Joseph H. Golden

National Severe Storms Laboratory
Norman, Oklahoma
June 1974

TABLE OF CONTENTS

LIST OF SYMBOLS

C	translational velocity
C_r	translational speed
d, ds, D_f	diameter, diameter of spiral, diameter of funnel
g	acceleration of gravity
H	height of cloud base
K	eddy viscosity
L	characteristic length scale
$\mathcal{O}$	order of magnitude
p	hydrostatic pressure
P	characteristic pressure
P_Γ	circulation-associated pressure
r	radius of curvature
R	radius magnitude
r_m	radius of maximum windspeed
T	ait temperature
T_d	dewpoint temperature
u	horizontal radial-speed component
U	characteristic value of u
v	horizontal tangential-speed component
V_m	maximum tangential speed
$\overline{V}$	mean 24-hr surface windspeed
V	characteristic value of v
V_c	the cyclostrophic windspeed
V_T	rotational (tangential) windspeed
w	vertical velocity (z-coordinate)
W	characteristic value of vertical velocity

α	lapse rate of potential temperature
β	stability parameter (in °K)
Γ	circulation
Γ_∞	circulation at infinite radius
δ	constant height
λ	buoyancy parameter
ϕ	azimuthal coordinate
ρ	density of air
θ	potential temperature
θ_e	equivalent potential temperature
θ_w	wet-bulb potential temperature
ν	molecular kinematic viscosity

LIST OF TABLES

LIFE CYCLE OF FLORIDA KEYS' WATERSPOUTS

Joseph H. Golden

ABSTRACT

Analyses show that waterspouts have a characteristic life cycle consisting of five overlapping stages: (1) the dark spot, identified by a prominent light-colored disc on the sea surface, surrounded by a dark patch diffuse on its outer edges, that is a manifestation of a complete vortex column from cloud base to sea surface; (2) the spiral pattern, characterized by development of alternating dark- and light-colored surface bands spiralling around the dark spot; (3) the spray ring (incipient spray vortex), concentrated around the dark spot, with a lengthening funnel above; (4) the mature waterspout (spray vortex), determined as the stage of maximum overall organization and intensity; and (5) the decay, recognized by waterspout dissipation (often abrupt) which is reinforced by cool downdrafts from a nearby developing rainshower.

Frequent waterspout formation in the Florida Keys and their life cycle apparently result from transfer of energy and angular momentum among five scales of atmospheric circulation: (1) the funnel scale, corresponding to the waterspout itself, with funnel diameters from 10 to 500 ft; (2) the spiral scale, from 500 to 3,000 ft at the surface; (3) the individual cumulus-cloud scale, from less than 1 to 5 mi; (4) the cumulus cloudline scale, from 5 to 100 mi; and (5) the synoptic scale, several hundred miles. The differing roles of these five scales of motion are assessed.

1. INTRODUCTION

A waterspout is defined as an intense columnar vortex (not necessarily containing a funnel-shaped cloud) of small horizontal extent over water. For South Florida waterspouts, only rarely does the visible funnel extend from cloud base to sea surface. Like the tornado, most of the visible funnel is condensate. Funnel cloud extension thus depends upon the distribution of ambient water vapor, ambient temperature, and pressure drop resulting from the vortex circulation. Assuming that the funnel and its immediate environment consist of well-mixed air, the funnel's outer surface would outline the surface of constant-isentropic condensation pressure (Glaser, 1960). This fact raises important questions concerning the level of turbulence (and hence of lateral mixing and lateral inflow).

Table 1. Broadly Representative Values of the Rossby Number[a]

Vortex type	L	H	V	R_o
Dust devils	10 m	10 m - 1 km	10 m/s	10^4
Waterspouts	10-100 m	500 m - 1 km	20-80 m/s	10^3 - 10^4
Tornadoes[b]	100-3,000 m	300 m - 2 km	40-150 m/s	10^3 - 10^4
Hurricanes	1,000 km	10 km	50 m/s	0.5

a Using similar table and discussion in Morton (1966).

b Using tornado statistics from Melaragno (1968), Fujita (1970b), and Fujita et al. (1970).

Among many meteorological phenomena yet to be adequately measured are small-scale intense vortices. Tornadoes have passed close to a few anemometers, and the instrument was either destroyed or the windspeed indicator blown off scale by speeds of about 150 mph or less (Fujita et al., 1970). Microbarograph traces obtained near a tornado show nearly instantaneous pressure drops up to 1.0 in. Hg (Ward, 1964); unofficial reports from aneroid barometers range as high as 5.67 in. Hg (Outram, 1904). However, no accurate minimum pressure or maximum rotational windspeed determination has been made for either tornado or waterspout.

The four basic types of vortices according to their characteristic scales and velocities are shown in table 1 with representative Rossby Number* values. Rossby Numbers much greater than one imply that the earth's rotation, although it can serve as vorticity source, does not constrain the flow.

The majority of waterspout literature describes single occurrences; a few are documented by photographs or drawings (Bundgaard, 1953;and Dinwiddie, 1959). An early article by Ferrel (1893, p. 370) attributed funnel cloud production to expansion of air in the vortex resulting from "the partial vacuum caused by the centrifugal force on the gyration"; pointed out that "most of the air is drawn in near the surface of the earth and moves rapidly upward in the funnel interior"; and, finally, noted that the effect of friction, except near the surface, is small. The rotational motion, therefore, approximated that of a free body responding to central forces.

The literature following Ferrel's work primarily reported mariners' eyewitness accounts. Hurd (1928) noted that waterspout observations from a vessel are often casual and hurried, and therefore most superficial. Nevertheless, such reports add to waterspout statistics and are valuable. Hurd observed that funnels generally evolve from a cylindrical or elephant-trunk

* The Rossby Number = U/fL, where U is a velocity characteristic of the flow, f is the coriolis parameter or twice the earth's effective angular rotation, and L is a dimension characteristic of the flow.

shape at maturity to a more narrow ropelike structure shortly before demise. The Cottage City, Mass., waterspout of August 19, 1896, was in clear view of hundreds of spectators. The formation was described by Hurd (1928) as "a projection which soon became a long pendant...seen dropping from a part of the cloud a mile or so to the rear of the region of heaviest rainfall..." Before its second disappearance, the waterspout had an "inner tube" upward from the water surface. Hurd (1950) reported a salty downpour 2 to 3 hr after the giant waterspout.

Such knowledge, although interesting, is insufficient for a proper understanding. For instance, the only early estimate of minimum surface pressure is given by Chollet (1958); a ship's barometer registered a pressure fall of 0.62 in. Hg when overtaken by a waterspout. The only aircraft observations at close range before Rossow's 1968 effort was reported by Johnson (1944).

More recent observations show that waterspouts may originate from "trade cumuli, with tops no higher than 12,000 feet" (Riehl, 1965) and may occur below shallow stratocumulus clouds (Dunn, personal communication) and below small cumulus congestus in midlatitudes (Smith, 1956). Pronounced low-level instability and vertical wind shear are typically absent in the environment of South Florida waterspouts. Gerrish (1965) examined 11 yr of Miami radiosonde data to determine static stabilities associated with moist-season waterspout occurrence. He found shallow-capping inversions within about 6 hr of most waterspout events. Averaged data up to 6 hr before and 6 hr after a waterspout revealed slightly cooler, more unstable air below 700 mb before occurrence. Witschi (1957) found that winds aloft during funnel activity are relatively light, ranging from a mean of 7.2 kt at 1000 mb to 11.6 kt at 400 mb. No high-level winds greater than 40 kt were recorded, and no systematic pattern was evident for the wind direction at any level. Witschi concluded that most Southeast Florida funnel clouds are initiated along the "land-seabreeze front". This front is more pronounced on days with light, variable winds.

Brooks (1951) emphasized the importance of the lower boundary by noting that waterspouts often dissipate on reaching a shoreline. The author (Golden, 1968) observed a waterspout that, soon after landfall, resembled a large dust devil. Low-level circulation decreased rapidly while moving over land; the visible funnel expanded, became hollow and translucent, and gradually retracted into the parent cloud. However, this average-sized waterspout maintained its circulation while crossing some 1,100 yd of flat land and reformed after moving off the north shore.

Various researchers have prepared schematic diagrams of waterspout circulation with major disagreement over structural features, especially the sense of the vertical motions within and surrounding the funnel. Kinematic structural models, deduced from surface observations and suggested by Bundgaard (1953), Dinwiddie (1959), and Rossman (1960), all have their difficulties.

The data source for this report was primarily obtained from the 1969 Lower Keys Waterspout Project (Golden, 1970) which was, to some extent, influenced by the successful 1968 close-range observations reported by Rossow (1970).

In the following sections, we shall use both quantitative and qualitative analyses to show that Florida Keys' waterspouts undergo a five-stage life cycle. We then demonstrate that the waterspout life-cycle results from an optimum interaction of five scales of atmospheric circulation. Finally, we present a recent climatology of Lower Keys' Waterspouts (1958-1969 data), some theoretical implications of the new results, and assess the relationship of the waterspout to the tornado.

2. DATA SOURCES AND ANALYSIS TECHNIQUES

Data include conventional surface observations and time-lapse photography combined with high-resolution airborne photography of natural and artificial airflow tracers. Other important data sources are: (a) aircraft missions flown to map sea-surface temperatures, air temperature, and moisture distributions in the cloudline genesis regions; and (b) close-range airborne observations of funnel structure. Data sources are summarized in table 2.

Key West International Airport was the base of all operations during the 1969 waterspout field program because the primary investigation area was confined to the Lower Florida Keys. Twenty-two observers were selected for the observing network shown in figure 1.

Observations during field tests are summarized in table 3. The first indication of a spiral pattern on the sea surface was given June 17. In this as in other cases, the spiral pattern evolved with the development of the waterspout. Most waterspouts move in a fairly regular, gently curving path;

Figure 1. Volunteer ground-observing network during the 1969 Lower Keys Waterspout Project; eighteen are plotted, and there were four more on Key West, on opposite sides of the island relative to the airport.

Table 2. Summary of Data Sources

Source	Observation period	Sensor or data type	Sensor accuracy	Remarks
Key West, private aircraft	15 Jun - 8 Jul 69 25 Aug - 30 Sep 69	35-mm slide, Super-8 and 16-mm movie photography	10-20%	See photogrammetry (pp. 4-9)
		Artificial airflow tracers;		
		Temperature (outside air)	±0.5°C	Time-constant = 30 s
		Airspeed	±5%	
		Altimeter altitude	±10 ft	
NOAA-RFF, DC-6B aircraft	9 Oct 69	35-mm cloud cameras	range∿±0.4-1.0 n mi; h∿+200 m	See Herrera-Cantilo (1969)
		Vortex, Rosemount		
		Temperatures	±1°C(±0.5° relative)	See Friedman et al. (1970); and Duchon (1970)
		Cambridge dewpoints	+0.5°C	
		Infrared hygrometer	±5%	
		Radar altitude	±1%	
		Doppler navigation	±2 n mi ±1 n mi relative	
		Doppler winds	±3 kt; ±0.4° direction	
		True airspeed	±5 kt	
		Pitch/roll angle	±0.1°	
Navy Super-Constellation aircraft	6 Jun 70	LORAN with landmark/photo fixes	±2 n mi	
		PRT-4A infrared radiometer	±0.4°C	
		Air temperature and dewpoint	?	Used only for checks See McFadden and Wilkerson (1967), McFadden (1967), and Saunders (1970)
University of Chicago, Braham Lodestar aircraft	21 Aug 70	Flight track from radio-navigation, nose-camera, and 35-mm slides	±1 n mi	See Golden (1973c)
		Rosemount air temperatures	±1.5°C ±0.15°C relative	
		Cambridge dewpoint hygrometer	±0.5°C	
Purdue University, towed waterspout-probe aircraft	10-15 days each: Sep 70, 71	Air temperature anomaly, using doped crystal of bismuth telluride with a self-powered reference thermocouple;	±0.1°F	Sensor time-constant + 300 ms. See Church et al. (1973)
		35-mm and zoom-movie photography		

Table 3. Summary of 1969 Field Testing

Date	Flight Time (hr)	Flare-Drop?	Phenomena Encountered	Data Taken
16 Jun	2	No	Cumulus cloudline	Slides, 16-mm
17 Jun	2	Yes, 2 (improperly aimed)	4 waterspouts, one large, one anticyclonic, from 1515-1600 EDT near Big Pine Key*	Slides, Super-8; Zoom; PPI and RHI radar sequence
18 Jun	2	Yes, 1 (good near heavy shower)	Cloudline over Keys with heavy thundershower over Big Pine Key*	Slides, 16-mm; Turret-zoom of flare
19 Jun	2 3/4	No	5 small waterpouts, all cyclonic, 7 mi NW of Key West at 1635-1709	Slides, Super-8
23 Jun	2 3/4	Yes, 1	Large spray vortex in weakening stage (slow rotation)	Slides, 16-mm Turret-zoom air temperatures
24 Jun	1	No	Developing cloudline	
25 Jun	2 1/4	No	Cloudline with few heavy thundershowers	Slides, air temperatures
30 Jun	2 3/4	Yes, 4	9 waterspouts, 5 with spray vortex on sea surface	Slides, Super-8 zoom, and 16-mm
1 Jul	1 3/4	No	Good cloudline with 2 cumulonimbi along Keys between Key West and Big Pine Key	Slides only
7 Jul	2	Yes, 5 (3 caught up in circulation)	6 waterspouts in cumulus congestus cloudline 10-15 mi NW Marquesas, near same time and location as 30 Jun**	Slides, Super-8 and 16-mm zoom movies; air temperatures
8 Jul	1/2	No	Clouds died rapidly after takeoff	
TOTAL	21 3/4			

* Observed first spiral pattern on sea surface.

** Pronounced spiral pattern with dark spot, dropped flares on periphery; spiral pattern pair (both same sense and approximate size), with flare showing development of accelerated inflow and formation of spray vortex in one spiral.

experience has demonstrated that once a sea-surface wake forms, it can be used to indicate the desired placement of the smoke plume tracers. Another important observation is the "dark-spot" phenomenon discussed in section 3.2. Early confusion between dark spots and shower-produced, striated outflow patterns on the water is eliminated by two dark-spot characteristics, a persistence and similar appearance at all viewing angles and in all lighting conditions.

During the 1969 project, 54 sequences of WSR-57 radar Plan-Position Indicator (PPI) film were collected for known waterspout occurrences. Some concurrent Range-Height Indicator (RHI) scans allowed determination of heights and growth characteristics of parent cells. A short-pulse WSR-57 PPI presentation of a waterspout-active cloudline is shown in figure 2. The pronounced spike protruding outward from the western echo boundary corresponds to two aircraft-documented waterspouts. Most radar data were taken in the special short-pulse, short-range mode to obtain higher resolution.

Analysis of film segments to obtain natural and artificial air-tracer motions is divided into two parts, scaling and tracking. Techniques drawn from Fujita's (1960) study of the Fargo tornadoes were used to derive tangential speed profiles. The Manual of Photogrammetry (1966), Volumes I and II, was also consulted.

Cloud-base height measured by the aircraft altimeter and known camera characteristics were used as reference for the scaling. Calculated-spray vortex diameters were weighted, depending upon transparency resolution, contrast, and time proximity to a tracked movie sequence. From known surface-spray vortex dimensions, it was possible to track spray plumes and particles at various radii for one or more vortex resolutions. Angular velocities of the air-spray mixture at various radii were obtained by use of a frame-counter or stopwatch.

Mean-angular aircraft velocity as it circled the waterspout was computed from the indicated airspeed and slant range found from: (a) the time required to complete one-quarter revolution around the vortex obtained from the movie sequence; and (b) camera framing tests on a nearby 1,000-ft radio antenna. The two methods agreed within 2 percent and the first method was generally used for 1969-70 waterspouts. In a few cases, the aircraft did not circle the waterspout, but rather passed the funnel on a diagonal fly-by. For these observations, the aircraft track relative to the waterspout was reconstructed by computing the angular displacement rate of background clouds and land-

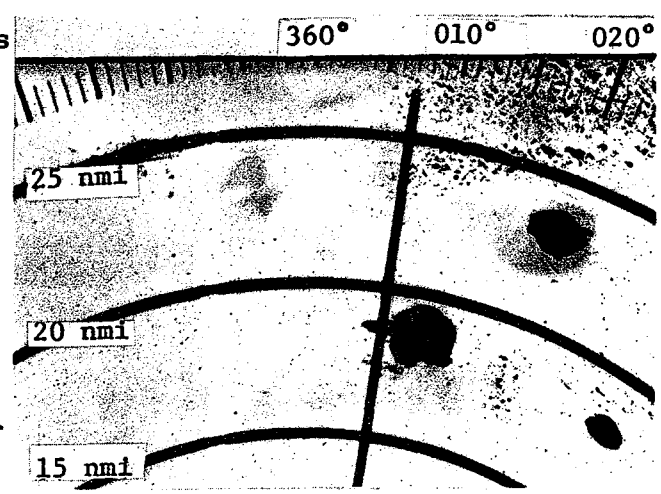

Figure 2. Key West WSR-57, September 4, 1970, at 1528 GMT. Two waterspouts reported by research aircraft at 18 NNE, began at 1517 and ended at 1533 GMT. Short-pulse, 1.5° tilt. Both waterspouts were located in westward "spike" protrusion which often appears as a signature of waterspout activity.

marks relative to the line through the waterspout.

A new analysis technique has been devised to obtain the vector motion field in the waterspout and the spray vortex, utilizing aircraft film. This technique employs Fujita's (1970c) system of gridding and rectifying photographs in a time-sequence. Frames are rephotographed on a special hole-punch easel to produce time-lapse movie loops for detailed analysis. Three 1969 cases were selected for application of this technique. In one case, the inner ropelike funnel retained a nearly constant diameter during the observation period. Because of this feature, it was possible to prepare a sequence of normalized enlargements in which the inner funnel diameter was held constant. Each normalized enlargement was gridded, using the horizon, the slowly changing orientation of the inner funnel, and the background clouds for reference. In this manner, a loop was produced that removed the aircraft bumps and displacements relative to the funnel. The outer funnel diameter at horizon level was determined from two transparencies taken at right angles a few minutes before the movie sequence.

Movie loops were prepared for spray vortex cases by making enlargements of selected aircraft film. Grids for each print sequence were prepared, using waves, wave-trains, and portions of the wake away from the spray vortex as reference. Features which evolved and moved slowly over the sea surface were interpolated on the grids. Transparent copies of the grid were positioned over each print. After correct orientation was established, the gridded sequence was rephotographed to produce the final loop. Each loop encompasses about 1 or 2 s of real-time. The analysis technique concerns systematic tracking of features such as spray aggregates, "holes" in the spray, cloud tags, and "holes" in the funnel walls to obtain particle trajectories. Application of this technique before tracer analyses greatly improves resultant trajectory resolution and accuracy.

A cooperative effort with the Key West Weather Service Office to document both waterspout-active and nonwaterspout cloudlines with ground-based time-lapse photography contributed greatly to the study. We hoped to document, with the vital support of the Weather Service personnel, the complete evolution of building cumulus cloudlines. The observer was asked to zoom the camera on sighted funnels to document its life history and motion relative to neighboring showers. Time and camera azimuth were documented on the film. In mid-September, two wide-angle cameras were added to the program. The time-lapse program was important because more than 50 separate sequences of cloudline development and growth with subsequent waterspout formation were obtained. Additionally, some sequences overlapped aircraft measurements in the same cloudline or waterspout system.

The basic scaling factor was cloud-base height above the apparent horizon. Cloud base was determined from altimeter measurements in one case and by evaluating official estimates from sounding data and pilot reports in the two other cases. Cloud-base heights used for scaling are considered accurate within 100 ft. Azimuth and range of various cloudline elements were determined from short-pulse radar echoes and theodolite measurements on known landmarks. Individual frames at 10-frame intervals in the time-lapse sequences were scaled, using the known cloud-base height. Cloud turrets and

cumulus "bubble caps" were measured and growth rates for each 10-frame interval were tabulated for the appropriate cloudline section.

Marine smoke flares were found to be very effective. In one case, four marine smoke flares were dropped on the sea surface around a giant waterspout. Vector displacements of perturbations in the upper and lower edges of the plume were photogrammetrically calculated at successive 10-frame intervals. Perturbations traveling along each smoke plume were tracked on movie film until diffusion made the perturbations indistinct. Perturbations near the source were symmetric and in-phase on the upper and lower edges of the plume. However, it was apparent that substantial vertical shear was present in the ambient boundary-layer flow through the depth of the plume. Scaling was similar, but less accurate, than for natural tracers. Smoke-plume trajectories relative to the aircraft track were derived, and mean speeds of perturbations along the upper and lower edges of plumes were plotted.

Instrumented aircraft flights are listed in table 2, together with sensor or data types and sensor accuracies. Data taken during each flight have been composited over time periods ranging from 1 to 30 min. Primary concern in data analysis has been the accurate depiction of maxima, minima, and strong gradients in the meteorological fields and the location of these features relative to the cloudline, waterspout, or islands. Absolute values of parameters have been checked, when possible, for consistency with other data sources.

Aircraft participating in various data collection efforts include two Key West private aircraft, the University of Chicago (Braham) Lodestar, a Navy Super Constellation, a NOAA Research Flight Facility (RFF) DC-6B, and the Purdue University probe aircraft. Details on data reduction and analysis procedures for these flight data were given by Golden (1973c). In summary, data from several different sources, taken at different times, have been composited, and the representativeness of specific features and of conditions for each flight and waterspout case has been assessed.

3. THE LIFE CYCLE OF KEYS' WATERSPOUTS

3.1 Overall View

Previous observational literature on waterspouts gives no hint of a coherent life cycle for waterspouts. Probably the most important discovery during the 1969 Lower Keys Waterspout Project was that waterspouts of all sizes and intensities undergo a regular life cycle. This waterspout life cycle has five discrete, but overlapping stages: (a) the <u>dark spot stage</u>, characterized by a prominent light-colored disc on the sea surface, surrounded by a dark patch diffuse on its outer edges--the dark spot may or may not have a small funnel cloud above it initially, but does represent a complete vortex column extending from cloud base to sea surface; (b) the <u>spiral pattern primary growth stage</u>, characterized by development of alternating dark- and light-colored bands spiralling around the sea-surface dark spot; (c) the

spray ring (incipient spray vortex) stage, characterized by a concentrated spray ring around the dark spot, with a lengthening funnel cloud above; (d) the mature waterspout (spray vortex) stage, characterized by a spray vortex of maximum organized intensity, the gradual weakening of the spiral pattern, with maximum funnel cloud length and diameter; (e) the decay stage, characterized by a waterspout that dissipates (often abruptly) as cool downdrafts from a nearby rainshower intercept it.

Not every waterspout observed from its inception continued to evolve through all other stages; however, combinations of stages 1-2-3-4-5, 1-2-5, 1-3-4-5, and 1-5 have been documented. A few typical 1969-70 cases are presented in subsequent sections and summarized in table 4. Stages 1 and 4, having the greatest duration range, often comprise the bulk of a waterspout's total lifetime.

3.2 Stage 1: The Dark Spot

Ninety-five waterspouts were documented by aircraft during the 1969 Lower Keys Waterspout Project; 86 had condensation funnels, of which 66 initially were observed as dark spots on the sea surface. The remainder, 20, already had evolved past the first stage or were observed as distant funnels. In some cases four or five dark spots initially were present in a very localized area. Only one subsequently became a mature waterspout. Multiple dark spots usually were positioned quasi-linearly beneath one flank of the parent cloudline. In general, just one waterspout event was logged for each multiple dark-spot situation. Exceptions occurred when dark spot "eddies" with definite rotation were observed over very shallow water. These systems were listed as separate waterspouts. Although a funnel cloud may appear if the waterspout progresses through its life cycle, there are many more dark spots than funnels. Throughout the field observations, dark spots always were seen with a cumulus cloud above.

It is important to note that dark spots never could be observed from the earth's surface. This implies that the average 14.6-min lifetime for funnel events (recorded at the Key West Weather Service Office, 1958-67) likely was biased toward larger funnels and would generally exclude the first stage of the life cycle. Including the first stage would undoubtedly add from 1 to 13 min to the lifetimes of those waterspouts observed from the ground. Small short-lived funnels (7.7-min average duration) were seen from the aircraft in 1969; however, a wide spectrum of funnel sizes was observed. About 30 percent of the funnels were the narrow, ropelike variety which easily might be missed in surface observations.

After some flight experience in dark spot recognition, it was noted that dark spots frequently appear in multiples of two, four, and even six simultaneously. (Even multiples seem more common than odd multiples of dark spots. As some of these dark spots evolved further in the life cycle about 90 percent were cyclonic.) These observations suggest (but do not prove) that multiple dark spots form along a quasi-vertical vortex sheet and therefore are caused by a shearing instability. The frequent occurrence and multiple nature of dark spot activity became even more apparent during the week of operations with the Purdue University Tornado Group, September 1970. The average life-

Table 4. 1969-70 Statistical Summary of Documented Stages in Waterspout Life Cycle

Stage	#1	#2	#3	#4	#5
Major Feature	Dark Spot	Spiral	Spray Ring	Spray Vortex	Decay
1969: Of 95	66 initially observed in stage #1	16 had spirals, and smoke flares showed circulation on this scale in several other cases	56 attained the sustained stage #3; short duration, transitional stage	51 reached this stage	51 decayed as heavy showers or cool outflow overtook spout; also 33 dark spots simply decayed by fading away
1970: Of 33	All initially observed in stage #1, and 17 had an associated funnel at some time in life cycle; V_{max} = 20-30 kt in broad band just outside circular light-colored disc	Only 7 evolved to this stage and beyond; d_s + 500 - 3,000 ft	$V_{max} \geq 45$ kt in narrow band around dark spot periphery	86 had an associated funnel at some time in life cycle; $V_{max} \leq 170$ kt in in sharply defined peak just outside "eye" of spray vortex in bright band of concentrated spray	Some spiral rain curtains observed around decaying waterspouts
Duration range of stage: (1969-70)	t_1 = 1 - 22 min	t_2 = 2 - 7 min	t_3 = 1 - 2 min	t_4 = 2 - 17 min	t_5 = 1 - 3, up to 7 min

time of individual 1969 dark spots ranges from 1 to 22 min (the latter was associated with an intense anticyclonic waterspout). Dark spots may appear as close together as 100 ft, but only persist in this juxtaposition from 5 to 7 min. In general, no apparent feature distinguishes a dark spot which will develop into a mature waterspout from the majority which slowly expand and diffuse. However, the appearance of a funnel cloud above the dark spot (allowing for some vertical tilt) indicates strongly that development will proceed.

The higher ratio of dark spots to waterspouts in stage 2 or beyond for 1970 than for 1969 (table 4) results partly from delay in recognition of the significance of dark spots. One of the important contributions of the 1969 field program was the linkage of the dark spot to a waterspout life cycle. Dark spots can remain quasi-stationary or move slowly, and the apparent visual structure of a dark spot remains the same at all viewing angles, that is, it is independent of sea surface albedo.

Artificial tracer experiments, using marine smoke flares dropped from a low-flying aircraft, were used to determine dark-spot flow characteristics. Accurate smoke flare placement for subsequent interaction with a traveling dark spot was achieved on September 23, 1969 (fig. 3a and 3b).

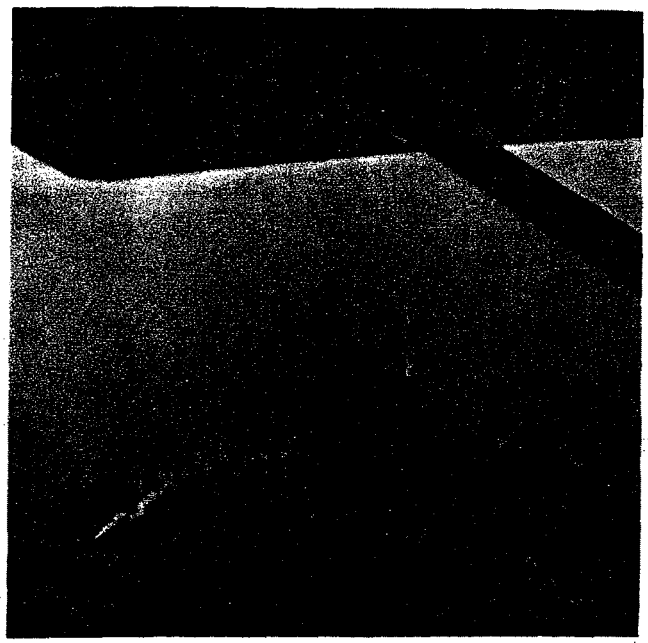

Figure 3a. View from aircraft; looking NE at two marine smoke flares and dark spot (center right), just before the interception by the dark spot of the second smoke plume as the plume moved into plane of picture. Note cyclonic bending and inflow into dark spot indicated by first plume.

Figure 3b. Taken approximately 15 s after fig. 5b, showing nearly complete closed-cyclonic circulation around the dark spot boundary, with major portion of smoke plume being advected away by the gentle northeasterly environmental boundary flow.

As the dark spot continued to move north-northeastward, the second plume continued to be drawn into the circulation from as far away as 760 m. As it spiralled upward around the dark spot to a height of 180 m, the smoke gradually evolved from hollow cuplike to hollow cylindrical shape with gradually expanding diameter. The slight slope of this "tapered cylinder" in the direction of the dark spot's movement agrees with several of Sinclair's (1966) dust devil observations. Figure 4 schematically represents the flow field inferred from smoke plume trajectories. Subsiding air in the broad dark-spot core occupied at least the lower portion of the vortex column, and the vertical flow maintained the hollow structure of the smoke column.

In a few cases (events #285 and #316, app. A), organized rotation was documented in dark spots which formed over very shallow water. Dark spot "eddies" were made visible by wavelet striations in the dark patch surrounding the inner light disc. The striations could be seen clearly forming and rotating (cyclonically) around the right semicircle of the light disc.

Organized rotation could not be detected, either visually or in slow motion projection of the film data, in any dark spots which formed over water greater than 2 m deep. Even in the large dark spot of figures 5a and 5b, that formed in water 40 to 50 ft deep, only horizontal cyclonic shear could be detected across the dark spot region. Estimates made from high-resolution motion-picture data yield a maximum horizontal shear of about ±15 m/s across the 90 m diameter of this dark spot. This estimate was made by tracking water waves produced by outflowing, relatively cool air from a nearby developing rainshower in the cloudline. Wind-driven water waves of short wavelength and of small amplitude (not the swells shown in fig. 5a and 5b) could be seen penetrating through the inner light circle of the dark spot on telephoto movie data.

The dark spot represents the downward termination of a complete waterspout vortex column. Photogrammetric estimates on the circulating smoke plume reveal that a broad speed maximum of 5 to 10 m/s occurred midway between the inner light-colored disc and the outer extent of the surrounding dark area (about 70 ft from the center). The inner light-colored disc is deduced to be a region of light, variable winds with a flat, nondisturbed highly reflective sea surface. Available evidence indicates that the low albedo of the surrounding dark patch is caused by locally produced capillary water waves. However, the precise physical explanation for the visual structure of the dark spot will remain in doubt until detailed measurements of boundary layer flow, ocean wave microstructure, and sea-surface temperatures in the dark spot can be made.

3.3 Stage 2: The Spiral Pattern

The spiral stage is characterized by a series of alternating dark and light streaks which form an unmistakable sea-surface spiral pattern around the dark spot. Frequently, the spiral pattern initially has one major dark bank which emanates from a nearby shower (the shower itself is sometimes contiguous with the spiral pattern around a 120° arc, with the major dark band forming the outer spiral boundary; examples include events #285, #289, #310, and #373, app. A). Sixteen spiral patterns were documented during the 1969 field program. Although the number appears relatively small, two reasons

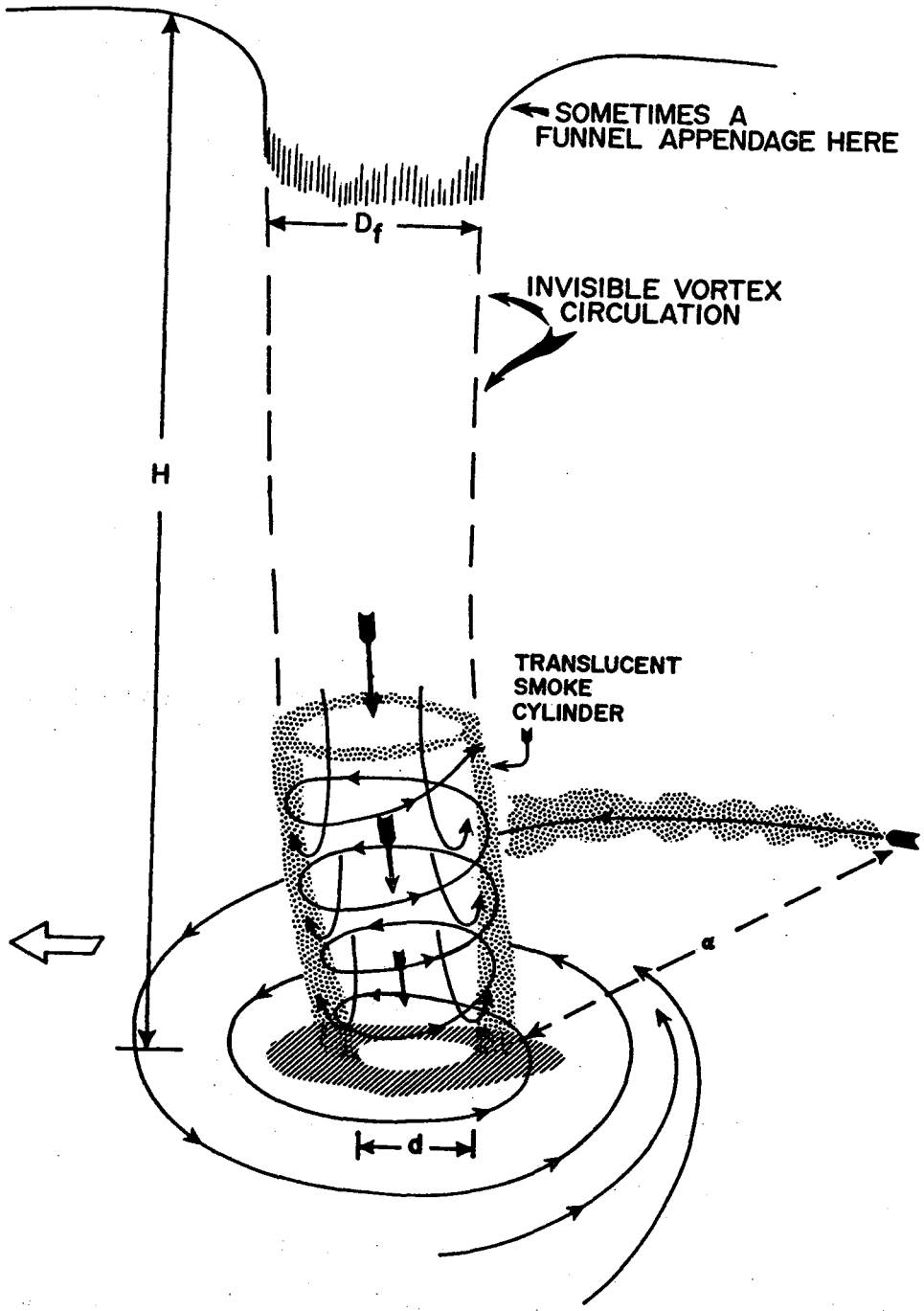

Figure 4. Composite structural-flow model for the dark spot stage of the waterspout life cycle. Compare with figures 5a and 5b. Characteristic range of scales is: H(cloud base) = 550 to 670 m MSL, D_f (maximum funnel diameter) = 3 to 150 m, d = 3 to 45 m, and α = 15 to 760 m.

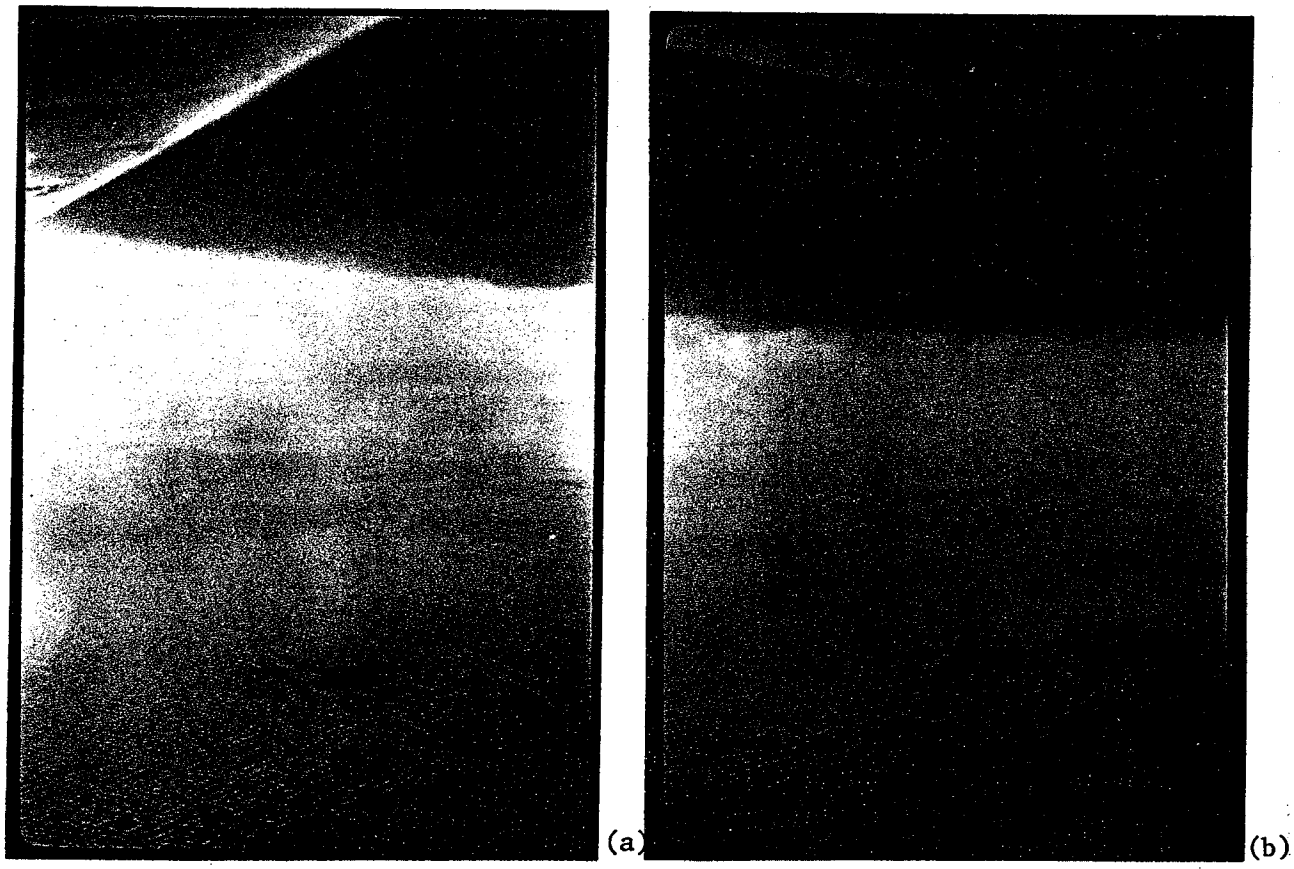

Figures 5a and 5b. Development of large funnel over preexisting dark spot (September 10, 1969).

necessitate this phenomenon as a separate stage in the waterspout life cycle: (a) several waterspout events during 1969 exhibited ill-defined or short-lived spiral patterns not included in the above statistics (examples are events #9 and #26--the latter produced a possible anticyclonic spiral); and (b) with one or two exceptions, every observed 1969-70 waterspout that reached the spiral pattern stage continued to evolve through the complete life cycle, becoming an intense waterspout. Note that although Rossow (1970) never mentions a spiral pattern with his aircraft observations of 79 small waterspouts, his photographs clearly indicate a large spiral pattern around the spray vortex of a large, double-walled waterspout (cf. Rossow's fig. 10).

Flare data and other observations suggest that horizontal convergence increases significantly once the spiral pattern forms around a dark spot. As the spiral pattern becomes established, relative vorticity increases at some limiting radius in a horizontally converging flow until development proceeds to stage 3.

The duration of the spiral pattern stage is difficult to determine because it wraps around a preexistent dark spot from afar. Only half of the 16 documented spiral patterns were observed from initial dark spot to surrounding spiral pattern stage; the remaining eight were spotted from the aircraft

at a distance (up to 5 n mi away). The spiral pattern is so large (150 to 920 m diameter on the sea surface), compared to the funnel cloud and dark spot combination, that it can be readily detected at great distances from an aircraft. Smoke plume data consistently suggest that the physical mechanism for spiral banding is similar to that hypothesized for the dark spot: localized generation of capillary waves.

Waterspouts which passed through the spiral pattern stage had durations ranging from 5 to 28 min, with a mean of 11.1 min. This compared with a mean total lifetime of 7.7 min for the other 80 waterspouts.

During the evolution of the waterspout from stage 2 to 3, the dark spot becomes more pronounced, with the dark bands of the spiral extending inward toward the dark spot. As the same time, the brightness contrast between the inner light-colored disc of the dark spot and the surrounding dark patch increases dramatically. The inward extent of spiral banding relative to the outer dark-spot boundary ranges from 30 to 240 m. Finally, within a minute or two, a concentrated spray ring forms around the perimeter of the light-colored disc of the dark spot. The development of the large spiral pattern for the third and largest waterspout of September 10, 1969, is shown in figures 6a and 6b, and the evolution of this waterspout to stage 3 is shown in figures 6c and 6d. (See the dark spot stage for this case in fig. 5a and 5b.) The sequence begins with the first visual indication of a dark east-west band on the sea surface beneath the southwestern flank of the cloudline (fig. 6a). This dark band began to elongate toward the east and northeast around the dark spot, and by 1154 EDT (Eastern Daylight Time) curved in a semicircular arc around an incipient spray ring (fig. 6b). By 1156 EDT, the funnel was wider and longer and was pendant from a cyclonically rotating collar cloud (fig. 6c), and a complete spiral pattern had developed from the preexistent dark band on the sea surface by 1157 EDT (fig. 6d). Overall, the spiral pattern slowly shrunk from 1154 EDT onward.

The dark spot stage represents the waterspout embryo, and the spiral stage represents the primary growth phase in which the vortex intensifies with simultaneous expansion of its radius of influence in the surface boundary layer. To test this hypothesis, marine smoke flares were carefully dropped around the periphery of a few selected spirals. The results for some spiral patterns were somewhat complicated. A few illustrative cases with quantitative assessment of plume displacements are presented in the next section. A schematic model for the spiral pattern stage is given in figure 7. Note that a "collar cloud" structure (Fujita, 1960) sometimes forms during stage 2. The visible condensation funnel generally lengthens downward during this stage and often expands. The preexistent, dark-shear band from which the major outer band of the spiral evolves is not always observed, especially in the smaller spiral cases.

3.4 Stage 3: The Spray Ring

Fifty-six of the 95 documented cases reached this stage, and 40 of those did so apparently without passing through stage 2. The derived-tangential windspeed profile through the large Matecumbe waterspout (fig. 14) reveals that the spray-air velocities at the outermost edge of the spray

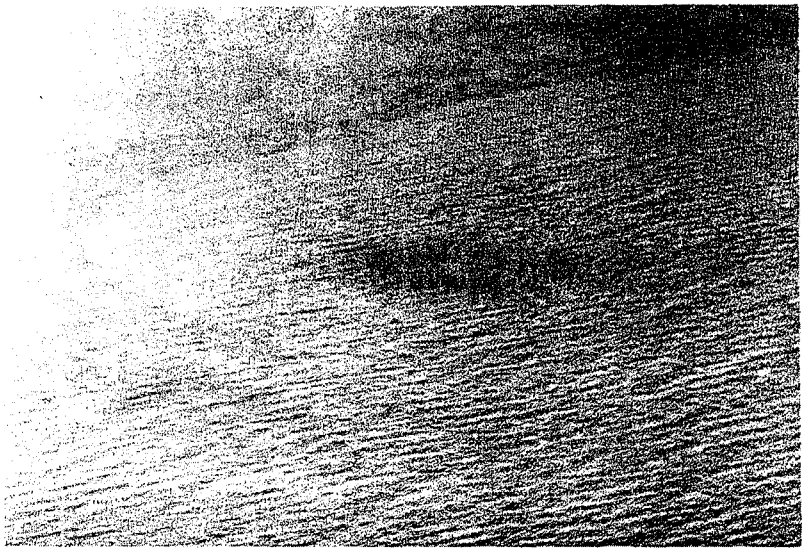

Figure 6a. Beginning of spiral pattern stage of giant waterspout on September 10, 1969; looking SW at 1152 EDT.

Figure 6b. Incipient spray ring and elongation of dark shear band around eastern semicircle of vortex; looking S at 1154 EDT.

Figure 6c. Upper portion of lengthening funnel and peripheral — rotating collar cloud at 1156 EDT.

Figure 6d. Preexistent shear band (far left) and newly developed spiral pattern at 1157 EDT; looking W.

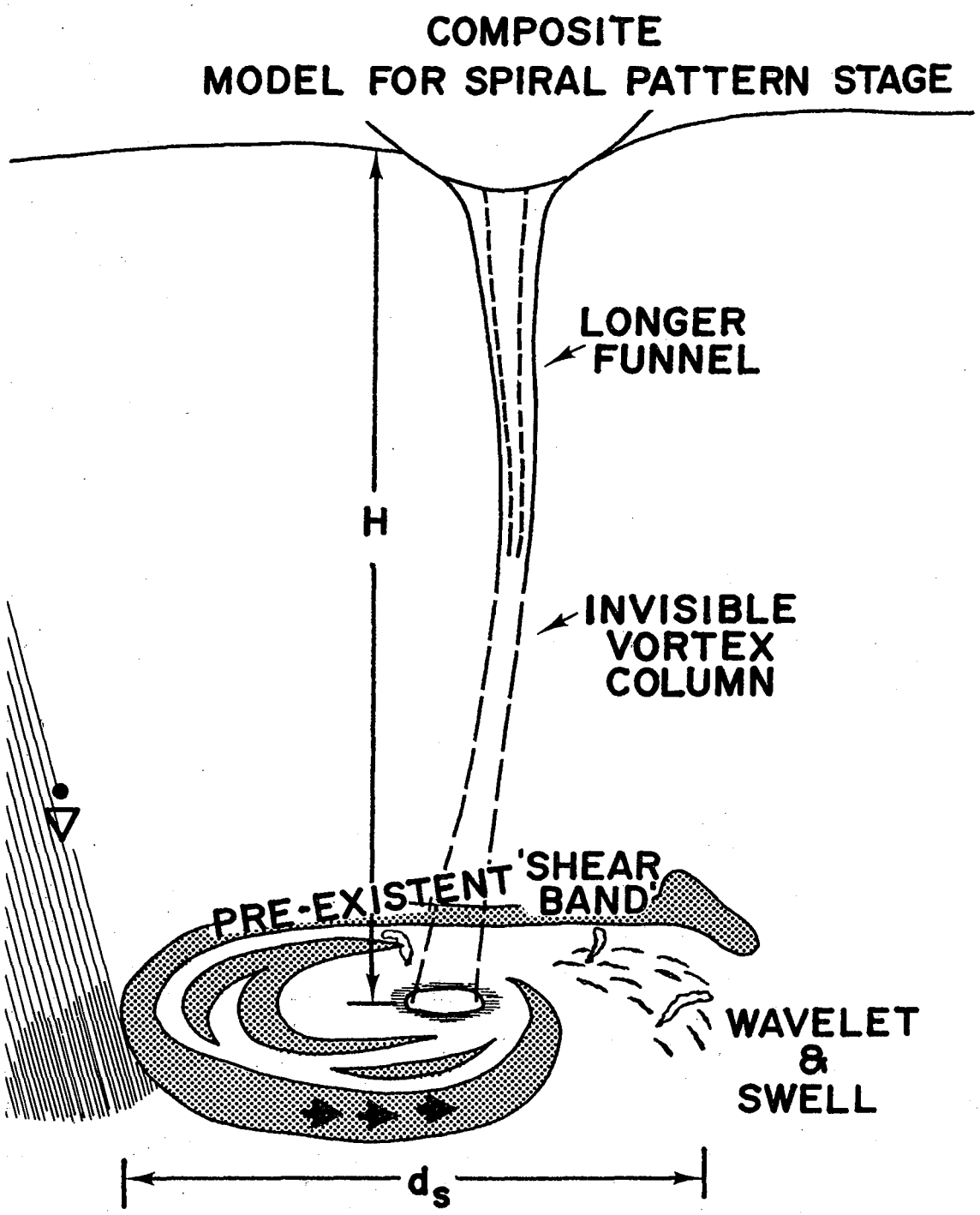

Figure 7. Composited schematic model for the spiral pattern (stage 2) in the waterspout life cycle. Vertical scale is contracted, H (cloud-base height) varies from 550 to 670 m MSL, and d_s varies from 150 to 920 m. Bold arrows in spiral indicate that major band evolves around dark spot during this stage.

vortex (r = 36.5 m) averaged about 22.5 m/s. This is the (straight-line) windspeed quoted in the U. S. Navy Hurricane Reconnaissance Manual as the minimum necessary to pick up spray off the sea surface in developing tropical storms. (This is also the theoretical windspeed value for Kelvin-Helmholtz instability to occur on an air-water interface-- Lamb, 1945)

During the period encompassed by the spiral and spray ring stages, the condensation funnel diameter often increases by a factor of two. The reasons for this are probably the increased moisture available for condensation in the vortex column caused by inflow on the spiral scale and the decreased pressure in the developing vortex core. Moreover, after horizontal funnel expansion becomes evident, a secondary growth phase begins during which the funnel cloud lengthens downward.

The spray ring forms rapidly around the preexisting dark spot and is the shortest lived portion of the life cycle, lasting only a minute or two. Note in figures 6b and 6d that the spray ring forms just outside the circular light-colored inner region of the dark spot.

Apparently, the spray ring stage marks the time when angular momentum reaches a critical value in an annulus surrounding the dark spot and is accompanied by a gradual speed increase in the belt of maximum tangential winds. The critical value necessary for spray pickup is attained, and a pulsating spray ring forms in a progressively narrower circle surrounding the dark spot. Once the spray ring has developed, the lower waterspout vortex column begins to move with a steady increase in funnel tilt. Finally, during the latter portion of this stage (and continuing through the first half of stage 4), the spiral pattern shrinks and the internal banding gradually disappears.

A three-dimensional schematic model for the spray ring stage is shown in figure 8. Note that the spiral pattern is still present, and the funnel is both longer and wider than in stage 2.

3.5 Stage 4: The Mature Waterspout

This stage is characterized by maximum intensity and organization. Maximum intensity means that rotational speeds in the wind belt around the spray vortex eye and the rising motions in the funnel cloud wall and spray sheath reach peak values. In terms of organization, the condensation funnel grows to its maximum diameter and length (in a few cases during 1969-70, a double-walled funnel formed during the first half of the mature stage). The spiral pattern with weak internal banding shrinks and just one or two major dark bands define its outer boundary. The vertical tilt (noted initially in stage 3) continues to increase while the lower half of the vortex column moves faster than the upper funnel portion. The propagation speed of spray vortices in this stage ranges from 3 to 8 m/s; and a few waterspouts have speeds near the surface of up to 15 m/s for short periods later in the mature stage. Frequently at these higher propagation speeds, erratic spray-vortex motion accompanies intensity fluctuations. In some cases, relative location is such that the waterspout moves away from the shower in a direction nearly perpendicular to the cloudline and lower level mean-flow. In a few such cases,

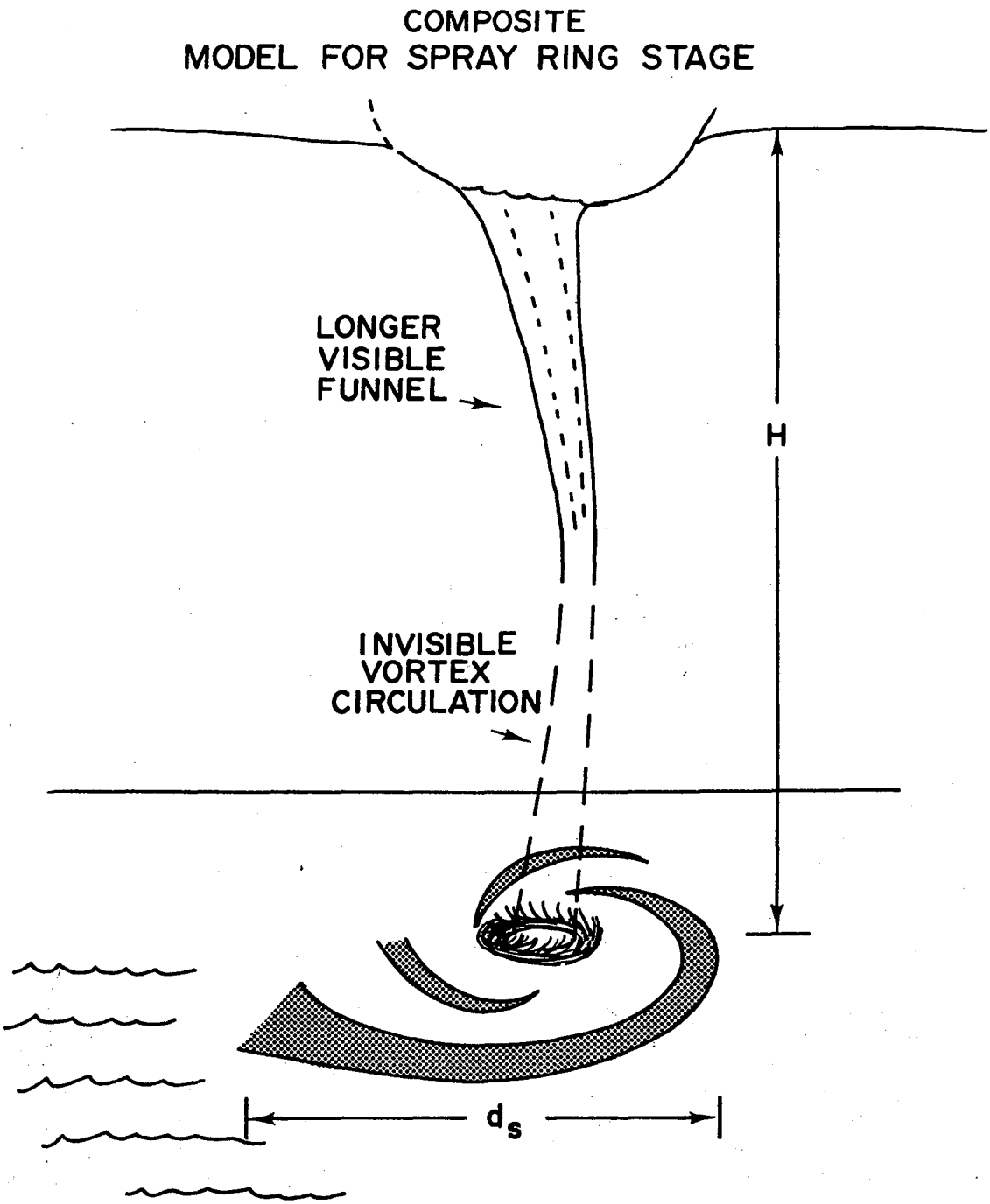

Figure 8. Composited schematic model for the spray ring (stage 3) of the waterspout life cycle. The vertical scale is contracted, H varies from 550 to 670 m MSL, and d_s from 45 to 260 m. See section 3.4 for details.

the waterspout continues moving away from the cloudline edge for several hundred yards before finally dissipating. Thus, the funnel becomes greatly tilted and contorted, so that the spray vortex and lower funnel are in strong sunlight with clear skies overhead. Such cases are rare, but may illustrate a source of mariners' reports of "water devils."

Mature waterspout duration ranges from 2 to 17 min for the 1969 cases, and the dark spot and mature waterspout stages together comprise 70 to 80 percent of the average lifetime. The mature stage of the giant double-walled waterspout of September 10, 1969, is illustrated in figure 9. Life cycle stages 1, 2, and 3 for the same waterspout are shown earlier in figures 5 and 6. This waterspout entered the mature stage at around 1158 EDT. The rope-like funnel extended almost to the sea surface to meet an intensifying spray vortex and developing spray sheath at 1159 EDT (fig. 9a). As large quantities of spray were spiralling higher in the spray sheath, a secondary outer funnel wall developed downward from cloud base between 1159 to 1202 EDT (fig. 9b and 9c). During peak intensity, the waterspout had an inner funnel diameter of 8 ± 1 m and outer wall diameter of 30 ± 3 m (fig. 9d and 9e). The outer funnel is hypothesized to be the result of locally enhanced moisture content in the air outside the original funnel caused by spray evaporation.

The evolution of the spiral pattern during the mature stage is also seen in figure 9. Notice that the spiral pattern gradually shrunk in major chord-width with time.

The first detailed aircraft observations of a series of three waterspouts were obtained near Lower Matecumbe Key, Fla. (Woodley et al., 1967). Two cyclonic waterspouts, in the mature stage when first observed, have provided quantitative analyses of the structure and kinematics of mature waterspouts (Golden, 1968, 1971).

Important mature waterspout characteristics, initially deduced from the Matecumbe data, have been verified by the 1969-1970 field observations. These structural features include the visible funnel's hollow core, an outer "spray sheath" at low levels, a sea-surface wave-train, and a long, persistent narrow wake of disturbed sea water. The spray sheath outlines an intense rising annulus, surrounding the visible funnel, whose upward extent depends upon the mass of spray droplets, air resistance, and the total air velocity field. Maximum tangential winds occur at a radius generally just outside the "eye" region (see fig. 10), where the spray sheath rises out of the spray vortex. Maximum radial inflow occurs near the right-rear quadrant relative to the moving vortex (cyclonic cases). Periodically, the (cyclonic) spray vortex exhibits relative outflow in its left-front quadrant during peak intensity. Wind-generated waves on the sea surface form primarily to the right for cyclonic rotation (left for anticyclonic) and perpendicular to the trailing wake. Observations suggest that formation and persistence of the wake are intimately linked to the large pressure drop moving over the sea surface causing certain dissolved gases to effervesce. This process could form a narrow trailing band of tiny carbon dioxide bubbles in a thin surface layer as suggested by Keeling's (1968) oceanographic data. Also, the large wind shear at the spray vortex eye's edge, in combination with subsiding core air, promotes mixing of air bubbles into the sea. This

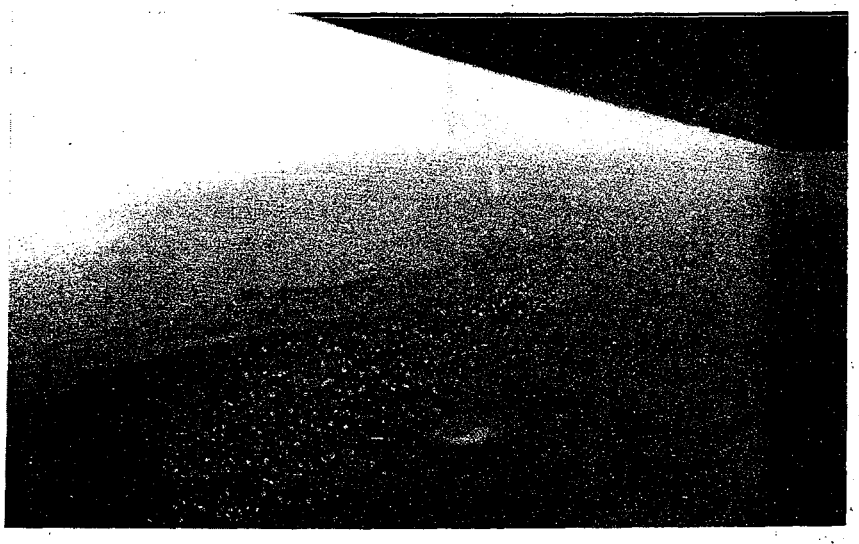

Figure 9a. Mature stage --spray vortex, rope-like funnel, and complete spiral; looking NE at 1159 EDT.

Figure 9b. Looking SE at 1200 EDT.

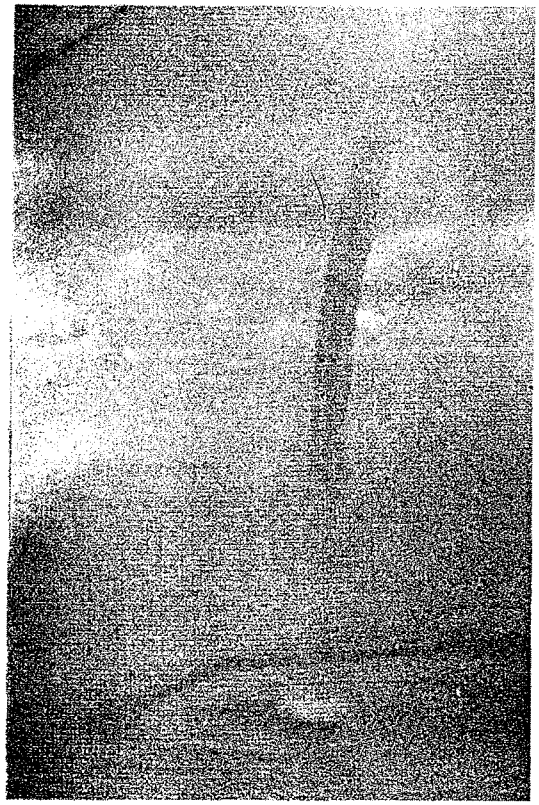

Figure 9c. Double-walled funnel, two-thirds complete; looking NW at 1202 EDT.

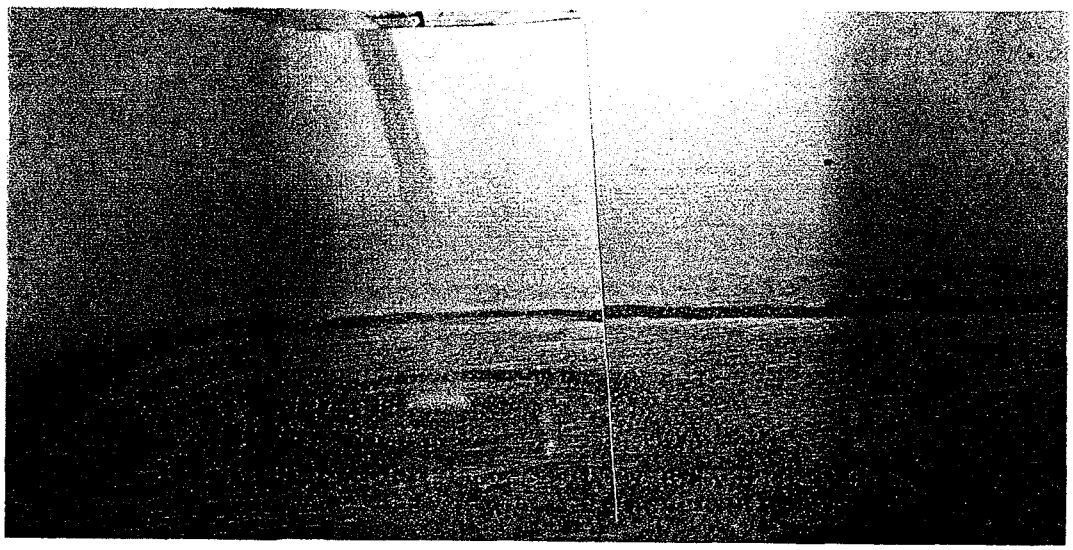

Figure 9d. Looking SE-SSW at 1203 EDT; note two smoke flares at far right.

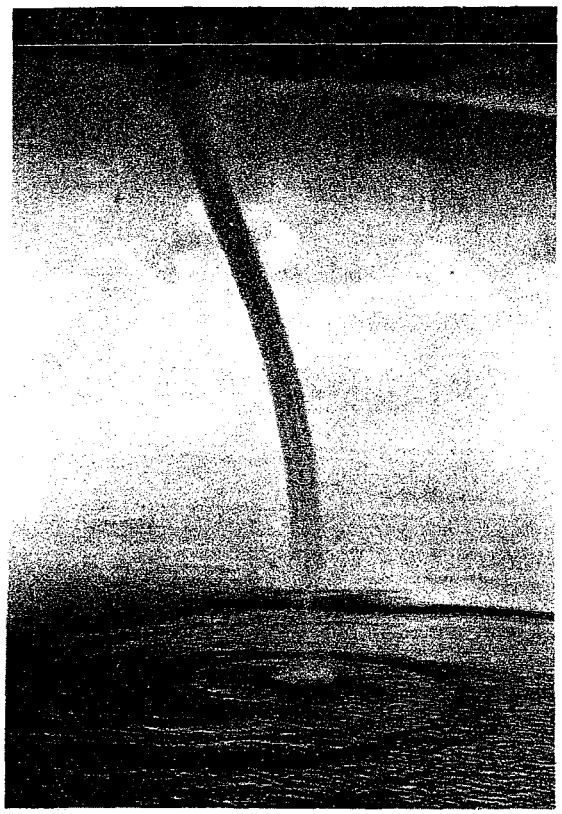

Figure 9e. Looking S at 1203:30 EDT. Complete double-walled waterspout.

Figure 9f. Full-length view of giant single-walled waterspout, with two flares; looking NE at 1204:30 EDT.

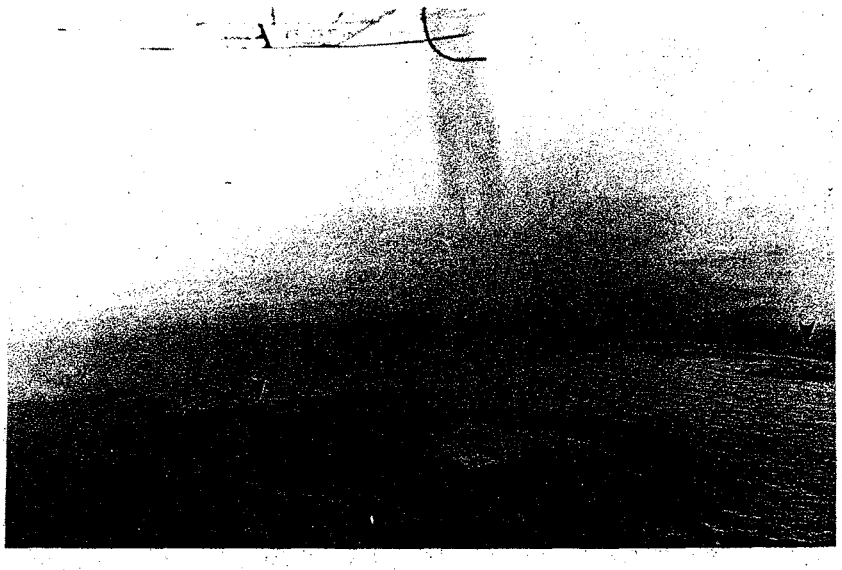

Figure 9g. Lower portion of funnel, spray sheath, and spray vortex with eye; looking ESE at 1205 EDT.

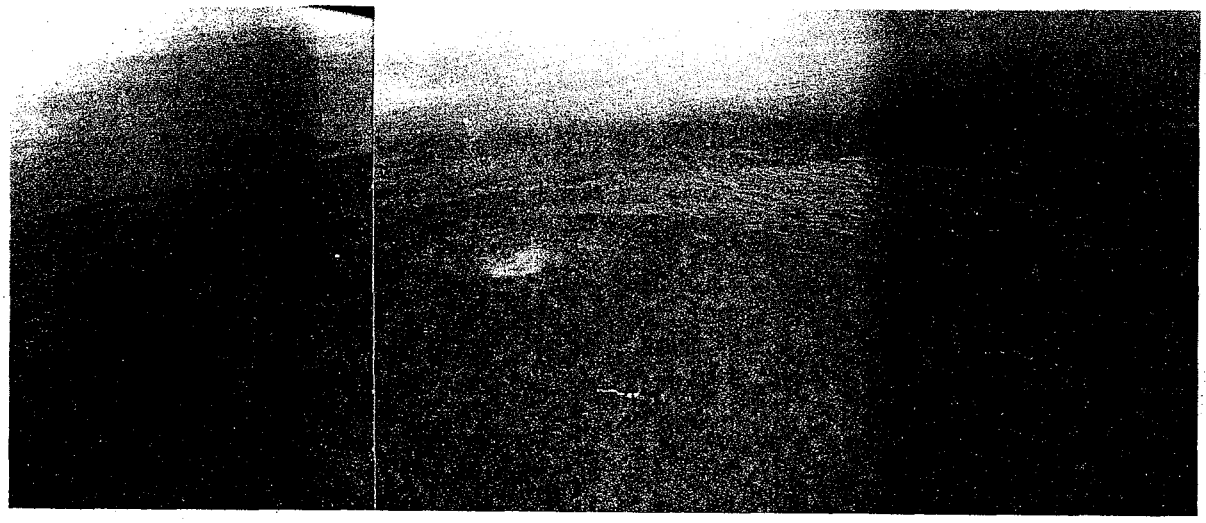

Figure 9h. Mosaic showing tight spiral, spray vortex with eye, shower boundaries (arrows), and two flares in outflow; looking ENE at 1205:30 EDT.

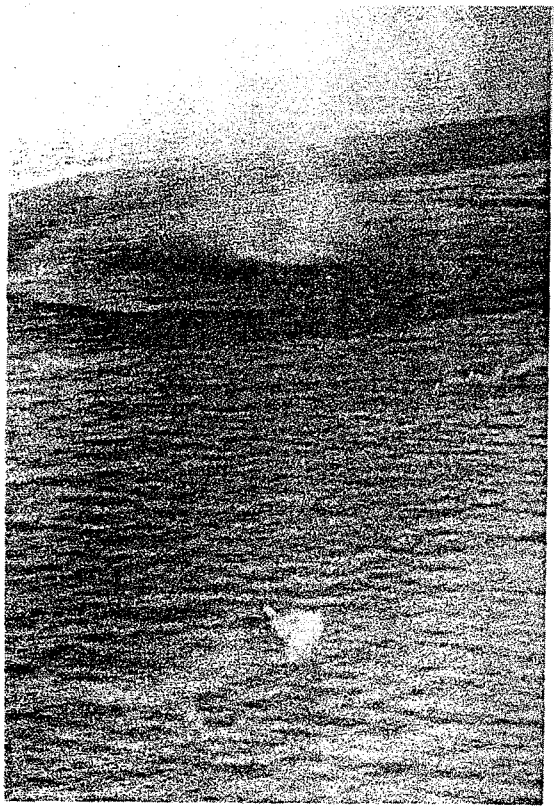

Figure 9i. Spray vortex and weakening spiral pattern, after interception of flare "A" by spiral edge; looking NNW at 1206 EDT.

mechanism is supported by the tendency for initial wake production to occur in the righthand semicircle of the eye, relative to the direction of (cyclonic) vortex motion.

The analytical results on waterspout structure and circulation during the mature stage have been assimilated into the three-dimensional composite model shown in figure 10. The tentative shape of the temperature anomaly profile through the hollow funnel of a mature waterspout, as derived from collaborative work with the Purdue University Tornado Group, is included. Preliminary analyses of temperature traces give positive temperature anomalies in the double peaks averaging to 0.3 to 0.6° C and ranging up to about 2.2° C for large waterspouts. Figure 10 may be compared with the model based on the large Matecumbe waterspout (Golden, 1971).

3.6 Stage 5: The Decay

Onset of this stage usually occurs abruptly as an advancing rainshower begins to overtake the waterspout. The funnel becomes greatly contorted, and perturbations appear on its outer surface. The spiral pattern, which begins to disappear during the latter portion of the mature stage, is now completely gone. The waterspout decelerates, the spray vortex weakens, and the condensation funnel becomes progressively shorter and more tapered, often assuming odd twisting shapes. On rare occasions, the weakening spray vortex makes a slow looping path (wake) over the sea surface. The funnel cloud attains maximum tilt from the vertical during the early portion of the decay stage.

A waterspout's demise apparently lies primarily in the interception and disruption of its helically upward flow by subsiding rain-cooled air. This occurrence was illustrated in several time-lapse sequences during the 1969 program (selected cases are presented later in this section).

Generally, final stage duration is only 1 to 3 min. However, there were a few cases in which the waterspout persisted up to 7 min in the decay stage while completely surrounded by heavy rainshowers. In such cases, the lower portion appeared contained by a hollow cylinder of ascending air while traveling through the shower. In one case, marine smoke plumes indicated a complex boundary-layer flow pattern around a decaying cyclonic waterspout. The most striking feature was the anticyclonic larger scale flow indicated by two smoke flares on opposite sides of the spray vortex. One flare did indicate some cyclonic turning as the plume approached the spray vortex. The implication is that whenever a cyclonic waterspout is intercepted by two merging rainshowers, its decay is caused both by the pronounced sinking of rain-cooled air and by a production of anticyclonic vorticity near the surface.

The decay stage of the large, double-walled waterspout of September 10, 1969 (the principal illustrative case of the complete life cycle), is shown in figures 11a through 11d. (Stages 1, 2, 3, and 4 for this same waterspout are illustrated in figures 5a, 5b, 6a, 6b, 6c, 6d, and 9a through 9i, respectively.)

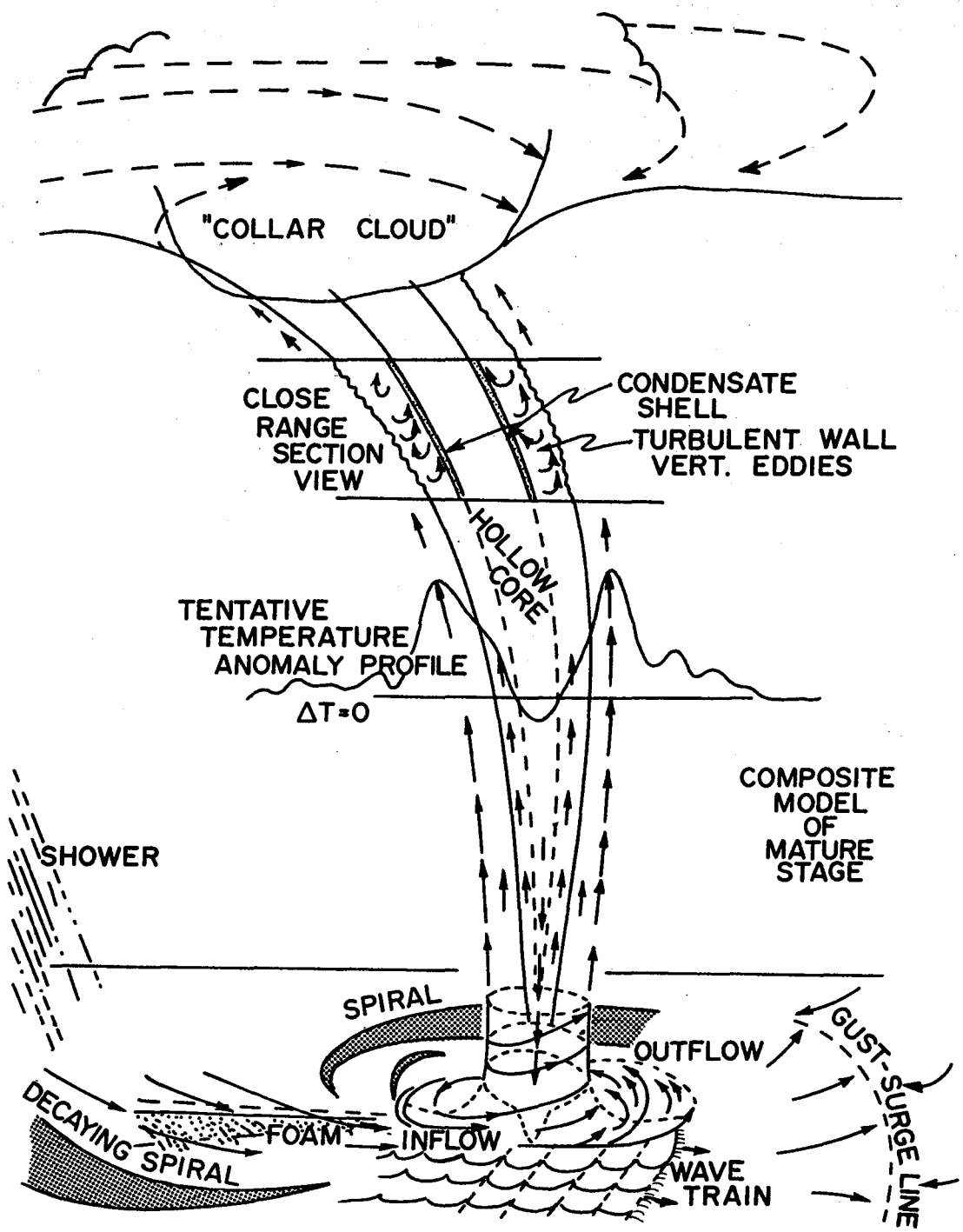

Figure 10. Composited schematic model of a mature waterspout (stage 4 in the life cycle). For scaling reference, the maximum funnel diameters in this stage, just below the "collar cloud," range from 3 to 140 m. See section 3.5 for details on structural, flow, and thermal features.

Figure 11a. Onset of decay stage, weakening spiral pattern,and feeder band; two flares at left; looking SW at 1207 EDT.

Figure 11b. Funnel retracting, diffuse spiral, and flare in buoyant inflow; looking NE at 1208 EDT.

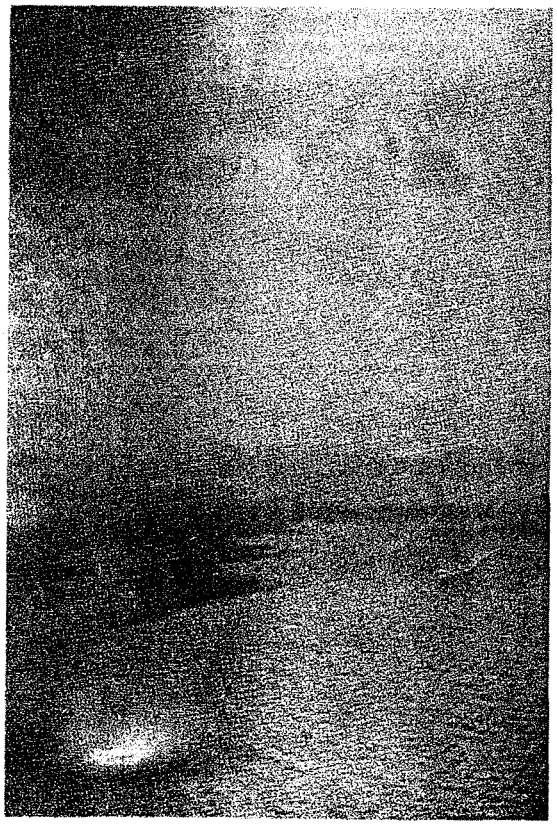

Figure 11c. Spiral gone, large eye in spray vortex; shorter, tapering funnel; smoke flares; looking ENE at 1210 EDT.

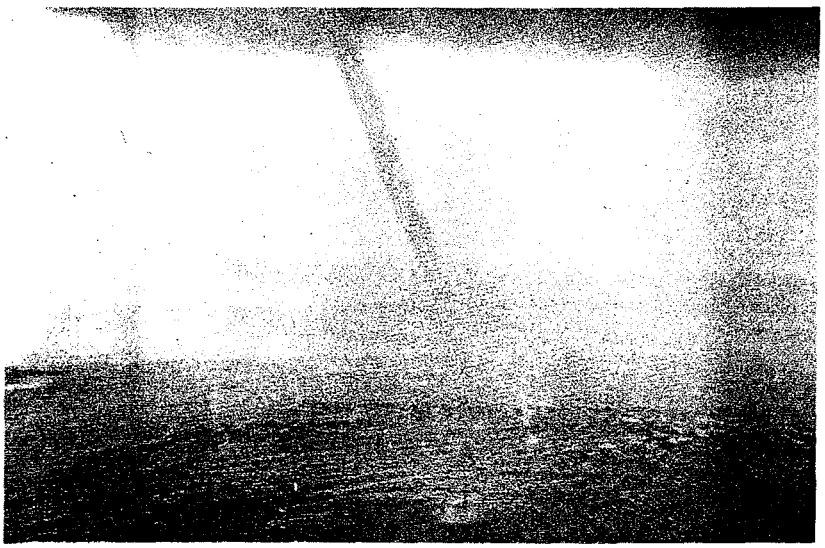

Figure 11d. Contorted funnel with perturbations, weakening spray vortex; looking S at 1212 EDT.

A three-dimensional flow and structure model of a waterspout in the decay stage, composited from the 1969-70 observations, is given in figure 12. Note that the waterspout has been overtaken by the "density-surge line" (Charba and Sasaki, 1971) from a nearby shower.

One further aspect of the decay stage should be reviewed. During the decay stage of a small waterspout, an evolving shower curtain created a large spiral pattern on the sea surface centered on the decayed spray vortex. The rain curtain's well-organized spiral structure is shown 3 min later in figure 13. During penetration (380 and 520 m MSL), the aircraft encountered two sharply defined heavy-rain curtains and strong downdrafts, but the interior region of the spiral was relatively quiescent with a high concentration of drizzle-size raindrops.

The spiral rain curtain had an observable lifetime of 5 min. Within 7 min from the waterspout's decay, the entire parent cloud cell was composed of heavy rain with only small fragments of cloud matter remaining. This particular mode of waterspout decay gives a manifestation of the waterspout's

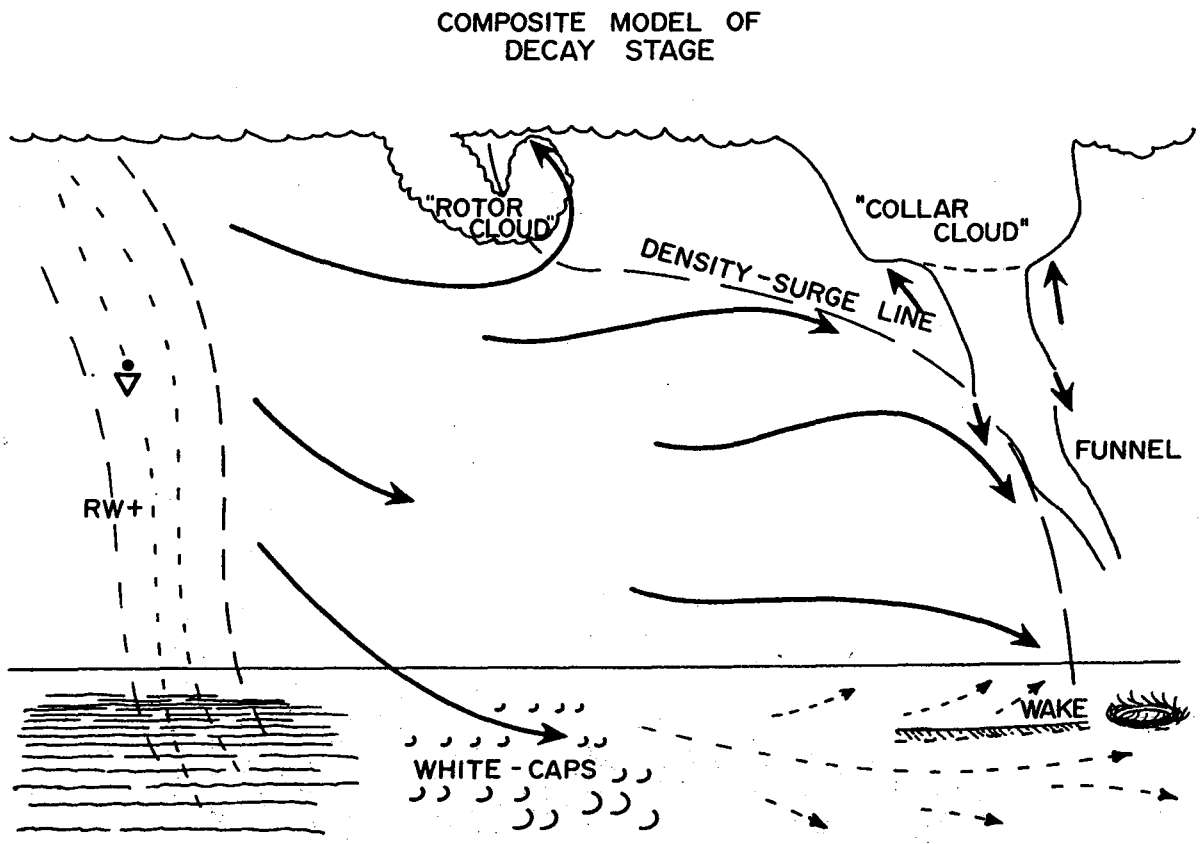

Figure 12. Composite model of decay (stage 5) in waterspout life cycle. Note that in some cases the density-surge line may be closely followed by the heavy rainshower. Also, the funnel cloud often undergoes rapid changes in shape and may become greatly contorted late in stage 5. For scaling purposes, maximum funnel diameters range from 3 to 105 m.

rotational circulation within the parent cloud by the spiral organization and concentration of large raindrops. Further, the horizontal extent of this spiral rain curtain at maximum organization was about 610 m, a scale typical of the spiral pattern stage of the waterspout life cycle. Additional similar cases were documented during 1969-70.

3.7 Quantitative Aspects

3.7.1 Derived Wind and Pressure Distributions

Using photogrammetric analysis techniques outlined in section 2, the rotations of spray plumes and aggregates around the spray vortex in the Matecumbe movies were tracked and timed with corrections for aircraft velocity. The resultant tangential windspeed values across the cyclonic spray vortex are plotted in figure 14. Note that the wind profiles for the Matecumbe cyclonic and 1969 anticyclonic waterspouts are the vertically averaged tangential speeds across the uppermost layers of the spray vortex. These wind profiles represent the flow near the top of the spray vortex (about 15 m MSL for the Matecumbe and about 23 m MSL for the 1969 anticyclonic spray vortices). It is often assumed that the cyclostrophic approximation is valid in small-scale vortices with very great windspeeds and streamline curvatuve (e.g., Hoecker, 1961; and Long 1958). Morton (1969) has theoretically validated the cyclostrophic wind relation for narrow, laminar vortex cores by using a scale analysis. The cyclostrophic wind relation

$$\frac{V_c^2}{r} = \frac{1}{\rho}\frac{\partial p}{\partial r}$$

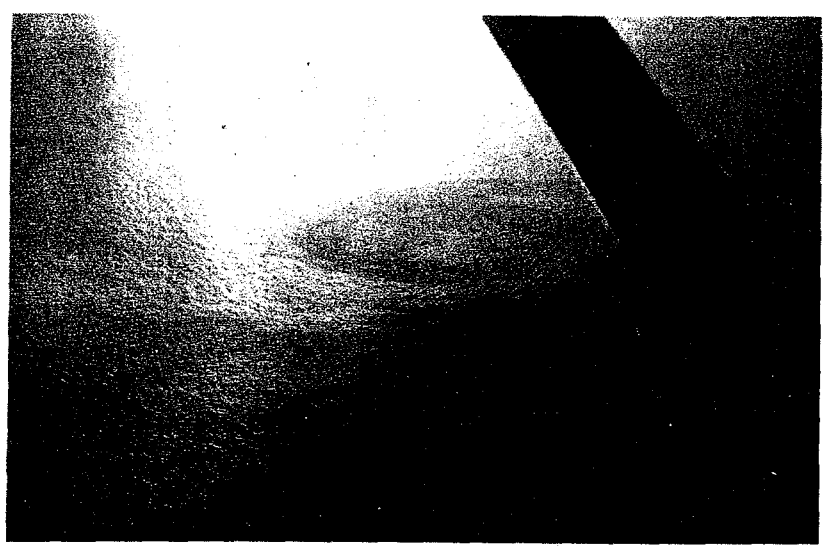

Figure 13. Spiral rain curtain, viewed in sunglint toward setting sun on September 4, 1970. Epicenter of spiral was located near final position of waterspout spray vortex which dissipated 6 min earlier.

was integrated, assuming a combined Rankine vortex-velocity profile. The computed pressure drop across the Matecumbe spray vortex was 44 mb, giving a central pressure of 971 mb. A similar integration for the 1969 anticyclonic profile in figure 14 yielded a pressure drop of about 64 mb. In view of the better data for the Matecumbe wind profile, the pressure-drop calculation for that case is probably more accurate and reliable.

The ring of maximum tangential wind in both the large Matecumbe and 1969 anticyclonic waterspouts occurred at a radius just outside the spray-free eye region. Precise photogrammetric determination of the wind profiles near the peaks, where there is a very bright ring of rapidly circulating spray, was most difficult with the projection equipment available. However, those points plotted on the profiles were carefully checked and were reproducible. Any questionable data points on the original profiles have been eliminated

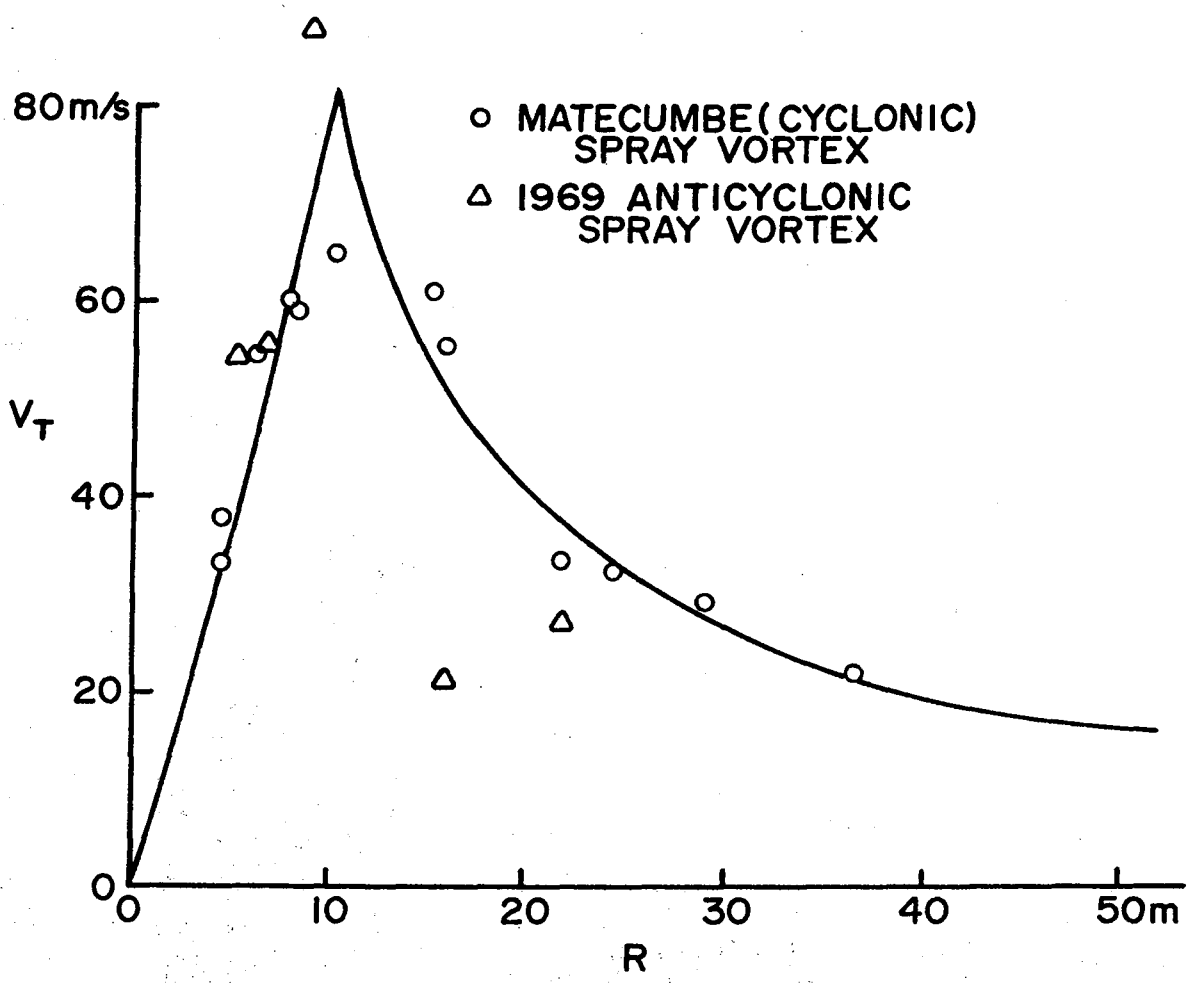

Figure 14. Photogrammetrically derived tangential windspeeds across cyclonic Matecumbe and 1969 anticyclonic spray vortices, plotted as a function of radius outward from center. Solid curves give theoretical profile of V_T for the Rankine-combined vortex model. Compare with Hoecker's (1960) analysis of windspeeds in the Dallas tornado.

in the results presented here. Allowing for errors, the maximum (65 m/s) is probably correct to within 10 percent (assuming that the spray drops are moving at the airspeed).

The mature waterspout spray vortex has a central spray-free "eye" containing a nearly calm visible disc of ocean surface. Surface depressions appear at times in the eye region and basal mounds (Hurd, 1950; and Battan, 1961) were never observed. Outward from the "eye", is a sloping wall of rapidly circulating spray which resembles a shallow bowl with the upper rim corresponding to the bottom of the spray sheath.

Using the derived wind and pressure distributions across the Matecumbe spray vortex, the wind forces necessary to produce a surface depression in the eye were computed. If the water surface reached hydrostatic equilibrium in the clear eye, the water would rise approximately 0.3 m for each inch of barometric pressure deficit (Dunn and Miller, 1964); for the derived 44-mb pressure drop, this effect would cause a 0.4-m rise. Since the wind profile closely fits a combined Rankine vortex, from Lamb (1945),

$$h = g^{-1} v_m^2$$

where h is the central depression depth below the general water-surface level, and v_m is the surface water speed at the radius of maximum wind. Assuming that the waterspout is quasi-steady and an equilibrium value of v_m has been reached, we find $v_m = 2\ m\ s^{-1}$ offsets the hydrostatic rise in water level. We conclude, then, that the water speed at a radius of 12 m from the spray vortex center need only exceed $2\ m\ s^{-1}$ to induce a depression in the water surface. These results should be compared with the tangential spray vortex wind speeds in figure 14.

3.7.2 Funnel Structure and Circulation

Additional details of the circulation within the condensation funnel were revealed by 1969 data. Even larger funnels had hollow cores, and cloud tags on the sloping collar cloud walls rose rapidly. Well-defined condensate filaments could be seen rotating cyclonically around the hollow core and spiralling upward in the funnel wall (fig. 9f is a well-documented case of this). Therefore, although the strongest rising motions occur outside the visible funnel, air parcels also are rising in a helical fashion in the funnel walls.

The rising annulus is manifested at lower levels by the spray sheath, which extends upward as high as 300 m in more intense waterspouts. The 1969 tracer experiments, using Very-pistol smoke cartridges fired toward the funnel, confirmed that this peak of rising motion (just outside the funnel walls) extends upward into cloud base. In near-miss, low-oblique firing cases, the horizontal displacements along the plume trajectory indicate that the weak inflow toward the funnel is largely confined to the lowest 300 m of the subcloud layer. Release of neutrally buoyant balloons 200 ft below cloud base, within 60 m of a small waterspout, reinforced the conclusion that the

intense rising annulus is surrounded by strong, cloud-scale rising motion in the subcloud layer.

To obtain quantitative and representative assessments of the vector motion fields on the funnel scale, the control-loop analysis technique was applied to three 1969 waterspouts filmed from aircraft. The first case was a large anticyclonic waterspout-funnel which was beginning to exhibit a double-walled structure. The second case was the associated anticyclonic spray-vortex during the most intense portion of its mature stage. The third case was an intense cyclonic spray-vortex with a well-formed, conservative eye structure, associated with the large double-walled waterspout of September 10, 1969. Results from the first two cases only are presented here; see Golden (1973c) for more details.

Fifty-four movie frames were used for the first case. During this sequence in the anticyclonic waterspout's life cycle, the spray vortex had weakened temporarily and a narrow ropelike funnel formed within the hollow core of the larger funnel. The smooth outer wall of the large funnel began to break down into turbulent cloud fragments which were clearly spiralling upward and outward. At the same time, the inner ropelike funnel maintained a nearly constant diameter while oscillating in a snakelike fashion about the vertical. During this process, each enlarged movie frame was normalized so that the diameter of the inner ropelike funnel was held constant.

The trajectory analysis of cloud tag and "clear hole" motions in the outer funnel wall is shown in figure 15a. Note that the inner funnel was tilted slightly and that the condensate trajectories nearest the inner funnel tend to follow its vertical orientation. We should emphasize that these trajectories are three-dimensional. Cloud tags and cloud-free holes in the funnel walls nearest the camera were indistinguishable from those in the rear. Tracking of these condensate aggregates and holes was repeated several times to ensure continuity. The overall impression is one of strong upward motion throughout the outer funnel, with inward-directed radial components during the first half and outward-directed radial components during the latter half of the trajectories.

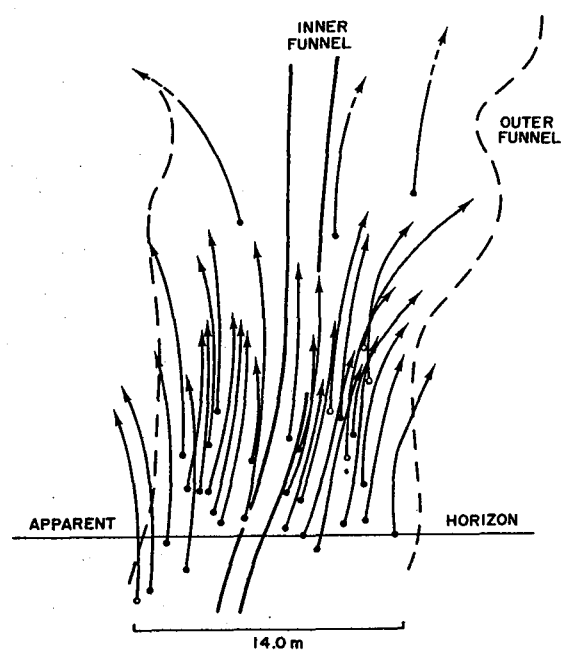

Figure 15a. Detailed trajectory analysis of cloud tags (black dots) and cloud-free holes (open circles) in outer walls of funnel, derived from the analysis of 14-frame control loop. This is the analog form of control loop results.

Figure 15b shows upward velocities, derived from the scaled trajectories, as a function of radial distance from the tilted inner funnel. Because the full 27-frame control loop

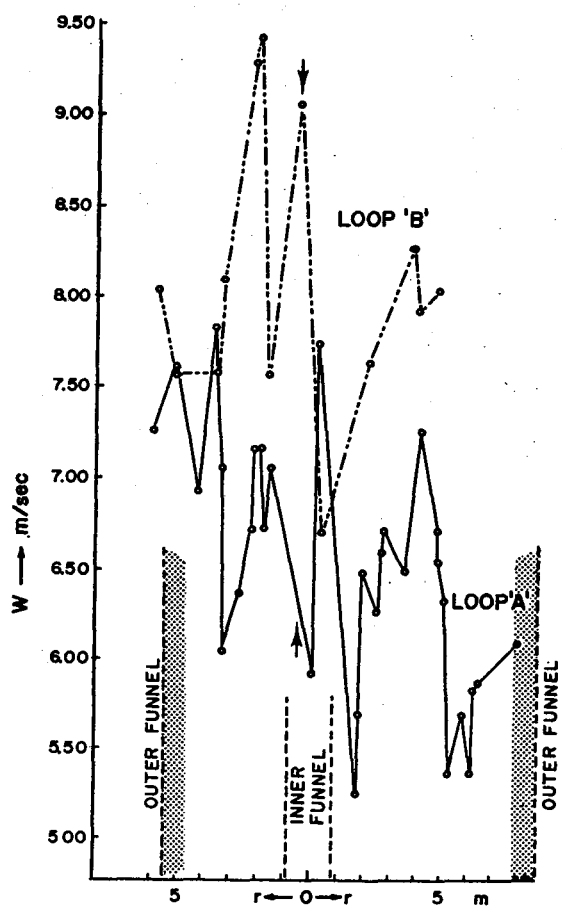

Figure 15b. Unsmoothed profiles of vertical motion across outer funnel walls of anticyclonic waterspout, derived from trajectory analyses of cloud-tag motion in two movie control loops "A" and "B". Digital form of control loop results.

had such long trajectories, it was subdivided into two overlapping 14-frame film loops-- "A" and "B", respectively (1.5 s of total real-time data each). The data points for loop "A" were more complete and homogeneously distributed across the outer funnel walls. There were at least four major peaks, with the higher maxima skewed toward the left. Values of w ranged from 5.3 to 7.8 m/s, with indicated radial gradients as high as 1.5 s^{-1}. The loop "B" profile was also skewed toward the left of the inner funnel, with values of w from 6.7 to 9.4 m/s. There was an implied upward acceleration through most of the outer funnel, reaching 2.1 m/s^2 at r = -0.5 m (arrows in fig. 15b).

The strongest rising motions in the outer walls were on the west side, the direction toward which the waterspout was moving. Aircraft film clearly show that just before the outer funnel's visible expansion, the spray vortex below weakened considerably. However, immediately after sequences "A" and "B" were filmed, the spray vortex reintensified rapidly for a few minutes before final decay. This is consistent with both the strong rising motion in the outer funnel walls and the transient upward accelerations there (> 0.2g).

Three anticyclonic cloud tags were tracked on loop "B" for about one-half revolution around the outside funnel. A conservative estimate for the average tangential speed in the outer walls is 27 m/s^{-1}.

During the September 1970 Purdue University waterspout experiment, the aircraft towing the instrumented drag body frequently passed within 15 to 30 m of the funnels (Church et al., 1973). This probing technique permitted observation of changes in the internal structure and midlevel circulations. A smooth funnel wall with a hollow inner core was noted from about 100 m away. However, as the aircraft approached within 30 m, the funnel's outward and internal appearance changed drastically. The condensation funnel was composed of a thin laminar shell of condensate, with no detectable motion, not more than 2 to 3 m thick just outside the hollow core. A much thicker layer, five to six times the condensate shell width, composed of turbulent cloud eddies of an order 1 m diameter spinning about their horizontal axes, was apparent just outside the shell. The cloud motion in this outer turbulent

layer was spiralling upward, similar to that shown in the composite model of the mature waterspout (fig. 10). Several other cases exhibiting this structure have been documented at close range since the 1969 program.

3.7.3 Waterspout Spray-Vortex Structure and Circulation

Pronounced nonsteady asymmetries in the circulation components around the spray vortex and insight into the trailing wake resulted from the 1969 observations. Two movie enlargements which illustrate aspects of these findings are given in figure 16. Note the eye and well-defined spiral-banded structure in the spray vortex in figures 16a and 16b (a time sequence). In particular, note also the outflow of spray bands in the left-front quadrant in figure 16b, taken about 1 s after figure 16a. As previously noted, the wake in figure 16a and 16b formed beneath the bright spray region (which corresponds closely to the belt of maximum winds) just to the right of the clear eye. In general, the width of the wake is proportional to the diameter of the spray vortex, but the longer, more persistent wakes form behind the smallest, fastest moving, and most intense spray vortices.

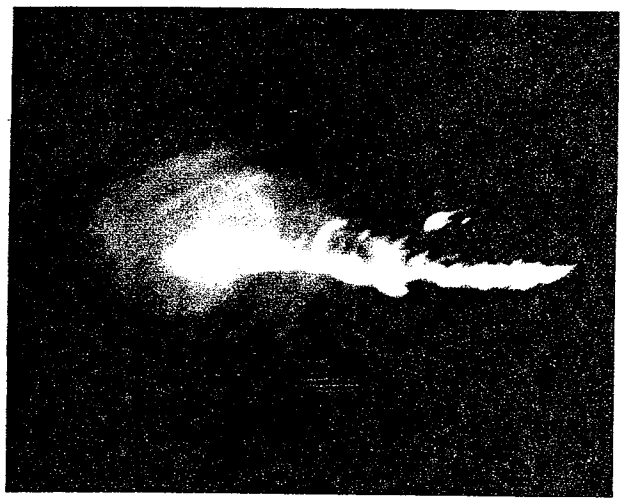

Figure 16a. Intense cyclonic spray vortex of waterspout #6 on August 26, 1969 (see appendix A). Note eye structure (large gray dot), trailing narrow wake, and spiral banding in spray.

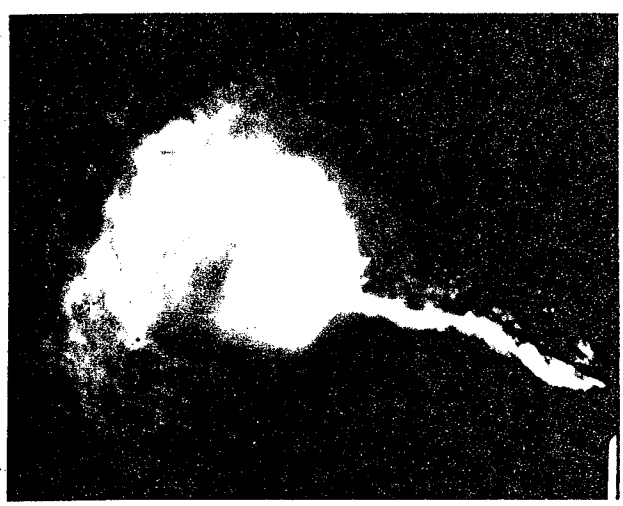

Figure 16b. Same spray vortex of waterspout #6 on August 26, 1969, 20 frames later on zoom 16-mm movie film (slightly more than 1 s). Compare with figure 16a.

A control loop analysis was performed on the spray and wave motion around an intense anticyclonic vortex (the mature stage of the waterspout in fig. 15). A control loop of a 51-frame sequence (nearly 3 s of real-time data) was prepared and analyzed, and a short-term loop of 15 frames (5/6 s real-time) was independently analyzed. At this time, a tongue of dry air was entrained into the right-rear quadrant, while the spray vortex moved westward. As the clear air mixed with the spray, the mixture accelerated upward and toward the right (illustrated in fig. 17). The concentrated upward jet was a transient feature during the most intense stage. There is an indication of a weak secondary anticyclonic eddy centered along the upward jet's axis. The largest tangential speeds appear to be in a belt to the left of the eye, and the trajectories show sinking motion in that region. Note the divergent wave motion in the right-front quadrant and the eastward-directed wave motion in

the wake. The latter feature may provide a mechanism for mass removal from the subsiding core during the trailing wake production. Subsidence through the length of the vortex core has yet to be quantitatively measured, but it has been qualitatively shown to occur in the dark spot stage.

There was large spray-trajectory diffluence in the left-rear quadrant, with some spray converging with the clear air tongue at low levels and rising to form the upward jet. The remainder of the spray flowed outward from the vortex center in the left-front quadrant. Using the assumptions made for the cyclonic case above, elliptical grids were applied to the spray vortex and wave trajectories. The (horizontal) tangential windspeed distribution relative to the spray vortex and vertical wind profile through the upward jet region of figure 17 will be reported in future work. The upward jet axis was located at a radius of 29 $\pm$ 3 m to the rear of the spray vortex center, and peak-value vertical motions of at least 4.6 m/s were reached at a height of 12 $\pm$ 2 m above the sea surface.

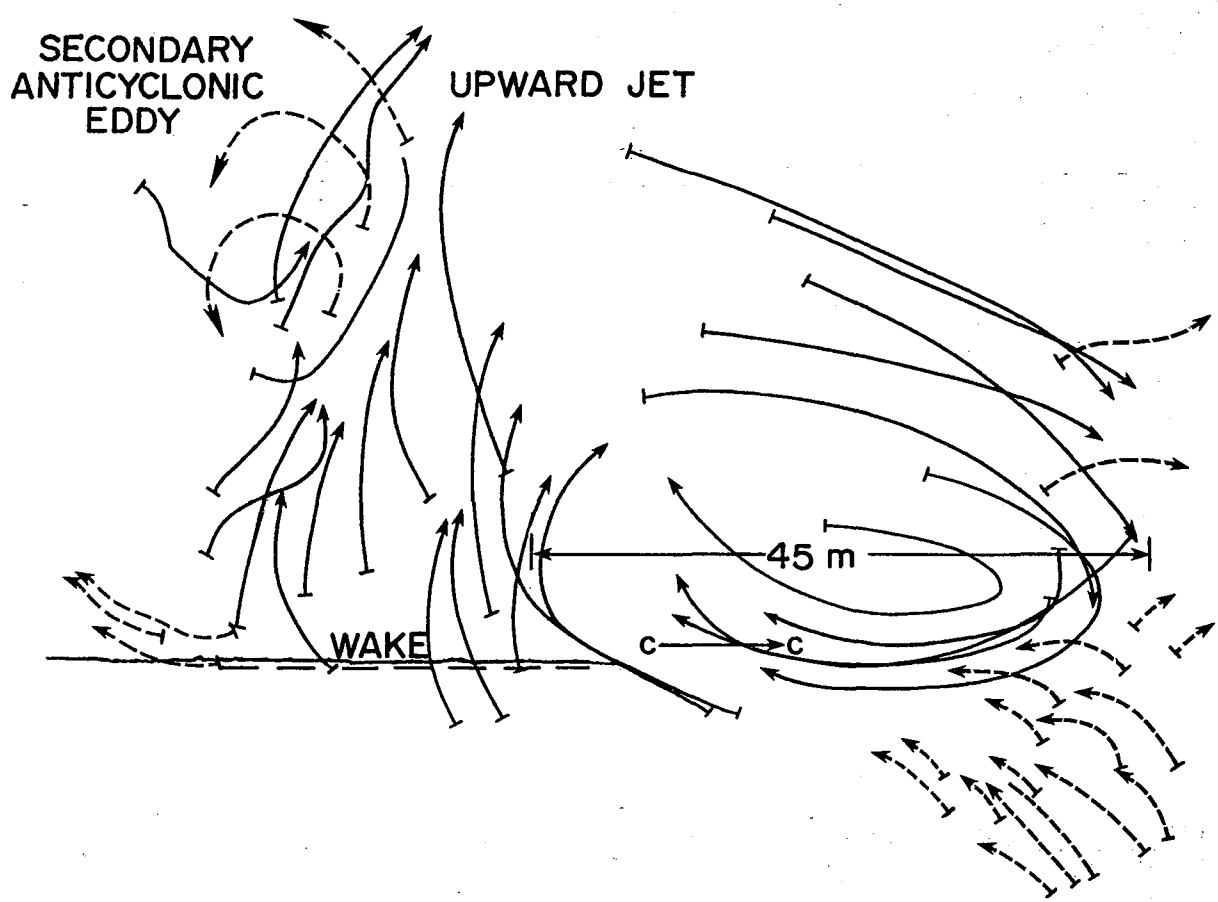

Figure 17. Long-term analysis of 51-frame control loop, showing spray trajectories (solid arrows) in an intense anticyclonic spray vortex of September 4, 1969. This is the unrectified, perspective, side view as seen in original film. Note upward jet to the rear of vortex and wave motion (dashed arrows).

The internal structure and circulation pattern in the anticyclonic spray vortex were in most respects mirror (reversed) images of corresponding features in the cyclonic case. The transient upward jet was accompanied by strong spray convergence and strong secondary anticyclonic rotation, an analogy to rotating "suction" vortices which Fujita (1971) hypothesized as the primary cause of tornado damage.

On August 12, the largest 1969 waterspout was recorded by the Key West time-lapse camera (summarized in fig. 18a through 18d). Because of the

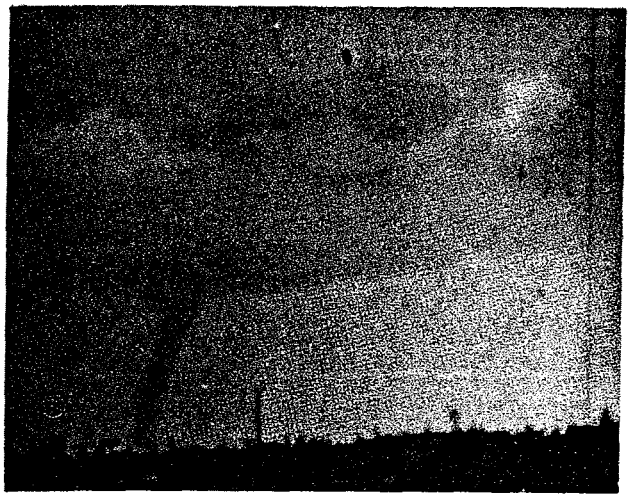

Figure 18a. Enlarged frame (#148) from 16-mm time-lapse sequence of giant waterspout life cycle on August 12, 1969.

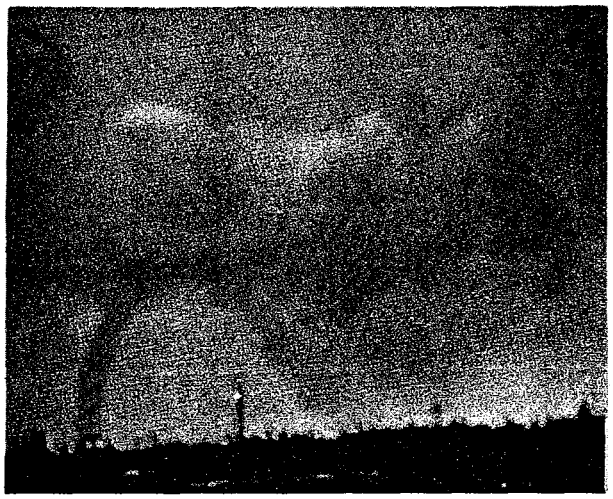

Figure 18b. Same waterspout of August 12, 1969, at a later time in time-lapse sequence (frame #216).

Figure 18c. Same waterspout of August 12, 1969, marking onset of decay stage (frame #223). By this time, rotor cloud has formed upwind (right) and funnel has grown to maximum overall size; rotor cloud is marked.

Figure 18d. Same waterspout of August 12, 1969, decaying rapidly, with perturbations traveling downward on funnel (frame #234). Note well-defined character of rotor cloud (arrow).

huge funnel and parent cloudline structure, this waterspout resembled a tornado at sea (Golden, 1969). During the first half of its life cycle, the funnel cloud had the shape shown in figure 18a. As a heavy rainshower developed to the northeast (right side of funnel in fig. 18a and 18b), the funnel grew considerably and moved southwest. This development implies that the near-surface part of the vortex accelerated somewhat relative to the cloud-base portion (compare funnel position and tilt in fig. 18a and 18b). A pronounced rotor cloud, which formed abruptly (at frame #205, fig. 18c) on the leading edge of the density-surge line, was first evident as a plunging cloud downdraft (about 3.5 m/s) centered about 930 m northeast of the funnel. During this period, several cloud-base protrusions between the rotor cloud and funnel could be tracked as they moved toward the funnel and downward (sinking rate about 1 m/s). The decay stage began with a sudden decrease in funnel diameter at all levels, followed by a short period of rapid oscillations in upper and middle-level diameters. These oscillations appeared as cloud bulges or outward protrusions which travel rapidly downward on the funnel walls (see fig. 18c). The bulges resembled Reber's (1954) observations of dissipating tornado funnels and Ward's (1972) laboratory vortex enlargement (associated with a transition from laminar to turbulent flow). Ward interpreted these enlargements as axial-flow stagnation points.

The last 10 time-lapse frames were analyzed to obtain speed estimates of downward-moving bulges. These speeds increased from 1 m/s at 500 m MSL to 4.6 m/s at 450 m MSL, and 6.7 m/s at 445 and 390 m MSL. During this period, the funnel tilt increased greatly. The rotor cloud was circulating clockwise and was best developed during the period of final funnel decay (fig. 18d); at the same time, the rotor cloud advanced with the top of the sinking rain-cooled air to within 510 m of the funnel. Immediately following the waterspout's demise, a heavy rainburst fell through the midsection of the cloudline. Cyclonic rotation then became evident in the cumuli bordering this heavy shower.

4. FIVE INTERACTING SCALES OF MOTION PRODUCING THE WATERSPOUT LIFE CYCLE

The high formation frequency (see section 5) and the life cycle of waterspouts in the Florida Keys result from energy and angular momentum exchanges among five scales of atmospheric circulation. These are: (a) the funnel scale, corresponding to the waterspout itself, with funnel diameters ranging from 10 to 500 ft; (b) the new spiral scale, ranging from 500 to 3,000 ft in diameter on the sea surface; (c) the individual cumulus-cloud scale, ranging from less than 1 up to 5 mi in diameter; (d) the cumulus cloudline scale, ranging from 5 to 100 mi in length; and (e) the synoptic scale, extending several hundreds of miles horizontally. The order of presentation of the interacting scales does not imply the sense of energy or momentum transfer. In fact, results suggest that the funnel scale is the end product of vorticity concentrated by larger scale convergence fields.

4.1 The Funnel Scale

The funnel scale is defined by the diameter of the condensation funnel, spray vortex, or dark spot which encompasses all stages of the water-

spout life cycle. Funnel diameters varied from 10 to 500 ft for waterspouts documented by time-lapse and aircraft film during the 1969 program. Hollow core diameters ranged from 5 to 300 ft. The vertical extent of funnel clouds ranged from about 100 to 200 ft during the dark spot stage to about 2,500 ft (from cloud base to sea surface) during the mature stage of some intense waterspouts. However, some mature waterspouts had funnel clouds which were only 500 to 700 ft long. Translational speeds ranged from a few miles per hour just below cloud base to an average of 5 to 10 mph at lower levels, and occasionally 15 to 30 mph at low levels in late stages. At least four of the 1969 waterspouts exhibited a double-wall structure at maturity. The largest of these formations (and the largest waterspout observed by aircraft in 1969) is shown in figures 9b through 9f. The largest waterspout documented during the entire 1969 program is shown in figures 18a through 18d.

4.1.1 Time-Lapse Photography Program

To quantify relations between waterspout life cycle and parent cloudline, three cases of time-lapse photography were analyzed photogrammetrically. All three cases have supporting WSR-57 radar data. Vertical cloud-turret growth rates, relative to the portion of the cloudline producing a waterspout, will be presented later for one representative case.

Figure 19a shows tracings of a ropelike waterspout. A shower developed underneath a rapidly rising cloud-tower (on the right side of the frame), and as it spread toward the left, the lower portion of the waterspout also accelerated toward the left. Thus, the maximum tilt of the funnel from the local vertical systematically increased, from 15° initially to 56° just before the shower intercepted the funnel. As listed, the funnel's speed component normal

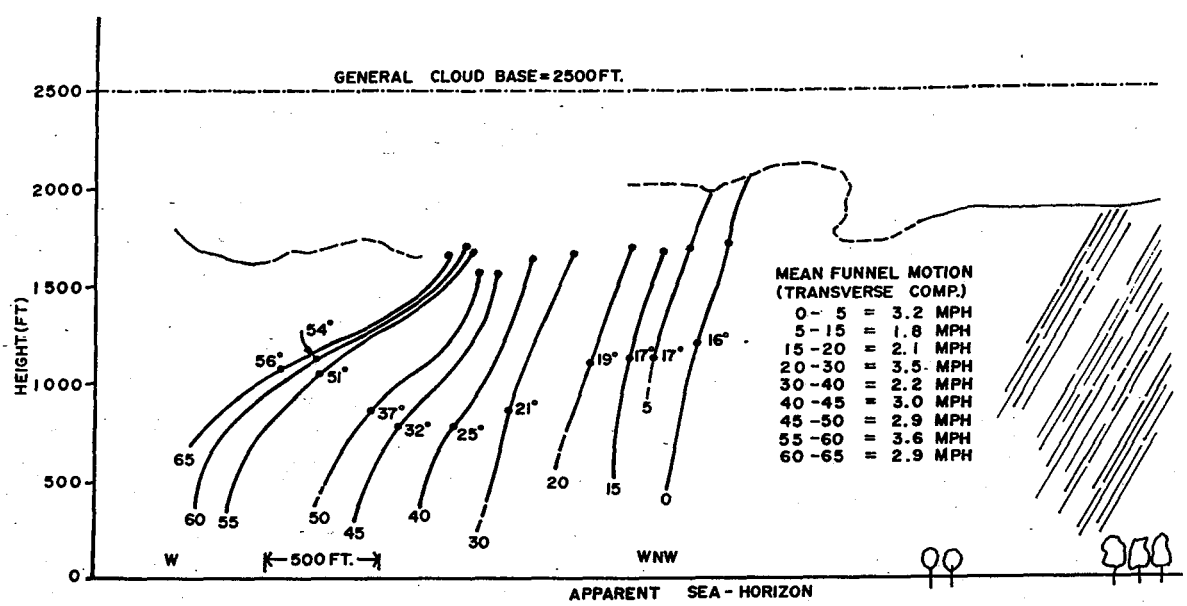

Figure 19a. Successive tracings of ropelike waterspout from time-lapse film on May 30, 1969. Frame numbers at lower tip; maximum tilt from local vertical in degrees. Filming rate: one frame each 7.3 s.

to the camera orientation varied from 1.8 to 3.6 mph. Other data indicated that these values represent total translational velocity (i.e., the waterspout was moving along the cloudline, toward the southwest, at a gradually increasing rate). This motion contrasts with the sounding indications (see section 6.4) of a low-level wind rapidly veering from light north-northeasterly at the surface to light south-southwesterly at 4,000 ft.

During the entire funnel lifetime, a major portion of the cloud base between the funnel and developing rainshower evidenced a pronounced cyclonic rotation, shown schematically in figure 19b. The funnel was located in the southwest quadrant relative to the apparent center of cloud base rotation. After the waterspout's demise (frame #65), cloud base rotation persisted for 71 min.

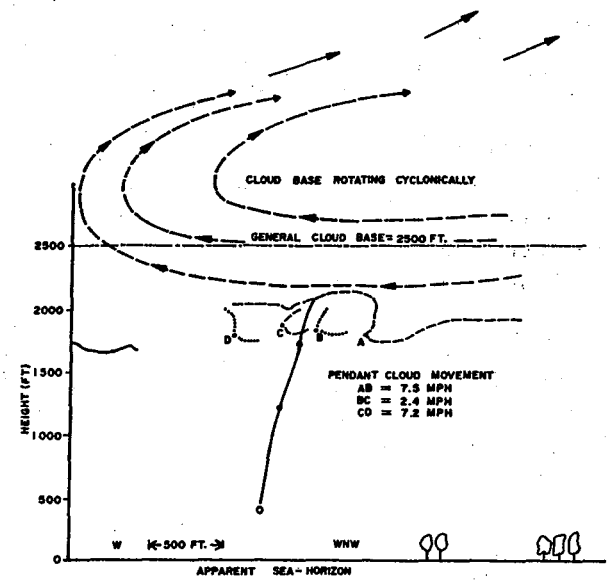

Figure 19b. Waterspout of May 30, 1969 (same as fig. 19a), except for schematic trajectories of cloud base rotation and motion of cloud pendant to rear of funnel.

This event and similar cases documented during the 1969 program demonstrate the following: (a) The waterspout generally forms within a mile or two of a developing rainshower in an adjacent cell of a cumulus-congestus cloudline; (b) the direction of funnel motion is largely determined by its location with respect to the shower and frequently is opposed to the environmental lower level flow, particularly if windspeeds are 10 kt or less; (c) the funnel moves with and is often preceded by the "wind gust front" from the shower (Charba and Sasaki, 1971); (d) the funnel tilt tends to increase, and low-level acceleration occurs primarily near the end of its lifetime when the tilt increases most rapidly; (e) during the last one-third of its lifetime, the lower portion of the funnel is frequently distorted by an advancing "density surge line" (Charba and Sasaki); and (f) the funnels occasionally form on the forward periphery of organized cloud-base rotation, with cloud base rotation persisting well after the funnel's decay. Many similarities with Fujita's (1960) Fargo tornado observations may be noted. The giant waterspout's morphology of August 12, 1969, is summarized in figure 20 for which every fifth or tenth time-lapse frame was photogrammetrically analyzed (filming rate was one frame per 7.3 s). The entire life cycle of the waterspout is shown in a sequence of selected time-lapse frames (fig. 18a through 18d).

Figures 18 and 20 illustrate that during the first half of its life cycle, the waterspout funnel had a stretched hour-glass shape with lower level diameters that were from 20 to 50 ft larger than those at the middle or top. The period of each growth cycle varied between 6 and 8 min. During quiescent periods in funnel expansion, the waterspout accelerated and then

generally decelerated during stages of growth. Up to the time of maximum funnel diameter, forward speeds were 1 mph or less. However, the decay stage began rather abruptly at 1715 EST (fig. 18 and 20), as the funnel's forward tilt (away from the shower) increased rapidly. At about the same time, the funnel diameter decreased rapidly, but bulges on the funnel could be tracked as they moved downward. These perturbations were responsible for secondary diameter increases, particularly in the middle level (fig. 18c and 18d). A marked forward acceleration occurred during the last 3 min of existence (fig. 20). These results on funnel tilt and acceleration are comparable with those for the event of May 30 (fig. 19a).

A distinct narrow funnel extending only 200 ft below cloud base moved from left to right and rotated cyclonically two-thirds of the way around the giant funnel at a radius of 800 ft and then disappeared. During most of its life, the small funnel motion was in the opposite direction to the giant funnel. If one assumes that angular momentum is conserved and that the mean

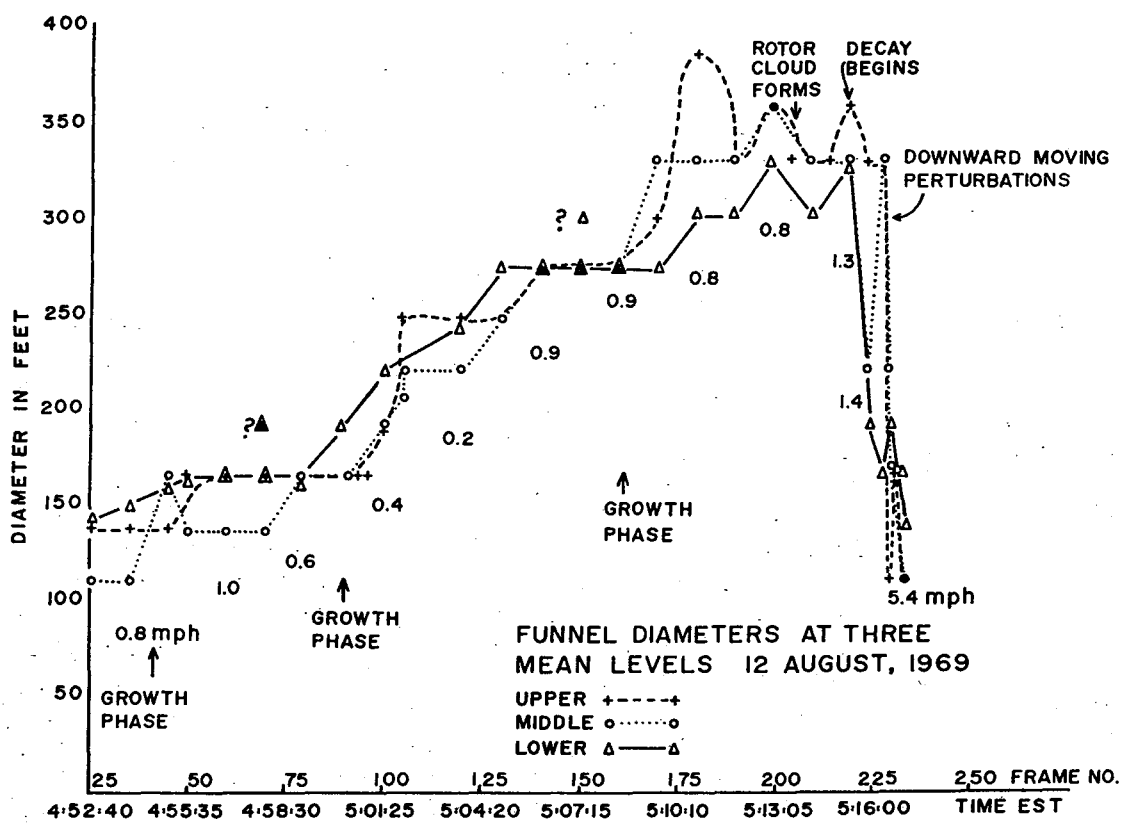

Figure 20. Giant waterspout time-lapse case of August 12, 1969. Graph of funnel diameter at three mean altitudes (one-quarter, one-half, and three-quarters of the distance from the cloud base at 2,200 ft MSL) and of accompanying parent-cloud structure changes as a function of time (frame number). Numbers below growth curves refer to mean-translational speed component of funnel, normal to camera azimuth, in each time interval. See also figures 18a through 18d.

motion of the small funnel is representative of tangential velocity at that radius, the rotational velocities around the edge of the 140-ft diameter giant waterspout would be 40 and 52 mph. These values were obtained from the conservation equation $V_oR_o = V_1R_1$, using V_o = 3.5 and 4.5 mph, the actual and relative speeds, respectively, of the small funnel around the giant funnel.

Vertical motions in the funnel walls of a mature waterspout are strongly upward. Therefore, contrary to Rossman's (1960) concept of a hail-induced, cold-plunging downdraft as the initiating mechanism, we find that strong, potentially cold downdrafts, produced by large liquid water accumulations within the parent cloudline, are responsible for waterspout decay. Waterspout motion and vertical tilt are largely determined in direction by location of the neighboring shower and in speed by the shower intensity and motion of the associated gust front. Flare data indicate that appreciable waterspout motion usually begins in the mature stage, when it is overtaken and passed by the primary windshift line (the "gust front") from a nearby shower.

The third time-lapse case documented the life history of a cloudline that spawned three waterspouts. These waterspouts were simultaneously studied by project aircraft. The third of these waterspouts had a giant double-walled funnel and was the largest and best-documented waterspout during the aircraft operations (September 10, 1969).

4.2 The Spiral Scale

This scale of motion is important because it defines the waterspout's primary growth phase (stage 2) and provides the first visual evidence of rotation and inflow in the surface boundary layer. The precise physical mechanism(s) responsible for the spiral-banded structure on the sea surface cannot yet be definitively specified. The most likely explanation for the major dark band is local generation and accumulation of short-wavelength, small-amplitude capillary waves produced by shower outflow. The spiral banding is then a wave interference zone, produced by elongated windspeed maxima of 20 to 30 kt of relatively short fetch, on which short-period higher gusts are likely superimposed. Although the spiral pattern was documented in only about one-sixth of the 95 waterspouts observed by project aircraft in 1969, boundary layer circulation and inflow on the spiral scale were documented by marine smoke flares during the mature spray vortex stage of several additional waterspouts.

Photography of smoke plumes and spiral patterns indicates that the waterspout vorticity may be initially present in the form of a boundary-layer shear zone or zero-order wind discontinuity. The shear zone is often manifested on the sea surface by a dark band from or within which the spiral pattern evolves (see fig. 21).

It does not appear fortuitous that spiral patterns usually form on the flank of a cloudline. A developing rainshower or two is generally within 1 n mi of the spiral's epicenter, and often the major feeder band of the spiral appears to emanate from a narrow noselike protrusion of the downwind

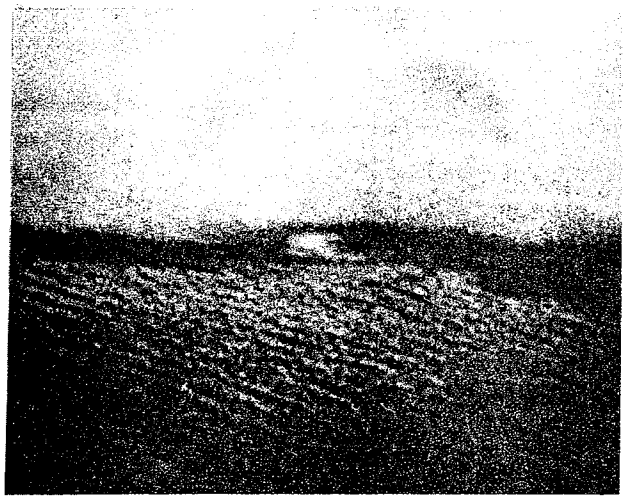

Figure 21. Overall view from aircraft of spiral pattern embedded in dark shear-band on sea surface (August 28, 1969). A light shower lies immediately to the rear of the band.

Figure 22. A well-documented example of spiral-scale circulation in the boundary layer around a mature waterspout on September 23, 1969. Note three smoke-plume streaklines with pronounced cyclonic curvature and small spray vortex (50 ft diameter) in center.

shower boundary. In virtually every instance, no significant precipitation was encountered by the aircraft over the major spiral bands during stage 2 of the waterspout life cycle. Showers were contiguous with less than one-half of the outer dark bands in all spiral patterns. We therefore conclude that the formation of spiral patterns is indirectly related to a nearby developing rainshower, but the spiral banding is due to other factors.

Smoke flares dropped on the sea surface outside the spiral pattern are affected by the outer circulation (see fig. 9f through 9i); that is, some smoke-plume trajectories exhibited both inflow and circulation at radii appreciably larger (by 200 to 300 ft) than the spiral pattern. Moreover, boundary layer flow often becomes complicated as development proceeds to the spray ring stage. During the transition from stage 2 to 3, a few plumes were observed to cross a spiral's major band at large angles. The evidence from a limited number of cases indicated that once a spray ring has formed, the flow on the spiral scale undergoes large radial accelerations inward for a short time. Under these circumstances, a spray vortex forms, begins to move, and the surrounding spiral pattern fades away, usually within 1 to 3 min. An example of a mature waterspout with a nearly decayed spiral pattern and a large spiral-scale circulation is shown in figure 22. Flares clearly indicated a closed circulation of at least 1,000 ft diameter. In most fully developed patterns, the alignment of major spiral bands and entrained smoke plumes agree to within 10° to 20°.

Four marine smoke flares were dropped around the giant double-walled waterspout of September 10, 1969. Photogrammetric analysis of the waterspout shows that the spray vortex and inner spiral band were moving toward the west-northwest at 8 to 10 mph during this

period (1203 to 1205 EDT). Smoke flare data indicated that the mature waterspout was embedded in anticyclonic boundary-layer outflow, especially in the forward quadrants. Moreover, streaklines from the two smoke plumes shortly after drop (see fig. 9d) indicated a pronounced cyclonic wind shift and likely a zero-order discontinuity in the vector wind field across the east-west dark-shear band (see fig. 6a and 6b). Surface observations during the waterspout's lifetime indicate the environmental surface winds were light (6 to 8 kt) from the south-southwest.

Flare "A" was dropped 500 ft from the center of the spray vortex; when intercepted by the outer edge of the spiral, it exhibited an orientation shift of more than 90° (compare fig. 9h and 9i). After being passed by the spray vortex, the smoke plume exhibited an inflow angle of about 10° to 20° relative to the outer spiral boundary.

A schematic streamline-and-isotach analysis, derived from photogrammetry of spiral features, smoke flare streaklines, and the Key West sounding is given in figure 23. Flare data also indicated that the shear band delineated a zone of strong boundary-layer convergence and cyclonic relative vorticity. The fact that this shear band formed late in the first life-cycle stage (see fig. 5b and 6a) indicated that interaction between shower outflow and cloudline environment may be a vorticity source. The dark shear band may represent a vortex sheet, but this cannot be positively determined from present data. Superimposed on the divergent outflow in the west and south quadrants of the spray vortex was a cyclonic wave perturbation with an isotach minimum. The axis of this perturbation spiraled inward toward the spray vortex. There was difluence along the outer boundary of the major dark spiral-band surrounding the spray vortex, separating the major inflow and outflow air. Smoke plume orientation (fig. 9i and 11b) also indicated that compensating upward motion was present along the dark shear band.

4.3 The Individual Cumulus-Cloud Scale

Early observations and deduced models of the growth characteristics of cumuli in the presence of external wind shear were given by Byers and Braham (1949), Malkus (1952), Scorer and Ludlam (1953), Malkus and Scorer (1955), Scorer and Ronne (1956), and Levine (1959). If we apply the Byers and Braham (1949) life cycle to cells of tropical cumulus clouds, the mature stage would be characterized by the presence of updrafts and downdrafts, with downdrafts directly associated with sudden shower onset. As the shower spreads through the cell, updrafts decrease until the cell is characterized by gradually weakening downdrafts and precipitation.

As was demonstrated by Rossow's 1968 field program (Rossow, 1970) and Golden's in 1969, waterspouts most commonly form in lines of building cumulus congestus, and most cells must be in the cumulus stage initially. At the time of waterspout formation (the dark spot stage), cells spawning the waterspouts have evolved into the mature stage. These observations are verified by 49 photographically documented cases of cloudlines with waterspouts. The average cloud tops ranged from 9,500 to 18,700 ft MSL, with an average of 12,300 ft. The maximum cloud tops ranged from 12,400 to 30,000+ ft MSL, with the average 17,000 ft. (In general, there were 1 to 3 cloud towers in a cloudline clearly

taller than the rest.) Only six cases had maximum cloud tops reaching 20,000 ft or higher.

It seems clear that cumulus cloudlines which are active waterspout producers are composed primarily of warm, actively growing clouds in the cumulus or early mature stage. Surface observations and aircraft documentation clearly indicate that thundershowers occasionally develop from cells which earlier had spawned waterspouts. Only in rare instances have waterspouts and thundershowers been observed simultaneously in the same cloudline. Hail occurrence in the Florida Keys is extremely rare, and the explosive vertical growth in cumulus cloudlines which spawn waterspouts is usually manifested by benign, heavy rainshowers. There was one well-documented case where marble-sized hail fell from a cloudline which earlier produced several waterspouts.

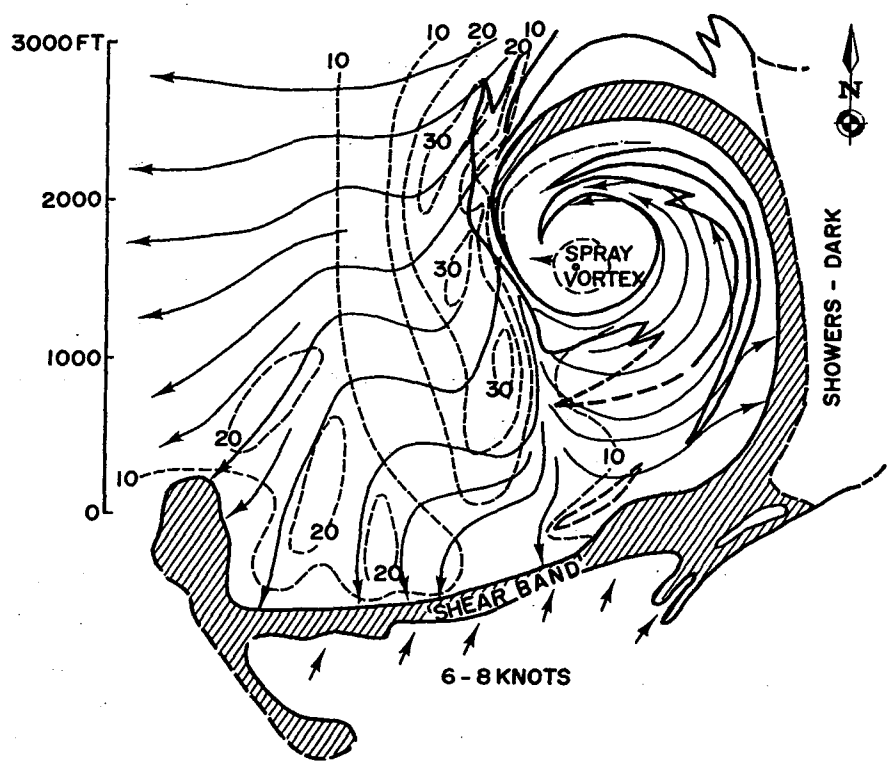

Figure 23. Composite streamline (solid) and isotach (dashed) analysis of boundary layer flow on spiral scale around waterspout of September 10, 1969, derived from the analysis of smoke plumes and photogrammetry of spiral features. Isotachs in knots. During the period of the compositing of flare data, we have assumed that the boundary layer circulation of the waterspout is a permanent-type system as the spray vortex advances toward the smoke flares. At each instant of time, therefore, a streakline approximates a relative streamline.

Time-lapse photography of cloudlines and concurrent waterspout developments has provided important data on the growth characteristics of cloud elements. The scaling procedure previously outlined was used to help compute the vertical growth rate of cloud turrets and bubbles. To relate cloud growth and waterspout formation, each time-lapse frame was arbitrarily divided into three sections. (The partitioning was done whenever possible to fit the natural division into individual cumuli or small groups of cloud towers.) Both the average and maximum vertical growth rates in each section were determined by tracking several features over consecutive 10-frame intervals.

Waterspout-producing cloudlines were frequently observed simultaneously by aircraft and the Key West radar. One case was an east-west oriented cumulus-congestus cloudline, 14 n mi north of the Key West Airport, that spawned three waterspouts during a 65-min period on September 10, 1969. The first two waterspouts had wide, but short funnels with pronounced dark spots which slowly decayed. The third waterspout formed as the second was in the decay stage and became the largest and best-documented event. Graphs of photogrammetrically derived vertical cloud-growth rates, computed over 20-frame intervals, are given in figures 24a through 24d. Times of major waterspout features have been bracketed on the abscissa. Although observations for sections II and III were somewhat limited by intervening cumulus development, the cloudline was building generally into the environmental flow.

The first two waterspouts formed and decayed entirely within section II. The largest waterspout formed near the western boundary of section II and moved in response to the shower outflow into section I near the end of its life cycle. Average cloud tops in section I were 8,000 to 10,000 ft and in section II were 12,000 to 15,000 ft. The highest cloud tops were generally found in section III (15,000 to 18,000 ft and occasionally higher) with periodic cumulonimbus-anvil production.

The average vertical growth-rate curves throughout the cloudline again demonstrate pulsations of the convective updrafts during waterspout formation and decay. The first two waterspouts formed simultaneously with an abrupt rise in cloud-growth rates and dissipated at relative minima. Rapid increases in growth rates also occurred in section I during the formative stages of the first two waterspouts. The third waterspout formed in section II when average growth rates exceeded 4.3 m/s with a maximum value of 10.1 m/s. Finally, the waterspout reached the spray-ring stage just 2 min after a major peak in average growth rate for section I (6.7 m/s) and a sharp rise for section II to 5.2 m/s. There appears to be a good in-phase relation between growth rates for all three cloudline sections. The middle section contained the cell which was the parent to three waterspouts, and it had the largest average vertical-growth rate. The post-waterspout curves in figure 24d indicate the growth rate in all sections was smaller than in figures 24a through 24c.

Clemons' radar studies (1969) show that: (a) Most single waterspout events were associated with a narrow protrusion, occasionally in the form of a sharply defined "spike," near the waterspout location; (b) a few multiple waterspouts were observed with funnels located on the edge of a large crescent-shaped echo; and (c) no well-defined hook echoes were associated with waterspout occurrences during the 1968 pilot study.

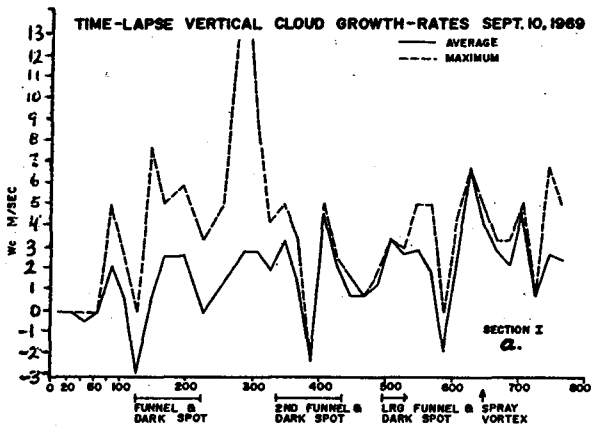

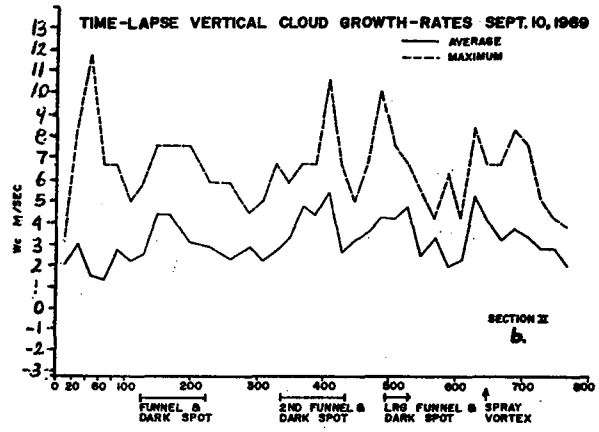

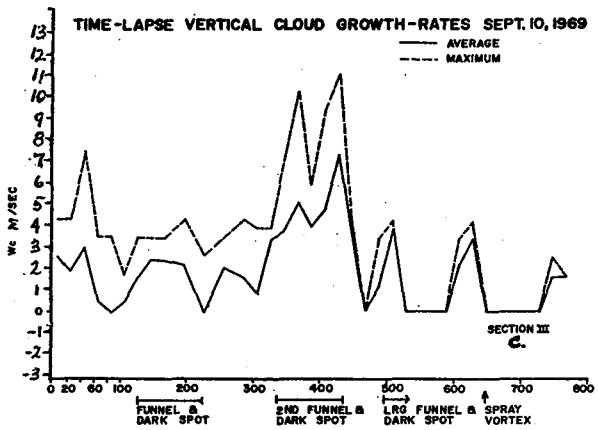

Figures 24a, 24b, and 24c. Average and maximum time-lapse vertical cloud-growth rates as a function of frame number (time) for each of three sections of cloudline on September 10, 1969. See section 4.3 for details.

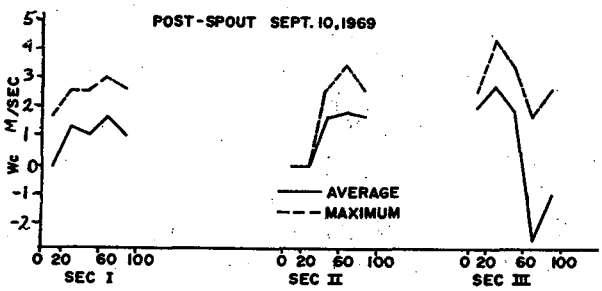

Figure 24d. Average and maximum time-lapse vertical cloud-growth rates as a function of frame number (time) for each of three sections of cloudline on September 10, 1969, following demise of giant double-walled waterspout.

Short-pulse radar documentation during 1969 shows that observed rotating hook echoes can be directly associated with large waterspouts in the mature stage, but well-defined hook echoes constitute only about 10 percent of the WSR-57 radar documentation of confirmed waterspouts. One of the best documented cases of this type is shown in figures 25a through 25d. The developing echo line was moving slowly eastward, while individual cells in the line were moving northeastward. Project aircraft monitored this cloudline in early stages, and documented five small cyclonic waterspouts 7 n mi northwest of Key West from 2035 to 2109 GMT (Greenwich Mean Time). Note the two "spikes" extending out of the southern flank of the echo line in this location on figure 25a. The expanding middle cell (arrow, fig. 25a) was overtaken by a split-off cell to the southwest (fig. 25b). As these two echo cells merged (fig. 25c and 25d), a rotating hook echo developed on the tip of an echo protrusion which rapidly emerged from the merged echo-complex. A large waterspout was photographed at about 7 n mi north of Boca Chica Naval Air Station (NAS) between 2123 and 2136 GMT.

A second case of nearly simultaneous radar hook-echo formation and confirmed visual sighting is shown in figures 26a through 26j. Waterspouts were observed from both the Key West Weather Service Office and Boca Chica NAS in conjunction with this hook-echo development. These observations were made at the following times and locations relative to Key West: funnel, 5 n mi north-northeast, 2320 to 2325 GMT; funnel 6 n mi north, 2320 to 2325 GMT; waterspout, 7 n mi northwest, 2328 to 0010 GMT; waterspout 5 n mi northwest, 2337 to 2349 GMT; and second waterspout, 5 n mi northwest, 2337 to 2349 GMT. The waterspout located 7 n mi northwest from Key West appeared to be the major one and was associated with the entire evolution of the hook echo. The last two short-lived waterspouts developed in the hook echo 3 min before figure 26d. Cell movement was toward the southwest; the hook developed toward the south in a flanking line. A unique aspect was the development of an anticyclonic hook or eddy upstream (northeast) from the decaying cyclonic hook echo, beginning at about 2354 GMT (fig. 26f). Fortner and Jordan (1960) document a similar spiral-shaped radar echo, apparently of nontornadic origin, which persisted for well over an hour in a region of airmass thundershowers.

4.4 The Cumulus Cloudline Scale

4.4.1 Surface Heating Contributions

The Big Pine Key area was earlier hypothesized as the primary cloudline-genesis region in the Lower Keys. The sea-surface temperature on the south shore of Big Pine Key, taken at 1650 EDT, August 21, 1970, was a very warm 33°C. The smoothed air-temperature data from the Braham Lodestar flight have been analyzed at 0.5°C intervals (fig. 27), with air temperatures plotted along the flight track at 10-s intervals.

The large warm-temperature anomaly was displaced with the wind from the northern portion of Big Pine Key northward into Florida Bay, and secondary warm anomalies of 26.5° to 27.0°C are also present over the smaller islands east of Big Pine. Only islands having the longest horizontal dimension of at least 1 to 2 n mi produce warm pockets large enough to be detected at flight altitude. These cloud-scale warm pockets are all systematically displaced

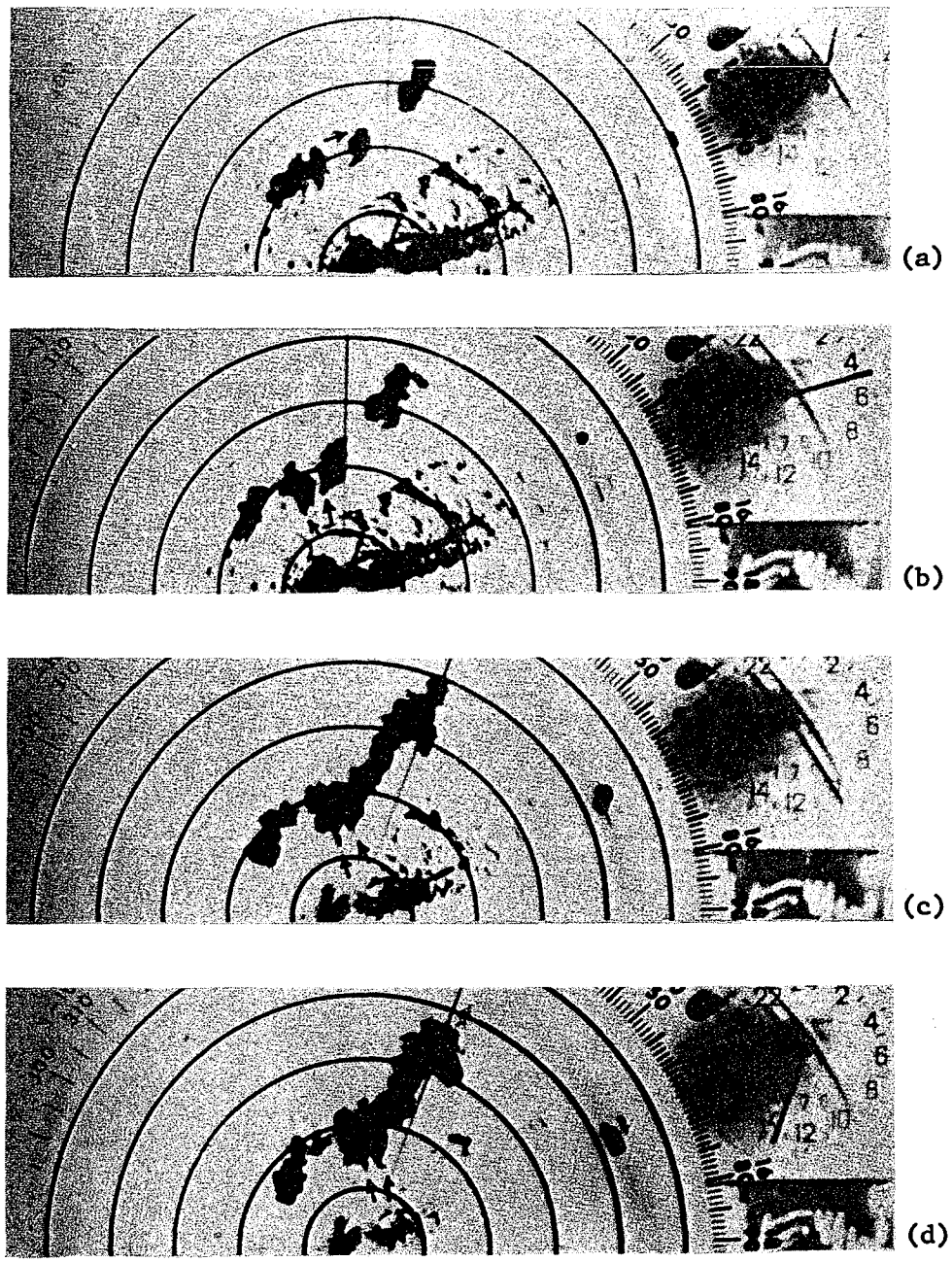

Figure 25. Short-pulse, short-range (25 n mi), Key West WSR-57 radar sequence showing development of rotating hook echo in line of building cumulus congestus. Two small waterspouts were documented by project aircraft 7 NW, early in sequence; one large waterspout was photographed 7 N from Boca Chica NAS at time and azran of hook echo on June 19, 1969. Range marks were 5 n mi. Cell motion indicated by arrows. (a) View at 2102 GMT; (b) View at 2112 GMT; (c) Antenna tilted 4°, view at 2125 GMT; and (d) Antenna tilted 4°, view at 2134 GMT.

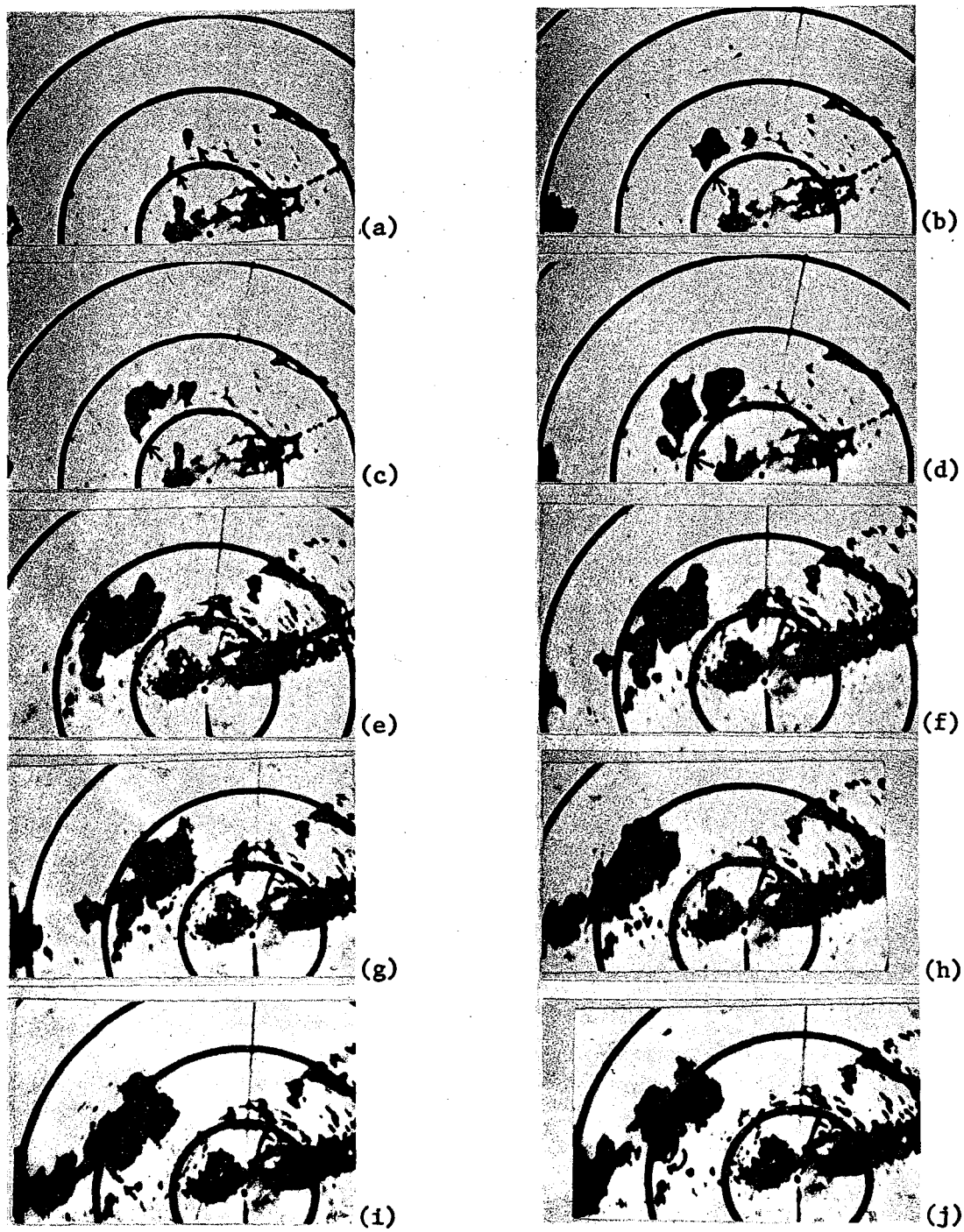

Figure 26. Key West WSR-57 short-pulse radar sequence on August 7, 1969. See Section 4.3 for details. (a) Time: 2323 GMT, incipient short-pulse echoes 7.5 n mi N and 6 n mi NNW; (b) Time: 2328 GMT, tilt 2.5°; (c) Time: 2334 GMT, tilt 2.5°; (d) Time: 2340 GMT, tilt 2.4° = 0.5 km at 6 n mi; (e) Time: 2351 GMT, tilt 1.5°; (f) Time: 2354 GMT, tilt 0.5°; (g) Time: 2355 GMT, no tilt; (h) Time: 2404 GMT, tilt 0.5°; (i) Time: 2407 GMT, tilt 0.5°; and (j) Time: 241230 GMT, tilt 0.5°.

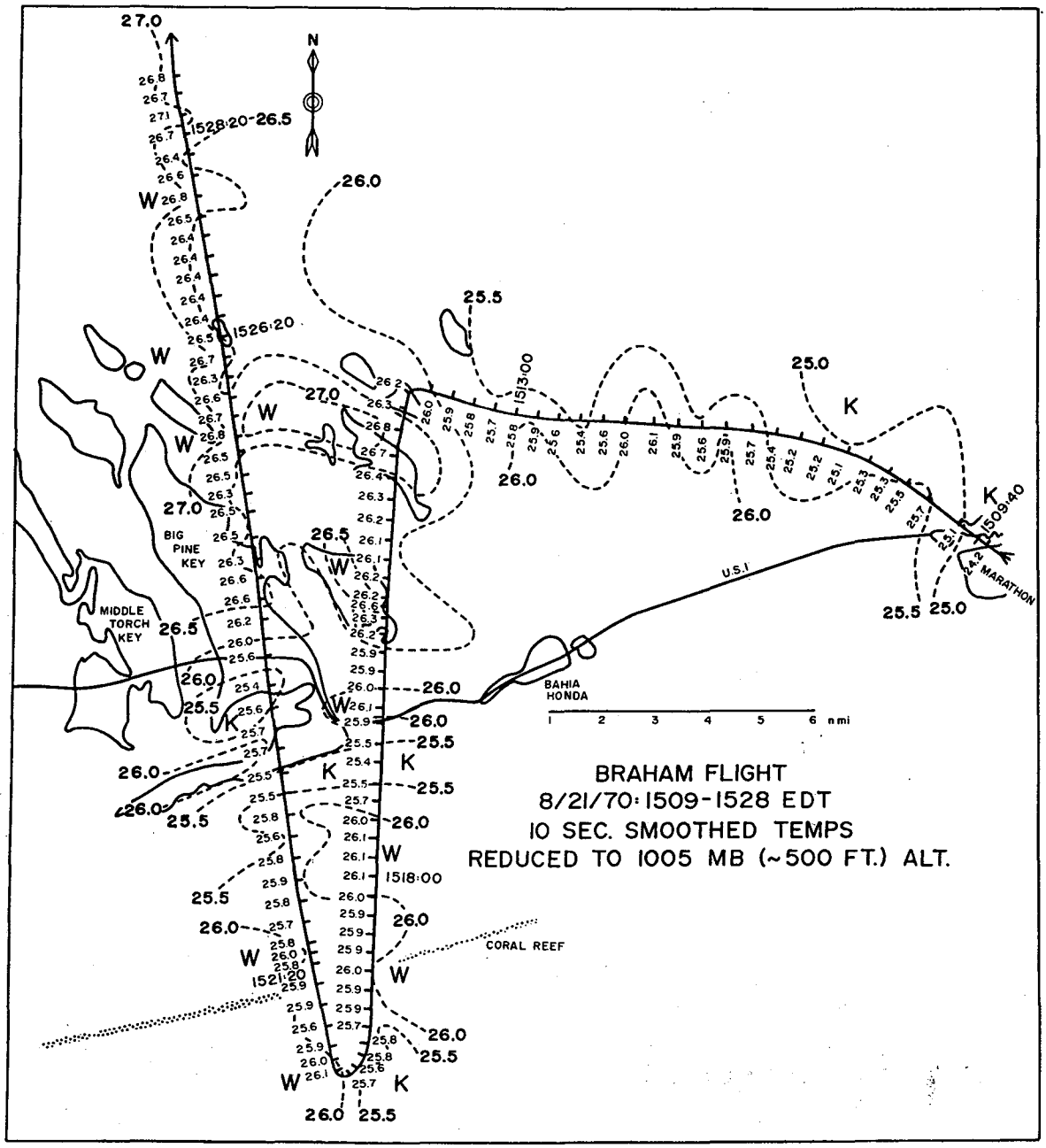

Figure 27. Isotherm analysis at 0.5°C intervals of smoothed air temperatures reduced to common level of about 500 ft MSL. Data measured by Rosemount sensor on Lockheed Lodestar aircraft from Cloud Physics Laboratory, University of Chicago.

northwest of the smaller islands. Horizontal temperature gradients over the south portion of Big Pine Key exceed 1°C per nautical mile in the north-south direction in qualitative agreement with Malkus (1963). Finally, if we consider the surface water temperature of 33°C as representative of the surface air temperature (1.5 hr after the flight), then the smoothed aircraft temperatures in this area indicate an absolutely unstable lapse rate through the lowest 500 ft.

The expected development over the Big Pine Key area failed to materialize because of a gradually thickening cirrus deck over South Florida. Solar insolation was greatly reduced over the Lower Keys, and normal convective cloudline development was inhibited.

Dewpoint time-sections along the two major north-south flight legs were prepared from 1-s data, without applying corrections for the small altitude changes. Dewpoint fluctuations up to 2.7°C occur on a time scale of about 10 s (1 n mi) on the southward leg over the small island group east of Big Pine Key (see flight track in fig. 27). Somewhat larger scale dewpoint fluctuations, of mean period 20 s (2 n mi) and of amplitude from 0.8° to 1.8°C, are found in the northward leg over Big Pine Key. It would appear from these results that bubbles or pockets of moisture transported upward by convective-eddy processes in the ground (mixed) layer are of smaller scale than the thermals produced by the larger islands.

4.4.2 1969 RFF Aircraft Waterspout/Cloudline Mission

A primary objective of the 1969 Lower Keys Waterspout Project was to map the three-dimensional structure beneath cumulus lines and its immediate environment. This goal was largely achieved by a RFF DC-6 mission on October 9, 1969 (Friedman and Callahan, 1970). A detailed description of the RFF DC-6 aircraft, navigational and operational practices, and data processing procedures regularly employed are outlined by Friedman et al. (1969).

Data were obtained on two cloudlines at three levels (1,000, 2,150, and 3,700 ft MSL of radar altitude), with box flight patterns displaced with the cloudline's movement. The first cloudline was about 30 n mi long and oriented northeast-southwest. Flight data were taken through the northeastern one-third of the line at 10-s intervals.

After completion of the investigation of this cloudline, a possible funnel cloud was sighted in a developing cloudline some 7 n mi west. This second cloudline was observed to produce at least three mature and four incipient waterspouts (dark spot or funnel combinations) during the 30 min that it was under investigation. Multilevel data were taken around the second cloudline, flying close to the waterspouts. The waterspout-active cloudline was somewhat smaller in horizontal dimensions (2 to 3 n mi wide; about 10 n mi long). Between 2228 and 2255 GMT, the aircraft flew a series of elliptical loops with major axes centered in the cloudline and parallel to its orientation.

Level-1 cloud mapping superimposed on a Calcomp plot of the loop, with radar altitude indicated along the track, is shown in figure 28. Hori-

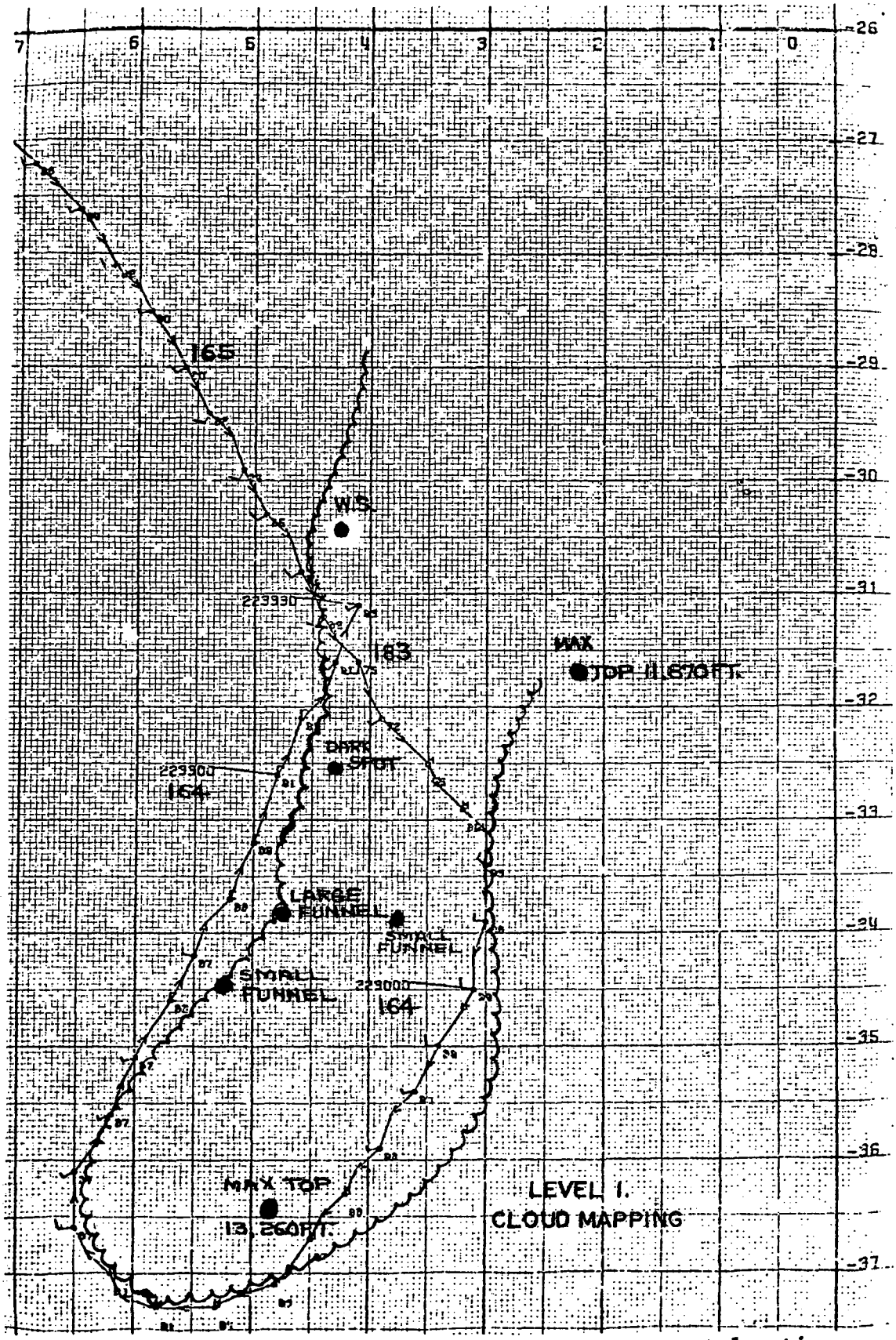

Figure 28. Photogrammetric cloud mapping, waterspout locations, and maximum cloud tops. Three-digit numbers are aircraft radar altitude in tens of feet. Mean aircraft altitude = 1,650 ft MSL.

zontal cloud boundaries, waterspout structures, and maximum visual cloud tops were located by the gridded photogrammetric method of Herrera-Cantilo (1969). Four of the five waterspouts were located on the leading (western) edge of the cloudline. Maximum visual cloud tops in two major towers on the northern and southern end of the line were 11,870 and 13,260 ft, respectively, at about 2225 GMT. Major cloud towers were strongly tilted toward the east, consistent with the vertical shear vector indicated through this layer on the Boca Chica sounding. No rainshowers of consequence were encountered on the first loop. The numbers plotted on the axes in this and subsequent Calcomp figures are virtual longitude and latitude referred to a fixed reference point. The large waterspout at point -33.85, 4.75 was tracked for a few frames on the right side camera film with velocity estimated at 15 kt toward 240°. An analysis of radar cloud-height topography, at 2,000-ft intervals for level 1, is shown in figure 29. The technique for obtaining radar cloud heights from a digitized analysis of Real-time Data Relay (RDR) cross-sectional radar film is given by Jarvinen and Black (1971). Maximum cloud-top positions from the RDR agree well with the photogrammetric locations. Radar and visual cloud tops agree to $\pm$ 2,000 ft, although the radar measurements of strongest discrepancy (on the southern end of the cloudline) were taken 7 min after the photogrammetric computations. The waterspouts are nearly all on the leading edge of the strong contour gradient in figure 29. Maximum RDR cloud tops for the level-1 flight track reached 14,000 ft in cells on the northern and southern ends of the line.

Analyzed streamlines for the level-1 NNV-Doppler winds have been superimposed with the radar echo tracing and range circles from the Key West WSR-57 in figure 30. There is a large, older radar echo in the northeast corner of the radar flow chart between virtual latitudes -27° and -32°. From the aircraft, it appeared that the cloudline spawning the waterspouts had developed and was building along the leading edge of the outflow from this large shower. A gradual change of flow curvature with latitude and vertical consistency are assumed. Note the anticyclonic turning of the flow downstream from the older shower and the pronounced cyclonic wave-perturbation coincident with the western boundary of the waterspout cloudline. Especially interesting is the flow deflection through an entrance-exit region, centered on the leading edge of the waterspout echo cell, with upstream difluence and downstream confluence. Note also that one mature waterspout (northernmost) lies outside any radar echoes at this time, while the other four are all located downwind from a major echo boundary. (Positioning of the scaled-radar echo tracings was accomplished by using the aircraft blip on the same frame as a reference point. In this technique, the location of radar echoes relative to the flight track is considered accurate to less than 1 n mi.) Even though the aircraft was flying through the WSR-57 radar echoes in the eastern one-half of loop 1 (fig. 30), no precipitation was encountered. Because the radar antenna was at 3° elevation, we surmise that the tilted cloud towers had liquid water suspended in developing updrafts above the five waterspouts.

Streamlines and isotachs for the level-1 renavigated (NNV) Doppler wind data are given in figure 31. Note the windspeed minimum along the axis of the entrance-exit region in the echo core. Horizontal convergence and relative vorticity were computed from the analyzed wind fields on the scale of the aircraft loop 1 and are both approximately $+3 \times 10^{-3}$ s^{-1}. The net

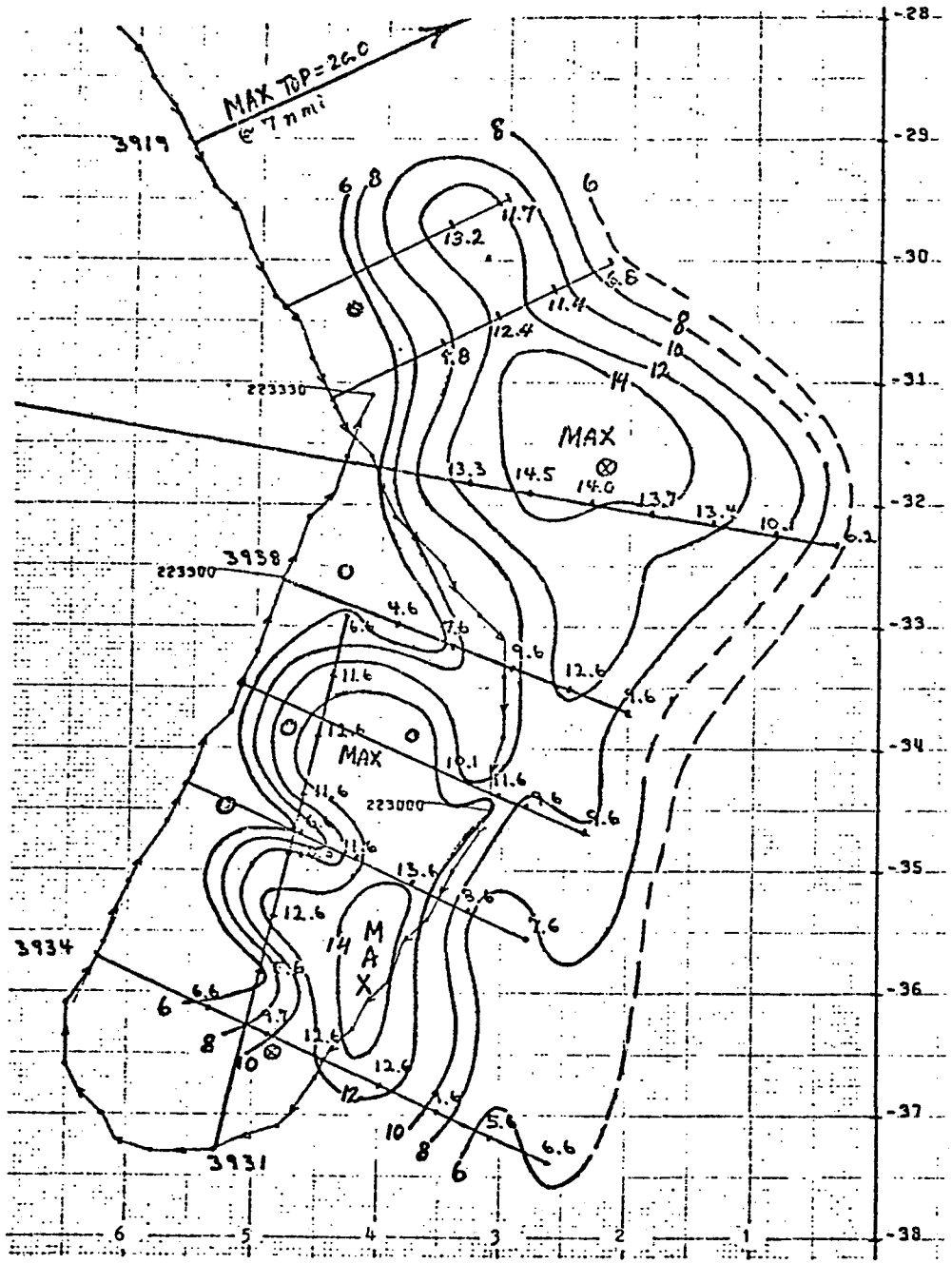

Figure 29. Contour analysis of cloud-height topography (x 1,000 ft), using radar cloud-top data generated by digitizing aircraft RDR radar film. Data from level-1 flight track, utilizing scheme devised by Jarvinen and Black (1971).

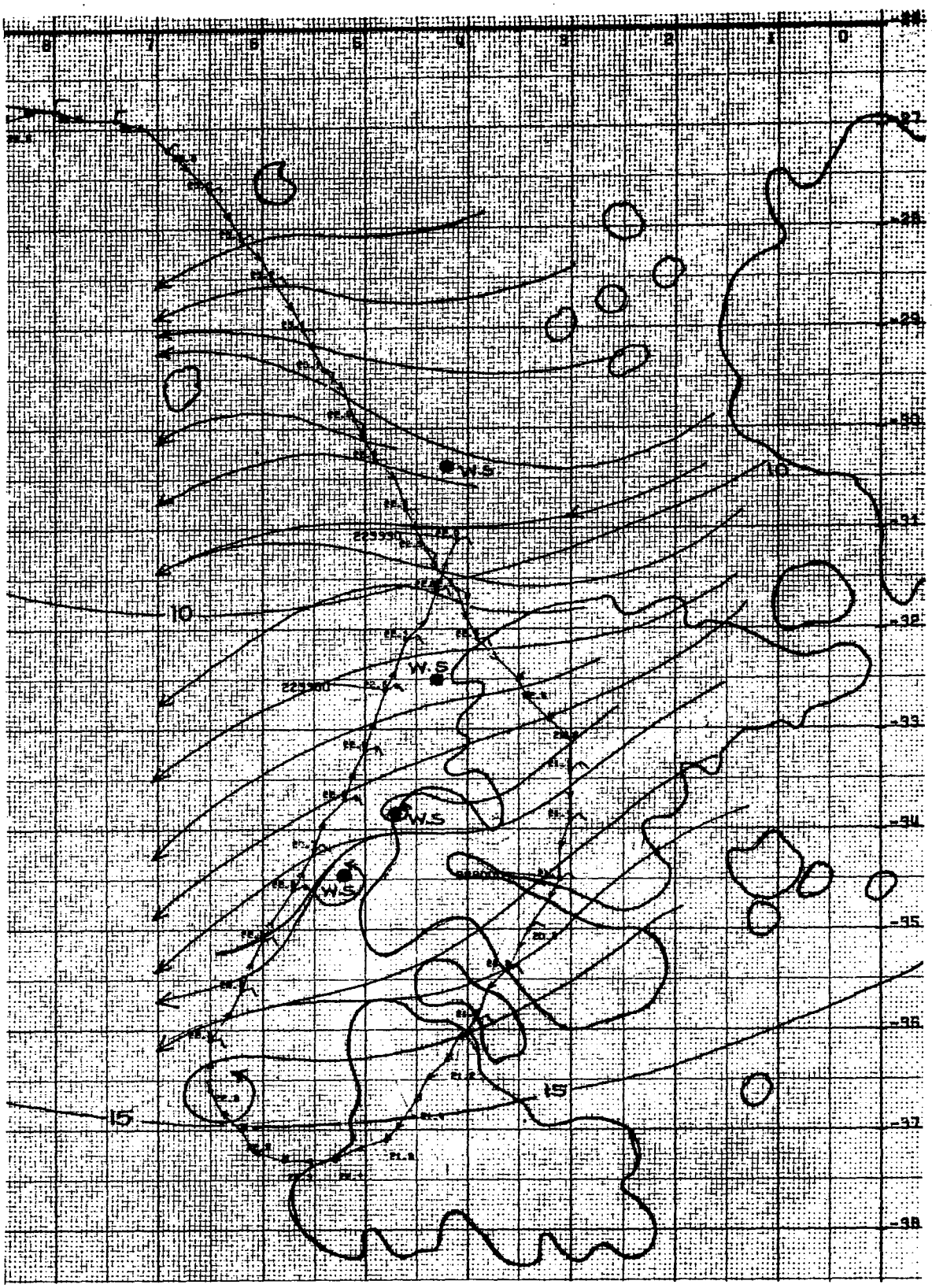

Figure 30. Level-1 scaled tracing of Key West radar (short-pulse, short-range modes) and superimposed NNV-Doppler wind streamlines.

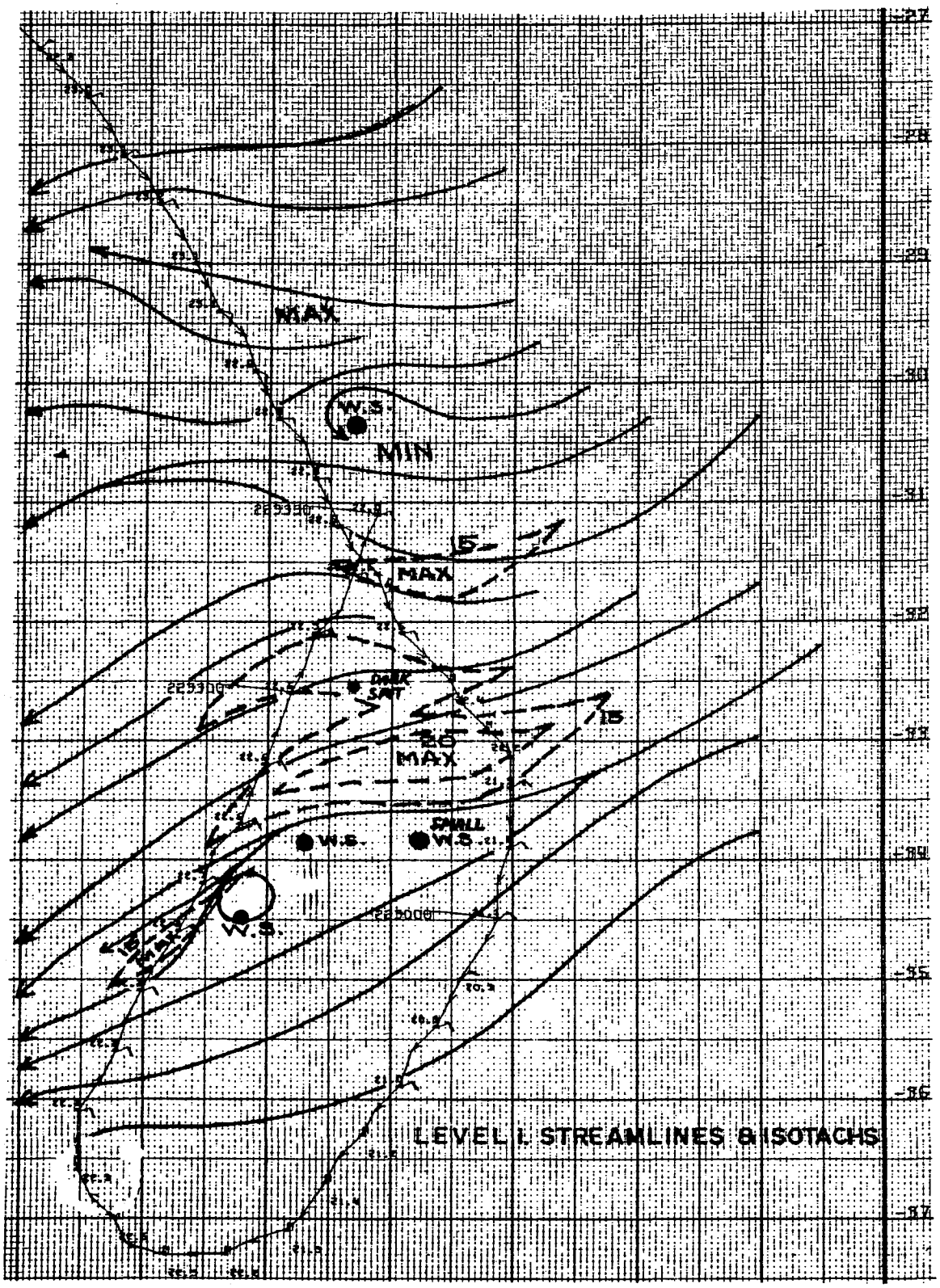

Figure 31. Level-1 RFF-Doppler wind streamlines and isotachs, with plotted waterspouts.

computed circulation (Γ) around the closed aircraft loop, using the plotted wind data directly, was 9.85×10^2 m^2 s^{-1}. All five waterspouts were in local maxima of cyclonic curvature, and relatively large values of cyclonic shear were found immediately to the north of each.

Isotherms have been superimposed on the NNV Doppler streamlines in figure 32 (Level 1, mean altitude 1,640 ft). The waterspouts generally lie along the leading edge of cool air outflow (temperatures below 21.0°C) which probably originated from the large decaying echo upstream. The temperature change across the cloudline in the level-1 analysis is about 2°C. Because no precipitation and little cloud matter were encountered, wet-bulb effects in the Vortex thermometer data should be small. The maximum horizontal temperature-gradient in the vicinity of the three waterspouts was about 1.8°C/n mi, while maximum temperature advection was -9°C/hr.

Infrared hygrometer measurements revealed that waterspouts are located in regions of relative humidity between 80 to 85 percent (fig. 33). Relative winds were computed by subtracting a photogrammetrically estimated vector motion for the largest waterspout (240°/15 kt) from the actual Doppler winds at each observation point. The three primary waterspouts are located in a sharp trough in the relative flow (fig. 33), and the axis of this trough extends along the cloudline's leading edge (fig. 28).

Draft-scale vertical-motion profiles were computed along straight or gently curving flight-track segments, using the Sheets and Carlson (1971) method. Because the aircraft probably does not respond well to vertical motion fluctuations at 1-s intervals, a one-two-one weighted smoother was applied to profile peaks, with only peaks defined by three or more data points smoothed. Significant peak values and smoothed vertical motion are given in figure 34. Note that the waterspout-active (southern) cloudline portion has draft-scale rising motions up to 2 m/s, while all waterspouts are in regions of rising motion of at least 1 m/s. Compensating sinking up to -2 m/s beneath the eastern cloud overhang agrees with the low relative-humidity tongue (fig. 33).

Cloudline-scale analyses and discussion of the RFF flight results for levels 2 and 3, corresponding to those given above for level 1 data, are presented in appendix B. Only an outline of the salient cloudline features deduced from the levels 2 and 3 will be presented here.

To study the energetics and scale of vertical convective transport processes in the waterspout-active cloudline, values of wet-bulb potential temperature were computed at 10-s intervals from adjusted Vortex temperatures, Cambridge hygrometer dewpoints, and ambient pressure. The analyzed fields of θ_w for levels 1 and 2 are given in figures 35a and 35b, respectively. Browning and Ludlam (1962) and others have shown that the severe thunderstorm environment is characterized by a wet-bulb potential temperature profile which exhibits a minimum at middle levels. Newton's (1950) squall line model contained this minimum as an essential component. Zipser (1969) has shown that tropical disturbances also derive energy from downdrafts formed by evaporation from midlevel, low θ_e-air. The importance of midlevel, low θ_e-values for tornado occurrence has been demonstrated by Darkow (1967). (Because θ_e

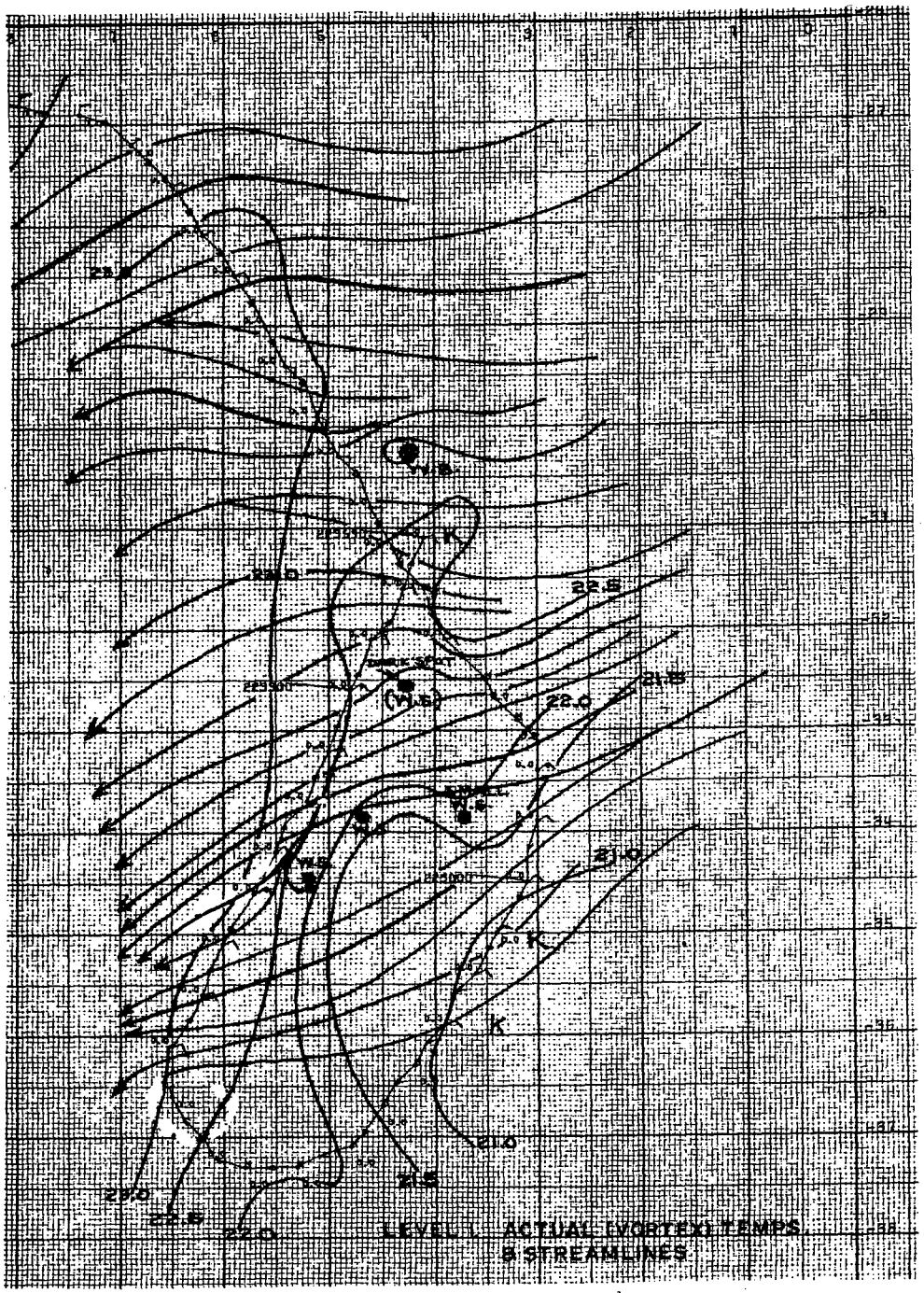

Figure 32. Level-1 actual (Vortex) isotherms (0.5°C interval) and RFF-Doppler streamline analysis.

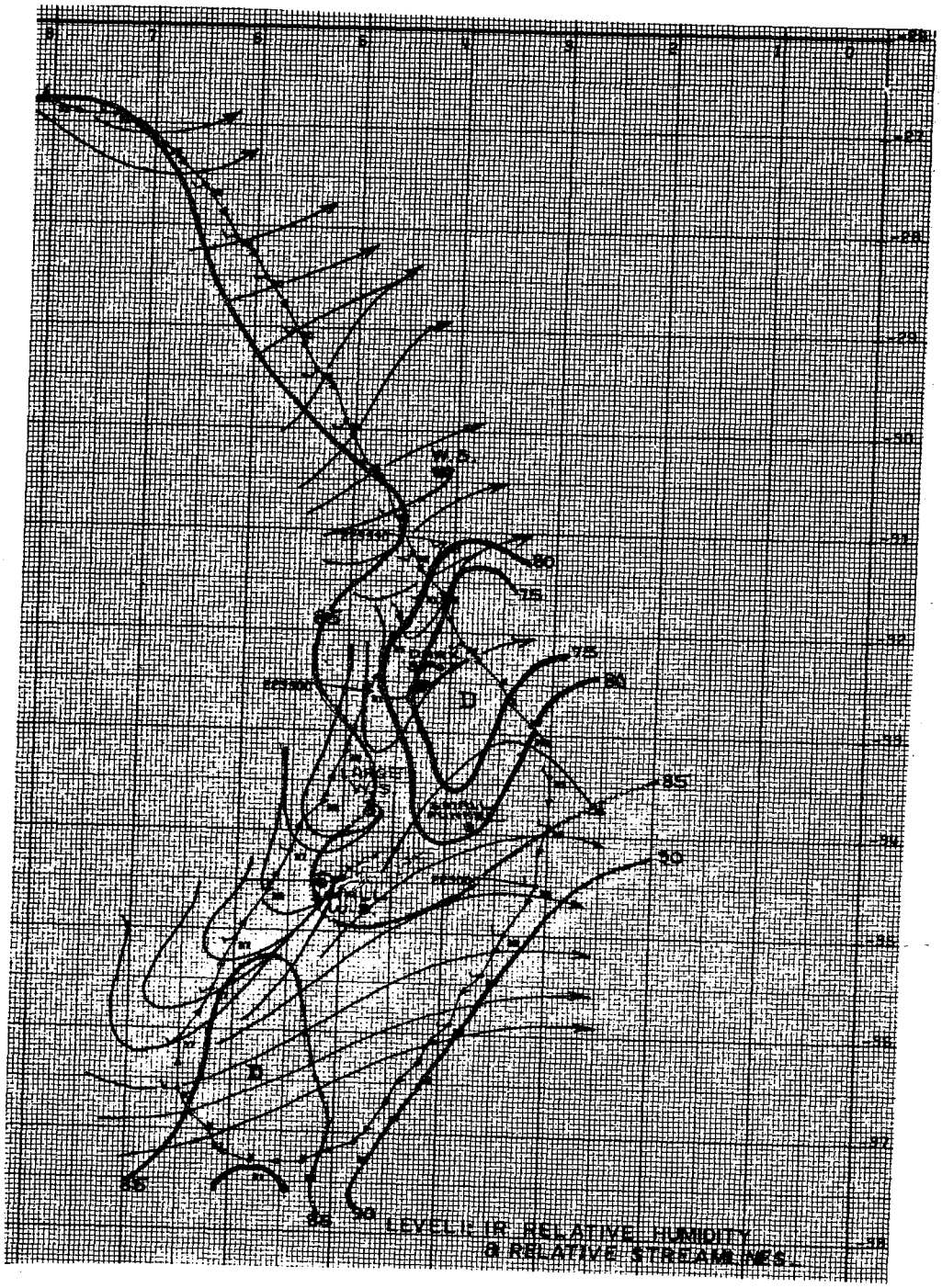

Figure 33. Level-1 infrared relative humidity at intervals of 5 percent and relative streamlines (derived from Doppler winds and estimated waterspout movement).

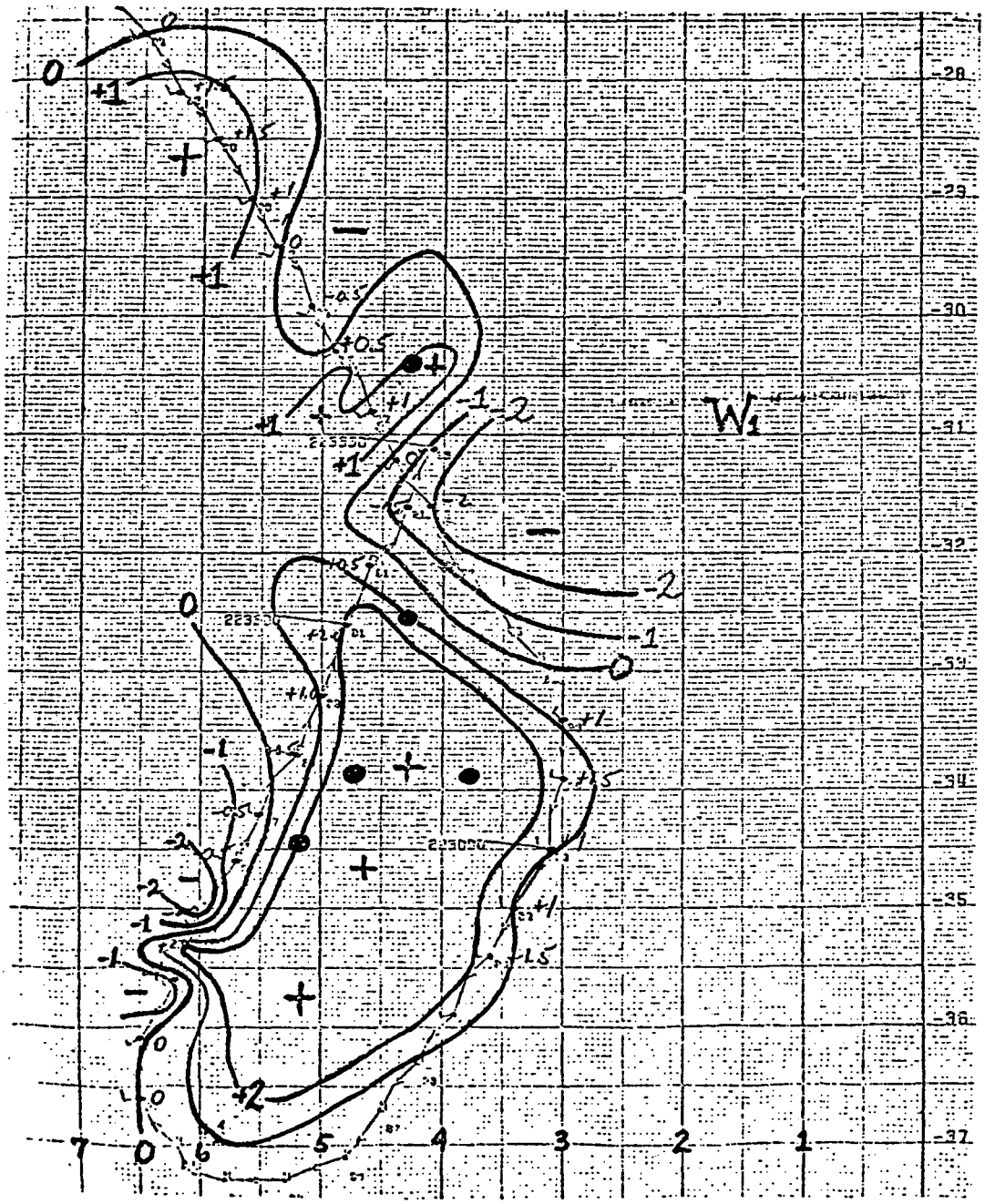

Figure 34. Analysis of smoothed draft-scale vertical velocity field in units of meters per second for quasi-straight segments of level-1 flight track on October 9, 1969.

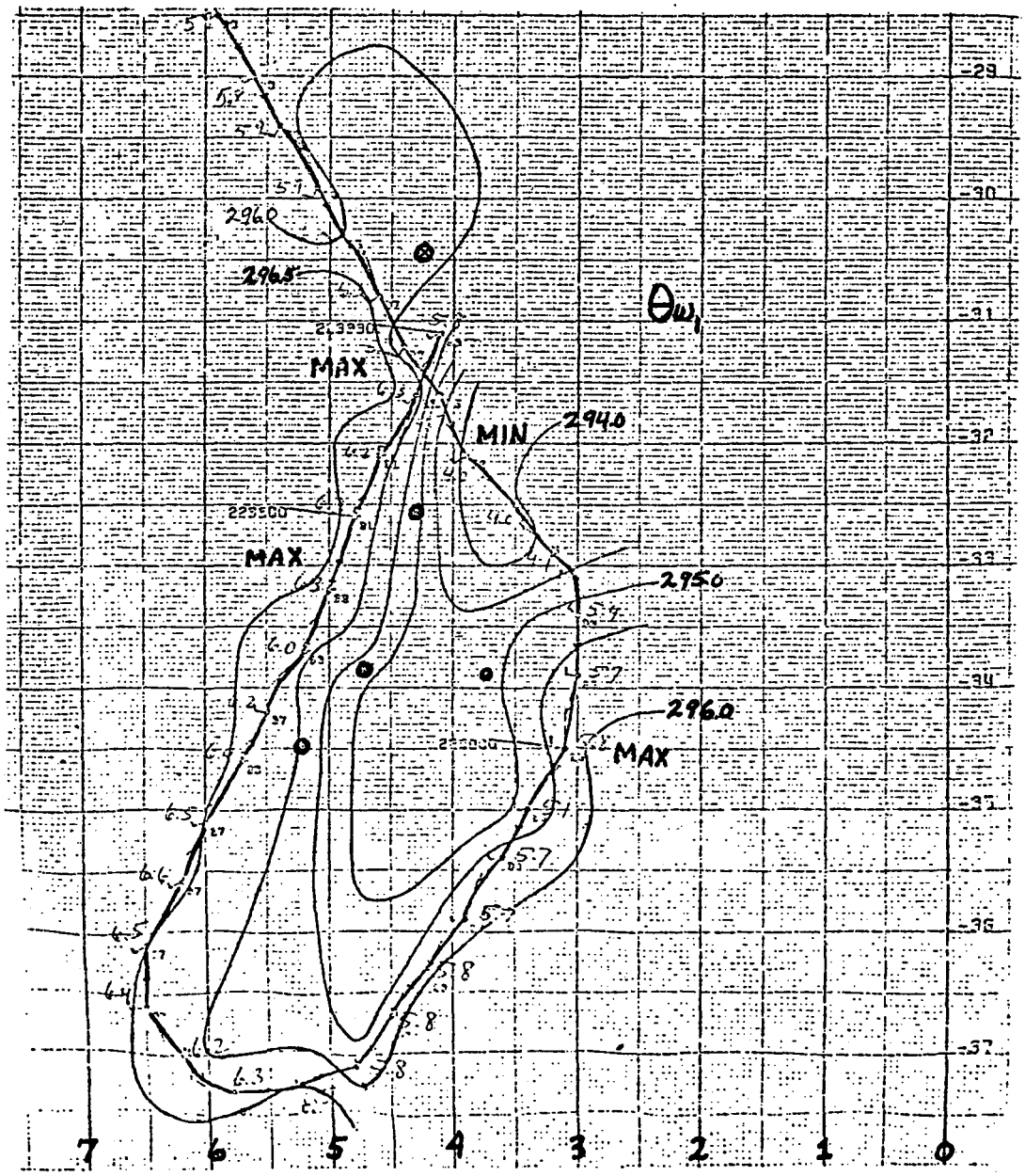

Figure 35a. Wet-bulb potential temperature analysis for level-1 at 0.5°C intervals. See section 4.4.2 for method of computation.

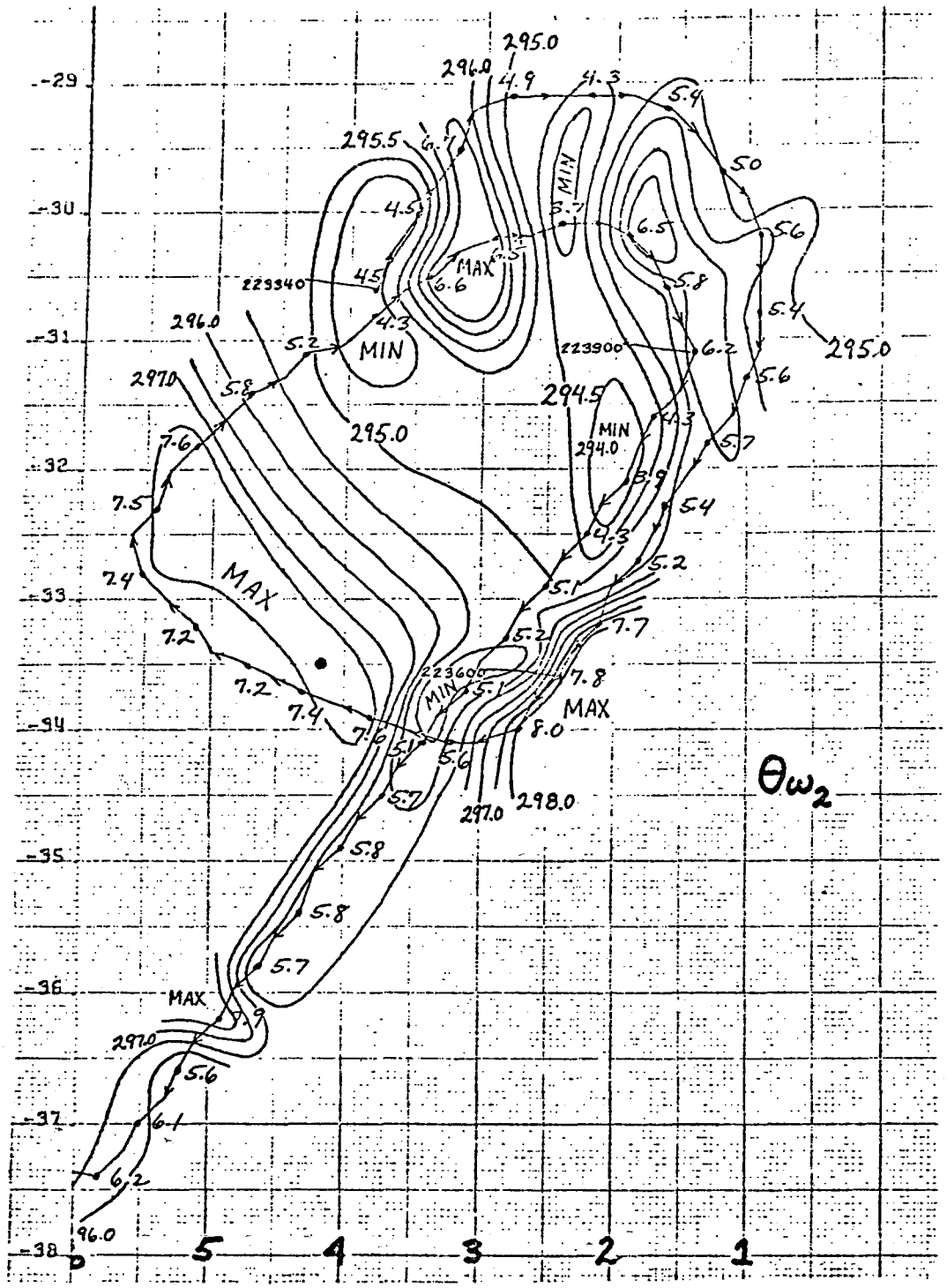

Figure 35b. Wet-bulb potential temperature analysis for level-2 data.

uniquely determines θ_w and vice versa, conclusions reached for one also apply to the other.) Garstang et al. (1967) have examined tropical soundings in terms of θ_e (which closely approximates the total static energy) and found that midtropospheric minima nearly vanish in synoptic disturbances and are intensified during periods of fair weather. Waterspouts are most commonly observed in the Florida Keys on weakly disturbed or "fair weather" days.

Morgan and Beebe (1971) analyzed the time-space behavior of θ_e fields during a severe weather situation. The θ_e minimum is important in two distinct ways: (a) If lifted or stretched, low θ_e-air will become colder than the undisturbed environment, and the lapse rate will increase; and (b) if rained into, the low θ_e-air will become colder in situ than the surrounding undisturbed environment, and the resulting downdraft can provide lifting for low-level, high θ_e-air. The second process is believed important to waterspout cloudlines in the Lower Keys.

Examination of wet-bulb potential temperature fields (fig. 35a and 35b) and comparison with draft-scale vertical motion fields (fig. 34 and appendix B) lead to the following conclusions: (a) All waterspouts are in regions with subcloud values of $\theta_w \geq 295°K$. Before the onset of precipitation, major waterspout developments occurred in regions of strong θ_w gradient; thereafter, the waterspouts are located within the maxima of θ_w. (b) Primary sinking motions are associated with θ_w minima, while the major rising-motion regions are associated with high values. The largest horizontal θ_w changes are found at the lower level (fig. 35b, level 2) and amount to more than 4°K. From the Boca Chica sounding, it appears that the low θ_w-air at level 2 (values of θ_w between 294° and 295°K) originated from the 6,000- to 11,000-ft layer. This is consistent with the vertical extent of the cloudline during the early phase.

In summary, the maximum tops initially were 17,000 ft in the nonwaterspout cloudline, while the waterspout cloudline had two maximum cloud tops to about 13,000 ft initially. Cloud tops in the first line decayed as new cloudlines formed on both flanks of the shower-outflow boundary, and tops in the waterspout line grew to at least 17,000 ft in about 12 min.

Flow through the first cloudline showed two confluent asymptotes; one along the right-downwind boundary of the line and another 3 to 4 n mi northwest. The slope and structure of these asymptotes and the associated moisture field accounted for the difference between cell movement and line propagation. There was a broad cyclonic curvature region in the northeastern portion and anticyclonic curvature in the southwestern end of the first cloudline, and the winds backed with height; this structure was consistent with the large vertical tilt of clouds in the line. The apparent split in the flow around major echoes was most pronounced at the upper level (3,700 ft), with cyclonic shear on the north flanks and anticyclonic shear on the south flanks at all levels. Regions of cyclonic curvature and shear tended to occur in sinking air or on the edge of major cloud boundaries with weak temperature advection.

The waterspout-active cloudline exhibited hydrodynamic-flow deflection around the main waterspout echo at each level, with large values of cyclonic

curvature and shear on the north side. All waterspouts were north of the split, with large upward vertical motion along the leading edge of the cold-temperature advection region. The draft-scale vertical motions attained their largest magnitude during the later aircraft loops, while the original cloudline was decaying and a new line of towering cumuli was developing along the major shower-outflow boundary (appendix B).

There was larger and more concentrated temperature advection in the waterspout cloudline (up to 43°C/hr), implying a more baroclinic structure. The nonwaterspout cloudline and its associated thermodynamic fields were oriented mainly parallel to the low-level flow. Finally, the main waterspout echo-complex in the second cloudline had a cycloidal motion, while the mature waterspouts were in progress (levels 1 and 2).

Vertical motion and temperature advection were more organized in the waterspout cloudline, but there were more pockets of up-and-down draft-scale vertical velocities in the first cloudline. Waterspouts were on the leading edge of strong temperature and moisture gradient belts in the second cloudline. Both cloudline systems had maximum vertical motions late in their respective life cycles. The first cloudline had a rapid transition from -4.5 to +6 m/s in a new outflow-associated cloudline which formed along the original southeastern flank. There were maximum draft-scale vertical velocities of +4 m/s during the final loop around the decaying waterspout cloudline. These rising motions were encountered in the subcloud layer just below cloud base. Magnitudes of positive relative vorticity and convergence in the subcloud layer beneath the waterspout-active cloudline were both $\simeq 3 \times 10^{-3}\ s^{-1}$.

4.4.3 Sea-Surface Temperature Heating Mechanism

A Navy Super-Constellation flight was made on June 6, 1970, in meteorological conditions unfavorable for determining maximum heating effects. The flight encountered a few lines of suppressed cumuli and broken-to-overcast altocumulus. The sun broke through only near the end of the flight. A Barnes Engineering Company radiation thermometer (PRT-4A model) was used to obtain sea-surface temperatures at 1-s intervals. The flight track, with sea-surface temperatures plotted along it at 5-s intervals, is shown in figure 36.

Smoothed sea-surface temperatures range from 23°C in a deep water belt northwest of Key West to 28.7°C near Little Torch Key. Sea-surface temperature maxima lie along a broken, winding belt of 27.0°C and higher through Big Pine Key. High surface-water temperatures (26.0°C) are found along the reef parallel to the Lower Keys and through the "out islands" 5 to 7 n mi north of the Keys.

The mapping was intended to test the hypothesis that Big Pine Key and surrounding shallow water provide the primary heating mechanism for cloudline formations. Three factors influenced measurement of this surface heating distribution: (a) The early morning flight, over which we had no control; (b) the broken-to-overcast sky condition which effectively cutoff most of the solar heating; and (c) the radar-indicated extensive shower and thundershower

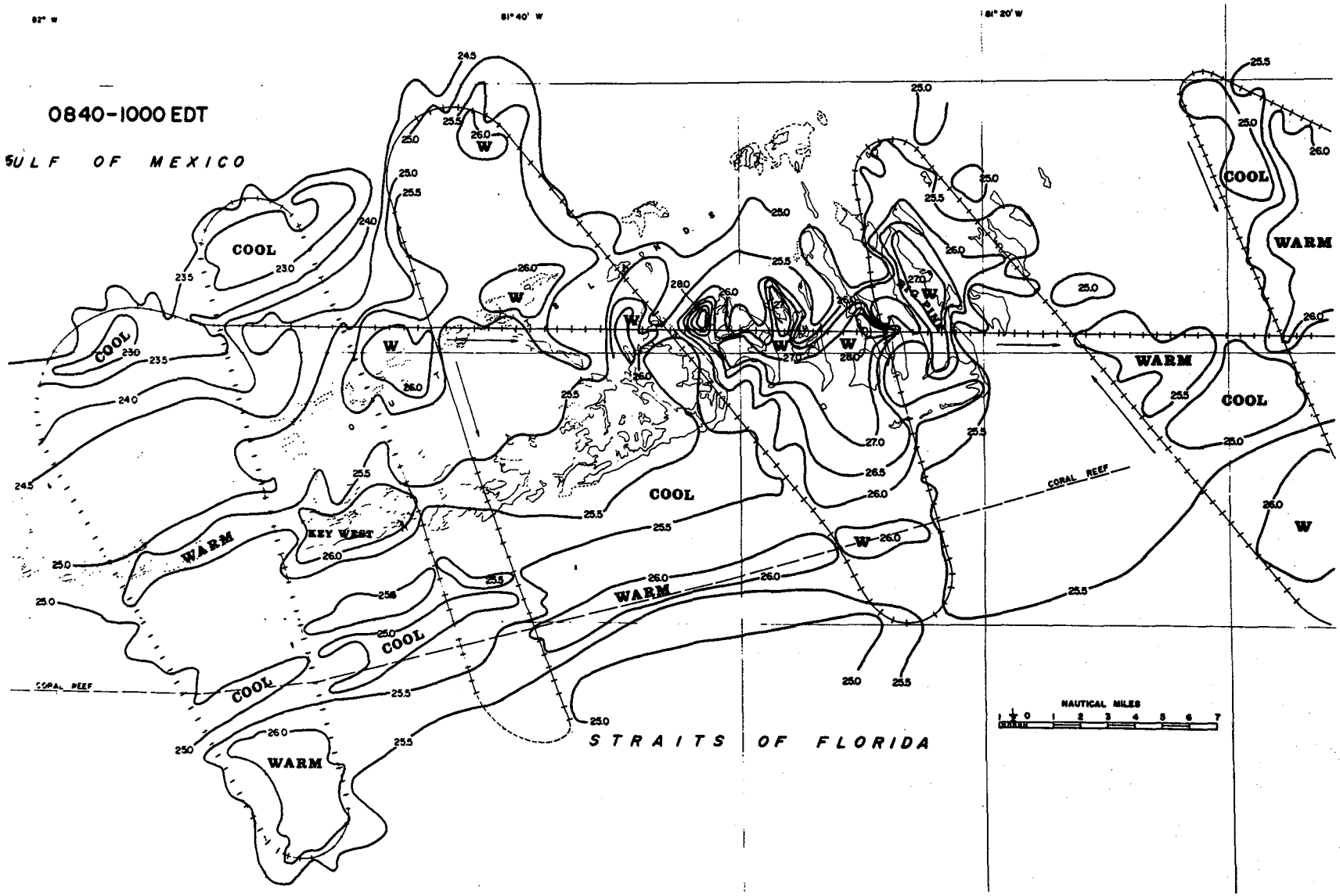

Figure 36. Final, smoothed sea-surface temperature analysis over Lower Keys at 0.5°C intervals. Raw data were obtained with Barnes PRT-4A infrared radiometer during Navy flight on June 6, 1970. Observations plotted along track are running means over 10 s, spaced about 0.5 n mi apart. Distance scale is at bottom.

activity over most of Florida Bay the previous night. These factors and the smoothing imply that surface water temperatures shown should be taken as conservative estimates, under meteorological conditions poorly representative of the waterspout environment.

A second flight was made with the NOAA RFF DC-6 aircraft on September 3, 1971. This flight utilized a Barnes PRT-5 radiometer (with improved resolution capability) and was made on a day ideal for waterspout development. Analysis of these temperatures has not yet been completed. However, water temperatures ranged from 28° to 29°C throughout most of the Lower Keys to 29° to 31°C in the Marquesas Keys westward 20 n mi from Key West (recall that the shallowest water is found there). The aircraft descended to 50-ft radar altitude over the Marquesas Keys and measured a peak-sustained water temperature reading of 33.5°C over a large shallow lagoon in the Marquesas Key. Two waterspouts (one of them large) were observed from the aircraft. In general, the sea-surface temperature pattern from the 1971 RFF PRT-5 radiometer flight compared favorably with those of the 1970 Navy PRT-4A flight. The major difference is that water temperatures everywhere were 2° to 4°C higher in the later flight.

4.5 Synoptic-Scale Contributions

The few studies of environmental settings conducive to waterspout formation have either taken the form of correlating waterspout occurrence with synoptic regimes (Gerrish, 1967) or compositing "mean environmental soundings" from land-based rawinsonde data (Witschi, 1957; Gerrish, 1965; and Garza, 1971). Neither approach has shed much light on the structure of the waterspout environment. However, Gerrish (1967) used surface pressure charts to delineate the synoptic situation over South Florida on active waterspout days. Conventional isobaric charts utilized during fieldwork tended to corroborate Gerrish's 1967 findings that the Florida peninsula is typically influenced by a surface pressure ridge. However, as may be seen from appendix A, for some days during 1969 that were either very productive of waterspouts or of exceptionally large waterspouts, the charts showed the usual Bermuda high-pressure ridge to the north. Moreover, conventional surface and upper air pressure-analyses gave little indication of synoptic-scale perturbations which might account for periodic changes in convective cloudline development.

Wise and Simpson (1971) have described automated analysis techniques primarily concerned with tropical weather disturbances and their growth potential. One of these useful tools is the Tropospheric Layer Mean Chart, which depicts the instantaneous major characteristics of most low-latitude disturbances that can best be identified and tracked using analyses of pressure-weighted layer-mean data for the lower troposphere (1000 to 600 mb) and the upper troposphere (600 to 200 mb).

Thirteen "active waterspout days" were selected from the list in appendix A. A sequence of Lower Tropospheric Mean Charts for each case was subjected to post analysis, utilizing late surface, rawinsonde, and ship data as well as the Applications Technology Satellite (ATS-III) derived winds. Six of these cases were selected on the basis of waterspout observations, aircraft observations, and time-lapse coverage from the ground. Each case also

had a sequence of ATS-III photographs showing cloud system evolution. The two most representative and best documented cases are presented below to show the basic synoptic-scale systems.

4.5.1 June 30, 1969--An Active Waterspout Day With an Easterly Wave Passage

This day is especially interesting and important because of 15 waterspout funnels of which nine were studied by project aircraft during the period from 1621 to 1735 EST (table 3), including three simultaneous waterspouts in different stages of the life cycle.

The sequence of Lower Tropospheric Mean Charts, shown in figures 37a through 37c, gives a typical synoptic-scale flow pattern. A tropical wave south of latitude 33°N, indicated by the dashed line, approached southeast Florida late on June 29 (fig. 37a). It continued moving westward across southern Florida the next morning (fig. 37b) and crossed into the eastern Gulf of Mexico by nightfall (fig. 37c). During this period, the Upper Tropospheric Mean Charts (600 to 200 mb layer, not shown) indicated the development of an upper closed low off the lower Florida east coast. This closed cyclonic circulation is clearly evident near the middle Florida east coast in ATS-III photographs. Interaction between upper and lower tropospheric disturbances is further complicated by the land-sea breeze circulation induced by the Florida peninsula. The strong diurnal control exerted by this mesoscale circulation on cloud disturbances over and near the Florida peninsula was well documented by Golden (1967).

Kinematic results from the hand-analyzed vector wind field for the Lower Tropospheric Mean Chart in figure 37b are shown in figures 38a and 38b. Windspeeds and directions are linearly interpolated from the streamline-isotach analysis to each grid point, with directions read to the nearest 10° and speeds to the nearest knot, down to an arbitrarily specified 5-kt minimum. Figure 38a gives the field of 1000 to 600-mb mean divergence and figure 38b gives the mean relative vorticity. Most of the mean convergence in the 1000- to 600-mb layer lies in an east-west belt across central Florida where maximum values are 10-15 x 10^{-6} s^{-1}. Note that most of the convergence is west of the tropical wave axis shown in figure 37b. This does not fit classical convergence patterns in an easterly wave found by Riehl (1945). However, complicated vertical coupling exists between the lower level wave and an upper cold low. Finally, note that a secondary maximum of layer-mean convergence (5-10 x 10^{-6} s^{-1}) extends in a belt northwestward from Cape Sable and the Lower Keys.

Other investigators of tropical systems have used averaging techniques to obtain fields of surface or layer-mean divergence and relative vorticity (Miller and Keshavamurthy, 1968; Gordon and Taylor, 1970). In this case, agreement between convergence and convective cloudiness is poor, with the exception of a broken convection area extending northward into the Straits of Florida. However, subsequent extensive cumulonimbus convection, noted in ATS-III satellite photographs, fits well with the location of synoptic-scale convergence early in the day. Also, the major waterspout-producing cloudline developed in the region of the secondary convergence maximum.

Figure 37a. Lower Troposphere Mean-Flow Chart (1000- to 600-mb winds) on June 30, 1969, at 0000 GMT.

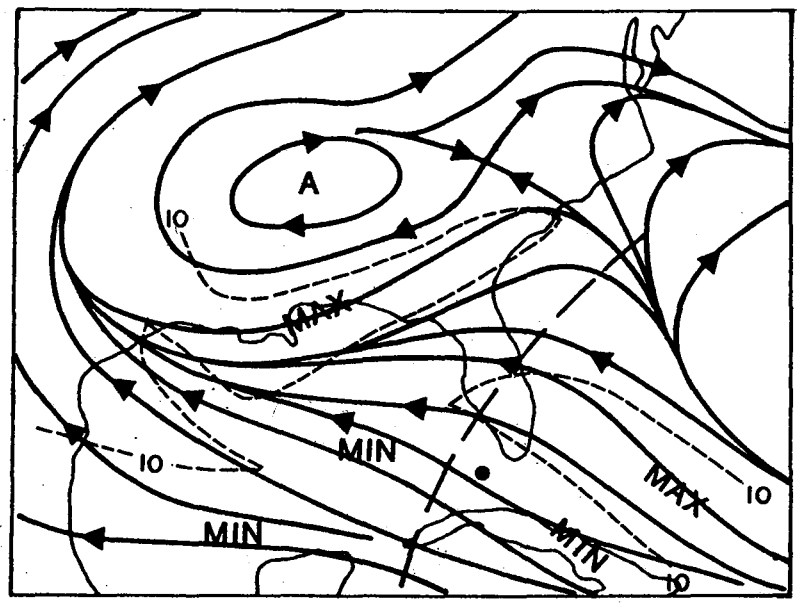

Figure 37b. Lower Troposphere Mean-Flow Chart (1000- to 600-mb winds) on June 30, 1969, at 1200 GMT.

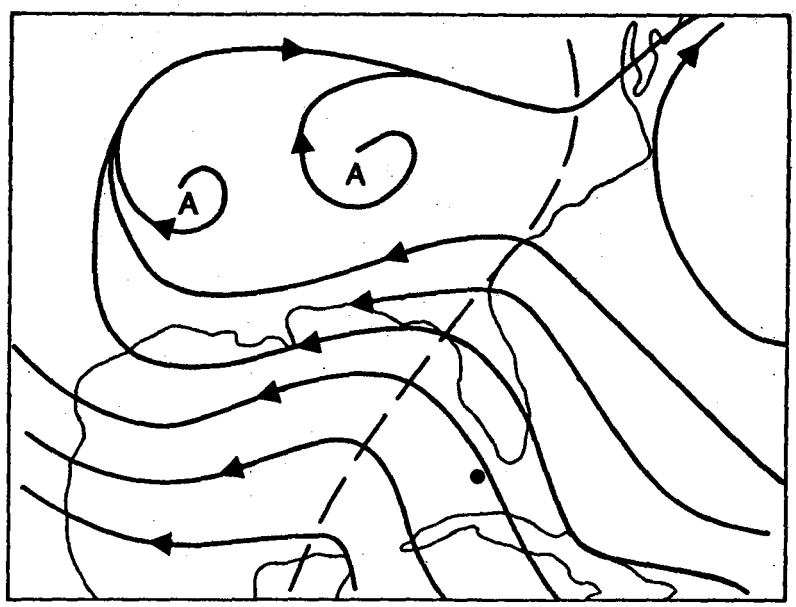

Figure 37c. Lower Troposphere Mean-Flow Chart (1000- to 600-mb winds) on July 1, 1969, at 0000 GMT.

The relative vorticity field (fig. 38b) shows positive values (+10-20 x 10^{-6} s^{-1}) extending across South Florida. Comparing figures 38a and 38b, we find coexistent maxima of convergence and positive relative vorticity $\geq 5 \times 10^{-6}$ s^{-1} just off the southwest Florida coast. The region investigated by aircraft is contained by the envelope of convergence and relative vorticity maxima. Weak lower level mean convergence associated with a synoptic-scale perturbation apparently enhances normal convective development, and the superposition of synoptic-scale positive relative vorticity provides rotation which could be concentrated by cumulus-scale convergence. The convergence in this case is most likely dynamically produced by the disturbance (Riehl, 1954).

4.5.2 September 10, 1969--Large Waterspouts With a Troughline

This day was selected because of the presence of the largest and best documented waterspout of the 1969 program. Lower Tropospheric Mean-Flow Charts are shown in figures 39a through 39c for September 9-10, 1969. Hand-drawn isotach analyses are included for the first two charts (0000 and 1200 GMT, September 10). Two shortwave troughs (bold dashed lines) dropped into the longwave trough position along the east coast. The first shortwave approached Florida from the eastern Gulf of Mexico on the evening of September 9 (fig. 39a), and its southern portion moved slowly across southern Florida during the following day (fig. 39b and 39c). (Note the 55° shift in the layer-mean wind direction at Key West between fig. 39b and 39c.) The low-level structure and position of this shortwave trough and associated frontal wave are shown in figure 40. The second shortwave trough, extending southwestward from a small closed low over Georgia (fig. 39b), was likely associated with the sloping frontal surface across North Central Florida (fig. 40). The first shortwave

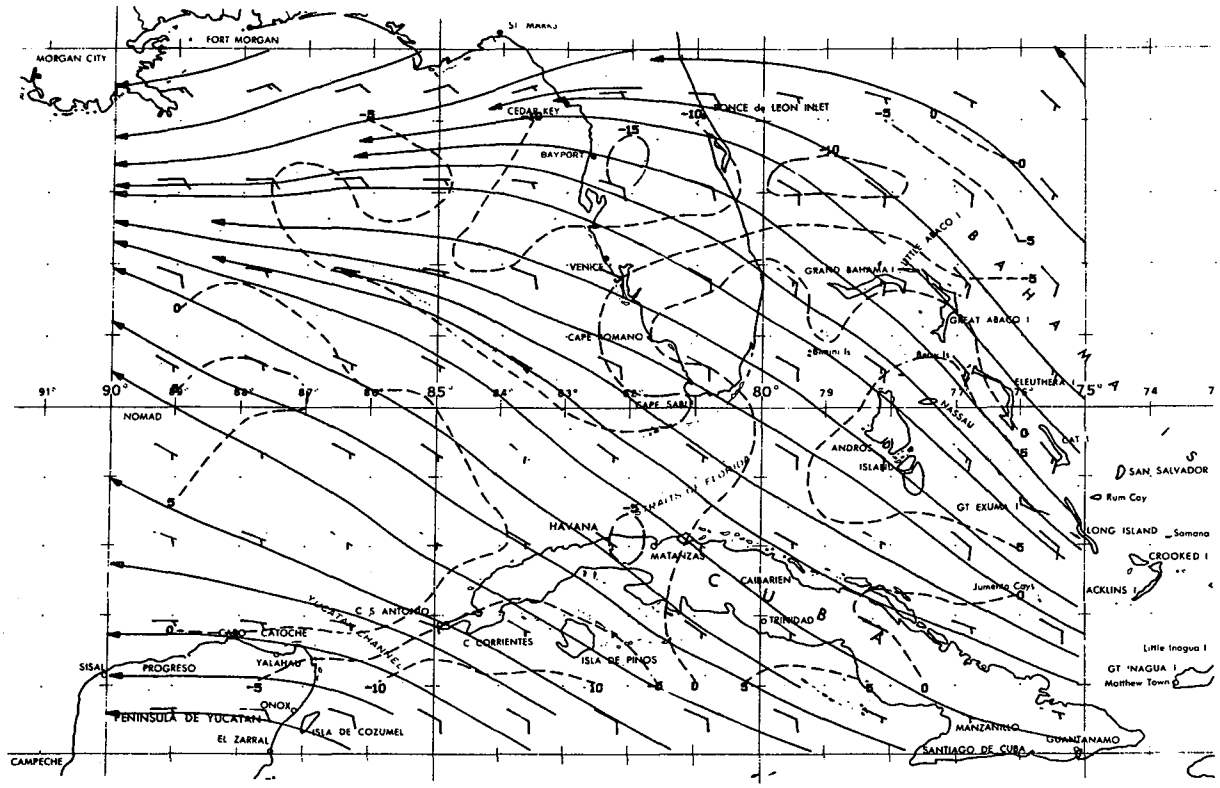

Figure 38a. Layer-mean divergence (times 10^6) with streamlines and wind barbs. Computed from 1,000- to 600-mb mean winds for June 30, 1969, at 1200 GMT. Units are $seconds^{-1}$.

trough across the South Florida coast (fig. 39b) also had some westward slope. The first trough line, just north of Key West at 1200 GMT, was manifested on the Key West and Miami radars by a series of east-northeast to west-southwest echo lines which propagated slowly southeastward. The orientation of these echolines corresponded well to a major confluent asymptote in figure 40. Figure 41 shows isochrones of approximate echo-line positions between 1222 and 1651 GMT traced from the Miami radar film. The three waterspouts extensively studied by the project aircraft occurred between 1520 and 1613 GMT. Note especially the large echo labeled "1626 GMT" in figure 41 and its westward propagation relative to the small cluster of echoes on the 1555 GMT isochrone. This was the only major echo observed on the Key West WSR-57 in the short line of building cumuli which spawned the waterspouts.

The ATS-III satellite provided excellent coverage of the development. A sequence of 10 partial-disc ATS-III photographs is shown in figures 42a through 42f. Note the east-northeast to west-southwest cloudlines across southern Florida in figure 42a and the two echo-line isochrones at 1322 GMT in figure 41. The cloudline which spawned the waterspouts is shown by the ATS-III pictures in figures 42b through 42d. After that time (1647 GMT), new cumulonimbi developed on the north side of the major, decaying cell (fig. 42e and 42f).

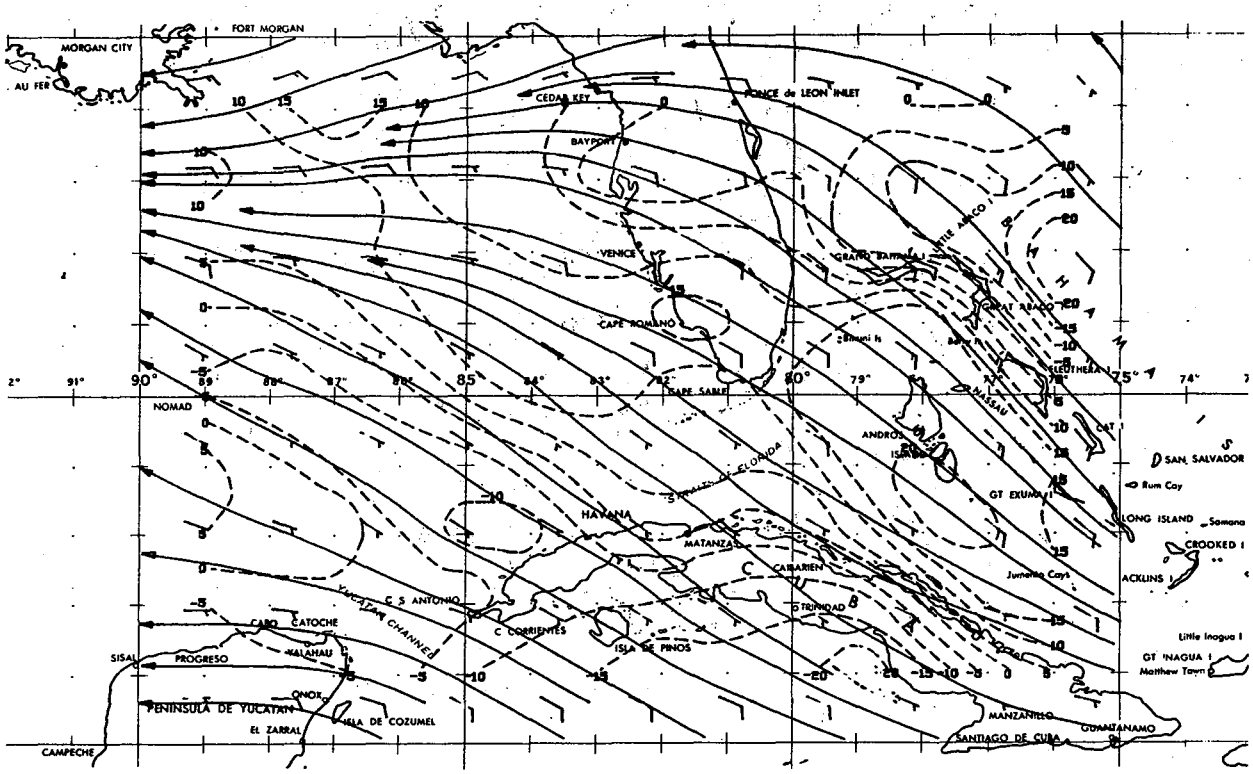

Figure 38b. Layer-mean relative vorticity (times 10^6) with streamlines and wind barbs. Computed from 1,000- to 600-mb mean winds for June 30, 1969, at 1200 GMT. Units are $seconds^{-1}$.

A grid was prepared for digitized ATS-III enlargements of the southwestern Atlantic sector, using visible landmarks and coastlines. The 16-mm movie loop was made to study motion and cloud developments in the major cloudline. Two small cumulonimbi on the northeast end of the main cloudline grew most rapidly (i.e., had the greatest rate of anvil production) after figure 42b. When this sequence was studied in time lapse, the following features were noted: (a) While the line drifted slowly eastward, there was a pronounced cyclonic spiral to the individual cells within the line, especially in the cumulonimbi on the northeast end of the line; (b) after the split in the cloudline, the northeastern end continued to produce active cumulonimbus growth while the southwestern end of the line decayed; and (c) some weak cyclonic spiral circulation in the southwestern end of the line was apparent in the last five or six frames (after 1710 GMT).

Objective analyses (using Eddy's 1967 scheme) of the 1000- to 600-mb mean-layer divergence and relative vorticity are shown in figures 43a and 43b, respectively. Wind direction and windspeed were interpolated at each grid point from hand-analyzed streamlines and isotachs of the Lower Tropospheric Mean-Flow Chart (fig. 39b). The belt of convergence extended eastward through the Straits of Florida, with maximum values between -5 and -15 x 10^{-6} s^{-1}. The southern tip of Florida and most of the Keys were within the convergence

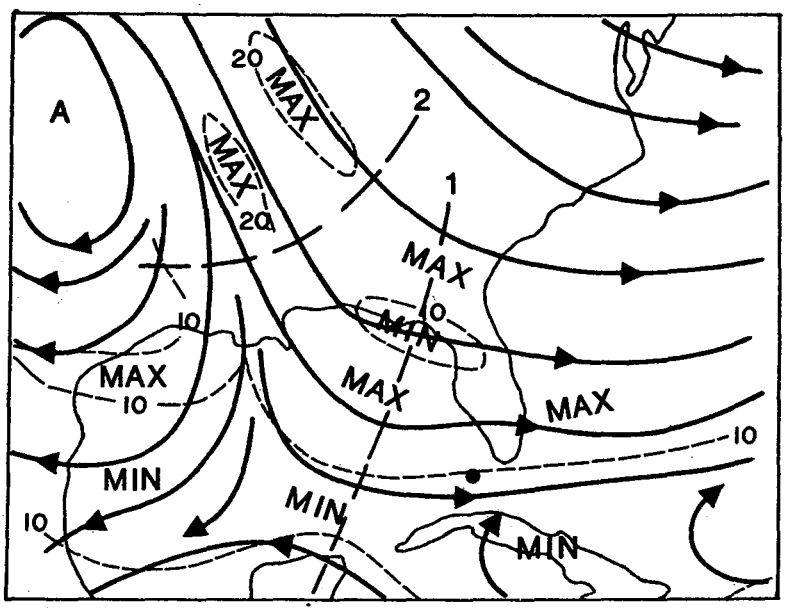

Figure 39a. Lower Troposphere Mean-Flow Chart, 1000 to 600 mb, on September 10, 1969, at 0000 GMT.

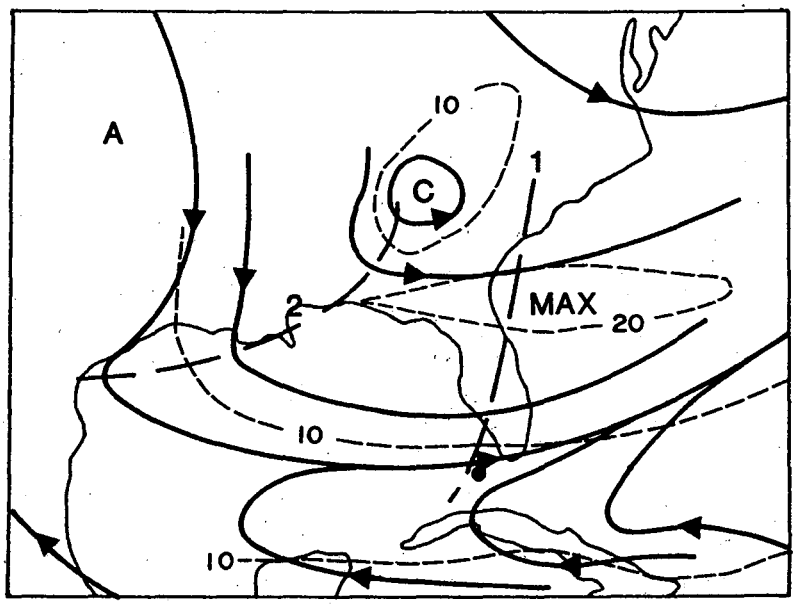

Figure 39b. Lower Troposphere Mean-Flow Chart, 1000 to 600 mb, on September 10, 1969, at 1200 GMT.

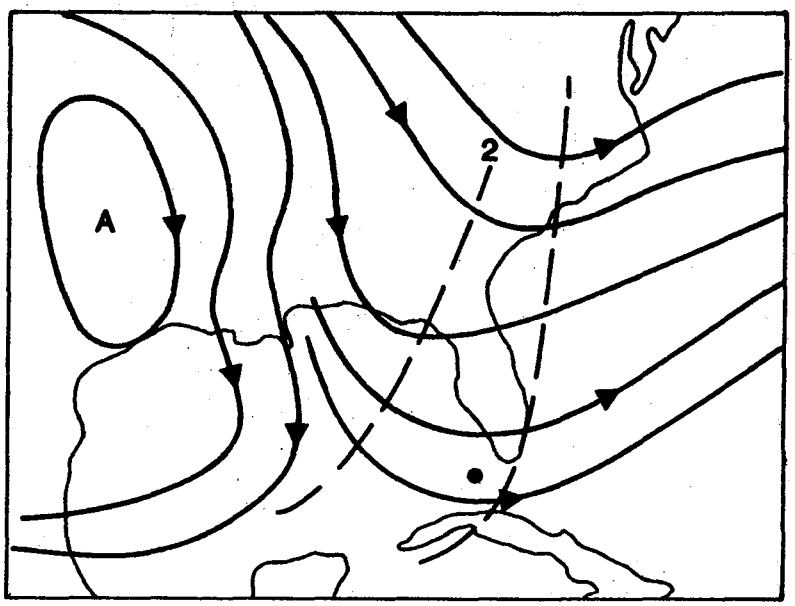

Figure 39c. Lower Troposphere Mean-Flow Chart, 1000 to 600 mb, on September 11, 1969, at 0000 GMT.

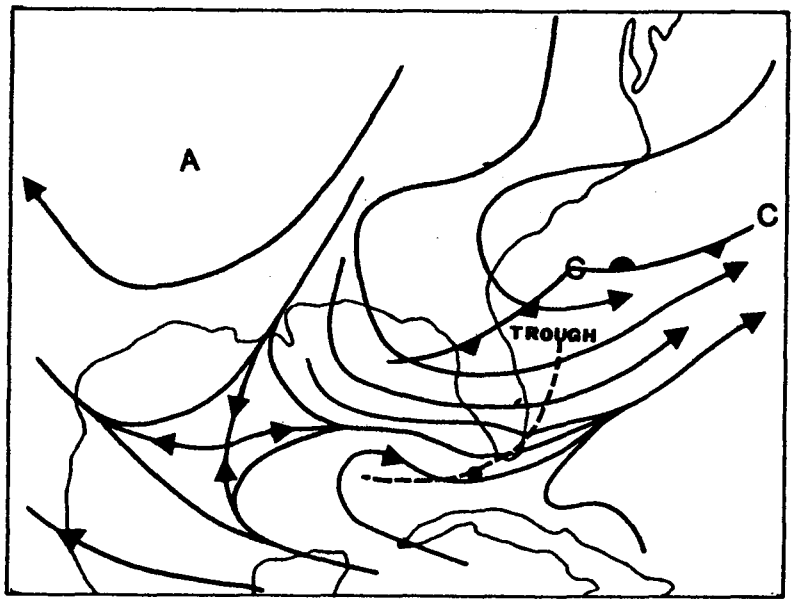

Figure 40. Streamline analysis of the "top of the Ekman layer" (TOE) pibal and ship winds on September 10, 1969, at 1200 GMT. This is the National Hurricane Center TOE ("top of the Ekman layer" refers to 3,000-ft and ship's surface winds). Chart for 1200 GMT, September 10, 1969 (see Wise and Simpson, 1971, for description).

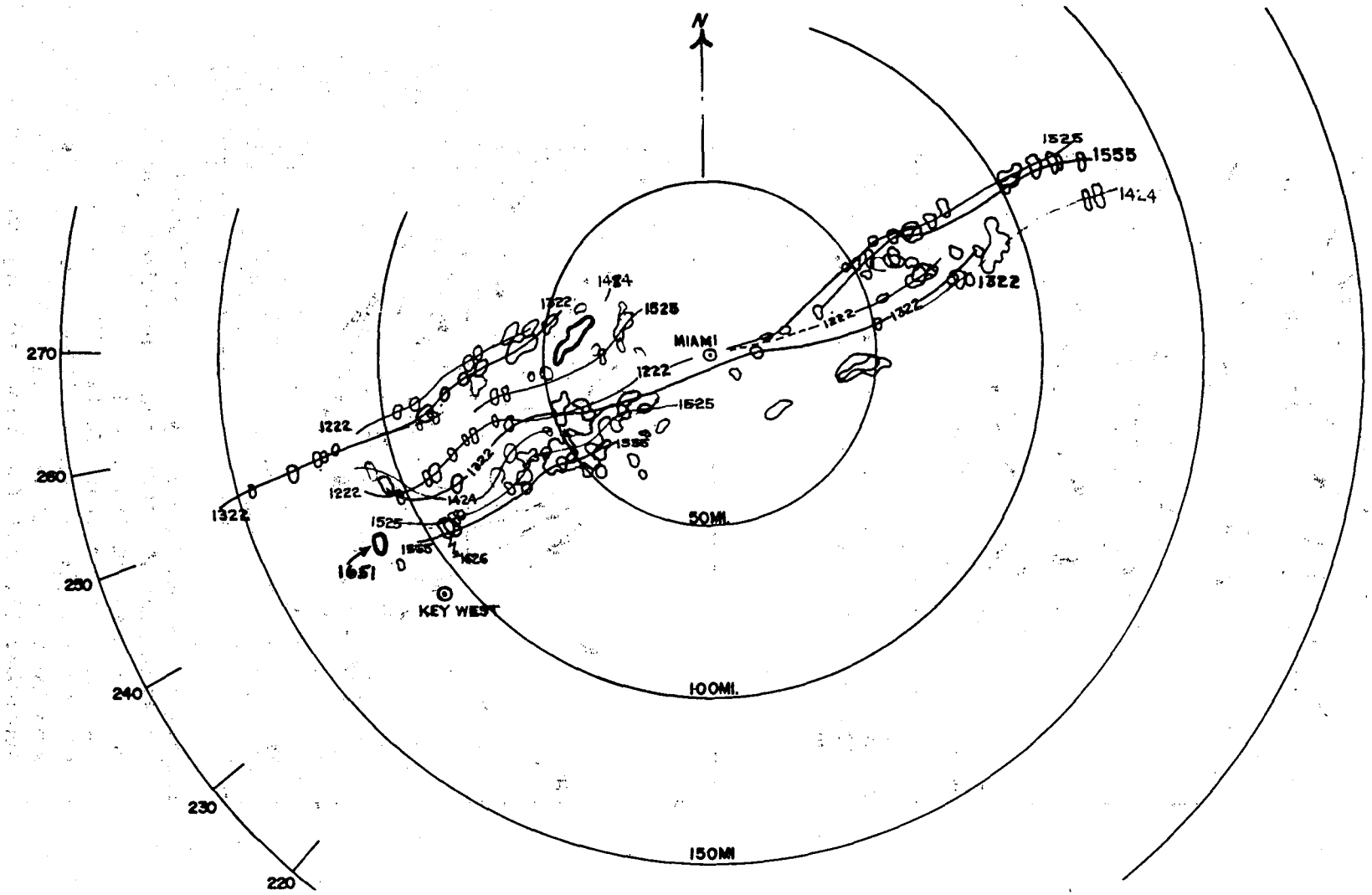

Figure 41. Miami WSR-57 radar coverage of echo troughline on September 10, 1969. Isochrones of approximate echo-line position at given times (GMT).

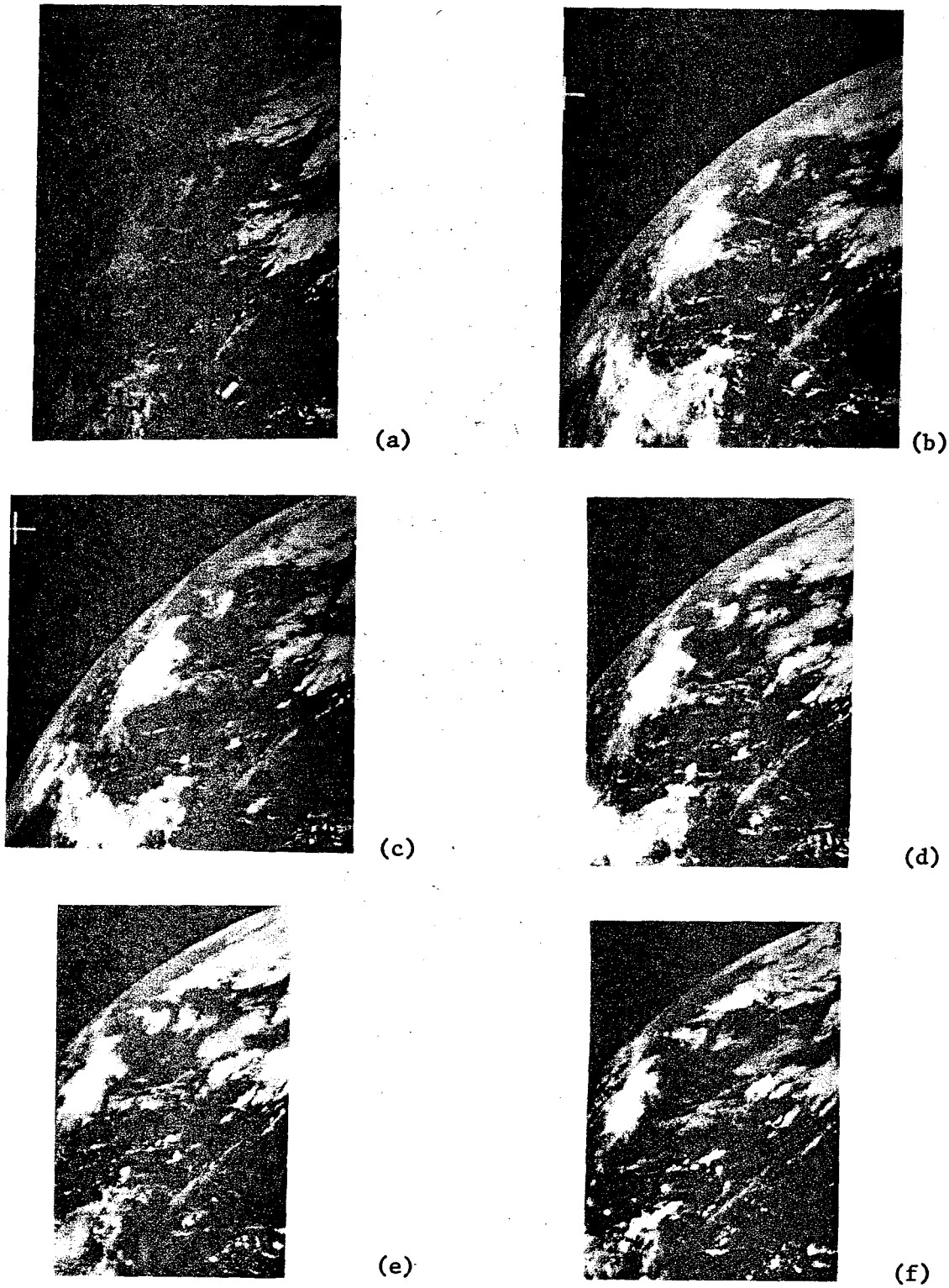

Figure 42. Sequence of ATS-III photographs showing cloudline developments over Florida and the Gulf of Mexico on September 10, 1969. (a) View at 133145 GMT; (b) View at 144751 GMT; (c) View at 154921 GMT; (d) View at 164744 GMT; (e) View at 173425 GMT; and (f) View at 191630 GMT.

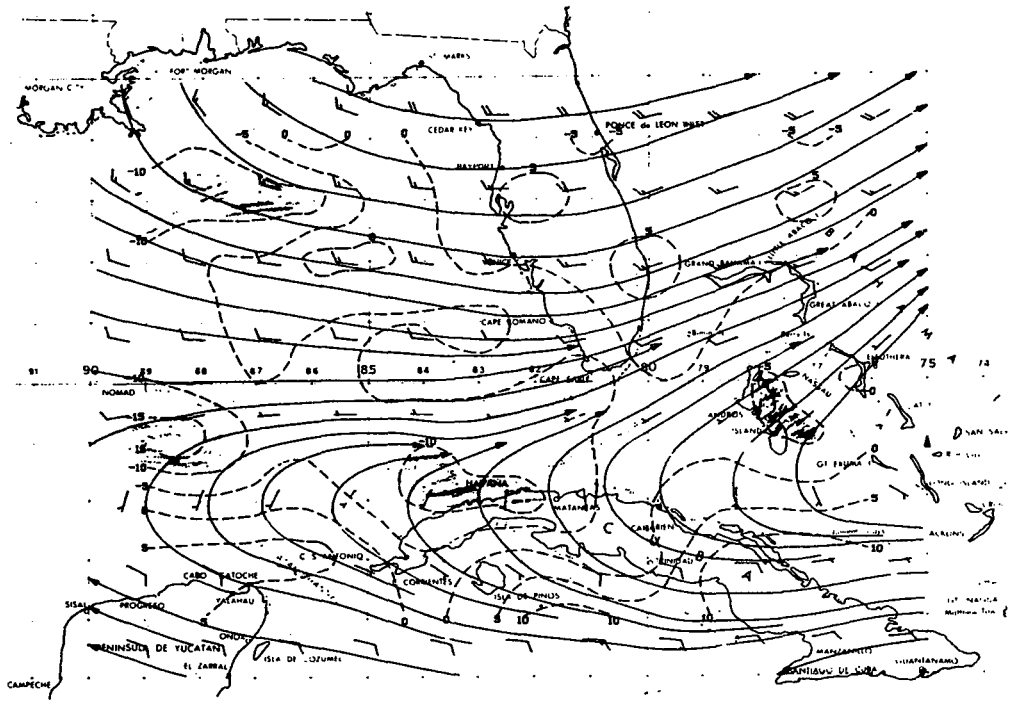

Figure 43a. Horizontal divergence (times 10^6) with streamlines and wind barbs, computed from 1000- to 600-mb mean winds for September 10, 1969, at 1200 GMT.

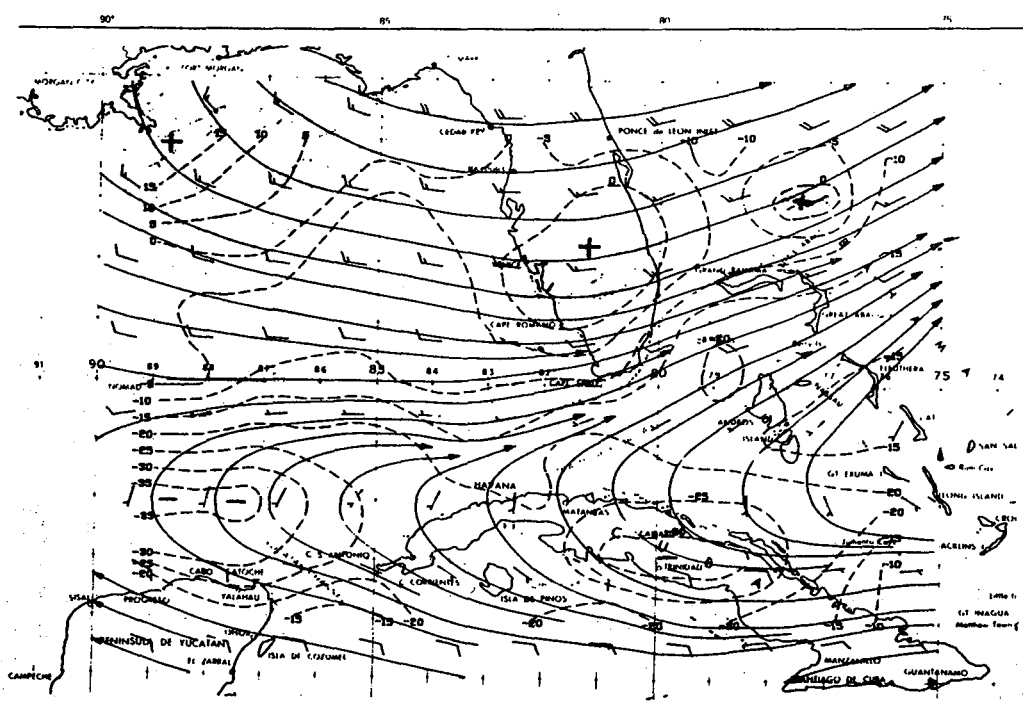

Figure 43b. Relative vorticity (times 10^6), shown as dashed lines, with streamlines and wind barbs, computed from 1000- to 600-mb mean winds for September 10, 1969, at 1200 GMT.

belt which corresponded well to developing east-northeast to west-southwest lines of cumuli on the early ATS-III pictures (fig. 42a and 42b). The only area of significant positive relative vorticity was centered over South Central Florida, with values to 5×10^{-6} s^{-1}. However, the Lower Keys were in a region of weak positive vorticity advection. Comparison of this case with the mean-layer vorticity and divergence analyses for the June 30 case reveals, in both situations, a belt of maximum layer-mean convergence over the Keys.

Both weak convergence and layer-mean positive vorticity advection enhance cloudline developments in the Keys, the former by bringing low-level moisture into a localized area and the latter by providing synoptic-scale rising motions over the same area. Further, it is strongly suggested that once a cumulus cloudline forms over the heated Keys and adjacent warm waters, convergence on the cloudline scale (mainly in the subcloud layer) and on the synoptic scale acts together to concentrate preexisting vorticity.

Empirical criteria developed during field observation and post-analysis reveal that the following synoptic-scale conditions are favorable for waterspout activity in the Lower Keys: (a) an approaching weak synoptic-scale disturbance accompanied by weak convergence and positive absolute vorticity; (b) weak vertical wind shear in the lower troposphere, implying a quasi-barotropic synoptic-scale disturbance in this layer; and (c) a moist, convectively unstable sounding to at least 850 mb and more typically to 700 mb, with substantial dryness above. It is not unusual to see adiabatic or slightly super-adiabatic 50- to 75-mb layers below 500 mb. Such unstable layers are often found in the subcloud layer on especially active waterspout days. Strong synoptic-scale disturbances which periodically affect the Lower Keys through the waterspout season have a pronounced inhibiting effect on waterspout formation there because they are accompanied by moderate-to-strong vertical wind shear and a near-saturated, very deep moist layer. During these conditions, which are considered in more detail in section 6.4, the Key West radar shows large coverage by convective cells. Most echoes are in clusters, and lines, if present, are short-lived because of the pumping nature of the convection.

5. STATISTICAL ASPECTS OF LOWER KEYS' WATERSPOUTS

A more comprehensive treatment of annual frequency, seasonal and diurnal distribution, duration, multiple funnel frequency, and local weather situations for the Keys' area along with other favored occurrence regions may be found in Golden (1973b and 1973c). Selected summaries of the most important statistics follow.

5.1 Spatial and Temporal Distribution

The 95 waterspouts documented by project aircraft during the 1969 season have been plotted in figure 44. Locations have been cross-checked with all data sources and are considered accurate within 1 n mi. The Marquesas Keys appear to be a waterspout "hot spot," especially on days with light and variable winds in the lowest 10,000 ft. Recall that at low tide the water depths in this area are only 1 to 3 ft.

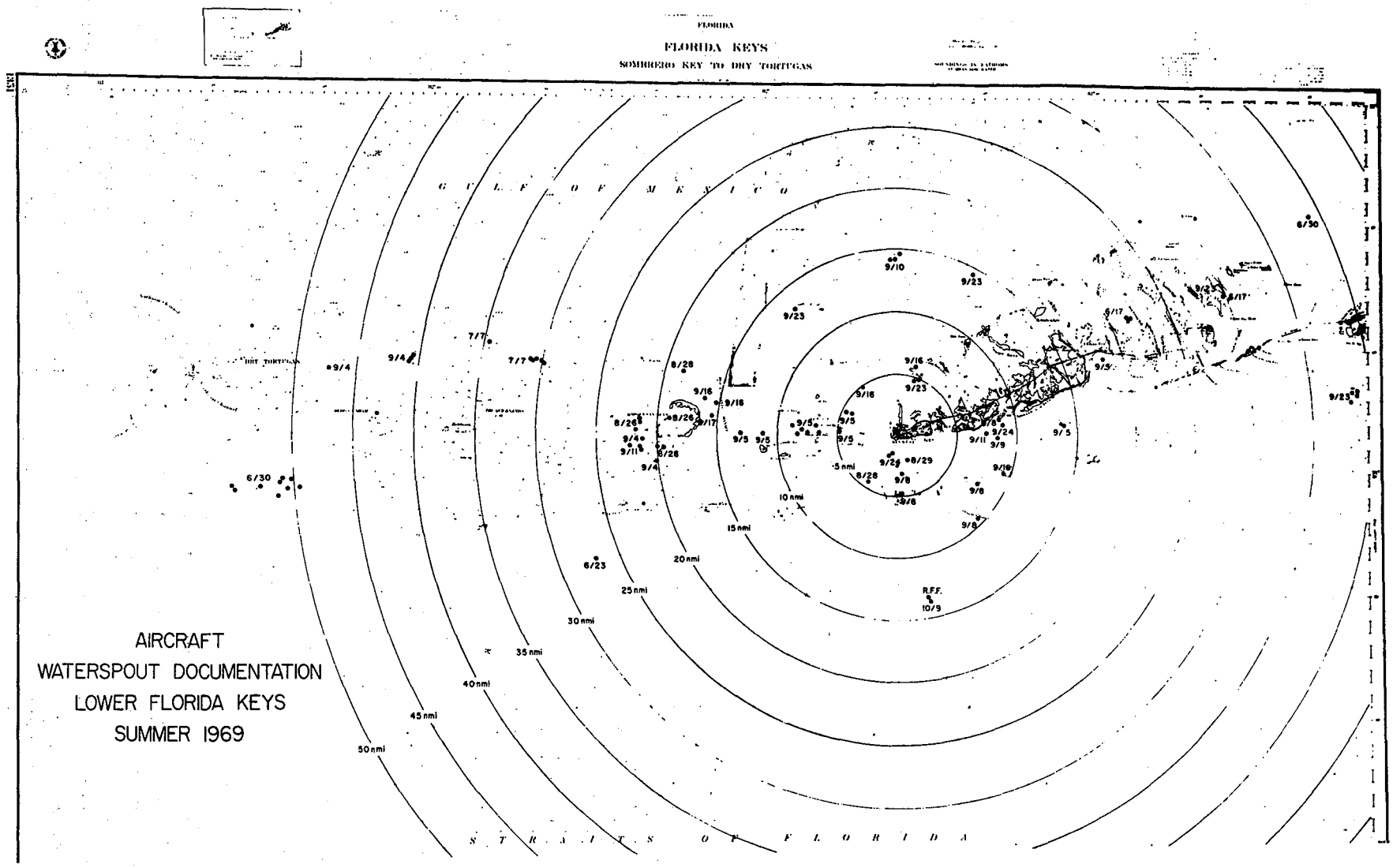

Figure 44. Waterspouts documented only by project aircraft during the 1969 Lower Keys Waterspout Project. Note that 5-n mi range circles are centered on downtown Key West.

The waterspout population (396) derived from all data sources during the 1969 program has been plotted in figure 45. With certain recognized limitations, the aircraft waterspout documentation and total waterspout population clearly indicate a zonal distribution and tendency toward clustering in the shallow waters. The concept is strengthened by figure 46 which shows the number of 1969 funnels for each of 16 compass points from Key West. Most waterspouts, in order of decreasing frequency, occurred east, northeast, and west of Key West. The double belt of waterspout maxima just north and south of Key West in the shallow water (fig. 45) results from the low-level mean flow that is light from the southeast in early summer; therefore, cloudlines drift downwind from the Big Pine Key genesis area to a position north of Key West. Later in the summer, the low-level mean winds gradually back to the east-northeast, and waterspout-active cumulus cloudlines then tend to drift off the south shore of Key West. Table 5 summarizes 1969 waterspout frequency in 5-n mi rings centered on the Key West Airport. The largest number of funnels were observed between 5 and 10 n mi from Key West Airport; nearly one-half of the total 1969 funnel population was documented within a 10-n mi radius.

After a reexamination of Gordon's (1951) global waterspout frequency map, Garza's (1971) funnel cloud census for the upper Texas gulf coast and the waterspout climatology for the Lower Florida Keys, the author concludes that the Florida Keys region probably has an exceptionally high waterspout frequency. Less frequent waterspouts, some of which move ashore with tornadic intensity and damage, have been reported in Japan (Fujita et al., 1972), Hawaii, the Philippines, Trinidad (Nancoo, 1959), Puerto Rico, and the Bahamas. Garza's data indicate that for the past 15 years, the yearly waterspout frequency along the upper Texas coast averages only 50 to 60 percent of the average annual frequency in the Lower Florida Keys. From 1969 to the present, the difference is much larger (close to an order of magnitude).

Table 6 gives the total funnels per month for 1969 and figure 47 the monthly totals for 1958-68 and 1969 (Golden, 1973c). The 1969 waterspout activity sharply increased from late April to mid-May, reached a relative maximum in late May and June, fell significantly in July, and reached its primary peak in August. The 1969 season started earlier and lasted longer than the previous 11. The waterspout season generally begins rather abruptly between April 25 and May 15. Data for the individual years 1958-67 showed that the months of May, September, and October have the greatest standard deviation in frequency. In addition to the aperiodic influence of tropical disturbances, the effect of decreased outdoors activities for residents of and tourists to the Keys must be recognized. Figure 48 and table 6 show that the number of funnel days per month (a funnel day is one in which one or more funnels are reported) was about the same during June, August, and September 1969. This compared favorably with the trend for cumulative funnel days per month for 1958-68, with the major exception of September.

The diurnal distribution of all 1969 waterspouts is given in figure 49, with curves for the period 1958-68 and for the 1969 aircraft data alone. In contrast to the results from the waterspout climatology before the 1969 program, the 1969 waterspout maximum extended from 1530 to 1830 EST. A secondary maximum occurred around 1100 EST, with smaller 1969 peaks evident at 1500 and 0800 EST. The major difference between the 1969 results and the

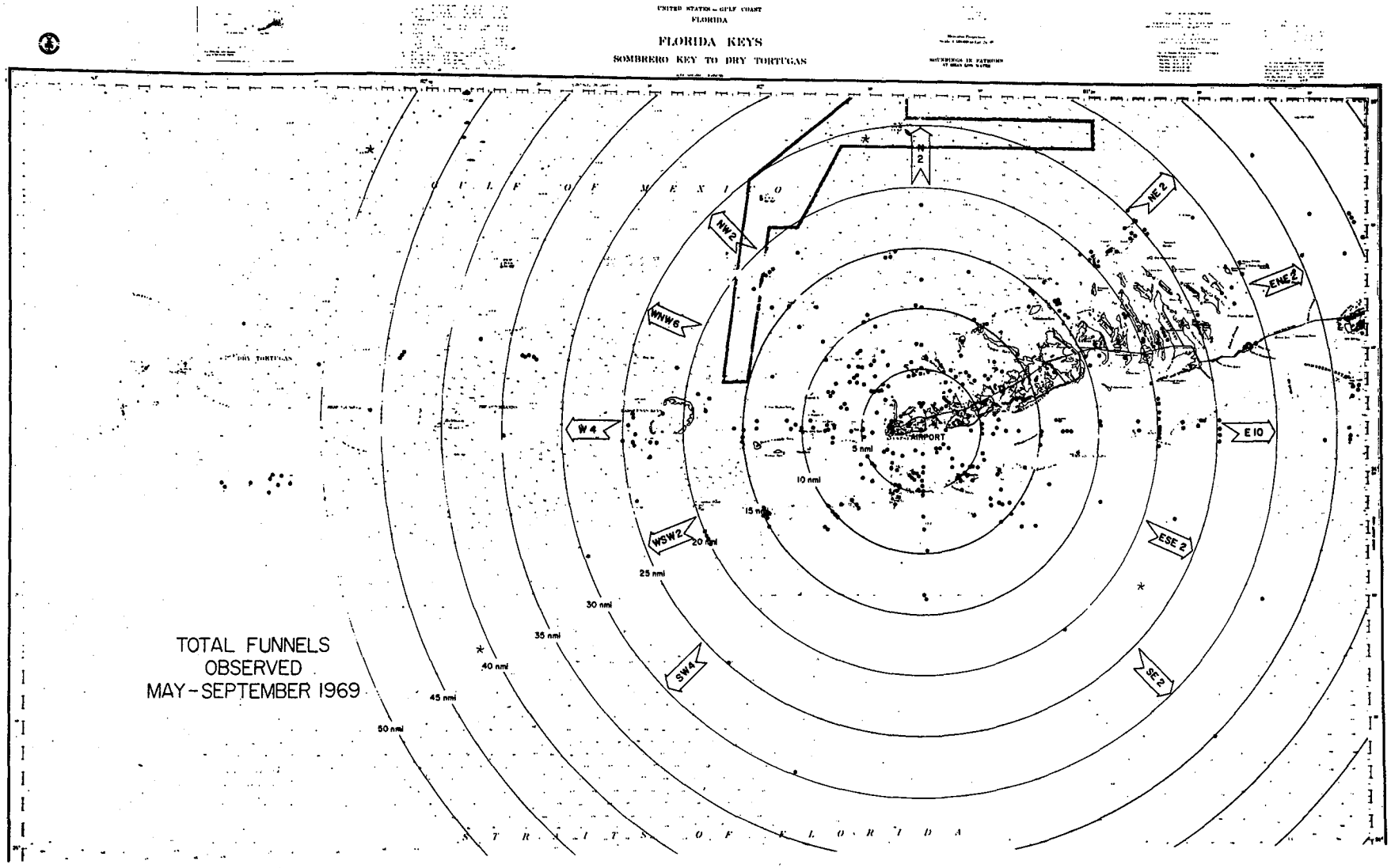

Figure 45. Waterspout funnel population in Lower Florida Keys during the 1969 field season, using data from all sources (cross-checked to avoid duplication). Range circles are centered on the airport at Key West. Numbers in open directional arrows are 1969 waterspouts of known azimuth but of unknown range.

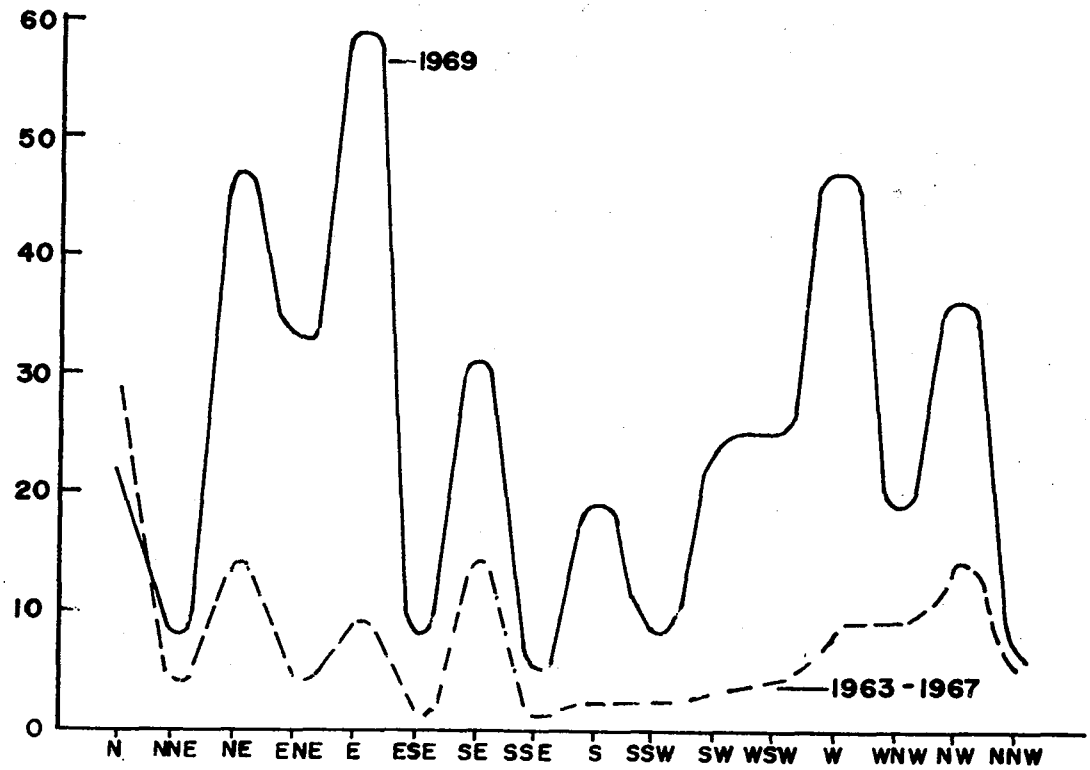

Figure 46. Number frequency distribution of waterspouts by azimuth (16 compass points) from Key West Weather Service Office.

Table 5. Number of Funnel Observations Contained in 5-n mi Rings*

Distance interval from Key West	Number of observations	Percentage of total
0- 5	72	20
5-10	104	29
10-15	48	13
15-20	40	11
20-25	40	11
25-30	17	5
30-35	10	3
35-40	12	3
40-45	7	2
45-50	0	0
50-55	10	3
Total	360	100

* Funnels touching a range circle were included in the next lower annular-ring category.

Table 6. Waterspouts and Funnel Clouds, 1969

FUNNEL DAYS/MONTH 1969

APR.	MAY	JUNE	JULY	AUG.	SEPT.	OCT.
1	14	19	13	17	17	1

TOTAL 82

TOTAL FUNNELS/MONTH 1969

APR.	MAY	JUNE	JULY	AUG	SEPT	OCT
2	87	85	33	90	91	5

TOTAL 390

TOTAL FUNNELS OCCURRENCE BY HOUR†/QUAD.

	01	02	03	04	05	06	07	08	09	10	11	12	13	14	15	16	17	18	19	20	TOTALS
NW						1	1			3	6		4	3		7	1	4	6		36
NNW										2		1	2					1			6
N						2				1	3	1	6	1	2	2		2	2		22*
NNE									1	1			1	1		1		3			8
NE						1		3		7	3	2	5	5		2	9	8	2		47*
ENE	1						1	2		4	1		2	1	4	5	8	3	1		33
E							4	1		3	9	7	1	5	3	10	7	4	5		59
ESE						1		2			1				2			1	1		8
SE						1	2	1	2		4	2	1	10	2		1	3	2		31*
SSE						1			1						1		1	1			5*
S						1			1		2	2	3	2	2	1		4	1		19
SSW										1			1		3			3			8
SW							2	4			3	1	2		3	3	4	1	1		24
WSW													4	4	5	2	7	1	2		25*
W						1			1	1	7	7	3	2	3	14		4	2	2	47*
WNW						1					2	1		2		1	5		3	4	19*
TOTALS	1	0	0	0	0	10	10	13	6	23	41	24	35	36	30	48	43	43	28	6	397*

† An hour is from one-half hour to one-half hour; Ex. 06 hours is 5:31 to 6:30.

* Seven funnels spanned 2 different hours.

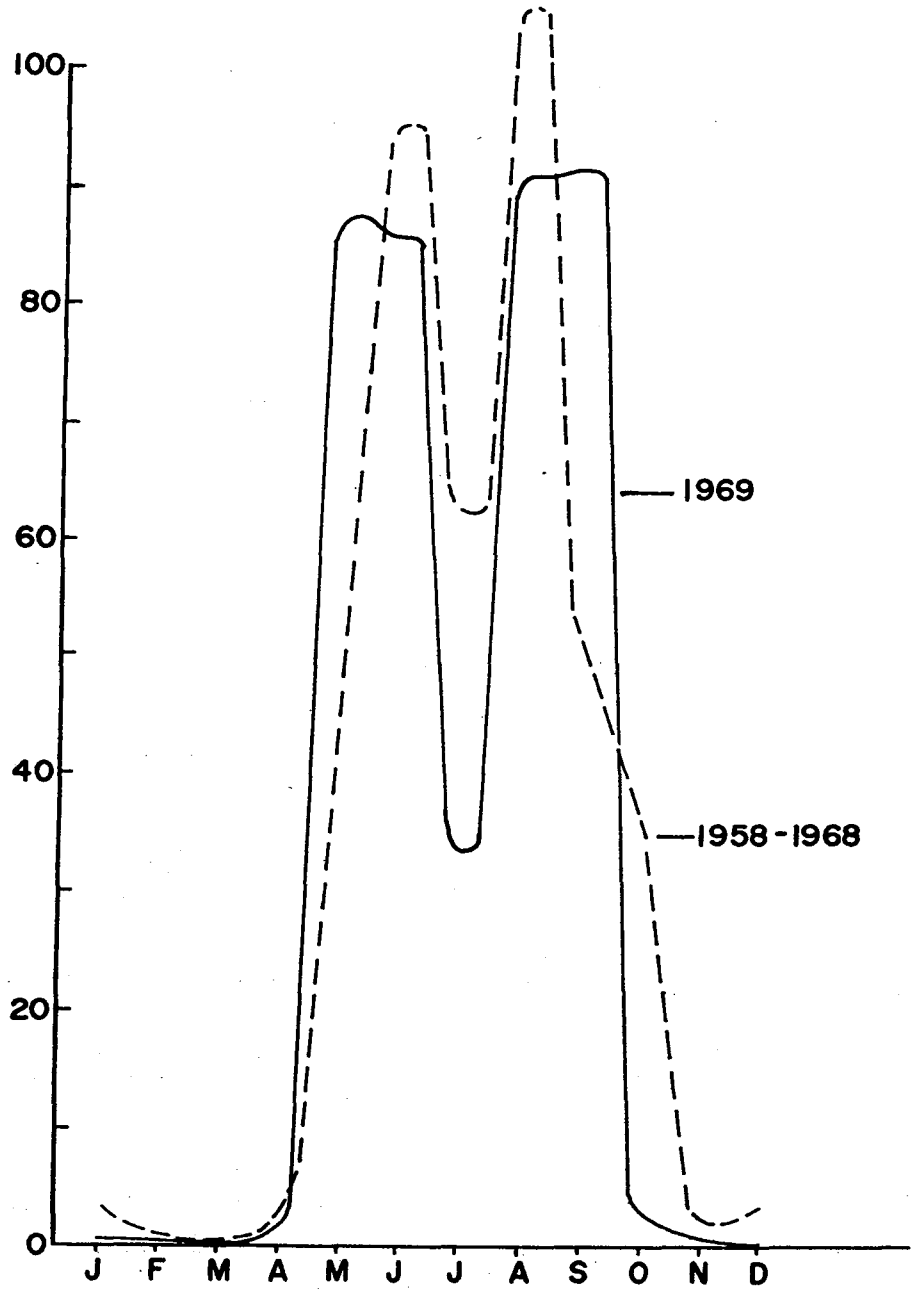

Figure 47. The number of funnel clouds per month for period 1958-68 (dashed) and for 1969 (solid) from Key West data. Note double-peak in each curve and distinct minimum in July.

cumulative 11-year curve was the more pronounced double peak in the 1969 diurnal plot. The diurnal trends in the 1969 aircraft data (dotted curve, bottom of fig. 49) closely followed those in the 11-year curve.

Table 6 indicates that most of the 1969 waterspouts in the early morning hours occurred in a semicircle ranging from northeast to southwest through the southeast from Key West, with a majority in the Straits of Florida (also pointed out by Clemons, personal communication, 1968). Clemons' study and the table both show that afternoon waterspouts form primarily over the shallow waters of Florida Bay and along the Keys (i.e., northwest and northeast from Key West).

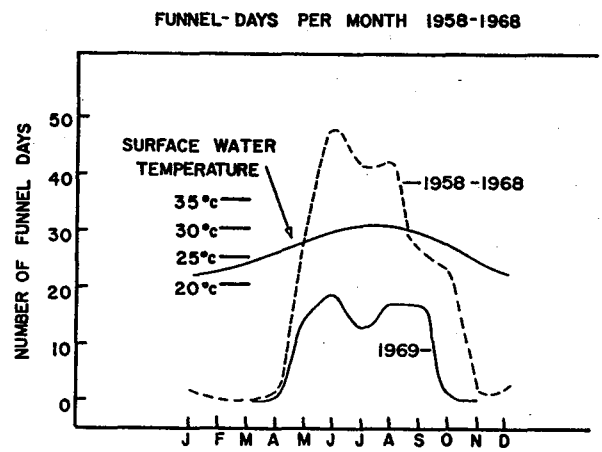

Figure 48. Funnel days per month for the period 1958-68 (dashed) and for 1969 (bottom solid) from Key West data. Top solid line is the mean monthly sea-surface temperatures at Key West pier during 1958-68.

5.2 Seasonal and Diurnal Variations of Sea-Surface Temperature

Waterspouts tend to form over shallow waters, as illustrated in figure 45. The relation between monthly mean temperature of such waters and funnel days per month (1958-69) is shown in figure 48. Daily surface-water temperature curves at Key West for 1969 and 1970 are shown in figures 50a and 50b. Note that the waterspout season in each year coincides well with water temperatures above 82°F. During the annual cycle, several intermittent drops of 2° to 3°F occur. Some decreases are associated with tropical disturbances, but many are not. Surface evaporation, surface cooling by extensive shower activity, and forced vertical mixing extending below the thermocline also contribute to short-term surface-water temperature drops. Of course, tropical cyclones have the greatest effect on surface water temperatures.

Table 7 reveals that the most active waterspout year (1969) has a higher water temperature for May, June, and July than the corresponding means for 1968 and 1970 (1969 had three times as many observed waterspouts as 1968 and 10 times as many as 1970). The onset of the waterspout "season" in any given year depends upon the continuing rise in sea and air temperatures countered by the southward penetration of middle-latitude frontal systems or the influence of early-season tropical disturbances. The end of the season depends primarily upon tropical disturbances (widespread convective echoes and strong low-level winds and vertical wind shear).

The diurnal range of sea-surface temperatures over the open ocean is generally about 1°. However, in the partially enclosed Florida Bay and in shallow water areas along the Keys, the diurnal fluctuation may be appreciably higher. Goodell and Gorsline (1961) found that the intradiurnal range in July near the tidal channels was as much as 3.4°C, while in northern Florida Bay, the maximum range was 3.1°C. The diurnal variation in sea-surface temperature partly accounts for the afternoon waterspout maximum.

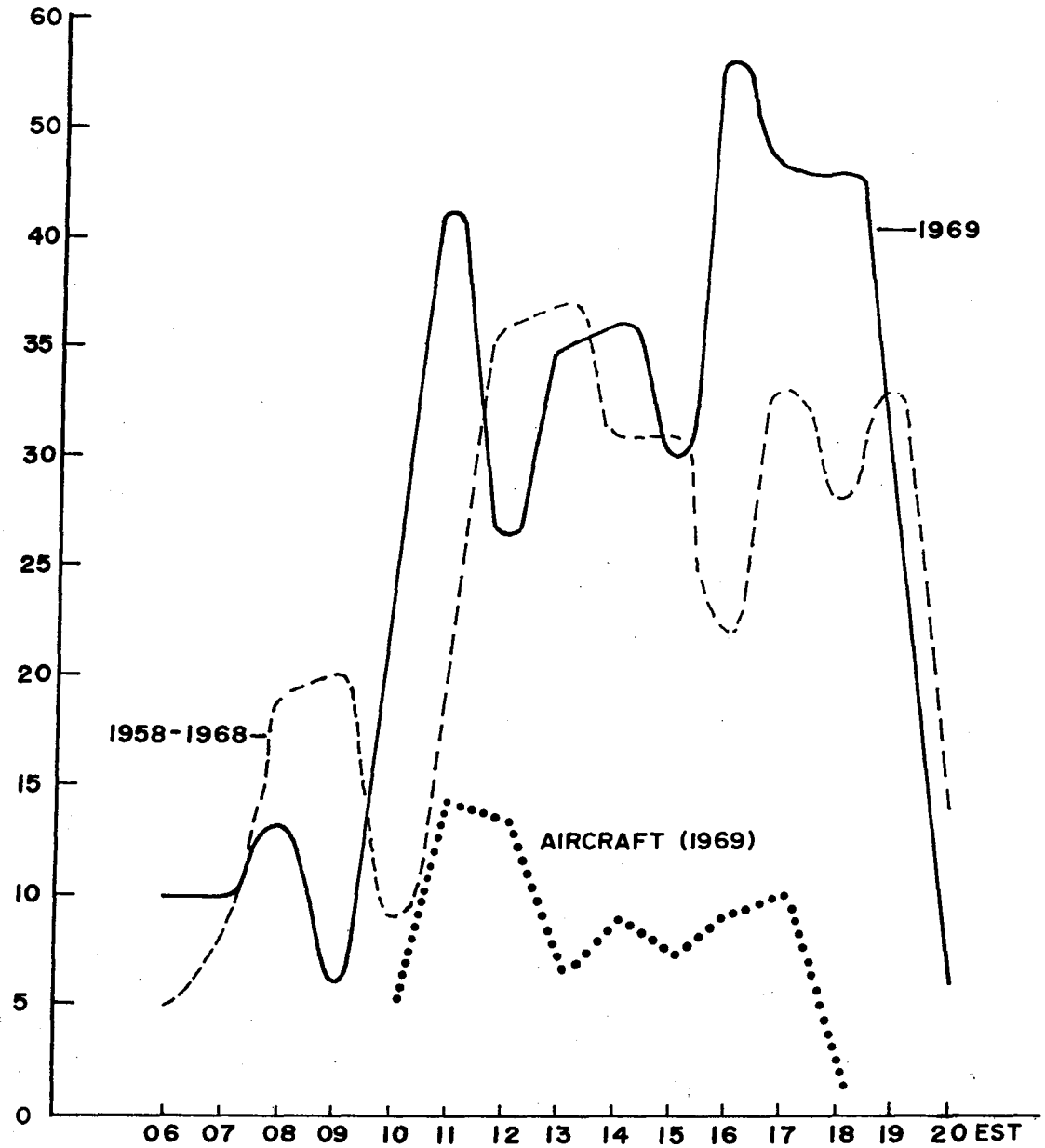

Figure 49. Diurnal trends in total number of funnels observed each hour (EST) during 1969 (solid) and 1958-68 (dashed); funnel observations from aircraft are for 1969 (dotted).

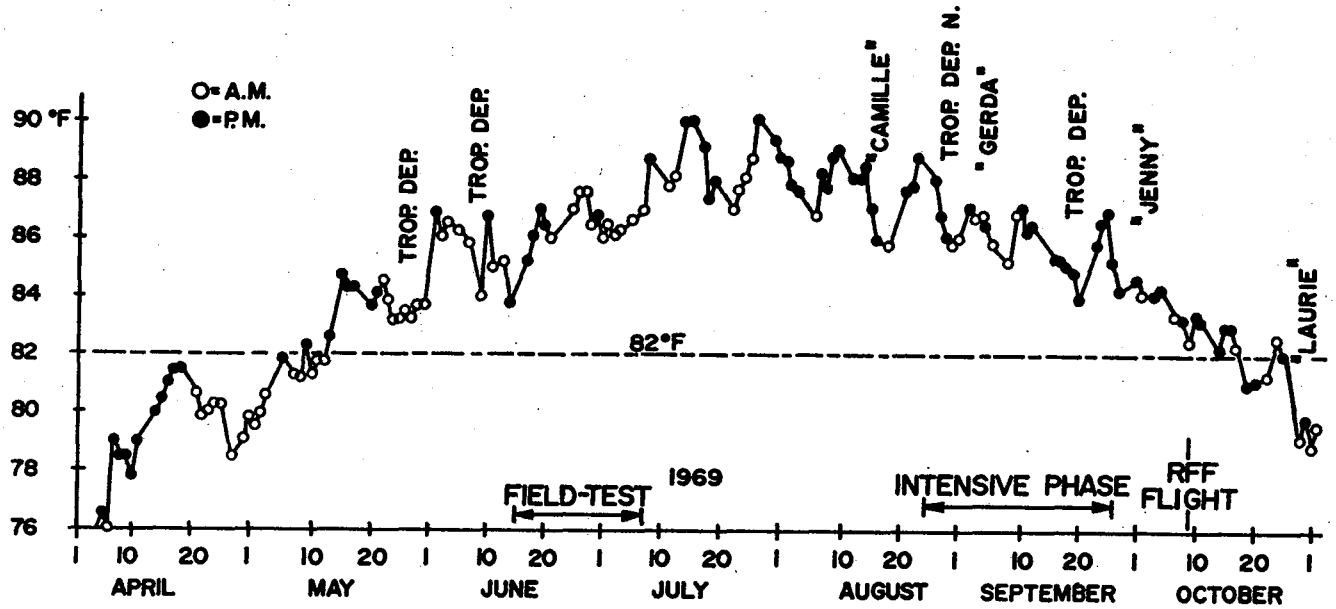

Figure 50a. Daily surface-water temperatures from pier on west end of Key West during 1969. Water depth, 20 ft. Tropical disturbances affecting Keys area are noted.

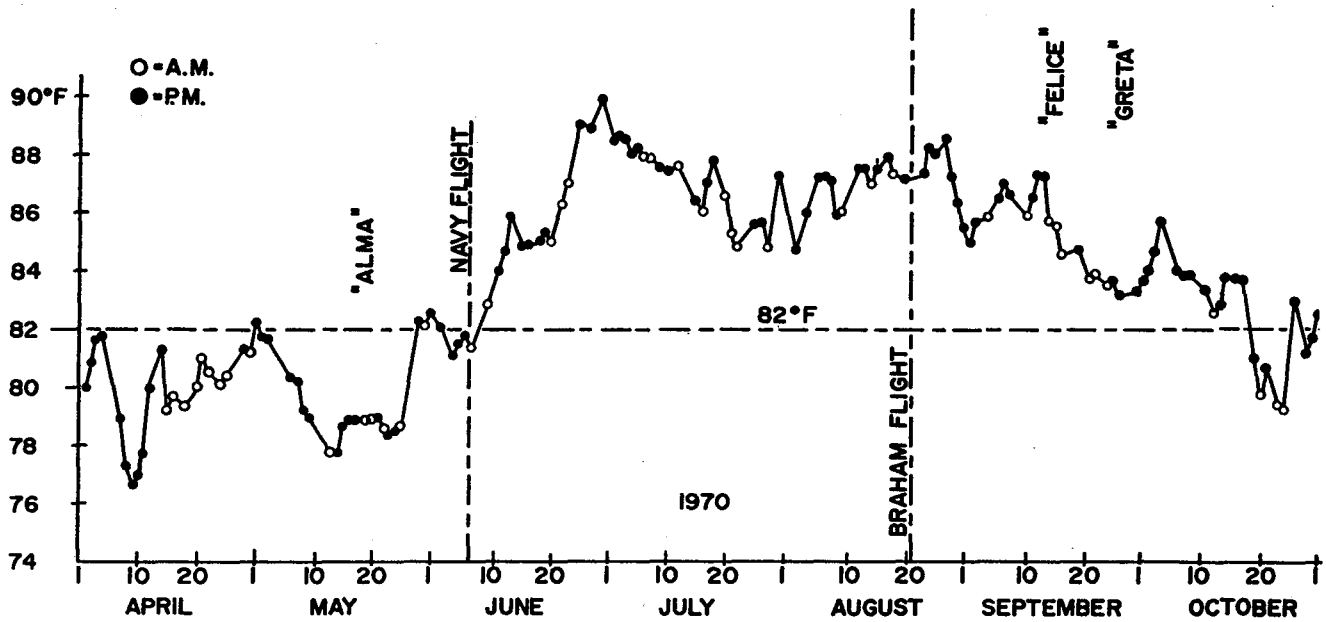

Figure 50b. Daily surface-water temperatures from pier on west end of Key West during 1970. Water depth, 20 ft. Tropical disturbances affecting Keys area are noted.

Table 7. Comparison of Monthly and Seasonal Mean Water Temperatures at Sub Pier, Key West

	1968 (°F)	1969 (°F)	1970 (°F)
May	82.6	82.9	79.6
June	85.1	86.1	84.7
July	86.4	88.1	87.0
August	87.5	87.4	86.9
September	86.5	85.8	85.2
Season average	85.6	86.1	84.6

To assess the importance of light surface winds for waterspout formation and to show the inhibiting effects of strong winds, a histogram of waterspout frequency imposed on a line graph of daily mean windspeeds at the Key West Airport was plotted (fig. 51). Note the correlation (from fig. 50a and 51) between water temperature drops, minimum number of funnels, and periodic mean-windspeed maxima. Virtually all waterspouts occurred with winds below 11 mph. Exceptions occurred on May 23, July 7, and September 17 (with two, eleven, and one waterspouts, respectively). Moreover, all but one of the multiple waterspout days (with five or more) had mean windspeeds between 7 and 11 mph. The main quiescent funnel periods corresponded well with recurrent mean windspeeds above 10 mph (May 1-18, July 15-20, August 7-9, August 13-19, August 29-September 3, and September 17-22).

5.3 Duration, Rotation, and Size

Two different approaches to the study of 1969 waterspout duration were attempted. The first included all documented waterspouts which had an average lifetime of 9.5 min. The second included the 80 aircraft-documented waterspouts from the 1969 program.

The number frequency of waterspout duration from the 1969 aircraft data is shown in figure 52. Note that although most of the waterspouts lasted 10 min or less, a few persisted about 30 min. Both aircraft and surface records indicate a strong positive correlation between waterspout size (maximum funnel diameter and length) and duration.

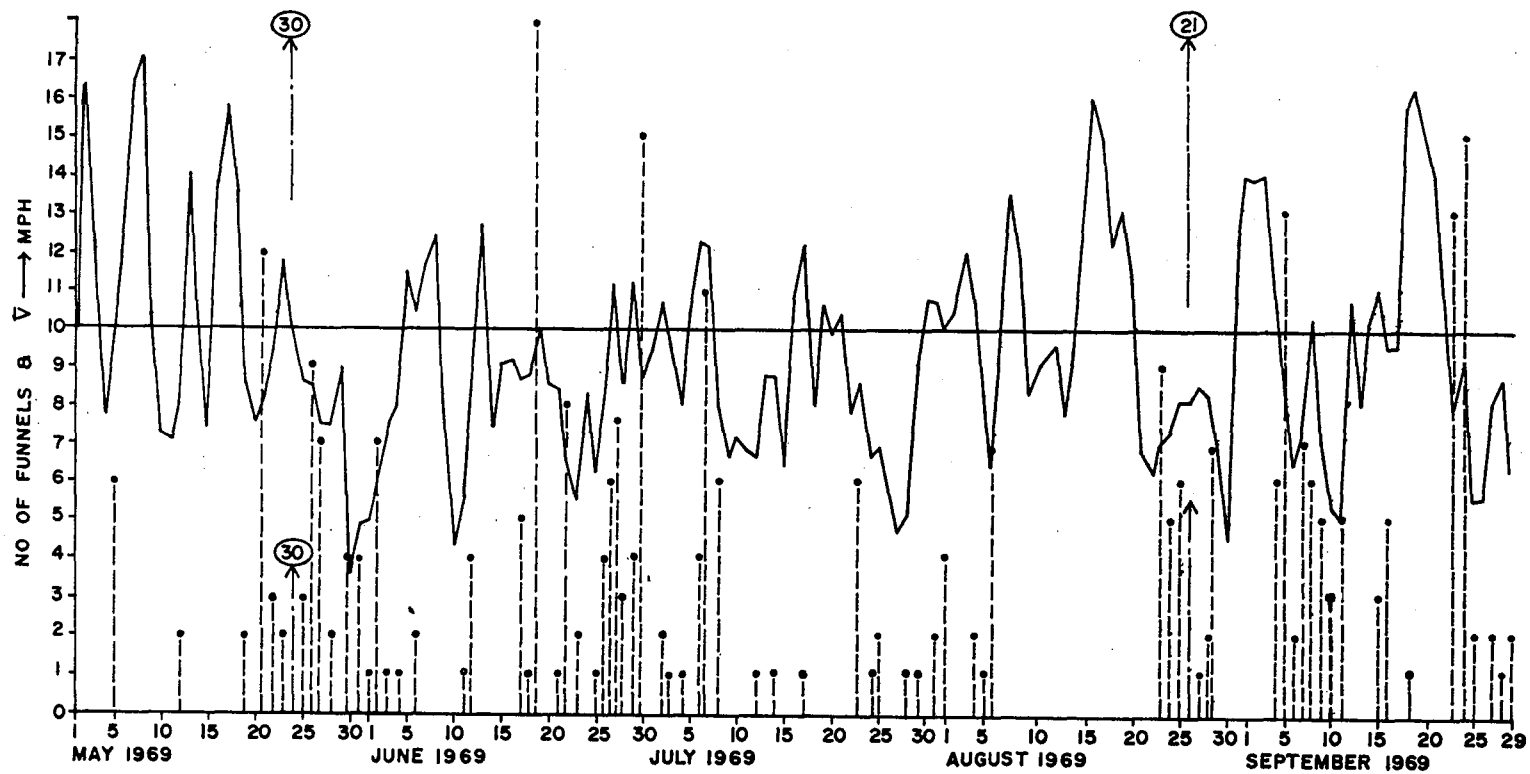

Figure 51. Daily mean 24-hr surface windspeed at Key West as related to total funnel clouds observed each day (all data sources) during 1969. The ordinate refers both to the number of funnels observed each day and to the mean 24-hr surface windspeed for that day.

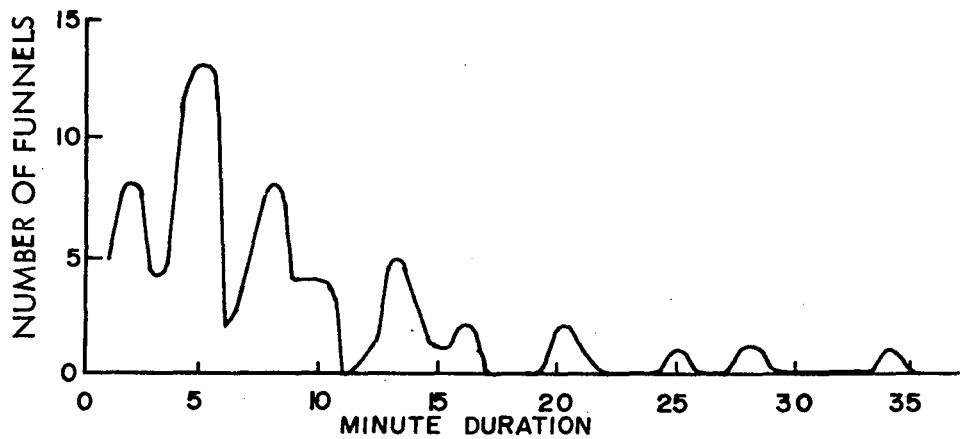

Figure 52. Number frequency of waterspout durations (in minutes) as observed by aircraft in 1969 during entire life cycle.

Of the 95 aircraft-documented waterspouts, rotation was discernible in 54, including a few of the "dark spot eddies" over extremely shallow water. Anticyclonic rotation was documented in six cases and cyclonic rotation in the remaining 48. Two of the anticyclonic waterspouts approached tornadic intensity (estimated maximum rotational windspeeds in excess of 150 kt). Each anticyclonic waterspout occurred as one in a family of two to five, with no more than one other member of the family in progress simultaneously.

Waterspouts varied widely in size and shape, but most of the 95 waterspouts had ropelike funnels that intermittently extended downward from cloud base only 600 to 800 ft. Nearly all of these funnels had some tilt which tended to increase during the lifetime. A few waterspouts had nearly horizontal funnels (yet produced dark spots); and very rarely, short funnels shaped like corkscrews were observed. Two-thirds of the 1969 aircraft-observed waterspouts had a maximum funnel diameter of 80 ft or less; the remaining one-third had maximum diameters of 100 ft or more sometime during their life cycles.

6. THEORETICAL CONSIDERATIONS

6.1 Applicable Theoretical Studies

Formulators of current theoretical descriptions of tornado and waterspout vortices (e.g., Gutman, 1957) agree that formation is related to the concentration of preexisting vorticity by convective processes. Lilly (1965) pointed out that, at the present time, no theoretical treatment of these convective vortexes is adequate. Early solutions were the "one-celled" Burgers (1948) type or the "two-celled" Sullivan vortex (1959), the latter yielding flows with downflow along the axis. Both Burgers (1948) and Rott (1958) produced an exact solution of the incompressible steady-state Navier-Stokes equations for the case of uniform horizontal convergence and vertical

divergence. (The vertical motion profiles across a funnel, section 3.5.3, suggest that the vertical divergence is highly nonuniform.) These solutions become more realistic when thermal effects are considered. The Gutman (1957) and Kuo (1966) numerical models contained buoyancy terms, but still do not include frictional drag at the lower boundary. Kuo's two-celled solution only superficially resembled the flow structure of the Dallas tornado as derived by Hoecker (1960) and has a potentially cold downdraft in the center. Lilly (1969) pointed out that, in a conditionally unstable atmosphere, there is no way to produce a cold downdraft except by evaporation, and a sufficient liquid-water concentration would quickly be thrown out of the vortex by centrifugal action. Lilly (1969) computed a momentum budget in the turbulent boundary layer of the Dallas tornado from Hoecker's data. One major conclusion was that it is doubtful whether one can reasonably assume constant viscosity values as was done by both Gutman and Kuo.

Bergman (1970) has studied the dynamic stability of atmospheric convective vortices. He cited observational evidence to show that these concentrated vortices exhibit a decided preference for the two-celled Sullivan flow structure. This preference appeared to be related to boundary considerations, with respect to either or both the surface friction layer and the shear layer around the vortex axis (Turner, 1967; Rott and Lewellan, 1964). Bergman found that unstable disturbance modes of an oscillatory, nonaxisymmetric kind characterize a convective vortex with two-cell structure. This finding is consistent with the multiple "suction-vortex" concept for tornadoes and waterspouts. It was also suggested that "dynamic instability does play a role in the formation and dissipation of atmospheric vortices, although the effects of preexisting turbulence eddies of sufficiently large scale, especially those within the surface friction layer, are also considered important in this respect" (Bergman, 1970, p. 106).

Kuo's vortex model (1966) and his boundary-layer flow (1969) solutions most closely fit current observational knowledge of the flow and temperature patterns in a waterspout. The primary drawback in the Kuo and Gutman models is their symmetry assumption and the overly complicated split-flow around the core stagnation point at midlevels in the latter. Recent tornado and waterspout observations suggest that "suction vortices" or concentrated, secondary eddies with upward jets rotating around the vortex core account for the most damage and for the asymmetric vortex structure apparent at the surface. The waterspout as presently understood is best modeled by the two-celled vortex (Sullivan, 1959), with downflow along the axis.

Laboratory models of tall, thin convective vortices have been developed (Ward, 1956 and 1972; Long, 1958, 1960, and 1961; Turner and Lilly, 1963; Lilly, 1965; and Ying and Chang, 1970). The life cycle sequence of a waterspout has yet to be adequately modeled in the laboratory. In particular, it would be interesting to see whether spiral patterns could be simulated in the boundary layer of a model.

6.2 Dynamical Implications of Matecumbe Results

The air-spray mixture for the Matecumbe vortex was in solid-body rotation inward from the speed maximum near 12 m. Outward from the speed

maximum, the observed profile fitted the theoretical Rankine curve (VR = constant) very well. The above results compared favorably with the tangential velocity profile assumed by Glaser (1960) to analyze a still tornado photograph. Glaser derived a simple mathematical expression, subject to several doubtful assumptions, for using a good tornado photograph to estimate the maximum tangential speed. Glasser's equation, which relates maximum V_T to D_f, was used to calculate velocities as functions of height (shown in fig. 53). Because each height corresponds to a different radius, a radius scale is included. Velocity distributions derived from various transparencies of the large Matecumbe waterspout are not in good agreement. Application of Glaser's formula results in an increase of tangential velocities with height up to about 1,400 ft; this is inconsistent with aircraft observations.

The great lateral velocity shear at the boundary of the central core (eye region, fig. 10) suggests the flow in that region is inertially stable. In the eye, radial perturbations are damped because circulation is increasing with radius; conversely, the outer region, where circulation is independent of radius, is a zone of inertial neutrality (Hess, 1959, p. 306).

Morton's (1969) scale analysis of the equations of motion for tall thin vortices appears relevant to our waterspout observations. He used the component equations for steady, incompressible, axisymmetric, laminar flows referred to cylindrical polar coordinates. Morton's assumptions do not hold in certain regions of the waterspout vortex column at specific times in the life cycle. However, if one uses characteristic values of the scaling parameters that represent typical maxima during the mature stage, assuming quasi-steady state and quasi-axisymmetry (terms $\partial/\partial\theta$ relatively small) may be justified. For strong, narrow vortex cores, where the axial viscous diffusion is negligible compared to lateral diffusion, Morton found from his scaling that $V \sim W$ and $P \sim \rho V^2$. This result implies that the pressure perturbation P provides strong coupling between the tangential and radial-vertical flows near the core. Morton applied the derived scales to the v-component equations of motion and obtained a relation for the pressure deficit on the axis: $p_\infty - p_o(z) = \rho\int_0^\infty \frac{v^2}{r}\,dr$, corresponding to cyclostrophic balance. Morton (1969) pointed out that the pressure deficit on the axis of a rotating core, embedded in a quiescent environment at uniform pressure p_∞, is constant only in a cylindrical azimuthal velocity field $v = v(r)$; thus, "axial pressure gradients are the rule in all swirling flows suffering progressive lateral spread by either viscous or turbulent diffusion with increasing axial distance from the source" (Morton, 1969, p. 319). This result implies: (a) Stagnation points are possible in the axial flow; and (b) V is a function of height from the cyclostrophic balance derived above.

6.3 Scale Analysis for the Waterspout

Following Sinclair (1966) and Morton (1966, 1969), the equations of motion for steady, incompressible, axisymmetric, turbulent flow with velocity components $(\overline{u}, \overline{v}, \overline{w})$ referred to cylindrical polar coordinates $(r, \emptyset, z)$, take the forms

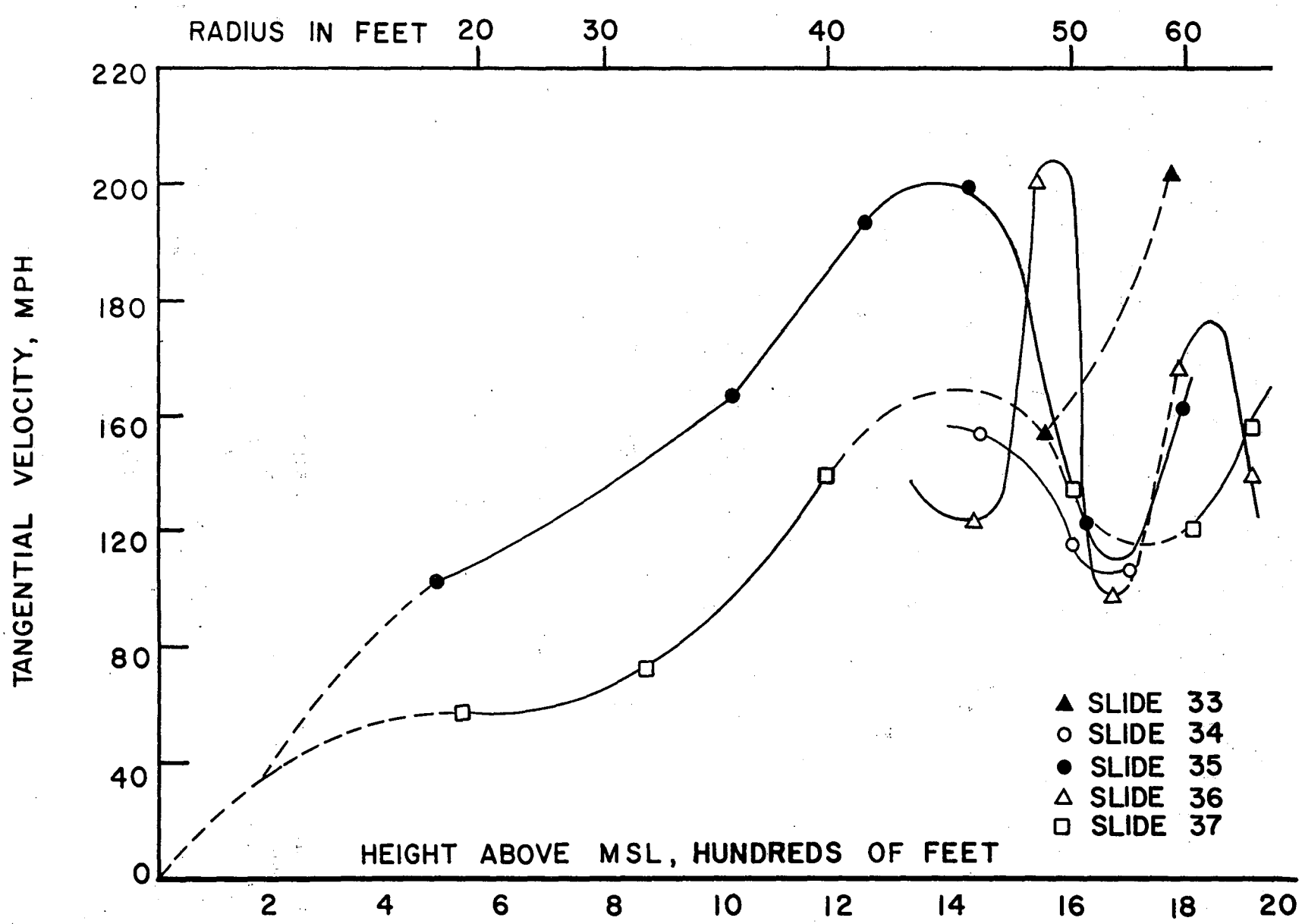

Figure 53. Application of Glaser's (1960) empirical tornado-windspeed formula to slides of the large Matecumbe waterspout. The different curves correspond to the numbered transparencies.

$$\bar{u}\frac{\partial\bar{u}}{\partial r} + \bar{w}\frac{\partial\bar{u}}{\partial z} - \frac{\bar{v}^2}{r} = \frac{1}{\rho}\frac{\partial\bar{p}}{\partial r} + K\left[\frac{\partial^2\bar{u}}{\partial r^2} + \frac{\partial^2\bar{u}}{\partial z^2} + \frac{1}{r}\frac{\partial\bar{u}}{\partial r}\right], \tag{1}$$

$$\frac{U^2}{R} \qquad \frac{UW}{Z} \qquad \frac{V^2}{R} \qquad \frac{P}{\rho R} \qquad \frac{KU}{R^2} \gg \frac{KU}{Z^2}$$

$$\bar{u}\frac{\partial\bar{v}}{\partial r} + \bar{w}\frac{\partial\bar{v}}{\partial r} + \frac{\bar{u}\bar{v}}{r} = K\left[\frac{\partial^2\bar{v}}{\partial r^2} + \frac{\partial^2\bar{v}}{\partial z^2} + \frac{2}{r}\frac{\partial\bar{v}}{\partial r}\right], \tag{2}$$

$$\frac{UV}{R} \qquad \frac{VW}{Z} \qquad \frac{UV}{R} \qquad \frac{KV}{R^2} \gg \frac{KV}{Z^2}$$

and

$$\bar{u}\frac{\partial\bar{w}}{\partial r} + \bar{w}\frac{\partial\bar{w}}{\partial z} = \frac{1}{\rho}\frac{\partial\bar{p}}{\partial z} + K\left[\frac{\partial^2\bar{w}}{\partial r^2} + \frac{\partial^2\bar{w}}{\partial z^2} + \frac{1}{r}\frac{\partial\bar{w}}{\partial r}\right], \tag{3}$$

$$\frac{UW}{R} \qquad \frac{W^2}{Z} \qquad \frac{P}{\rho Z} \qquad \frac{KW}{R^2} \gg \frac{KW}{Z^2}$$

and the corresponding equation of continuity for this system takes the form

$$\frac{\partial\bar{u}}{\partial r} + \frac{\bar{u}}{r} + \frac{\partial\bar{w}}{\partial z} = 0, \tag{4}$$

$$\frac{U}{R} \qquad \frac{U}{R} \qquad \frac{W}{Z}$$

In applying the above simplified equations of motion and continuity to the waterspout, we assume a quasi-steady state; that is, local accelerations are much smaller than the advection terms in the equations. This assumption does not necessarily imply that the waterspout flow is invariant with time, but rather than the evolution with time of the waterspout may be approximated by a succession of quasi-steady states. The assumption of axial symmetry is not always valid in the waterspout boundary layer. However, the symmetric structure of the visible funnel and spray sheath in mature waterspouts suggest that the assumption of axial symmetry may be valid at this stage of its life cycle.

Capital letters in equations (1) through (4) represent characteristic magnitudes (above the boundary layer) for the variables. R and Z are

considered to be the characteristic width and length of the waterspout vortex column. We assume that $R/Z << 1$ and that $Z \sim 600$ m. Based on our observations, we take $V = 75$ m/s, $U = 2$ m/s, $W = 10$ m/s, $R = 50$ m, and $Z = 600$ m. (The magnitude for U was subjectively estimated because, in the surface boundary layer, U has been estimated as high as about 20 m/s, but appeared to decrease by an order of magnitude above the top of the spray vortex.) We take an average cloud base height to represent Z. To check on the internal consistency of the characteristic values chosen for scaling, note from equation (4) that

$$\frac{U}{R} \sim \frac{W}{Z} \text{ yields } \frac{2}{50} \sim \frac{10}{600} . \tag{5}$$

The scaled continuity equation (5) shows that the three inertial terms on the left-hand side of equation (2) are all of the same order. Therefore, $\frac{UV}{R} \sim \frac{KV}{R^2}$ and $K \sim UR \sim 100$ m^2/s. This magnitude for K seems reasonable in light of Sinclair's (1966) calculated values of K for dust devils.

From equation (1), we find $\mathcal{O}(\frac{4}{50}) + \mathcal{O}(\frac{2}{60}) + \mathcal{O}(112.5) \sim P/\rho R + \mathcal{O}(\frac{2}{25})$. Note that the eddy stress term on the right is of the same order as the two inertial terms on the left. Most important, the centrifugal term dominates these terms and must be balanced by the radial pressure gradient force. Therefore, the motion in the core of the waterspout is well approximated by the cyclostrophic wind relation. This result implies that $P \sim \rho V^2 \sim \mathcal{O}(50 \text{ mb})$.

Finally, using characteristic values above in equation (3), we find that the vertical pressure gradient is larger than the other terms by more than an order of magnitude, apparently implying that the waterspout as a system is in approximate hydrostatic balance. However, we have not yet obtained measurements of the vertical pressure differential in waterspout cores. Further, our scaling of the advection terms in equation (3) depends crucially on the characteristic values chosen for W and Z. We have measurements of W only in certain restricted regions of mature waterspouts. Preliminary analyses of the spray vortex trajectories indicate that the term $\bar{w}\frac{\partial \bar{w}}{\partial z} \sim \frac{W^2}{Z}$ may become much larger than indicated above, especially near the top of the boundary layer (in the spray sheath). Larger values of W may also be present within the parent cloud above the waterspout.

Our scale analysis with the waterspout data verifies Morton's (1969) conclusion that the flow near the vortex core must be cyclostrophic. However, the present data are insufficient to comment definitely on his conclusion that $V \sim W$ and that V is a function of height. Our analyses of spray trajectories and marine smoke plumes do suggest, however, that the maximum of V is reached in the upper portion of the spray vortex at low levels.

6.4 Environmental Inputs for Modeling

A representative sample of four rawinsonde soundings taken at the Boca Chica NAS during the 1969 field project are presented in figures 54 through 57. These soundings are considered to represent the mesoscale environ-

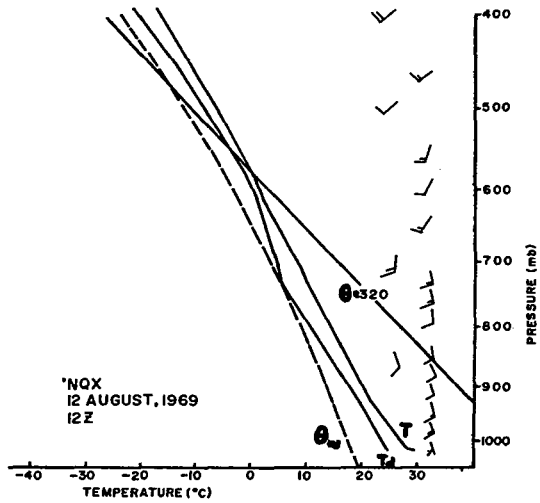

Figure 54. Morning sounding and vertical wind profile at Boca Chica NAS for August 12, 1969, at 1200 GMT.

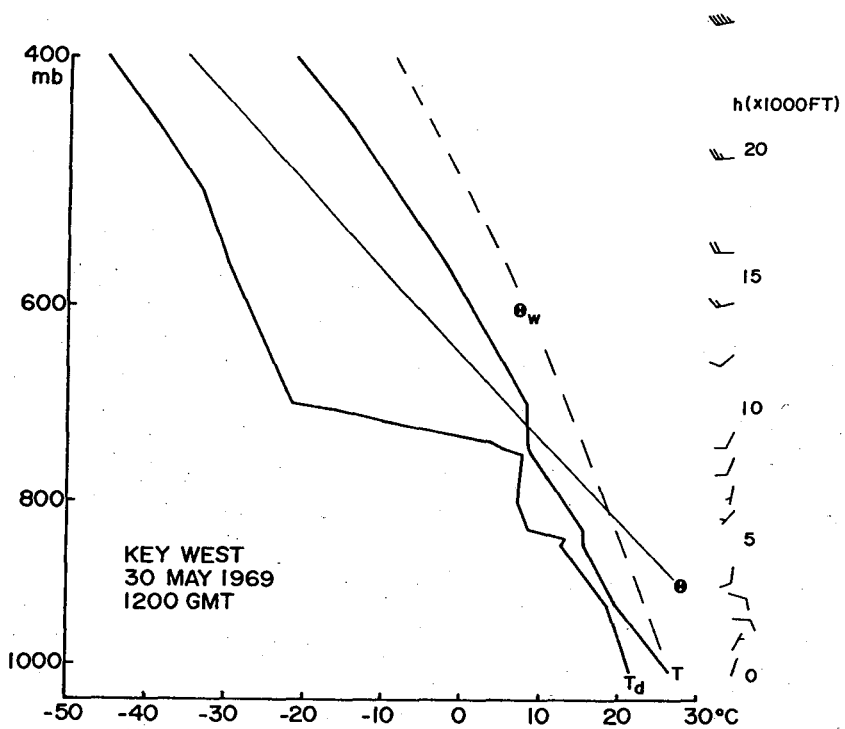

Figure 55. Temperature-dewpoint sounding at Key West on May 30, 1969, at 1200 GMT.

ment of cumulus-congestus cloudlines which spawned large or numerous waterspouts. Notice, in general, that the low-level winds in the morning "waterspout proximity soundings" are light from a southwest-southeast-northeast direction and veer with height up to 600 and 700 mb. With the exception of figure 54, the soundings all indicate abundant moisture up to 700 mb with dryer air above. In the reduction of conventional rawinsonde data, superadiabatic lapse rates through layers of 50 mb or more are usually regarded with suspicion and smoothed out in the final processing. Nevertheless, the data indicate that dry or superadiabatic lapse rates are often present below about 900 mb. The remaining levels are convectively unstable, and lifted indices are near or below zero. There was a pronounced veering of the winds at all levels and drying aloft during the 12 hr after figures 54, 55, and 57; this wind shift is clearly indicated in figure 56. These diurnal changes in the wind and moisture properties of the waterspout-producing environment are related to the weak synoptic-scale disturbances previously described.

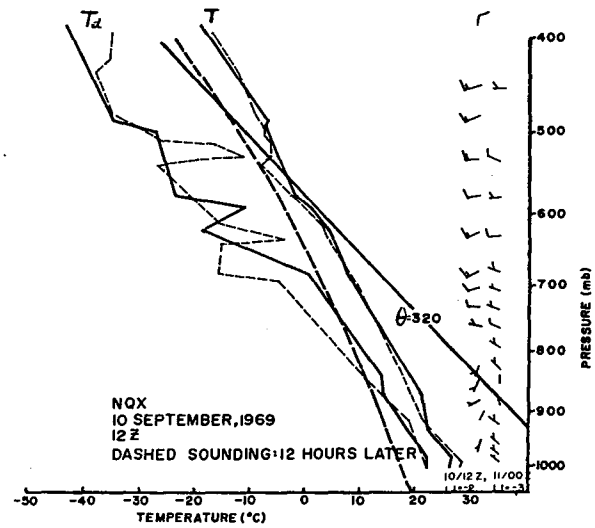

Figure 56. Key West soundings on September 10-11, 1969 at 1200 and 0000 GMT, respectively, with dry adiabat (solid) and moist adiabat (long dashed). Profiles and lifted index values (below) at right.

No attempt was made to construct "mean waterspout soundings." The reasons become clear upon examination of figure 58 showing spiral-ascent aircraft temperatures beneath and just outside a cloudline that produced seven sequential waterspouts. The Key West sounding, taken earlier the same day, is also plotted. Note especially the observed superadiabatic lapse-rate up to about 900 ft MSL. The outflow from a nearby shower apparently contributed to the greater instability beneath the cloudline, up to 900 ft, and there were two inversions in the upper half of the subcloud layer. Air and sea-surface temperatures obtained during the midafternoon Braham flight (see section 4.4) also indicated a superadiabatic lapse rate in the lower half of the subcloud layer. If

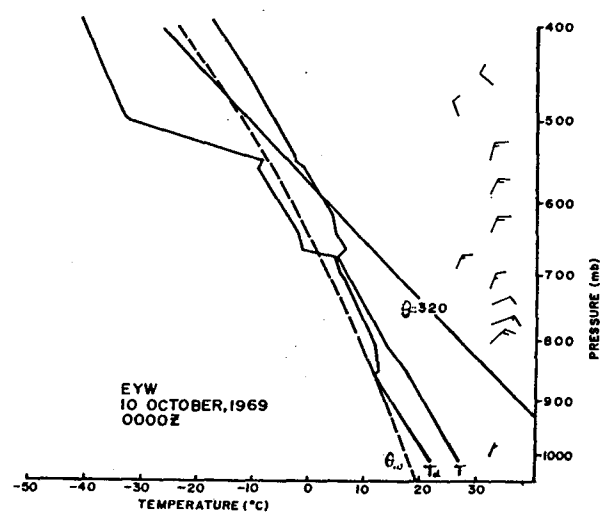

Figure 57. Key West sounding and winds near time of RFF DC-6 flight. Dry adiabat is θ = 320°K; moist adiabat (dashed) is θ_w.

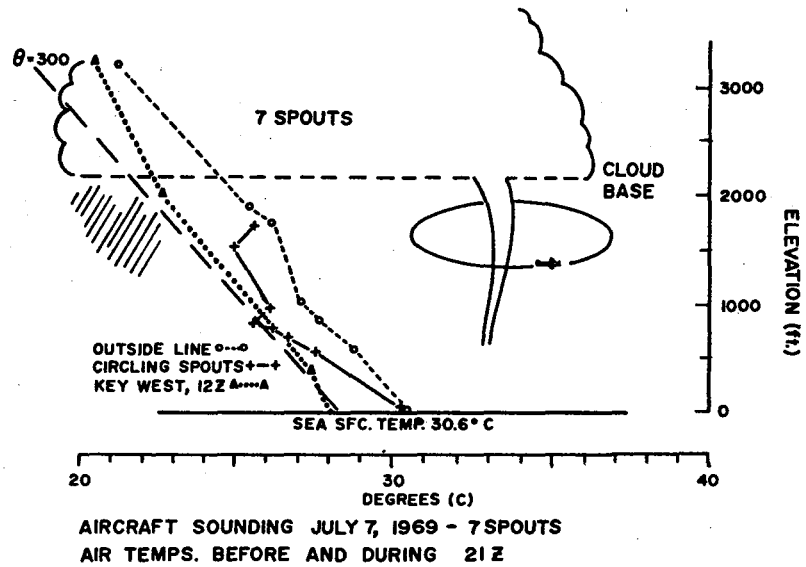

Figure 58. Temperature sounding taken from outside-dial temperature gage on Tri-Pacer aircraft (read to nearest 0.5°C) beneath (dashed, small) and just outside (solid) waterspout-active cloudline on July 7, 1969. Key West sounding at 1200 GMT is also plotted for comparison.

these results hold in general, they strongly suggest that the low-level thermodynamic properties of the waterspout environment are poorly represented by conventional land-based soundings.

We have previously shown that while the synoptic-scale circulation acts as an overall controlling factor in waterspout formation, the cloudline scale is also crucial. It is estimated from the 1968-72 waterspout data that at least 90 percent of the Keys' waterspouts are spawned by cumulus cloudlines (i.e., not isolated cumuli). It is significant that spiral patterns usually form on the flanking edge of a cloudline, with the developing rainshower or two generally within 1 to 2 n mi of the epicenter. Frequently, the tail or major "feeder-band" of the spiral appears to eminate from a narrow protrusion of the downwind shower boundary. These features are summarized in figure 59. Generally, there are both cyclonic shear and curvature in the low-level mesoscale flow through the cloudline. The updrafts and subcloud-layer convergence are enhanced by converging shower outflows, and the waterspouts move in the directions of these outflows.

In summary, it appears that complete waterspout models should concentrate on simulation of intermediate scales of motion (i.e., spiral and cloudline scales) in the scale-interaction process. Because 90 percent of the Keys' waterspouts are cyclonic and because the favorable synoptic-scale disturbances are (weakly) cyclonic, the Coriolis force has an indirect influence on waterspout formations, but is not a crucial factor.

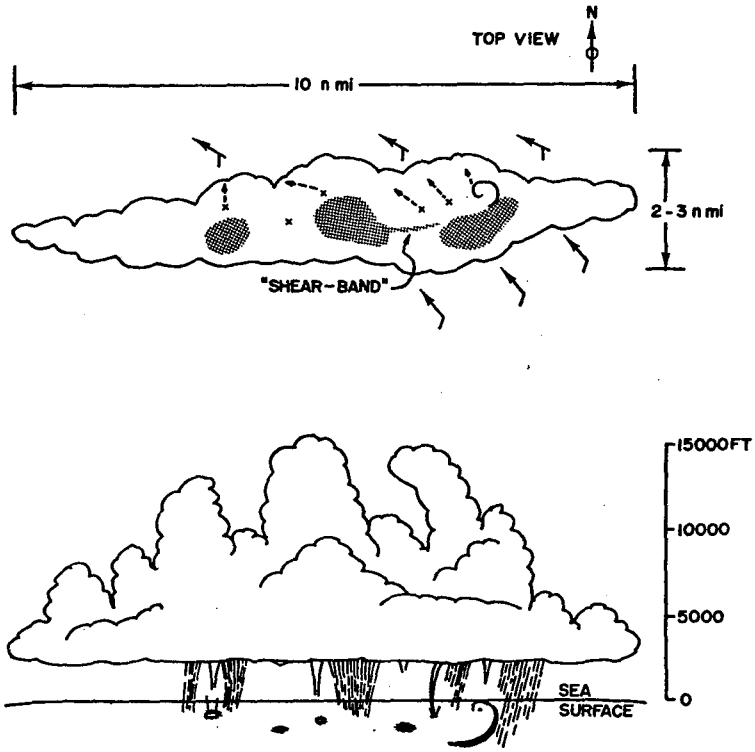

Figure 59. Schematic, composite scaled model of a waterspout-active cloudline, illustrating typical locations of waterspouts in various stages of life cycle, motion relative to showers, and mesoscale flow (plan view above; side view below).

7. CONCLUSIONS AND PROPOSED FUTURE FIELD EXPERIMENTS

7.1 The Waterspout Life Cycle Summarized

Perhaps the most important discovery from the 1969 Lower Keys Waterspout Project was that waterspouts of all sizes and intensities undergo a regular life cycle. This life cycle may be conveniently divided into five discrete but overlapping stages. However, these five stages should not be taken as separate sequences of growth and decay. During a transition phase, two stages may overlap; the first two often do. The five stages are: (a) the dark spot; (b) the spiral pattern; (c) the spray ring (incipient spray vortex); (d) the mature waterspout (spray vortex); and (e) the decay. Not every waterspout observed from its inception evolved through all stages. The combination of stages 1-2-3-4-5, 1-3-4-5, 1-5, and rarely, 1-2-5, have been documented.

7.2 Summary of Scale Interaction Processes

The funnel scale of motion, corresponding to the scale of the waterspout itself (i.e., dark spot, spray ring, and spray vortex or funnel cloud),

is the end product of a descending hierarcy of interacting motion scales. The funnel scale appears to be the most complicated; pronounced asymmetries in the horizontal and vertical flow components in the spray vortex and funnel walls have been documented. The length and maximum diameter of the funnel cloud appear directly related to the surface intensity, but a complete vortex column frequently occurs with only a short funnel cloud and dark spot on the sea surface below. The waterspout appears to be a two-cell type of radial-vertical circulation, with weak descent in the hollow core surrounded by a rising annulus which reaches a maximum a short distance outward from the visible funnel.

The spiral scale of motion is manifested by a spiral pattern on the sea surface. It has been observed during stages 2 through 5, and its presence in the parent cloud is indicated by the spiral rain-pattern evolution during the decay stage of some waterspouts. The spiral pattern on the sea surface during stage 2 is not directly related to the boundary-layer flow characteristics; the dark banding appears to be a wave interference zone. Smoke flares indicate confluent and diffluent asymptotes in a sometimes complicated flow pattern around the spiral. The initial source of the waterspout's large vorticity is often indicated by a dark band on the sea surface, indicative of a zero-order wind discontinuity with cyclonic shear, produced by the interaction of shower outflow with environmental winds. This preexistent elongated band ultimately wraps around the developing waterspout to form the spiral pattern. The spiral scale is important because it reflects the primary growth phase (stage 2) and because it gives the first visual evidence of rotation and inflow in the surface boundary layer.

Another important motion scale is the individual cumulus-cloud scale. Well-organized cyclonic circulations in the cloud base and the lower cloud body precedent to and accompanying waterspout development were documented by WSR-57 radar and time-lapse photography. Photogrammetric computations of vertical cloud-growth rates from time-lapse cloudline photography showed a pulsating cumulus-scale updraft structure which can be related to periodic waterspout production. Large peaks in the cloud-growth rate curves are related to major funnel growth and the relative minima related to the waterspout decay.

Surface heating contributions were assessed from a low-level temperature flight. Analysis of air temperature over the islands showed cloud-scale warm (up to 2°C) pockets, displaced slightly relative to the islands by the low-level winds. Only islands having a length of at least 1 to 2 n mi produced detectable warm air pockets at flight altitude.

The cloudline scale is perhaps most crucial to waterspout formation. Both a waterspout-active and a nonwaterspout cumulus cloudline in the same general area were investigated in comparable detail by the RFF DC-6 aircraft. Analyses of the data fields at flight levels up to 3,700 ft MSL for both cloudlines have, for the first time, permitted a structural comparison. Both cloudlines exhibited splitting flow around the major radar echoes, with cyclonic shear to the north and anticyclonic shear to the south at all levels. The waterspout-active cloudline had large cyclonic relative-vorticity in the form of both curvature and shear on the north flank of the major echo complex. All waterspouts were located on the north side of the split, coincident with

large upward vertical motion and strong cold-temperature advection. Temperature advection and gradients were much larger and were organized on a larger scale in the waterspout-active cloudline than those observed in the nonwaterspout cloudline. Before precipitation onset in the waterspout cloudline, the major waterspout developments occurred in regions of strong horizontal gradient of wet-bulb potential temperature; thereafter, the waterspouts were found in maxima of θ_w.

Finally, the synoptic scale was found to be the controlling influence on convective-cloudline developments in the Lower Keys. If strong anticyclonic conditions persist in the 1,000 to 600-mb layer, subsidence will inhibit cumulus-cloudline development over the heated islands and shallow water. Additionally, if a strong cyclonic synoptic-scale disturbance affects the Keys, the strong low-level winds and vertical wind shear will disrupt the surface heating mechanism. The accompanying strong low-level convergence and positive relative vorticity will overwhelm the differential heating mechanism. Whenever either several waterspouts or giant, long-lived waterspouts were observed, a weak but well-defined synoptic-scale troughline in the lower tropospheric mean flow approached and passed through the Keys, causing enhanced cumulus-cloudline development.

7.3 Suggestions for Future Work

Some results are based on analyses of quantitative data; others are deduced from data of a more qualitative nature. The majority of the 1969 data were obtained in the lower vortex column. Additional measurements of wind and thermal properties in the lower half of the subcloud layer and within the waterspout's parent cloud are needed. Time-lapse film data clearly show preexistent, organized circulation on the spiral scale accompanies waterspout formation. Moreover, well-documented cases of a spiral rain curtain evolving around a decaying waterspout strongly suggest that spiral-scale horizontal circulation also occurs within the parent cloud, with strong organized updrafts. The horizontal spreading of the vortex column at cloud base has been demonstrated qualitatively in the present work.

A feasible method for determining the horizontal circulation pattern within the parent cloud is the utilization of twin mobile Doppler radars. Lhermitte's field studies (1966, 1968, and 1969) of thunderstorms suggested that the mesoscale wind field could be obtained around waterspouts and their parent cloudlines by tracking precipitation particles and properly dispersed chaff. The twin Dopplers would be optimally spaced about 30 km apart in the Lower Keys, and, at the ranges typical for cloudline formations, the radar system could resolve motions in the x, y plane down to 150 m. Further, smoothed vertical motions could be derived from the continuity equation. Even a single Doppler radar could provide useful data on radial velocity components and might imply closed vortex circulations within the waterspout cloudline (see Brown et al., 1971). Little (1972) has indicated that optical Doppler technology could be effectively applied to the problem of obtaining direct wind measurements on the waterspout scale.

Detailed aircraft measurements have been made through waterspout-active cloudlines above 1,000 ft with the RFF DC-6. Because Doppler wind

equipment does not function well below 1,000 ft, an aircraft with an inertial guidance platform must be used to study motions on the spiral scale below this height. (Limited measurements were obtained with the NCAR Buffalo aircraft in September 1972). Gradients of thermal properties across the wind-shift and density-surge lines, which are so important in the waterspout's life cycle, are of special interest. The aircraft should be additionally equipped to determine droplet size distributions and liquid water contents of the waterspout's parent cloud and adjacent cells. Qualitative observations during the 1969 and 1970 waterspout flights indicated that shallow cumulus cloudlines spawning waterspouts have a more efficient precipitation mechanism than those which remain benigh. This apparently resulted from rotation reducing the entrainment, thereby producing stronger, more organized updrafts in the waterspout-producing cells. The aircraft penetrated extremely heavy rainshowers produced by warm clouds (tops at or below the freezing level) on several occasions while it was orbiting waterspouts in the subcloud layer.

Continued work with the Purdue University Tornado Group, using a trailing-wire probe with fast-response sensors for temperature and pressure, is planned. An experimental fast-response humidity sensor has recently been added to the probe. If this addition proves satisfactory, it will allow determination of θ_w in the waterspout core and, therefore, permit indications of the subsiding air's origin. Additional quantitative subcloud vertical-motion measurements will be needed within and surrounding the waterspout funnel.

A third method under consideration for measuring temperature, pressure, relative humidity, and vertical motions around and through the waterspout is a radio-controlled model aircraft of the type developed by Konrad et al. (1970).

Additional wind and temperature data in the surface boundary-inflow layer of the waterspout are needed. One means of obtaining these data would be to airdrop recoverable buoys equipped with anemometers and temperature sensors. These small buoys could be placed systematically in each quadrant of the waterspout region and later recovered.

Finally, the physical mechanism producing the brightness contrasts on the sea surface in spiral patterns and dark spots should be further investigated. Differential upwelling and a resultant sharp horizontal sea-surface temperature gradient is one mechanism which has been suggested. This author doubts that this is the primary mechanism because of the shallow water depths and very short time scales involved. Based on existing telephoto film data, we hypothesize that the major dark bands result from local generation of low-amplitude, short-wavelength surface capillary waves. This hypothesis could be tested with a suitable wave-measuring device on a low-flying aircraft. Another method has been suggested by aircraft observations of windrows made by Boston et al. (1971). They used a fixed-wing aircraft and a helicopter to study the windrow regime in both the offshore and nearshore environment off Monterey Bay of California. In both regimes, windrow direction changed surprisingly fast with a change in wind direction; response times fell between 2 and 4 min. Windrows are often associated with Langmuir circulations (Langmuir, 1938). Alternating regions of convergence and divergence occur at

the water surface as the result of this circulation. Organic oils concentrate at the convergent regions (Ewing, 1950), causing a decrease in surface tension, absence of capillary waves, and slick appearance of the surface. Several hypotheses have been offered to explain Langmuir circulations and associated windrows (Scott et al., 1969; Faller, 1969). According to Galt et al. (1972), the primary difficulty is in the need for sufficient field information to determine which is correct or to separate concurring mechanisms.

7.4 Relationship to Tornado Research

An important conclusion, supported by the author's recent fieldwork during the NOAA Tornado Intercept Program in Oklahoma, is that the difference between waterspouts and tornadoes is mainly quantitative. The latter are known to occur generally in association with intense, well-organized synoptic-scale and mesoscale ("tornado cyclone") disturbances. Waterspouts are linked, through the scale-interaction process, to weak but definable synoptic-scale disturbances which intermittently affect South Florida during the summer. A weak analog to the tornado cyclone is suggested by the organized flow perturbations (and attendant thermodynamic structure) observed in waterspout-active cloudlines. Rotating "mother clouds" (slightly smaller scale) of the type documented by Fujita (1960) for the Fargo tornadoes and by Koscielski (1967) for the Black Hills tornado were frequently documented during the 1969 Lower Keys Waterspout Project.

However, the more intense disturbances, such as tropical depressions and storms, which also periodically affect the Florida Keys during the summer months are associated with a definite minimum of waterspout activity and maximum likelihood of tornado occurrence. One reason for the waterspout minimum during these periods is the disruption by stronger-than-normal winds of the differential heating mechanism provided by the island chain and shallow, warm water. Spiral rainbands (i.e., cloudlines of cumulonimbi) are formed by the tropical storm or depression, and the strongly-sheared environment is conducive to tornado formation in a few major rainbands. A second reason for waterspout decrease during intensely disturbed weather in the Keys is the resultant, very deep, nearly saturated moist-layer and strong low-level convergence. Under these conditions, the Key West radar shows large areal coverage of convective precipitation. Aircraft flights made in futile attempts to find waterspouts in such situations in 1969 showed that cloudlines form, but individual cumuli are short lived. Waterspouts form in the cloudline section flanking an incipient shower and containing intense, persistent updrafts. We therefore conclude that, during intensely disturbed conditions in the Keys, waterspouts fail to form because organized updrafts in any existing cumulus cloudlines fail to persist long enough to concentrate preexistent vorticity.

Finally, we emphasize that tornadoes are usually associated with intense, <u>baroclinic</u> synoptic-scale disturbances with attendant strong vertical wind-shear, whereas waterspouts are associated with weak, <u>quasi-barotropic</u> disturbances and consequent weak vertical wind-shear.

8. ACKNOWLEDGMENTS

This author's initial interest was aroused by a chance encounter of an aerial waterspout while in the company of three friends and professional colleagues who were aiding in the initial phases of the Matecumbe data analysis. These three, Dr. William Woodley, Brad Halter, and James Bunting, encouraged my subsequent efforts. My major professor, Dr. Noel La Seur, at Florida State University, provided important guidance and conceptual focus throughout the course of this work. Drs. C. L. Jordan, Albert Barcilon, Ron Alberty, and R. P. Davies-Jones are thanked for their helpful suggestions and careful review of the manuscript. The bulk of the results have been derived from the 1969 Lower Keys Waterspout Project, which reached successful fruition only because of direct support and encouragement from the following people: Drs. Robert H. Simpson, Joanne Simpson, Edwin Kessler, John McCarthy, Joachim Kuettner, R. C. Gentry, and Messrs. George Faraldo (Airport Manager, Key West, Fla.), Jerry Clemons, Don Ocker, and the entire staff of the National Weather Service Office at Key West. Messrs. Rex Hamilton and Brad Halter were my "right-hand men" during the 1969 field operations. Mr. Jack Turken assisted in many laborious statistical computations and photogrammetric time-lapse tracing. I have benefited greatly from the NOAA-sponsored, collaborative waterspout-probing experiments with Drs. C. M. Ehresman and Chris Church of Purdue University. I am most indebted to my colleague, Dr. Ted Fujita, for his analytical insights and generous assistance in developing the "control loop" technique and for providing the rectified Apollo IX photograph. Finally, I wish to thank the flight crews and scientists of NOAA Research Flight Facility and the U. S. Navy. Financial support for the 1969 Lower Keys Waterspout Project was provided through a research grant from the National Severe Storms Laboratory.

Ms. Judy Lawrence typed the manuscript; Mr. Paul Hannum and Mrs. Jennifer Farris drafted the figures. Significant photographic support was provided by Messrs. Charles Clark and Charlie True.

9. REFERENCES

Alderman, D. D. (1965): Radar echoes associated with waterspout activity, U. S. Weather Bureau Tech. Memo. No. 5, Southern Region Headquarters, Ft. Worth, Tex., 2 pp.

Battan, L. J. (1961): The Nature of Violent Storms, Anchor Books, Garden City, N. Y., 158 pp.

Bergman, K. H. (1970): On the dynamic stability of convective atmospheric vortices, Ph.D. dissertation, Univ. of Washington, Seattle, 161 pp.

Boston, N., R. Ortengren, and A. Maratos (1971): Aircraft observations of windrows, In: Proc. Conf. on the Interaction of the Sea and the Atmosphere, Dec. 1-3, 1971, Ft. Lauderdale, Fla.

Brooks, E. M. (1951): Tornadoes and related phenomena, In: Compendium of Meteorology, T. F. Malone, ed., Amer. Meteorol. Soc., Boston, Mass., 673-680.

Brown, R. A., W. C. Bumgarner, K. D. Crawford, and D. Sirmans (1971): Preliminary Doppler velocity measurements in a developing radar hook echo, Bull. Amer. Meteorol. Soc. 52, 1186-1188.

Browning, K. A., and F. H. Ludlam (1962): Airflow in convective storms, Quart. J. Roy. Meteorol. Soc. 88, 117-137.

Bundgaard, R. C. (1953): On the formation and development of waterspouts, Detachment 4, Headquarters, Air Weather Service, MacDill AFB, Tampa, Fla., 29 pp, unpublished manuscript.

Burgers, J. M (1948): A mathematical model illustrating the theory of turbulence, Advan. Appl. Mech. 1, 197.

Byers, H. R., and R. R. Braham (1949): The Thunderstorm, U. S. Govt. Print. Off., Washington, D. C., 287 pp.

Charba, J., and Y. Sasaki (1971): Gravity current model applied to analysis of squall-line gust-front, In: Proc. Seventh Conf. on Severe Local Storms, Oct. 5-7, 1971, Kansas City, Mo., unpublished manuscript.

Chollet, R. (1958): Waterspouts, Mar. Weather Log 2, 152-156.

Church, C. R., C. M. Ehresman, and J. H. Golden (1973): Instrumentation for probing waterspouts, In: Proc. Eighth Conf. on Severe Local Storms, Oct. 15-17, 1973, Denver, Colo., unpublished manuscript.

Clemons, G. H. (1969): Detailed radar observations and recent climatology of waterspouts in the Key West area, In: Proc. Sixth Conf. on Severe Local Storms, Apr. 8-10, 1969, Chicago, Ill., unpublished manuscript.

Darkow, G. L. (1967): The total energy environment of severe storms, In: Proc. Fifth Conf. on Severe Local Storms, St. Louis, Mo., 99-108.

Dinwiddie, F. B. (1959): Waterspout-tornado structure and behavior at Nags Head, N. C., August 12, 1952, Monthly Weather Rev. 87, 239-250.

Duchon, C. E. (1970): Error variance analysis of meteorological data from the ESSA-RFF DC-6's, Dept. of Meteorol., Univ. of Oklahoma, Norman, 48 pp.

Dunn, G. E., and B. I. Miller (1964): Atlantic Hurricanes, Rev. Ed., Louisiana State Univ. Press, Baton Rouge, 377 pp.

Eddy, A. (1967): Two Dimensional Statistical Objective Analysis of Isotropical Scalar Data Fields, The Univ. of Texas, Coll. of Eng., Austin.

Ewing, G. (1950): Slicks, surface films and internal waves, J. Marine Res. 9, 161-181.

Faller, A. J. (1969): The generation of Langmuir circulations by the eddy pressure of surface waves, Limnol. Oceanogr. 14, 504 - 513.

Ferrel, W. (1893): A Popular Treatise on the Winds, John Wiley and Sons, New York, N. Y., 505 pp.

Flora, S. D. (1954): Tornadoes of the United States, Univ. of Oklahoma Press, Norman, 221 pp.

Fortner, Capt. L. E., and C. L. Jordan (1960): A non-tornadic spiral-shaped radar echo, Monthly Weather Rev. 88, 343-348.

Frank, N. L. (1969): The 'inverted V' cloud pattern—an easterly wave?, Monthly Weather Rev. 97, 130-140.

Friedman, H. A., and W. S. Callahan (1970): The ESSA Research Flight Facility's support of environmental research in 1969, Weatherwise 23, 174-181.

Friedman, H. A., M. R. Ahrens, and H. W. Davis (1969): The ESSA Research Flight Facility: data processing procedures, ESSA Tech. Rept. ERL 132-RFF 2, ESSA, Miami, Fla., 64 pp.

Friedman, H. A., J. D. Michie, and J. D. McFadden (1970): The Research Flight Facility's airborne data collection program in support of the Barbados Oceanographic and Meteorological Experiment, NOAA Tech. Rept. ERL 198-RFF 4, NOAA, Miami, Fla, 178 pp.

Fujita, T. T. (1970a): The Lubbock Tornadoes: A study of suction spots, Weatherwise 23, 160-173.

Fujita, T. T. (1970b): Estimate of areal probability of tornadoes from inflationary reporting of their frequencies, SMRP Research Paper No. 89, Dept. of the Geophys. Sci., Univ. of Chicago, Chicago, Ill., 23 pp.

Fujita, T. T. (1970c): Application of ATS III photographs for determination of dust and cloud velocities over the northern tropical Atlantic, SMRP Research Paper No. 90, Dept. of the Geophys. Sci., Univ. of Chicago, Chicago, Ill., 17 pp.

Fujita, T. T. (1971): Proposed mechanism of suction spots accompanied by tornadoes, In: Preprints of Seventh Conf. on Severe Local Storms, Oct. 5-7, 1971, Kansas City, Mo., 208-213.

Fujita, T. T., D. Bradbury, and C. F. Van Thullenar (1970): Palm Sunday tornadoes of April 11, 1965, Monthly Weather Rev. 98, 26-29.

Fujita, T. T., K. Watanabe, K. Tsuchiya, and M. Schimada (1972): Typhoon-associated tornadoes in Japan and new evidence of suction vortices in a tornado near Tokyo, J. Meteorol. Soc. Japan 50, 431-453.

Galt, J. A., A. Maratos, N. Boston, and E. D. Traganza (1972): A measurement of nearshore Langmuir circulation, to be published in J. Phys. Oceanogr., 1973.

Garstang, M., N. E. La Seur, and C. Aspliden (1967): Equivalent potential temperature as a measure of the structure of the tropical atmosphere, Final Rept. to U. S. Army Electronics Research and Development Lab., No. 67-10, Dept. of Meteorol., Florida State Univ., Tallahassee, 44 pp.

Garza, C., Jr. (1971): A study of funnel cloud occurrences in the Beaumont-Port Arthur-Orange area in Texas, NOAA Tech. Memo. NWS SR-52, Southern Region Headquarters, Ft. Worth, Tex., 11 pp.

Gerrish, H. P. (1965): A survey of extremely heavy and prolonged periods of hourly rainfall, tornadoes, funnel clouds, waterspouts and hail in South Florida, Proc. 1965 Army Conf. on Tropical Meteorol., Miami Beach, Fla., 52-59.

Gerrish, H. P. (1967): Tornadoes and waterspouts in the South Florida area, Proc. 1967 Army Conf. on Tropical Meteorol., June 8-9, 1967, Coral Gables, Fla.

Glaser, A. H. (1960): An observational deduction of the structure of a tornado vortex, In: Cumulus Dynamics: Proc. of the First Conf. on Cumulus Convection, May 19-22, 1959, AF Cambridge Research Center, Portsmouth, N. H., Pergamon Press, New York, N. Y., 157-166.

Golden, J. H. (1967): The life-cycle of convective cloud systems as portrayed by radar and TIROS photographs, Tech. Note No. 67-3, Dept. of Meteorol., Florida State Univ., Tallahassee.

Golden, J. H. (1968): Waterspouts at Lower Matecumbe Key, Florida, September 2, 1967, Weather 23, 103-114.

Golden, J. H. (1969): The Dinner Key 'Tornadic-Waterspout' of June 7, 1968, Mar. Weather Log 13, 139-147.

Golden, J. H. (1970): The Lower Florida Keys Waterspout Project, May-September, 1969, Bull. Amer. Meteorol. Soc. 51, 235-236.

Golden, J. H. (1971): Waterspouts and tornadoes over South Florida, Monthly Weather Rev. 99, 146-154.

Golden, J. H. (1973a): On the life-cycle of Florida waterspouts, Paper presented at 53rd Annual Meeting of the American Meteorological Society, Jan. 29 — Feb. 1, St. Petersburg, Fla, unpublished manuscript.

Golden, J. H. (1973b): Some statistical aspects of waterspout formation, Weatherwise 26, 108-117.

Golden, J. H. (1973c): The life cycle of the Florida Keys waterspout as a result of five interacting scales of motion, Ph.D. dissertation, Fla. State Univ., Tallahassee, 371 pp.

Goodell, H. G., and D. S. Gorsline (1961): The hydrography of Apalachicola and Florida Bays, Data Report, Dept. of Geol. and Oceanogr. Inst., Florida State Univ., Tallahassee, 260 pp.

Gordon, A. H. (1951): Waterspouts, Weather 6(12), 364-371.

Gordon, A. H., and R. C. Taylor (1970): Numerical steady-state friction layer trajectories over the oceanic tropics as related to weather, Intern. Indian Ocean Expedition, Meteorol. Monogr. 7.

Gutman, L. N. (1957): Theoretical model of a waterspout, Bull. Acad. Sci. U.S.S.R. (Geophys. Series), Pergamon Press translation, 1, 87-103.

Harger, G., and J. D. Warden (1962): A radar configuration associated with a series of waterspout, Monthly Weather Rev. 90, 197-200.

Herrera-Cantilo, L. (1969): Aerial cloud photogrammetry based on Doppler navigation, Final Rept. prepared for ESSA, Contract No. 22-2-69(N), Inst. of Atmospheric Sci., Univ. of Miami, Miami, Fla., 65 pp.

Hess, S. L. (1959): Introduction to Theoretical Meteorology, Henry Holt and Co., New York, N. Y., 362 pp.

Hoecker, W. H. (1960): Wind speed and air flow patterns in the Dallas tornado of April 2, 1957, Monthly Weather Rev. 88, 167-180.

Hoecker, W. H. (1961): Three-dimensional pressure pattern of the Dallas tornado and some resultant implications, Monthly Weather Rev. 89, 533-542.

Hurd, W. E. (1928): Waterspouts, On back: U. S. Hydrographic Office Pilot Chart of the North Pacific Ocean, Oct. 1928.

Hurd, W. E. (1950): Some phases of waterspout behavior, Weatherwise 3, 75-82.

Jarvinen, B., and P. G. Black (1971): A New Computerized Technique for Synthesizing RDR-1 Radar Height Contour Analyses, to be published in revised form, 1973.

Johnson, N. K. (1944): The structure of a waterspout, Quart. J. Roy. Meteorol. Soc. 70, 126-128.

Keeling, C. D. (1968): Carbon dioxide in surface ocean waters, 4. global distribution, J. Geophys. Res. 73, 4543-4553.

Konrad, T. G., M. L. Hill, J. R. Rowland, and J. H. Meyer (1970): A small, radio controlled aircraft as a platform for meteorological sensors, Tech. Rept., Appl. Phys. Lab., Johns Hopkins Univ, Silver Spring, Md., 23 pp.

Kuo, H. L. (1966): On the dynamics of convective atmospheric vortices, J. Atmospheric Sci. 23, 25-42.

Kuo, H. L. (1969): Axially-symmetric flows in the boundary layer of a maintained vortex, Planetary Circulation Project Report No. 15, Dept. of the Geophys. Sci., Univ. of Chicago, Chicago, Ill., 57 pp.

Lamb, Sir H. (1945): Hydrodynamics, Sixth Ed., Dover Publications, New York, N. Y., 29 pp.

Langmuir, I. (1938): Surface motion of water induced by wind, Science 87, 119-123.

Lemon, L. R. (1970): Formation and emergence of an anticyclonic eddy within a severe thunderstorm as revealed by radar and surface data, In: Proc. Fourteenth Radar Meteorol. Conf., Nov. 17-20, 1970, Tucson, Ariz., 323-327, unpublished manuscript.

Levine, J. (1959): Spherical vortex theory of bubble-like motion in cumulus clouds, J. Meteorol. 16, 635-662.

Lhermitte, R. M. (1966): Application of pulse Doppler radar technique to meteorology, Bull. Amer. Meteorol. Soc. 47, 703-711.

Lhermitte, R. M. (1968): Atmospheric probing by Doppler radar, In: Proc. NAS/CAS Panel on Remote Atmospheric Probing, April-May 1968, Chicago, Ill., National Research Council, Washington, D. C., 253-289.

Lhermitte, R. M. (1969): Doppler radar observation of a convective storm, In: Proc. Sixth Conf. on Severe Local Storms, April 8-10, 1969, Chicago, Ill., unpublished manuscript.

Lilly, D. K. (1965): Experimental generation of convectively driven vortices, Geofis. Intern. 5, 43-48.

Lilly, D. K. (1969): A comparison of the dynamics of hurricanes and tornadoes, Sixth Technical Conf. on Hurricanes, December 2-4, 1969, Miami, Fla., unpublished manuscript.

Little, C. G. (1972): Status of remote sensing of the troposphere, Bull. Amer. Meteorol. Soc. 53, 936-949.

Long, R. R. (1958): Vortex motion in a viscous fluid, J. Meteorol. 15, 1.

Long, R. R. (1960): Tornadoes and dust whirls, Technical Report No. 10, Dept. of Mech., Johns Hopkins Univ., Baltimore, Md.

Long, R. R. (1961): A vortex in an infinite viscous fluid, J. Fluid Mech. 11, 611-623.

Malkus, J. S. (1952): The slopes of cumulus clouds in relation to external wind shear, Quart. J. Roy. Meteorol. Soc. 78, 530-542.

Malkus, J. S. (1963): Tropical rain induced by a small natural heat source, J. Appl. Meteorol. 2, 547-556.

Malkus, J. S., and R. S. Scorer (1955): The erosion of cumulus towers, J. Meteorol. 12, 43-57.

McFadden, J. D. (1967): Sea-surface temperatures in the wake of Hurricane Betsy (1965), Monthly Weather Rev. 95, 299-302.

McFadden, J. D., and J. W. Wilkerson (1967): Compatibility of aircraft and shipborne instruments used in air-sea interaction research, Monthly Weather Rev. 95, 936-941.

Melaragno, M. G. (1968): Tornado Forces and Their Effects on Buildings, Kansas State Univ., Manhattan, 51 pp.

Miller, F. R., and R. N. Keshavamurthy (1968): Structure of an Arabian Sea summer monsoon system, Intern. Indian Ocean Expedition, Meteorol. Monogr. 1.

Morgan, G. M., Jr., and R. C. Beebe (1971): Analysis of the time-space behavior of the field of equivalent potential temperature during a severe weather situation, In: Preprints Seventh Conf. on Severe Local Storms, October 5-7, 1971, Kansas City, Mo., 54-59, unpublished manuscript.

Morton, B. R. (1966): Geophysical vortices, In: Progress in Aeronautical Sciences 7, Pergamon Press, New York, N. Y., 145-193.

Nancoo, M. E. (1959): Whirlwind in Trinidad, West Indies, Weather 14, 250-256.

Newton, C. W. (1950): Structure and mechanism of the prefrontal squall line, J. Meteorol. 7, 210-222.

Outram, T. S. (1904): Storm of August 20, 1904, in Minnesota, Monthly Weather Rev. 32, 365-366.

Reber, C. M. (1954): The South Platte Valley tornadoes of June 7, 1953, Bull. Amer. Meteorol. Soc. 35, 191-197.

Riehl, H. (1945): Waves in the easterlies, Miscellaneous Report No. 17, Univ. of Chicago Press, Chicago, Ill., 79 pp.

Riehl, H. (1954): Tropical Meteorology, McGraw-Hill Book Co., New York, N. Y., 83 pp.

Riehl, H. (1965): Introduction to the Atmosphere, McGraw-Hill Book Co., New York, N. Y., 365 pp.

Rossman, F. O. (1960): On the physics of tornadoes, In: Cumulus Dynamics, Pergamon Press, New York, N. Y., 167-174.

Rossow, V. J. (1970): Observations of waterspouts and their parent clouds, NASA Tech. Note D5854, NASA, Washington, D. C. 63 pp.

Rott, N. (1958): On the viscous core of a line vortex, Z. Angew. Math. Phys. 9, 543 pp.

Rott, N., and W. S. Lewellan (1964): Boundary layers in rotating flows, Aerospace Corp. Report ATN-64 (9227)-6.

Saunders, P. M. (1970): Corrections for airborne radiation thermometry, J. Geophys. Res. 75, 7597-7601.

Scorer, R. S., and F. H. Ludlam (1953): Bubble theory of penetrative convection, Quart. J. Roy. Meteorol. Soc. 79, 94-103.

Scorer, R. S., and C. Ronne (1956): Experiments with convection bubbles, Weather 11, 151-154.

Scott, J. T., G. E. Myer, R. Stewart, and E. A. Walther (1969): On the mechanism of Langmuir circulations and their role in epilimnion mixing, Limnol. Oceanogr. 14, 494-503.

Senn, H. V. (1971): Report on RFF DC-6 RDR-1 and other radar data, appendix A, unpublished report to Dr. R. C. Gentry, Director, National Hurricane Research Laboratory, 79-83.

Sheets, R. C., and T. N. Carlson (1971): Comparison of draft-scale vertical velocities computed from gust probe and conventional data collected by a DC-6 aircraft, NOAA Tech. Memo ERLTM-NHRL 91, NOAA, Miami, Fla., 16 pp.

Sinclair, P. C. (1966): A quantitative analysis of the dust devil, Ph.D. dissertation, Univ. of Arizona, Tucson, 292 pp.

Smith, T. (1956): Waterspouts off Cape Cod, Weatherwise 9, 174.

Stern, M. E., and J. S. Malkus (1953): The flow of a stable atmosphere over a heated island, Part II, J. Meteorol. 11, 105-120.

Sullivan, R. D. (1959): A two-cell vortex solution of the Navier-Stokes equations, J. Aerospace Sci. 20, 458-471.

Thompson, M., Ed. (1966): The Manual of Photogrammetry, Vol. I and II, Third Ed., Amer. Soc. Photogrammetry, Falls Church, Va., 1196 pp.

Turner, J. A. (1967): Some characteristics of concentrated convective vortices, In: Convective Elements, Final Report, Dept. of Atmospheric Sci., Univ. of Washington, Seattle, 11-26.

Turner, J. S., and D. K. Lilly (1963): The carbonated-water tornado vortex, J. Atmospheric Sci. 20, 458-471.

Ward, N. B. (1956): Temperature inversion as a factor in formation of tornadoes, Bull. Amer. Meteorol. Soc. 37, 145-151.

Ward, N. B. (1964): The Newton, Kansas tornado cyclone of May 24, 1962, Proc. Eleventh Weather Radar Conf., Amer. Meteorol. Soc., Boston, Mass., 410-415.

Ward, N. B. (1972): The exploration of certain features of tornado dynamics using a laboratory model, J. Atmospheric Sci. 29, 1194-1204.

Wise, C. W., and R. H. Simpson (1971): The tropical analysis program of the National Hurricane Center, Weatherwise 24, 164-173.

Witschi, H. W. (1957): Southeast Florida funnel clouds, 17 pp., unpublished manuscript.

Woodley, W. L., J. H. Golden, B. C. Halter, and J. T. Bunting (1967): Weather note--aircraft observations in the immediate vicinity of two waterspouts, Monthly Weather Rev. 95, 799-803.

Ying, S. J., and C. C. Chang (1970): Exploratory model study of tornado-like vortex dynamics, J. Atmospheric Sci. 27, 3-14.

Zipser, E. J. (1969): The role of organized unsaturated convective downdrafts in the structure and rapid decay of an equatorial disturbance, J. Appl. Meteorol. 8, 799-814.

APPENDIX A.

CHECKED TABULATION OF LOWER KEYS' 1969 WATERSPOUT EVENTS FROM ALL DATA SOURCES

The year 1969 was the best-observed waterspout season of any in the Lower Florida Keys. The table below is intended to provide future researchers and potential field experimentalists with a detailed summary.

Table 8. Summary of 1969 Lower Keys Waterspout Population

	Date	Event	Location (from NWS, Key West)	Time (EST) (began-ended)	Remarks
1.	4-28	Funnel	SE	1202-1205	NQX (Boca Chica NAS)
2.		Funnel	ENE	1818	Pirep (pilot report): N of MTH (Marathon)
3.					
4.	5-5	Funnel	7 NE	0804-0812	NQX
5.		Funnel	8 NE	0812-0816	NQX
6.		Funnel	7 NE	0816-0821	NQX
7.		Funnel	3 NE	1258-1309	
8.		Funnel	3 NE	1258-1309	

Table 8. Continued

	Date	Event	Location (from NWS, Key West	Time (EST) (began-ended)	Remarks
9.		Funnel	3 NE	1258-1309	
10.	5-7	Funnel	ESE	0535-0540	NQX
11.	5-12	WS	34 E	1900	Public: 080°/34
12.		WS	ENE	1900-1930	Public: 075°/35-40 (several)
13.	5-19	Funnel	3 S	1045	Pirep
14.		Tornado	16 E	1200	Public: (unconfirmed) 080°/16
15.	5-21	WS	20 WSW	1300-1318	
16.		Funnel	20 WSW	1320-1325	NQX-EYW (Key West): Reported funnels forming and dissipating
17.		Funnel	20 WSW	1325-1330	NQX
18.		Funnel	20 WSW	1331-1350	NQX
19		Funnel	15 WSW	1422-1431	
20.		Funnel	15 WSW	1425-1431	
21.		Funnel	15 WSW	1431-1441	
22.		Funnel	15 WSW	1442-1448	
23.		Funnel	15 WSW	1450-1453	
24.		WS	10 SW	1702-1708	Vicinity Sand Key
25.		WS	10 SW	1702-1708	Vicinity Sand Key
26.		WS	10 SW	1704-1708	Vicinity Sand Key
27.	5-22	Funnel	2 SE	0817-0825	NQX: Funnel S at 0825-0827
28.		WS	5 SE	1740-1750	
29.		WS	6 SSW	1800-1805	NQX: Funnel SW at 1802-1805
30.	5-23	WS	30 SSW	1018	Pirep: 204°/30 from NQX
31.		WS	4 E	1649-1652	NQX: WS S at 1649-1653
32.	5-24	Funnel	5 SE	1115-1122	
33.		Funnel	5 SE	1115-1122	
34.		WS	5 S	1127-1130	
35.		Funnel	2 S	1505-1509	
36.		Funnel	SE	1510-1522	
37.		Funnel	ESE	1510-1522	

Table 8. Continued

	Date	Event	Location (from NWS, Key West	Time (EST) (began-ended)	Remarks
38.		Funnel	SW	1515-1525	Observed six
39.		Funnel	SW	1520-1528	Photos taken
40.		WS	3 S	1523-1525	
41.		WS	12 E	1557	Public: 5 S of Sugarloaf at 090°/12
42.		WS	12 E	1557	Public: 5 S of Sugarloaf at 090°/12
43.		WS	12 E	1557	Public: 5 S of Sugarloaf at 090°/12
44.		WS	2 N	1858-1916	
45.		WS	2 N	1858-1947	
46.		WS	E	1858-1907	
47.		WS	W	1909-1916	
48.		WS	NW	1915-1930	
49.		WS	E	1916-1921	
50.		WS	WSW	1916-1922	
51.		WS	W	1920-1924	
52.		WS	WNW	1923-1926	
53.		WS	WNW	1924-1927	
54.	5-24	WS	WSW	1925-1931	
55.		WS	WNW	1927-1932	
56.		WS	WNW	1929-1939	
57.		WS	NW	1928-1938	
58.		WS	W	1931-1936	
59.		WS	W	1932-1937	
60.		WS	WNW	1940-1945	
61.		WS	WNW	1941-1946	
62.	5-25	WS	38 ENE	1627	Public: 3 N of MTH
63.		WS	E	1924-1931	NQX
64.		Funnel	18 E	1925	Public: Reported 2
65.	5-26	WS	8 WNW	0530-0552	
66.		WS	36 E	1550	Public: 1-2 SW of Sombrero Light

Table 8. Continued

	Date	Event	Location (from NWS, Key West	Time (EST) (began-ended)	Remarks
67.		Funnel	36 E	1550	Public: 1-2 SW of Sombrero Light
68.		Funnel	36 E	1550	Public: 1-2 SW of Sombrero Light
69.		WS	20 E	1554	Public: 10-12 W of MTH
70.		Funnel	20 E	1703	Public: 5 SE of Summerland
71.		Funnel	20 E	1703	Public: 5 SE of Summerland
72.		Funnel	20 E	1703	Public: 5 SE of Summerland
73.		Funnel	8 S	1843	Pirep: 10 SSW of NQX
74.	5-27	Funnel	5 S	0846-0905	
75.		Funnel	12 SE	0903-0910	
76.		Funnel	12 ENE	1014-1025	NQX
77.		Funnel	6 NW	1018-1025	
78.		WS	SW	1034-1107	NQX
79.		WS	5 WNW	1100-1105	NQX
80.		Funnel	15 ENE	1355-1402	NQX
81.	5-28	WS	25 SW	1609-1622	NQX
82.		WS	SW	1903	NQX: Pirep
83.	5-30	WS	13 E	1512	Public: S of Sugarloaf
84.		WS	15 E	1530-1545	Public
85.		Funnel	10 SW	1618-1624	NQX: Funnel E at 1550-1558
86.		Funnel	10 SW	1618-1624	
87.	5-31	WS	15 E	1030-1037	Public: 10 W of BPK (Big Pine Key)
88.		Funnel	25 E	1140-1150	Public: 5 E of BPK
89.		Funnel	2 N	1244-1245	NQX: (5 W)
90.		Funnel	9 SE	1352-1353	NQX: (10 S)
91.	6-1	WS	2 NW	1803	Public: Passed over NQX pier
92.	6-2	WS	35 #N#	0130	Pirep: (Delayed) 10 N of MTH
93.		WS	5 SW	1058	USCG (U. S. Coast Guard)
94.		WS	5 SW	1100	Public: Reported 2
95.		Funnel	2 SE	1315-1317	

Table 8. Continued

	Date	Event	Location (from NWS, Key West	Time (EST) (began-ended)	Remarks
96.		WS	4 SSW	1437-1438	
97.		WS	4 SSW	1437-1438	
98.		Funnel	4 SSW	1441-1443	
99.	6-3	Funnel	6 WSW	1605-1624	
100.	6-4	WS	16 ESE	1115	Public
101.	6-6	WS	5 N	0611-0620	
102.		WS	N	0609-0621	NQX: Reported 2
103.	6-11	Funnel	7 NNE	0905-0909	NQX: WS 5 NW at 0905-0909
104.	6-12	WS	10 NNW	1759-1811	
105.		WS	15 WSW	1804	Public
106.		Funnel	8 SE	1904-1925	
107.		Funnel	10 SE	1904-1925	NQX: Funnel 8 SSW at 1912-1915
108.	6-17	WS	19 NE	1415-1435	Golden: 050°/19
109.		WS	19 NE	1415-1435	Golden: 050°/19
110.		WS	19 NE	1415-1435	Golden: 050°/19
111.		WS	20 E	1420-1425	Public
112.		WS	27 ENE	1455-1500	Golden
113.	6-18	WS	30 ENE	1442	Public: (Large)
114.	6-19	Funnel	2 NE	0543-0541	0541-0550 2 S & 2 SE (sighted at Clemon's home)
115.		Funnel	7 NW	1026-1029	
116.		WS	6 NW	1055-1120	Public
117.		WS	7 NW	1114-1130	Reported as funnel at 1114-1123
118.	6-19	WS	7 NNW	1131-1140	
119.		WS	E	1320	Public: Long Key
120.		WS	7 WNW	1534-1550	
121.		WS	20 NE	1534-1535	Public
122.		WS	7 NW	1535	Golden
123.		WS	7 NW	1535-1609	Golden
124.		WS	7 NW	1545-1555	Golden
125.		WS	20 NE	1600-1604	Public

Table 8. Continued

	Date	Event	Location (from NWS, Key West	Time (EST) (began-ended)	Remarks
126.		WS	7 NW	1604-1609	Golden
127.		WS	7 NW	1604-1609	Golden
128.		WS	10 NNE	1605	Public
129.		WS	7 N	1623-1636	
130.		WS	18 ENE	1645-1650	Public
131.		WS	20 E	1703-1723	
132.		WS	15 NE	1715	Pirep
133.	6-21	Funnel	N	1820-1823	NQX
134.	6-22	WS	22 NE	1209-1217	Large
135.		WS	8 NE	1736-1740	Funnel continued until 1754
136.		WS	15 NE	1735-1740	Observed at Clemon's home
137.		WS	10 NE	1738-1742	Observed at Clemon's home
138.		WS	15 NE	1738-1743	Observed at Clemon's home
139.		WS	7 NE	1748-1753	Observed at Clemon's home at 1750-1755
140.		Funnel	2 SE	1805-1810	Observed at Clemon's home
141.		WS	3 SW	1812-1818	Observed at Clemon's home
142.	6-23	WS	3 SW	1230-1235	USCG: 4 NE of MTH
143.		WS	30 WSW	1300	Pirep: (Golden)
144.	6-25	Funnel	7 NE	1303-1318	NQX: Funnel NE at 1310-1317
145.	6-26	WS	16 NW	0620-0627	
146.		Funnel	5 NW	1807-1819	
147.		WS	5 NW	1807-1819	
148.		WS	3 NE	1815-1820	NQX: WS 3 NW at 1815-1820
149.	6-27	WS	5 SE	0618-1626	NQX: Funnel 5 S at 0615-0625
150.		WS	6 SSE	0618-0626	
151.		WS	20 SSE	0858-0905	Pirep: Visual at station EYW
152.		WS	9 SE	0858-0910	NQX: WS 7 S at 0858-0910
153.		WS	5 E	1132	Reported by Clemons
154.		WS	9 SE	1329-1333	NQX: WS 5 SSE at 1329-1338

Table 8. Continued

	Date	Event	Location (from NWS, Key West	Time (EST) (began-ended)	Remarks
155.	6-28	Funnel	2 NW	1128-1130	
156.		WS	40 NE	1145	Pirep: 5 to 10 N of MTH
157.		WS	25 NE	1200	Public
158.	6-29	Funnel	10 N	1241-1248	
159.		WS	10 NNW	1306-1314	NQX: WS 9 NNW at 1306-1329
160.		WS	11 NW	1314-1320	
161.		WS	7 N	1519-1525	NQX: Funnel 8 NWWS at 1512-1525
162.	6-30	WS	4 WNW	1135	Pirep: 8 W of NQX
163.		WS	30 NE	1328-1333	Golden
164.		WS	40 NE	1333	USCG: 5 N of MTH
165.		WS	60 WSW	1621-1635	Golden: Dry Tortugas area
166.		WS	50 WSW	1701	Golden: Dry Tortugas area
167.		WS	50 WSW	1701	Golden: Dry Tortugas area
168.		WS	50 WSW	1701	Golden: Dry Tortugas area
169.		WS	55 WSW	1710	Golden: Dry Tortugas area
170.		WS	55 WSW	1710	Golden: Dry Tortugas area
171.		WS	55 WSW	1720	Golden: Dry Tortugas area
172.		WS	55 WSW	1720	Golden: Dry Tortugas area
173.		Funnel	8 W	1806-1813	
174.		Funnel	10 W	1806-1813	
175.		Funnel	5 SSW	1813-1820	
176.		Funnel	5 SSW	1813-1820	
177.		WS	2 SE	1822-1826	NQX: Funnel SW at 1824-1826
178.	7-2	Funnel	30 ESE	1515-1520	Public: Small
179.		WS	35 N	1628	USCG: Near Pulaski Light
180.	7-3	WS	8 NE	1841-1900	NWX: Funnel 4 N at 1850-1855
181.	7-4	Funnel	20 NE	1057-1104	Public: 4 WNW of BPK
182.	7-6	Funnel	25 NE	0950-1000	Public: 15 N of BPK
183.		Funnel	5 NW	1250-1254	
184.		Funnel	35 SE	1424	Pirep: 30 SE of NQX
185.		WS	14 W	1814	USCG: Large-near Boca Grande

Table 8. Continued

	Date	Event	Location (from NWS, Key West	Time (EST) (began-ended)	Remarks
186.	7-7	WS	23 E	0800-0815	Public
187.		Funnel	5 NNE	1230-1245	
188.		WS	9 NNW	1303-1320	
189.		WS	10 N	1336-1345	
190.		WS	20 W	1551-1556	Golden
191.		WS	25 W	1601-1610	Golden
192.		WS	25 W	1605-1610	Golden
193.	7-7	WS	30 W	1614-1618	Golden
194.		WS	30 W	1614-1618	Golden
195.		WS	40 W	1622-1625	Golden
196.		Funnel	6 NE	1836-1839	NQX: 2 N
197.	7-8	Funnel	4 S	0545-0552	
198.		WS	20 ENE	0748	Public
199.		WS	20 ENE	0748	Public
200.		Funnel	7 ESE	0807-0815	
201.		WS	8 W	1349-1404	
202.		WS	8 W	1349-1404	Public: 2 S of Little Torch Key
203.	7-12	WS	22 E	1720	
204.	7-14	Funnel	22 ESE	1845-1850	Public: 10 S of BPK
205.	7-17	WS	12 N	1307-1324	NQX: WS NW at 1315-1320
206.	7-24	Funnel	20 E	0933-0950	Public: 3 SW of BPK
207.	7-25	WS	3 ENE	0715-0731	
208.		WS	5 NNE	0943-0951	
209.	7-28	WS	8 ENE	1819-1822	
210.	7-29	WS	11 SE	0720-0725	NQX: 8 SE
211.	8-1	WS	15 E	1114	Public
212.		WS	15 E	1114	Public
213.	8-2	WS	13 NE	1014-1019	NQX: 10 NE
214.		Funnel	5 NE	1016-1024	
215.		WS	15 W	1114	Pirep: 4 SE of Marquesas

Table 8. Continued

	Date	Event	Location (from NWS, Key West	Time (EST) (began-ended)	Remarks
216.		WS	15 W	1114	Pirep: 4 SE of Marquesas
217.	8-5	WS	7 E	0712-0715	
218.		WS	36 E	1439	USCG
219.	8-6	WS	4 NNE	1732-1738	NQX: 3 NW
220.	8-7	WS	5 W	1815	Pirep
221.		Funnel	5 NNE	1820-1825	NQX: Funnel 3 NNW at 1819-1858
222.		Funnel	6 N	1820-1825	NQX: Funnel 3 NNW at 1820-1823
223.		WS	7 NW	1828-1910	
224.		WS	5 NW	1837-1849	NQX: WS 4 NW at 1834-1855
225.		WS	5 NW	1837-1849	NQX: WS NW at 1836-1902
226.		WS	4 NW	1912-1922	
227.	8-11	Funnel	15 NE	1630-1632	Public
228.		WS	22 ENE	1715-1718	
229.		WS	22 ENE	1717-1719	
230.		Funnel	15 NE	1725-1730	Public
231.		Funnel	15 NE	1725-1730	Public
232.		WS	15 NE	1800	Public
233.		WS	10 NNE	1805-1811	
234.		WS	22 ENE	1808-1811	
235.	8-12	WS	5 W	0550-0603	
236.		WS	18 NW	1552-1616	NQX: WS NW at 1600-1617
237.		WS	15 W	1600-1620	USCG: Large
238.		WS	18 NW	1612-1617	
239.		WS	18 NW	1619-1635	
240.		Funnel	2 E	1743-1810	
241.	8-13	WS	5 SE	1031-1047	Pirep: 180°/6 from NQX at 1032-1037; NQX:Funnel 5 SW at 1029-1045
242.		WS	5 SE	1038-1040	Pirep
243.	8-14	WS	25 NE	1000	Public: 15 N of BPK
244.		WS	25 NE	1000	Public: 15 N of BPK
245.		WS	18 ENE	1005-1017	Public: Large

Table 8. Continued

	Date	Event	Location (from NWS, Key West	Time (EST) (began-ended)	Remarks
246.		WS	21 ENE	1008-1012	Pirep: 1010-1014
247.		WS	15 ENE	1010-1020	Public
248.	8-19	WS	18 N	1238-1250	
249.	8-23	Funnel	25 E	0715-0720	Public: S of BPK (089/25)
250.		Funnel	25 E	0715-0720	Public: S of BPK (089/25)
251.		Funnel	25 E	0715-0720	Public: S of BPK (089/25)
252.		Funnel	8 WNW	1701-1705	
253.		Funnel	8 WNW	1701-1705	
254.		Funnel	8 WNW	1701-1705	
255.		Funnel	25 ENE	1730	Public: 5 NNE of BPK
256.		Funnel	24 NE	1730	Public: 5 N of BPK
257.		Funnel	20 NE	1730	Public: 5 NW of BPK
258.	8-24	WS	10 S	1148-1205	
259.		WS	7 NW	1408-1420	
260.		WS	7 NW	1408-1420	
261.		WS	22 E	1610-1625	Public
262.		WS	23 E	1800-1830	
263.	8-25	WS	22 ENE	1610-1620	Public
264.		WS	28 ENE	1635-1640	Public & Pirep
265.		WS	40 ENE	1635-1645	USCG & Public
266.		WS	40 ENE	1637-1647	USCG & Public
267.		WS	35 NE	1640-1647	Pirep & Public
268.		WS	40 ENE	1641-1645	Public
269.	8-26	WS	5 SE	0713-0722	NQX: WS SW at 0714-0723
270.		WS	6 SW	0713-0715	
271.		WS	8 SW	0720-0728	
272.		WS	14 SW	0756	Pirep: 250°/14
273.		WS	14 SW	0756	Pirep: 250°/14
274.		WS	6 NNW	1011-1025	
275.		WS	7 NNW	1011-1025	

Table 8. Continued

	Date	Event	Location (from NWS, Key West	Time (EST) (began-ended)	Remarks
276.		WS	8 NW	1011-1025	
277.		WS	18 E	1052-1100	Public
278.		WS	24 NE	1116	Public: NNE of BPK
279.		WS	24 NE	1116	Public: NNE of BPK
280.		WS	20 E	1116	Public: NNE of BPK
281.		WS	20 E	1152-1159	Public
282.		WS	20 E	1208-1215	
283.		WS	5 WSW	1354-1401	
284.		WS	21 W	1434-1435	Golden: Funnel cld.-weak surface spot observed
285.		WS	22 WSW	1443-1457	Golden: Funnel cld. & small vortex (spiral and dark spot, spray ring; RW + nearby)
286.		WS	22 WSW	1504-1509	Golden: Spray vortex, no funnel cld. observed (small)
287.		WS	24 W	1550-1558	Golden: Funnel cld. & surface vortex (spiral first)
288.		WS	24 W	1559-1604	Golden: Well-developed funnel & surface vortex
289.		WS	24 W	1604-1613	Golden: Long, narrow funnel & surface vortex (spiral & dark spot; large with surface eye; accidentally penetrated at 700 ft)
290.	8-27	WS	18 NW	1123-1136	Pirep: 328°/18
291.	8-28	WS	11 ESE	0758-0802	
292.		WS	21 WNW	1030-1040	Golden: Small well-developed funnel & surface vortex (spiral with dark spot in shear band first)
293.	8-28	WS	4 W	1135-1140	EYW-TWR (tower)
294.	8-29	WS	2 S	1412-1420	Golden: WS 2 S of NQX at 1415-1420; NQX: Funnel 5 W at 1417-1419; well-developed funnel & surface vortex at a distance (moderate jolt when aircraft overflew it after demise)

Table 8. Continued

	Date	Event	Location (from NWS, Key West	Time (EST) (began-ended)	Remarks
295.		WS	5 SW	1443-1447	Golden: Funnel cld. & surface vortex (eye, large values dw/dz)
296.		Funnel	6 E	1758-1807	NQX: 3 SE
297.		Funnel	5 E	1758-1807	NQX: 3 SSE
298.		Funnel	4 S	1758-1807	NQX: 2 S
299.		Funnel	4 S	1758-1807	NQX: 2 S
300.		WS	2 ESE	1801-1811	NQX: Funnel 2 SW at 1758-1807
301.	9-4	WS	25 W	1437-1447	Golden: Brief funnel & surface vortex (large eye, spout 24-29 embedded in hollow cylinder in RW+)
302.		WS	20 W	1503-1518	Golden: Large anticyclonic (AC) waterspout-tornadic intensity (from 2-3 dark spots initially)
303.		WS	44 WNW	1532-1535	Golden: Funnel cloud only
304.		WS	44 WNW	1535-1536	Golden: Half-extended funnel at a distance in RW
305.		WS	44 WNW	1536-1540	Golden: Large funnel cloud 1/3 way down from base with small sfc. vortex (large dark spot initially)
306.		Funnel	49 WNW	1550-1552	Golden: Nearly horizontal fnl. cld., no sfc. vortex
307.	9-5	WS	5 W	1037-1045	Golden: Funnel cloud & surface vortex, dark spot, brief spray
308.		WS	4 W	1055-1101	Golden: WS 7 W at 1052-1053; dark spot only moving W
309.		WS	7 W	1117-1121	Golden: Fnl. cld. & sfc. vortex, occasional spray
310.		WS	9 W	1127-1132	Golden: Fnl. cld. & sfc. vortex (small spiral)
311.		WS	8 W	1132-1135	Golden: WS 8 W at 1135; funnel cloud, no surface vortex (weak dark spot)

Table 8. Continued

	Date	Event	Location (from NWS, Key West	Time (EST) (began-ended)	Remarks
312.		Funnel	10 W	1142-1144	Golden: Funnel cloud only
313.		Funnel	10 W	1153-1155	Golden: Funnel cloud at a distance
314.		WS	12 W	1203-1208	Golden: Well-developed small funnel, with dark spot surface vortex
315.		WS	15 W	1215-1216	Golden: Funnel cloud and surface spot
316.		Funnel	12 E	1540-1554	Golden: Half-extended funnel at a distance
317.		WS	16 ENE	1553-1601	Golden: Funnel cloud & surface vortex (likely AC with AC spiral; between 2 RW + cells in long cloudline)
318.		WS	6 WNW	1640-1649	Golden: Funnel cloud & surface vortex
319.		WS	6 WNW	1640-1647	Golden: Surface 'eddy'; no funnel cloud observed (dark spot, spray ring)
320.	9-6	WS	45 E	1445	Public: S at Key Colony Beach
321.		Funnel	5 SSE	1513-1514	
322.	9-7	Funnel	40 E	1350	Public: S of MTH
323.		Funnel	40 E	1350	Public: S of MTH
324.		Funnel	40 E	1350	Public: S of MTH
325.		WS	4 S	1549-1613	
326.		WS	10 SE	1632-1650	
327.		WS	14 SW	1636-1645	
328.		WS	13 NW	1748-1801	
329.	9-8	WS	3 S	1223-1227	Golden: Funnel cloud & surface spot (eddy decays)
330.		WS	5 S	1330-1338	Golden: Funnel cloud & surface vortex (from 2 dark spots, no shower initially)
331.		WS	3 SE	1333-1340	NQX: Funnel 8 S at 1335-1358
332.		WS	4 SE	1333-1340	

Table 8. Continued

	Date	Event	Location (from NWS, Key West	Time (EST) (began-ended)	Remarks
333.		WS	4 SE	1333-1340	Golden: WS 5 S of NQX at 1335-1400; Small well-developed funnel and surface vortex (dark spot; at end, spiral surrounded by heavy showers)
334.		WS	10 SE	1340-1401	NQX: WS 8 S at 1345-1355; Golden: WS 10 SE of NQX at 1358-1359; fully extended funnel at a distance
335.	9-9	Funnel	9 E	1018-1022	NQX: 5 E
336.		Funnel	8 ENE	1024-1038	
337.		Funnel	8 E	1055-1100	Golden: Funnel cloud observed at a distance
338.		WS	27 ENE	1300-1310	Public
339.		WS	6 ENE	1307-1317	Golden: WS 2 ENE of NQX at 1307-1316; small funnel & surface vortex (released colored balloons within 50 ft of cloud)
340.	9-10	WS	14 N	1020-1027	Golden: Funnel cloud at a distance
341.		WS	14 N	1035-1041	Golden: Wide, short funnel cloud & surface spot (gradually expanded and weakened)
342.		WS	14 N	1059-1114	Golden: WS 10 N of NQX at 1045-1113; NQX: WS 8 N at 1103-1111; large waterspout (largest with eye, double-walled, large initial spiral)
343.	9-11	WS	7 NW	0642-0656	
344.		WS	22 W	1230-1243	Golden: Funnel cloud & AC surface vortex, v-shaped wave train (from dark spot with very narrow funnel)
345.		Vortex	22 W	1240-1243	Golden: Surface vortex, no funnel observed
346.		WS	23 W	1253-1300	Golden: Funnel cloud & weak surface vortex (large dark spot eddy, brief spray)

Table 8. Continued

	Date	Event	Location (from NWS, Key West	Time (EST) (began-ended)	Remarks
347.		Funnel	6 E	1334-1337	Golden: Fully extended funnel at a distance
348.	9-14	WS	5 NW	1054-1124	
349.		WS	8 NW	1054-1124	
350.		Funnel	5 N	1100-1108	NQX: Funnel 6 NW at 1100-1108
351.	9-16	WS	7 SE	1130-1138	Golden: 5 SSE of NWX; funnel cloud & surface spot (greatly tilted, RW + nearby)
352.		WS	5 NW	1350-1352	Golden: Funnel cloud at a distance
353.		WS	18 WNW	1357-1405	Golden: Funnel cloud & surface vortex
354.		WS	17 WNW	1422-1430	Golden: Small well-developed funnel & surface vortex (dark spot SW of RW+ initially)
355.		WS	5 N	1455-1502	Golden: Funnel cloud & surface spot, "cork-screw" funnel
356.	9-17	Funnel	19 W	1052-1054	Golden: Funnel cloud, no surface circ. observed
357.	9-23	Funnel	27 NE	1006-1010	Golden: Funnel cloud from single towering cumulus (TCU), from a distance
358.		WS	27 NE	1022-1026	Golden: Funnel cloud with dark spot on surface, no circulation
359.		WS	36 E	1104-1120	Golden: Funnel cloud & surface spot, waterspout AC
360.		Funnel	35 E	1109-1118	Golden: Short, narrow funnel cloud, no apparent surface circulation (possible spiral and dark spot with shower around edge)
361.		WS	36 E	1121-1123	Golden: Short, wide funnel cloud NW of RW, surface spot
362.		WS	37 E	1129-1151	Golden: Funnel cloud, with surface spot, full large spout
363.		WS	36 E	1153-1158	Golden: Funnel cloud, small surface spot (NW of RW+)
364.		WS	4 N	1224-1237	Golden: Narrow funnel with dark spot

Table 8. Continued

	Date	Event	Location (from NWS, Key West	Time (EST) (began-ended)	Remarks
365.		WS	4 N	1248-1256	Golden: Short, narrow funnel with good surface spot (flare showed counterclockwise (CCW) circulation around spot)
366.		WS	15 NNE	1352-1404	Golden: Double-wall funnel, broad CCW spray vortex (in progress)
367.		WS	26 NE	1628-1703	Golden: Short funnel with dark spot, intense AC spout, large eye, asymmetric wave train
368.		Funnel	26 NE	1657-1702	Golden: Short funnel, no surface circulation
369.		Funnel	15 NW	1725-	Golden: Well-developed funnel N of RW under large TCU
370.	9-24	WS	8 W	0900-0910	
371.		WS	6 W	0935-0950	
372.		WS	5 E	1015-1025	Golden: Fnl. 2 E of NQX at 1025-1027; contorted, short vertical fnl. in distance
373.		WS	1 SW	1146-1218	Golden: WS 2 SW of NQX at 1145-1258; NQX: Funnel SW at 1159-1204; well-formed funnel with surface spot-weak spout (CCQ); dark spot spiral
374.		WS	6 SW	1235-1308	Golden: WS 2 1/2 SW at 1155-1205; small funnel, weak CCW spout (with spiral and dark spot initially)
375.		WS	5 S	1235-1259	NQX: Funnel SW at 1259-1301
376.		WS	5 SSW	1235-1259	NQX: Funnel SW at 1259-1301
377.		WS	5 S	1235-1311	NQX: WS SW at 1301-1312
378.		WS	7 S	1311-1318	
379.		WS	8 SE	1341-1346	

Table 8. Continued

	Date	Event	Location (from NWS, Key West	Time (EST) (began-ended)	Remarks
380.		WS	10 SE	1416-1432	NQX: WS S at 1420-1433
381.		WS	9 SE	1429-1432	
382.		WS	E	1630	USCG: Plantation Key
383.		WS	E	1645	USCG: Plantation Key
384.		WS	5 SSE	1722-1737	NQX: WS S at 1730-1737
385.	9-26	WS	8 SW	0810	Public
386.	9-26	WS	8 SW	0810	Public
387.	9-27	Funnel	6 NW	1300-1305	
388.		WS	8 NW	1300-1325	Public: Large
389.	9-28	WS	33 ENE	1428-1442	Clemons
390.	9-29	Funnel	10 ENE	1522-1530	NQX
391.		Funnel	5 ENE	1524-1540	
392.	10-9	WS	13 S	1728-1735	Golden
393.		WS	12 S	1725-1737	Golden
394.		WS	11 S	1729-	Golden
395.		Funnel	12 S	1730-	Golden
396.		WS	9 S	1728-	Golden
397.		WS	13 SSE	1745-	Golden

APPENDIX B.

SUPPLEMENTARY RFF AIRCRAFT RESULTS, OCTOBER 9, 1969

Cloud mapping derived photogrammetrically from the RFF aircraft cloud film on October 9, 1969, for level 2 (fig. B-1) illustrated the major change from the level-1 cloud mapping (fig. 28); that is, moderate showers had started to fall, primarily from sheared overhanging cloud tops. The southern one-half of the cloudline during level-2 flight appeared to be evolving rapidly with rain on the forward edge. The waterspout at point -33.5, +4.15 in figure B-1 apparently evolved from the dark spot at point -32.5, +4.25 on the level-1 cloud mapping (compare with fig. 28).

RDR cloud-height topography for level 2 is given in figure B-2. These measurements were taken from 7 to 15 min after those for level 1. Reliable cloud-height analysis could be made for only the northern one-half of the cloudline because of "side-lobing" and other problems which occur when the RDR radar scans strong targets at very short range (Senn, 1971). Maximum cloud heights have grown to nearly 17,000 ft near the northern end of the cloudline--a rise of at least 3,000 ft in no more than 12 min. There was again an arc-shaped cloud-top ridge above 10,000 ft extending south-southeastward, with a new cloud tower rising to 17,200 ft near point -34.5, 1. Another sheared cloud tower has grown to over 13,000 ft on the southeastern end of the ridge, up from about 10,000 ft in the same region 7 min earlier. The pronounced east-northeast and northeast elongation of cloud-height contours around the two major cloud cells agreed with the shear vector indicated by the Boca Chica sounding and by aircraft winds through this layer.

Figure B-3 illustrates the correspondence between precipitation areas in the cloud mapping (fig. B-1) and radar echoes. When the Key West radar film (from which the tracings were made) is viewed in time lapse, protrusions on the major waterspout echo-complex and the echo centroid itself executed a cycloidal motion toward the southwest and south. During the 8 min of level-2 flight, an indentation and echo protrusion developed on the southeastern boundary of the waterspout echo complex. The waterspout is located in the central southern one-half of the main complex, and there is well-organized flow splitting through this region. The echo indentation-protrusion resembled the hook echo and associated funnel-cloud development over the NSSL mesonetwork studied by Lemon (1970). As in the level-1 analysis, the waterspout is found within a cloudline-scale cyclonic wave-perturbation which probably extends northwestward beyond the echo boundary. The southernmost echo had fragmented by this time.

Streamlines and isotachs for the renavigated level-2 (NNV) Doppler winds are shown in figure B-4. A 15-kt speed maximum merged with the waterspout circulation, and a smaller 15-kt speed maximum occurred to the north. Both anticyclonic shear and curvature existed south of the isotach minimum along the splitting streamflow.

The level-2 isotherm-streamline analysis (fig. B-5) reveals that the coldest air (21.0° to 21.5°C) generally lies beneath the cloud overhang in occasional moderate rainshowers, with a secondary cold pocket in the northwest section. The concentrated isotherm ribbon extending southward from this

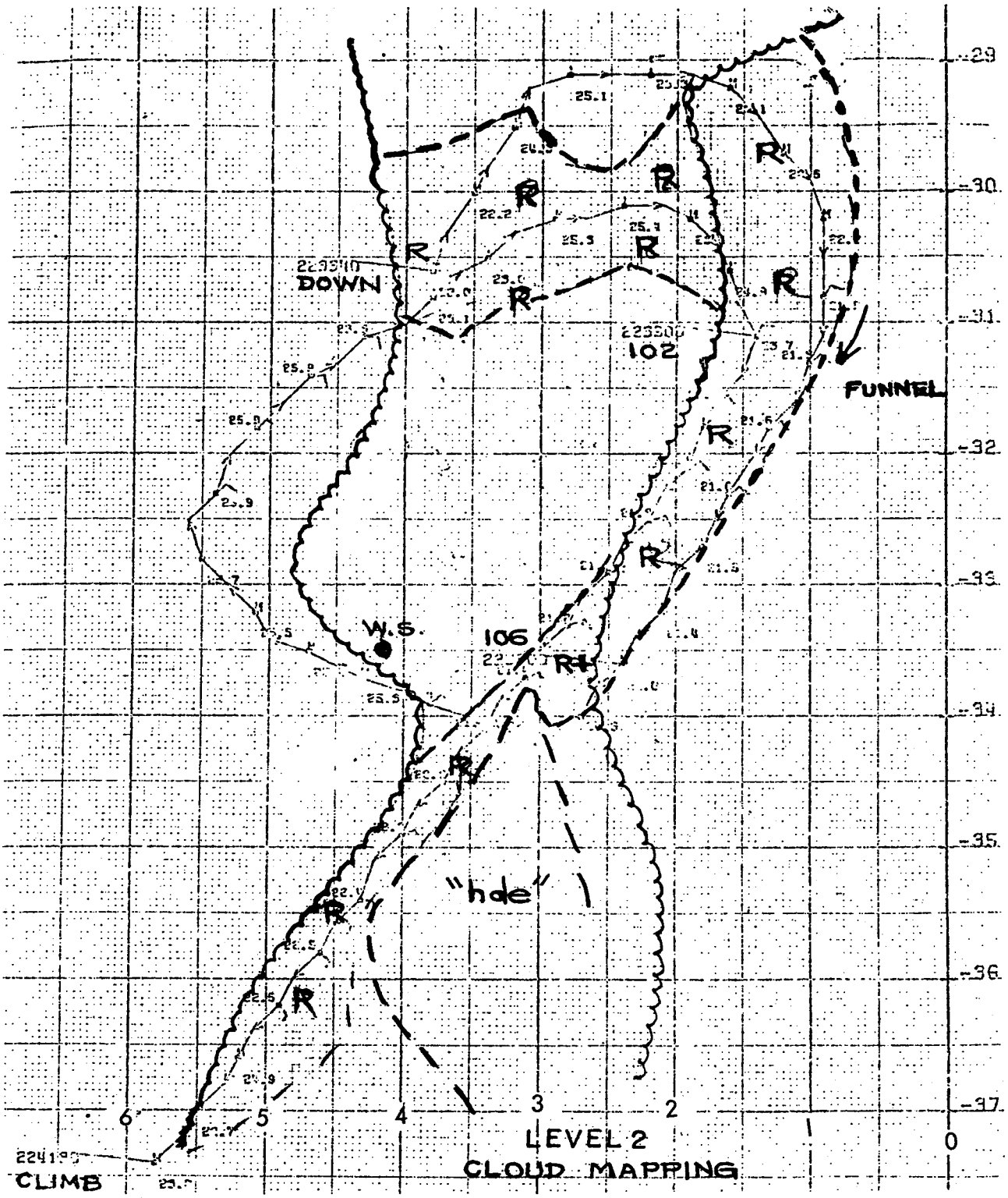

Figure B-1. Photogrammetric level-2 cloud mapping, with waterspout locations and rain areas. Aircraft radar altitude given in tens of feet by three-digit numbers. Mean aircraft altitude = 1,000 ft.

region (along the leading edge of the cloudline) is collocated with a developing line of towering cumuli subsequently found in the level-3 cloud mapping. The strongest temperature gradients are on the leading western boundary of the cloudline, and the waterspout is in the warmer air. The large temperature gradient in figure B-5 separates in a narrow cold tongue extending north-northeast to south-southwest through the southeastern portion of the waterspout echo complex and a warm pocket in the clear air east of the crescent echo boundary. (To investigate whether these thermal features may have been partly caused by wet-bulb effects in the Vortex Thermometer, the Rosemount temperatures were used to verify the results.) The total

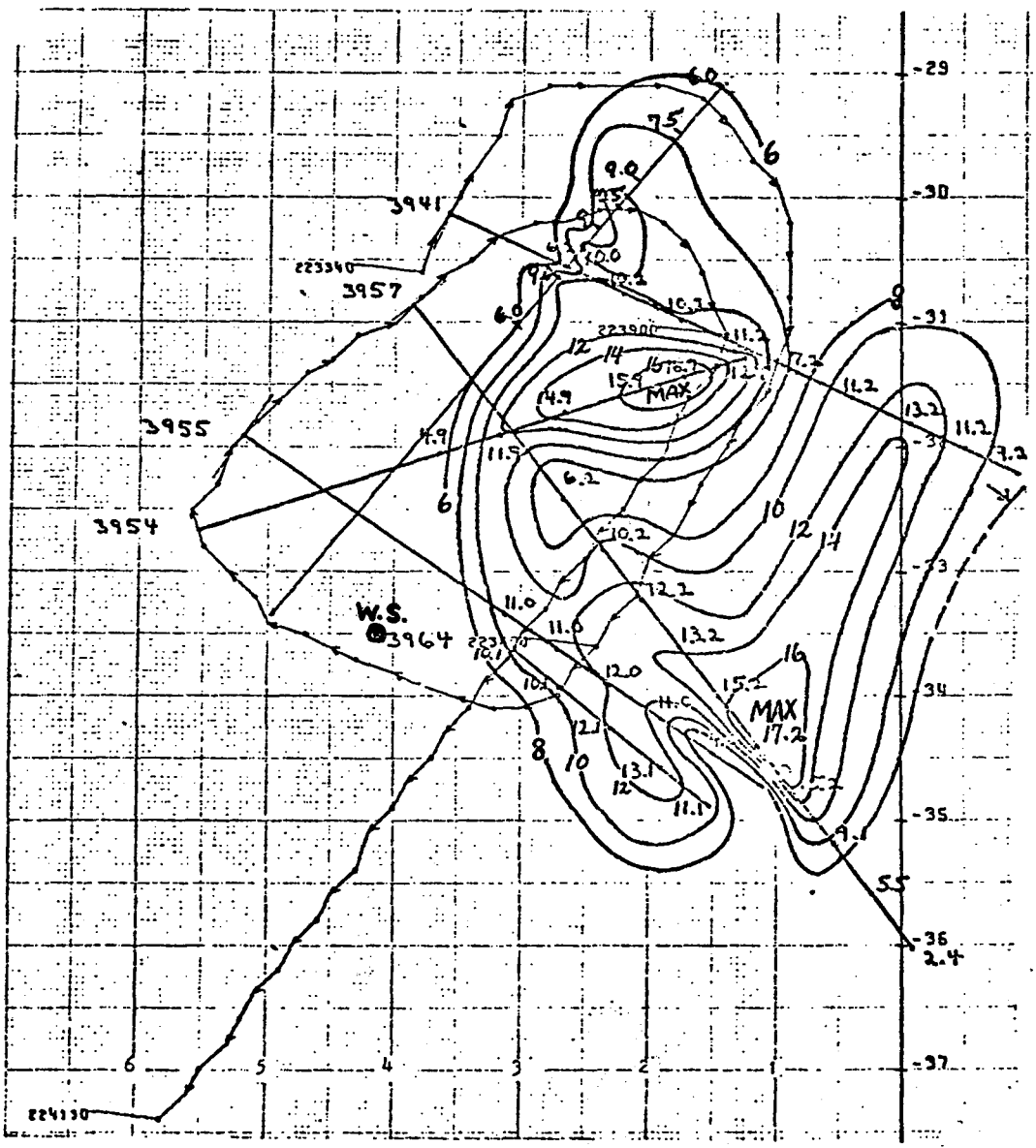

Figure B-2. Cloud-height contour mapping (units in thousands of feet) from digitized RDR radar frames on RFF flight. Level 2 data at 223340 to 224130 GMT.

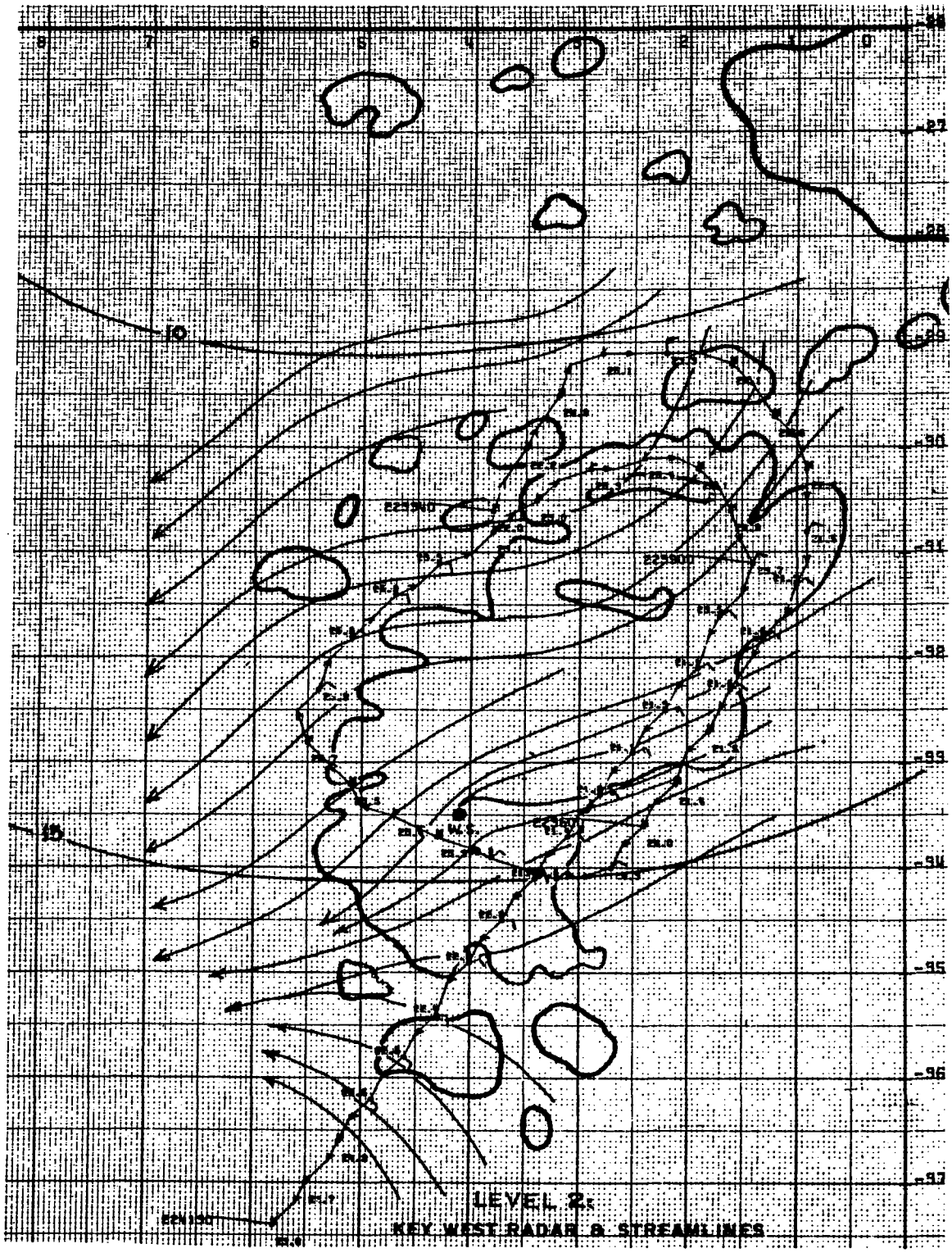

Figure B-3. Level-2 scaled tracing of Key West radar and superimposed streamlines from aircraft NNV-Doppler winds.

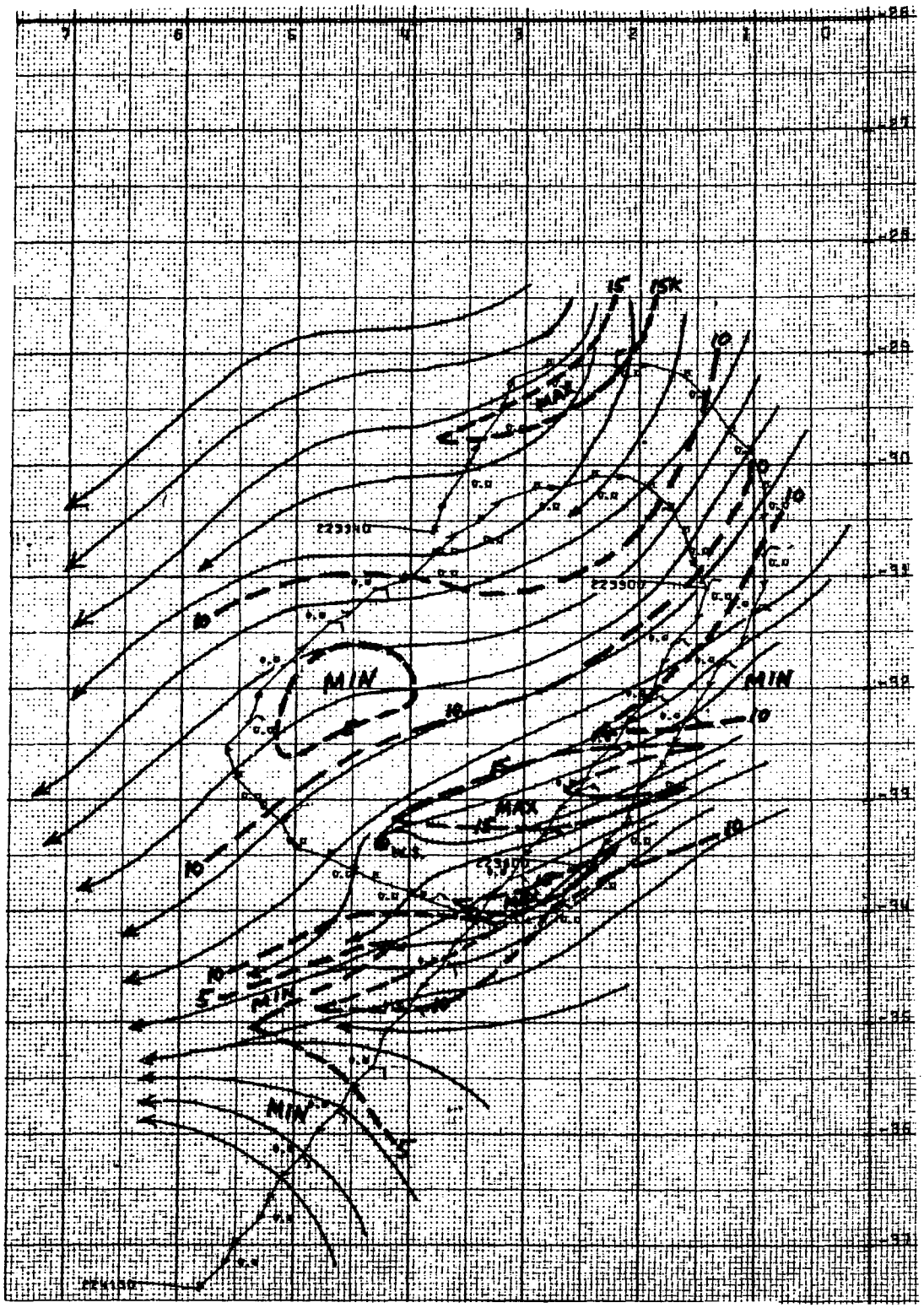

Figure B-4. Level-2 RFF-Doppler wind streamlines and isotachs.

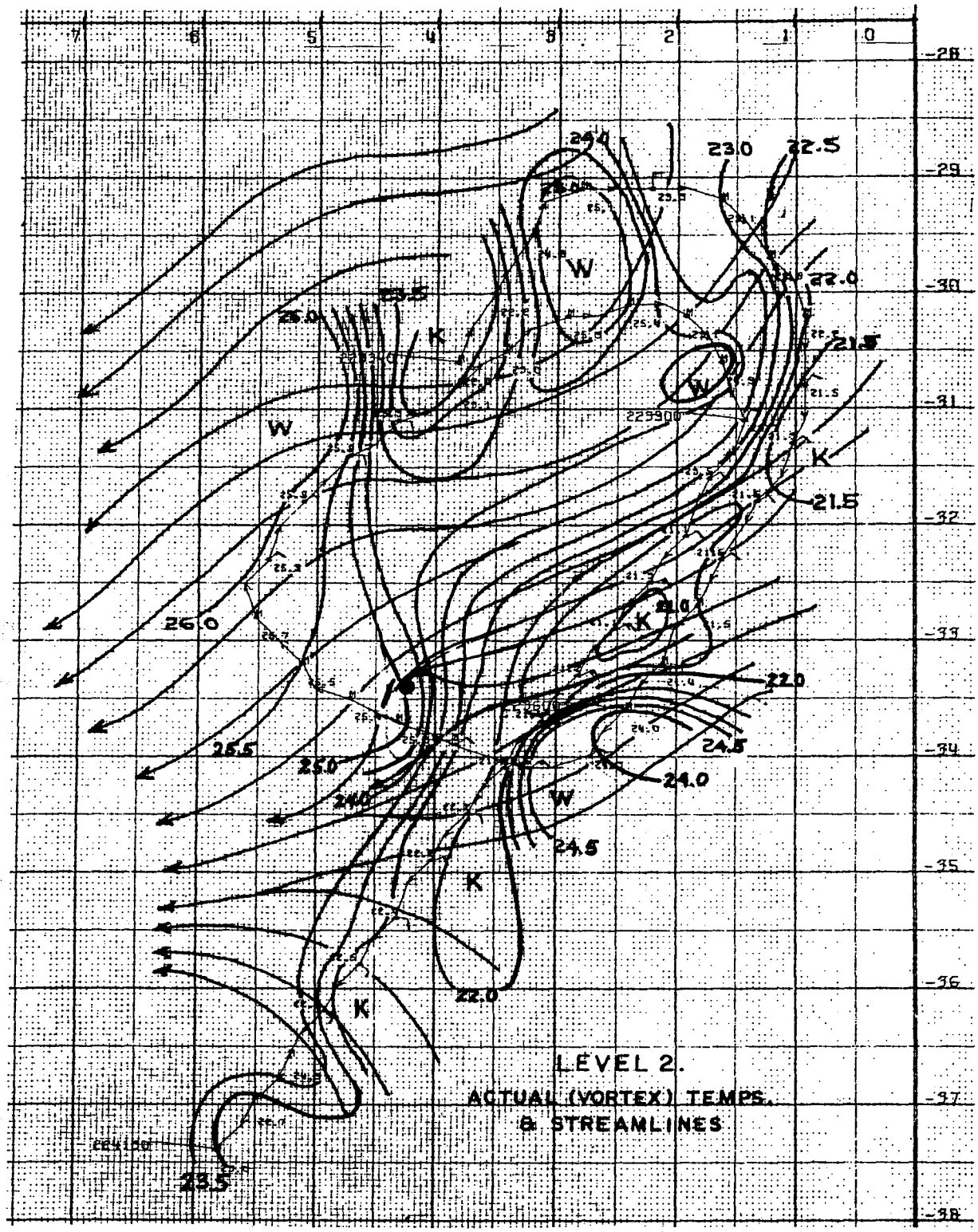

Figure B-5. Level-2 actual (Vortex) isotherms (0.5°C interval) and streamlines.

temperature variation was about 5°C. Maximum temperature gradients in the waterspout vicinity were 2.4°C/n mi, and the cold temperature advection in the region just upstream was 43°C/hr. All of these values are considerably larger than those computed for level 1 (fig. 32).

At level 2, the waterspout lies in a region of strong isohumal gradient (fig. B-6). Highest relative humidities are located in the precipitating

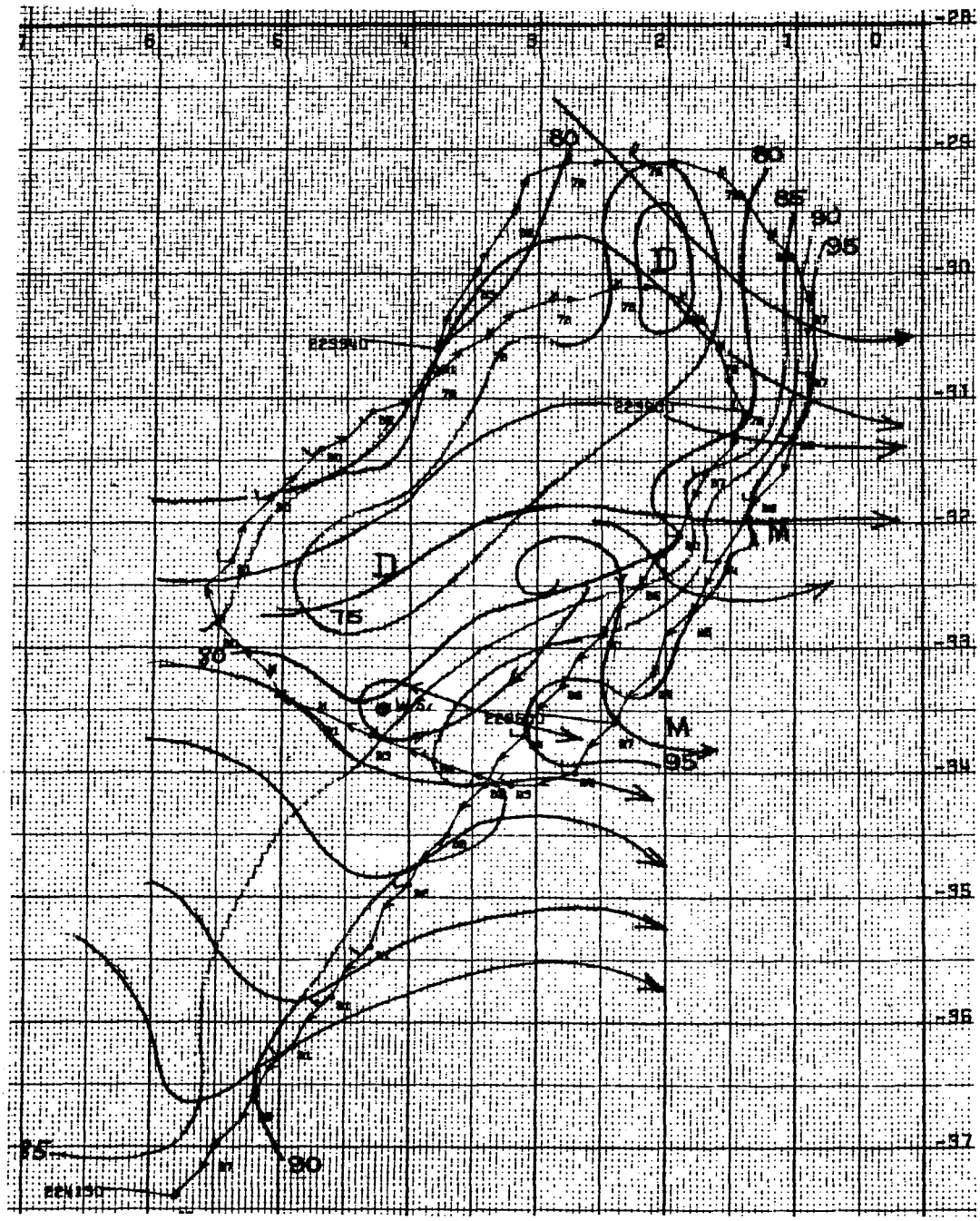

Figure B-6. Level-2 infrared relative humidity at intervals of 5 percent and relative streamlines (derived from Doppler winds and estimated waterspout movement).

eastern cloud overhang, with a pronounced dry tongue (70 to 75 percent) beneath the cloudline interior. Relative streamlines indicate splitting light westerly flow with a possible closed anticyclone and ridge north of the split. The waterspout is in a weak closed mesocyclone along the eastern cloudline flank.

The level-2 draft-scale vertical-motion pattern appears more broken (fig. B-7). Major rising motions (1 to 2 m/s) lie just inside the western edge of the cloudline. A small area of sinking (-2 m/s) is found in the clear air, with significant sinking (-1 to -2 m/s) through the precipitating

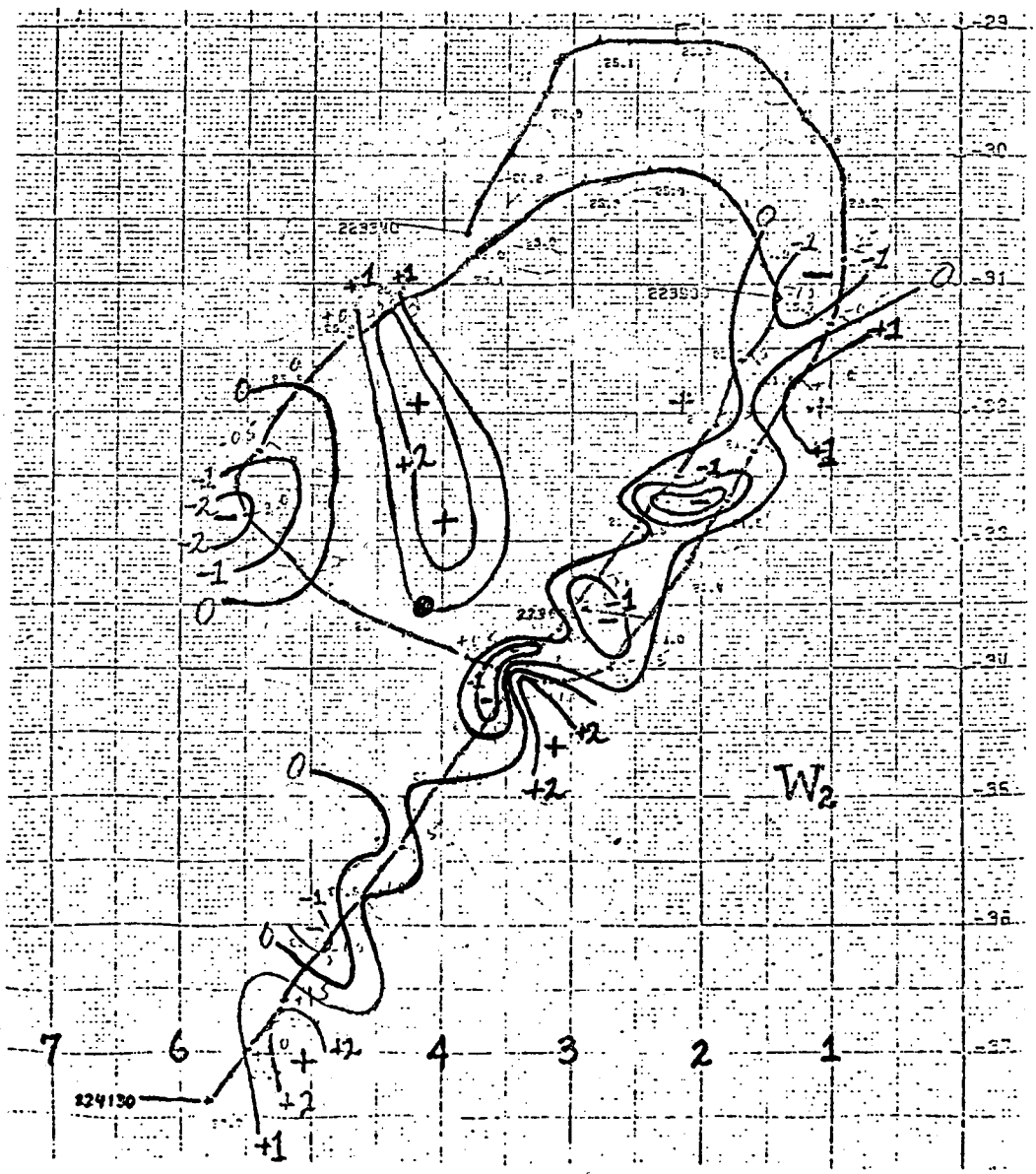

Figure B-7. Analysis of smoothed draft-scale vertical velocity field in units of meter per second for quasi-straight segments of level-2 flight track on October 9, 1969.

cloud overhang. The vertical motion pattern near the hooklike echo protrusion reveals an elliptically shaped tongue of -1 m/s sinking air just inside the crescent-echo boundary, while a +2 m/s rising-motion region extends into the echo protrusion. The horizontal gradients of vertical motion just inward from the crescent-shaped echo boundary are very large. This pattern resembles that found by Lemon (1970).

Cloud mapping for level 3 is shown in figure B-8. By this time (2242 to 2252 GMT), most of the cloudline was dissipating. Nearly continuous precipitation was encountered through the northern, northeastern, and southwestern (overhang) sections of the cloudline. The southern one-half had

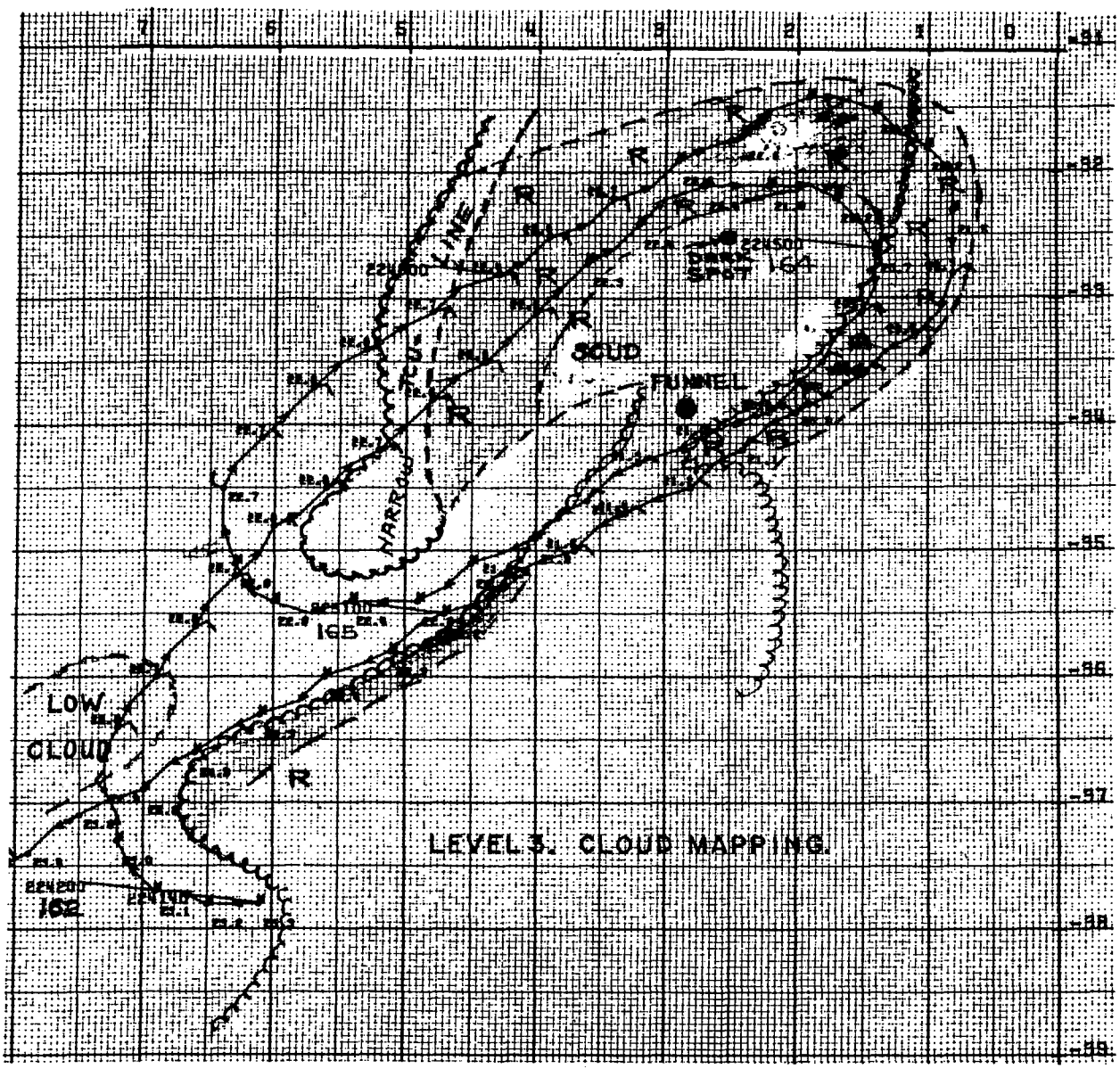

Figure B-8. Level-3 photogrammetric cloud mapping, with waterspout locations and rain areas. Three-digit numbers along flight track are altitude in tens of feet.

showers spreading along the forward boundaries of the line, and the northern one-half was decaying rapidly. A new funnel cloud and dark spot formed separately just inward from the precipitation boundaries. Most significant, a new sharply defined line of towering cumuli, oriented in a north-to-south arc, formed downwind of the decaying cells.

The cloud-height topography sequence (fig. 29, B-2, and B-9) shows rapid cloud growth during the first two aircraft loops, with cloud tops generally greatly sheared toward the east and northeast and the mature waterspouts on the downwind boundary. Between the last two loops, a region of extensive precipitation developed.

The largest draft-scale vertical motions are found in the level-3 aircraft data (see fig. B-10). The large funnel cloud and dark spot appeared to occur in a region of weak rising motions. Most of the split cloudline at

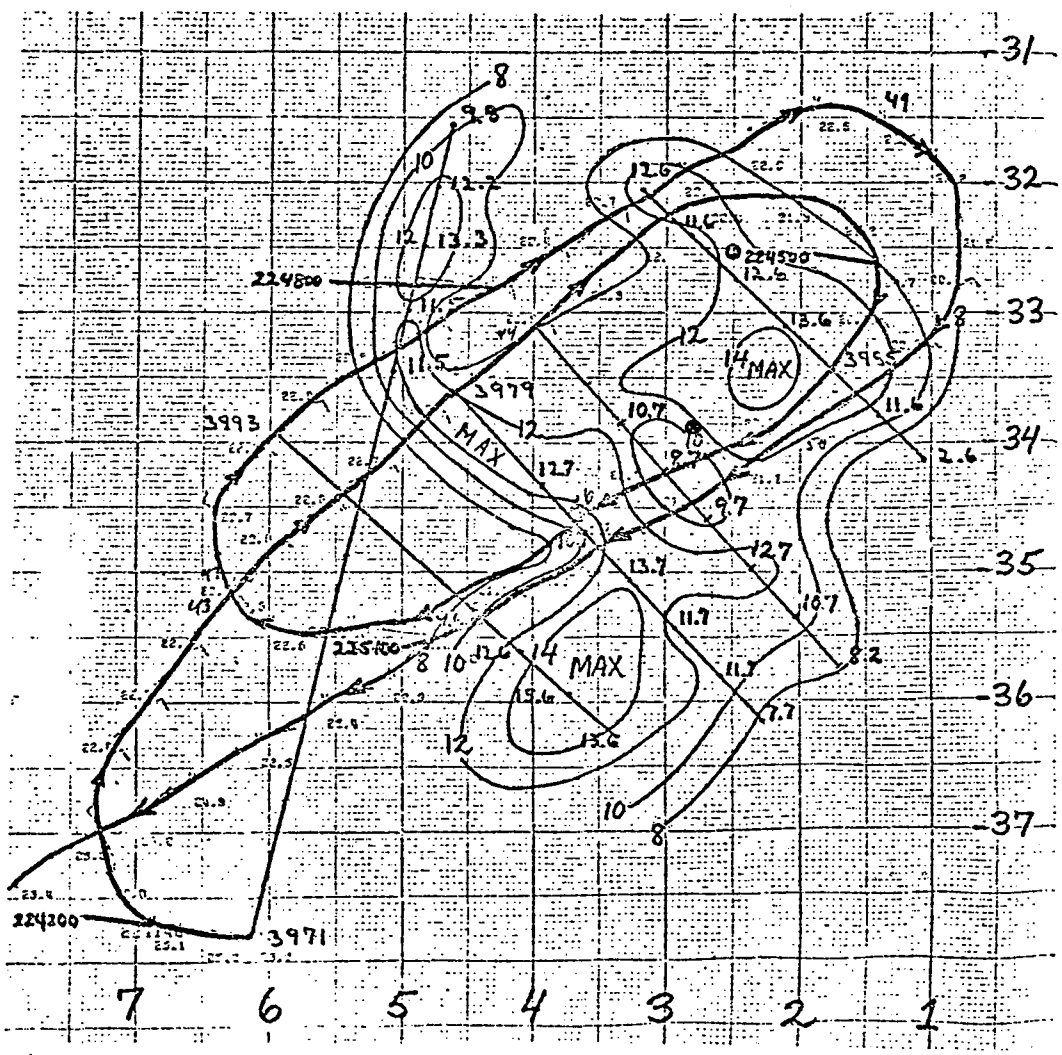

Figure B-9. Cloud-height contour mapping, units in thousands of feet, derived from digitized RDR radar film on RFF flight, October 9, 1969. Level 3 data with flight track superimposed.

this stage contained draft-scale sinking motions, with the strongest subsidence in the northeastern precipitating cloud overhang. The only region of organized, intense upward motion was in the developing towering cumuli.

The isohume analysis and relative flow for level 3 (fig. B-11) show that the large funnel is in a very moist trough. A secondary tongue of high relative humidity extends northwestward through the developing line of towering cumuli, with relative humidities as low as 70 percent. A pronounced ridge in the relative flow is oriented northeast-southwest through the precipitation region just east of the new line of towering cumuli. The wind analysis and its relation with the radar echo boundaries (fig. B-12) support the conclusion that the building line of towering cumuli in figure B-8 formed along the downwind boundary of the old shower outflow. A possible dark spot was located near the upstream end of a 15-kt isotach maximum in anticyclonic level-3 flow (fig. B-13).

Total temperature change was about 4.5°C, and the maximum temperature gradient in this region was 1.3°C/n mi (fig. B-14). The coldest air at this

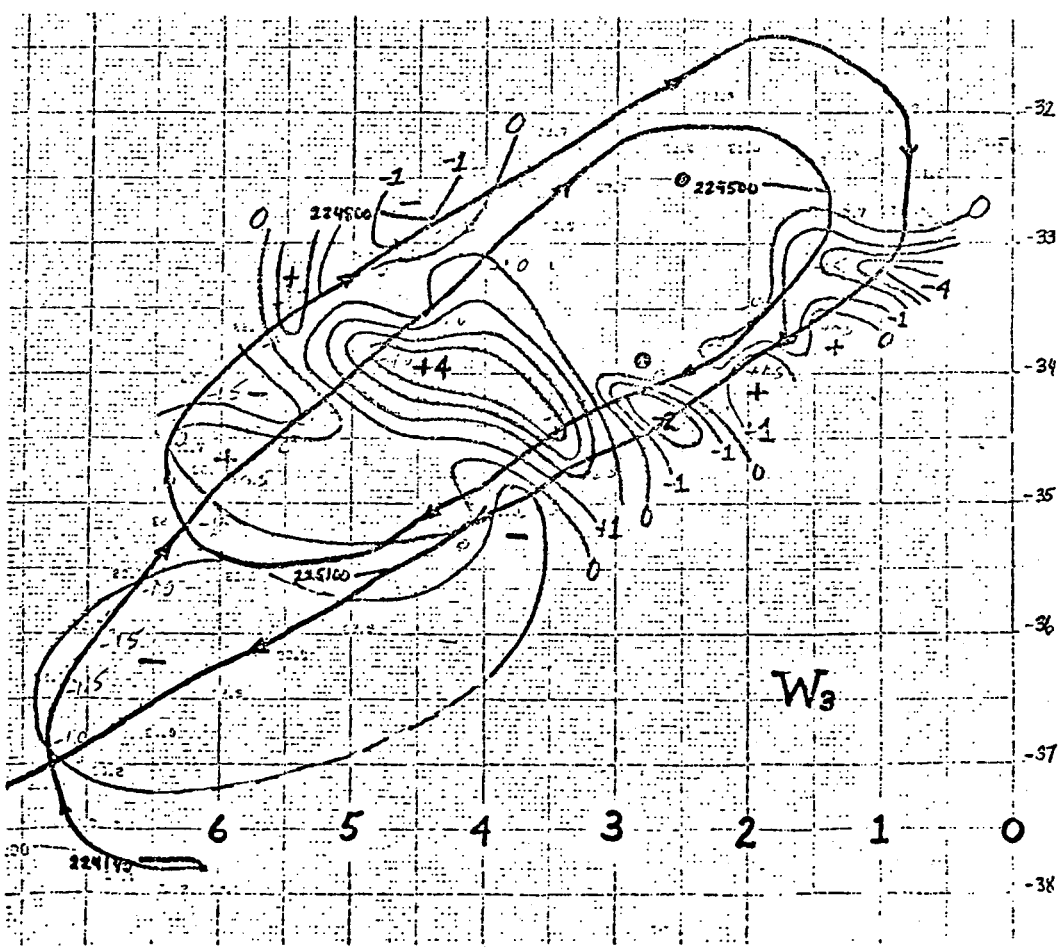

Figure B-10. Analysis of smoothed draft-scale vertical velocity field in units of meters per second for quasi-straight segments of level-3 flight track, October 9, 1969.

level (20.5°C) was just outside the eastern cloudline boundary in figure B-12, beneath the precipitating cloud-top overhang. Unlike locations at the lower levels, the waterspout funnel was found near the core of the cold tongue, with the maximum temperature gradient downstream. Most important, the (cold) temperature advection into newly developing cumuli in figure B-12 was about 7.7°C/hr. Finally, there was divergent flow of the cold air away from the funnel and strong speed convergence along the forward edge of the developing towering cumuli.

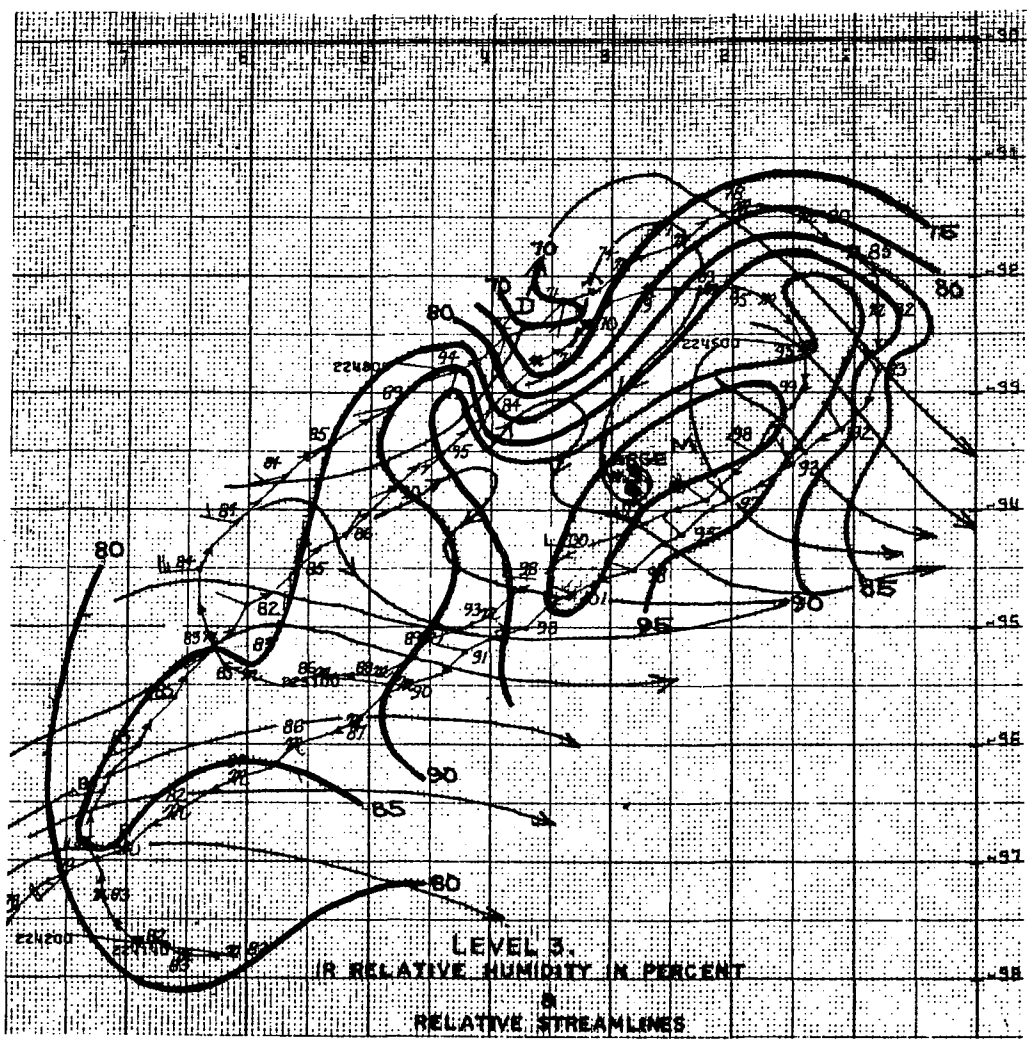

Figure B-11. Level-3 infrared relative humidity (isohumes at intervals of 5 percent) and relative streamlines (derived from Doppler winds and estimated motion of large waterspout).

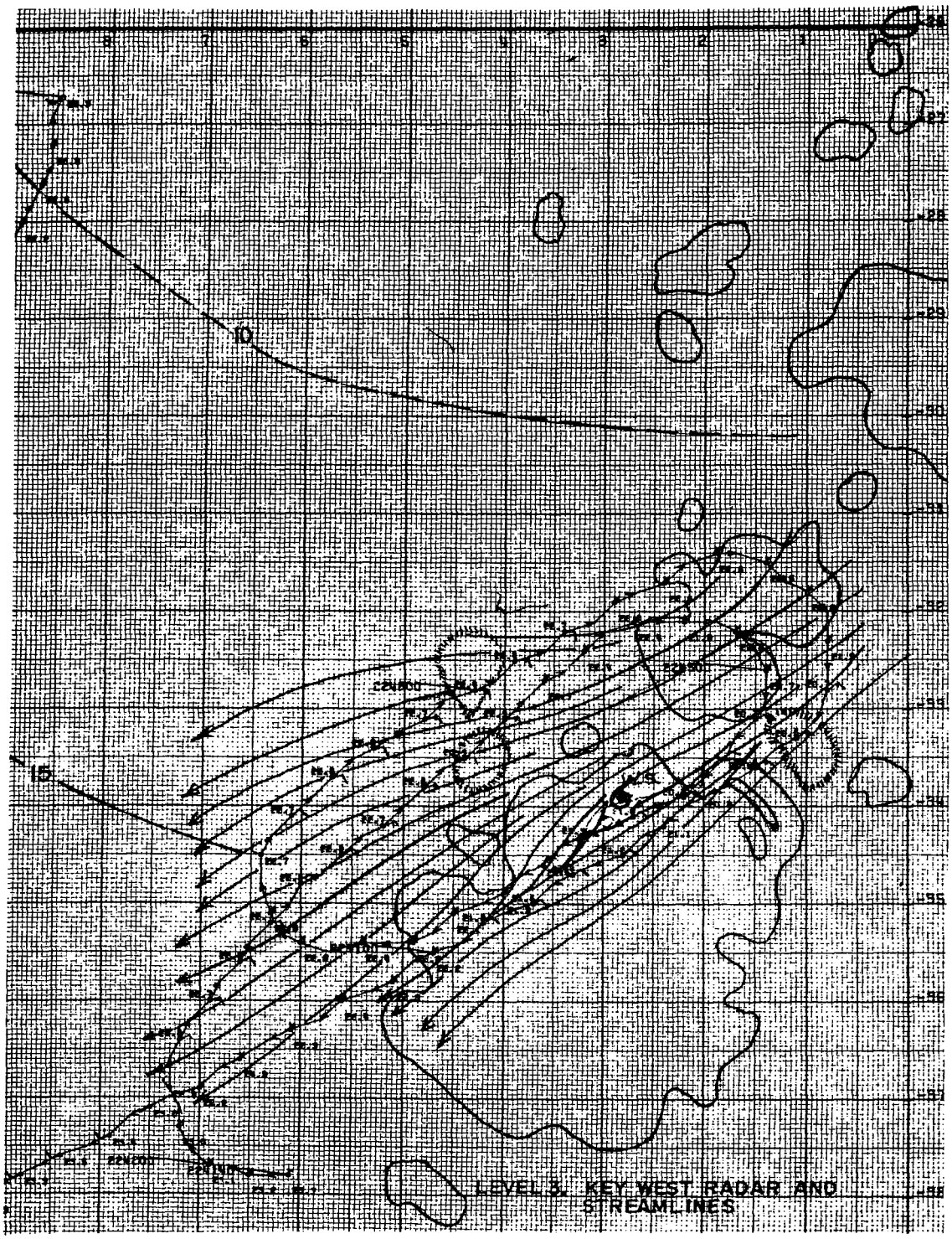

Figure B-12. Level-3 scaled tracing of Key West WSR-57 radar echoes with superimposed streamlines from aircraft Doppler winds. Stippled echoes appeared weak and decaying.

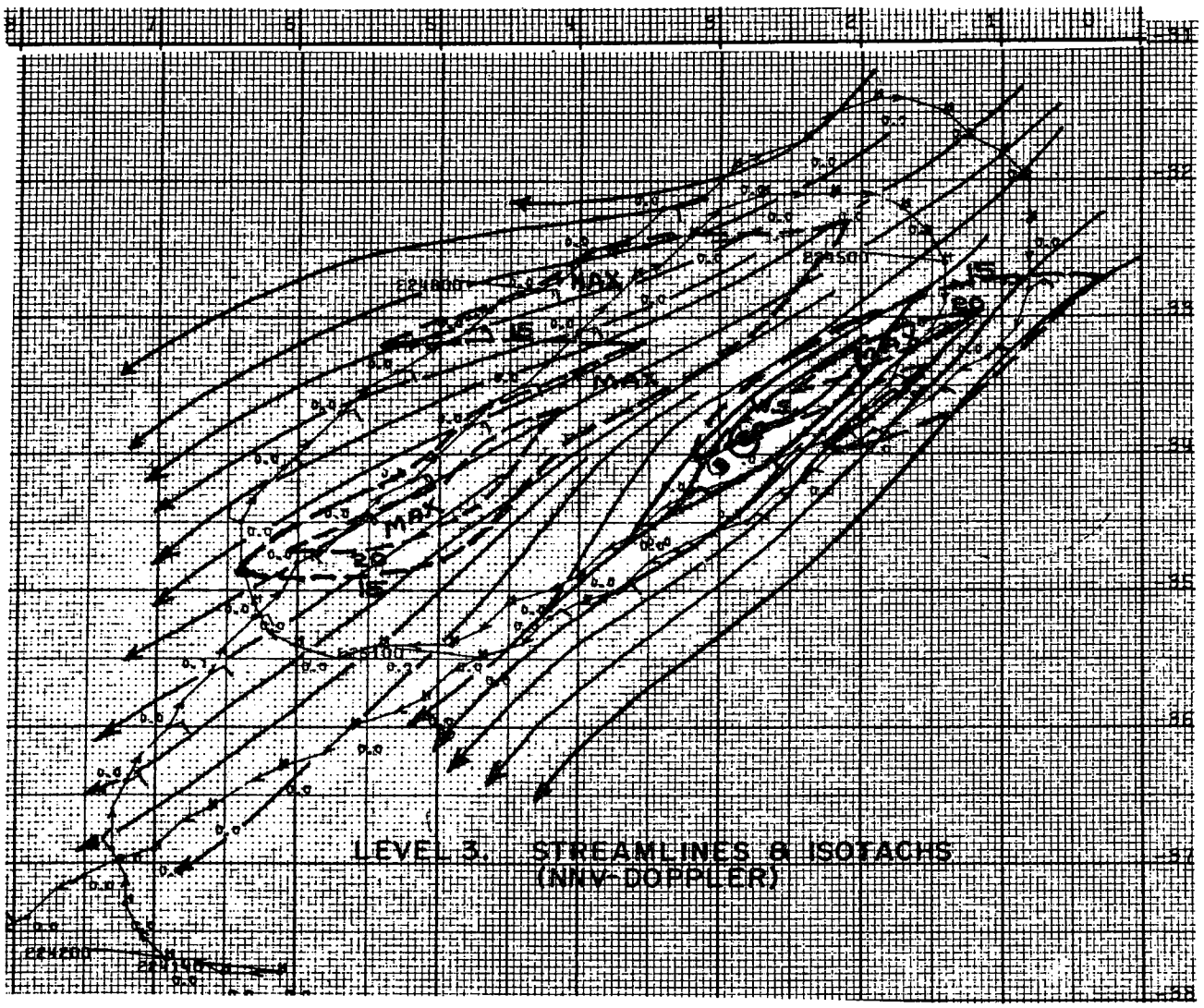

Figure B-13. Level-3 RFF renavigated-Doppler wind streamlines and isotachs (in knots).

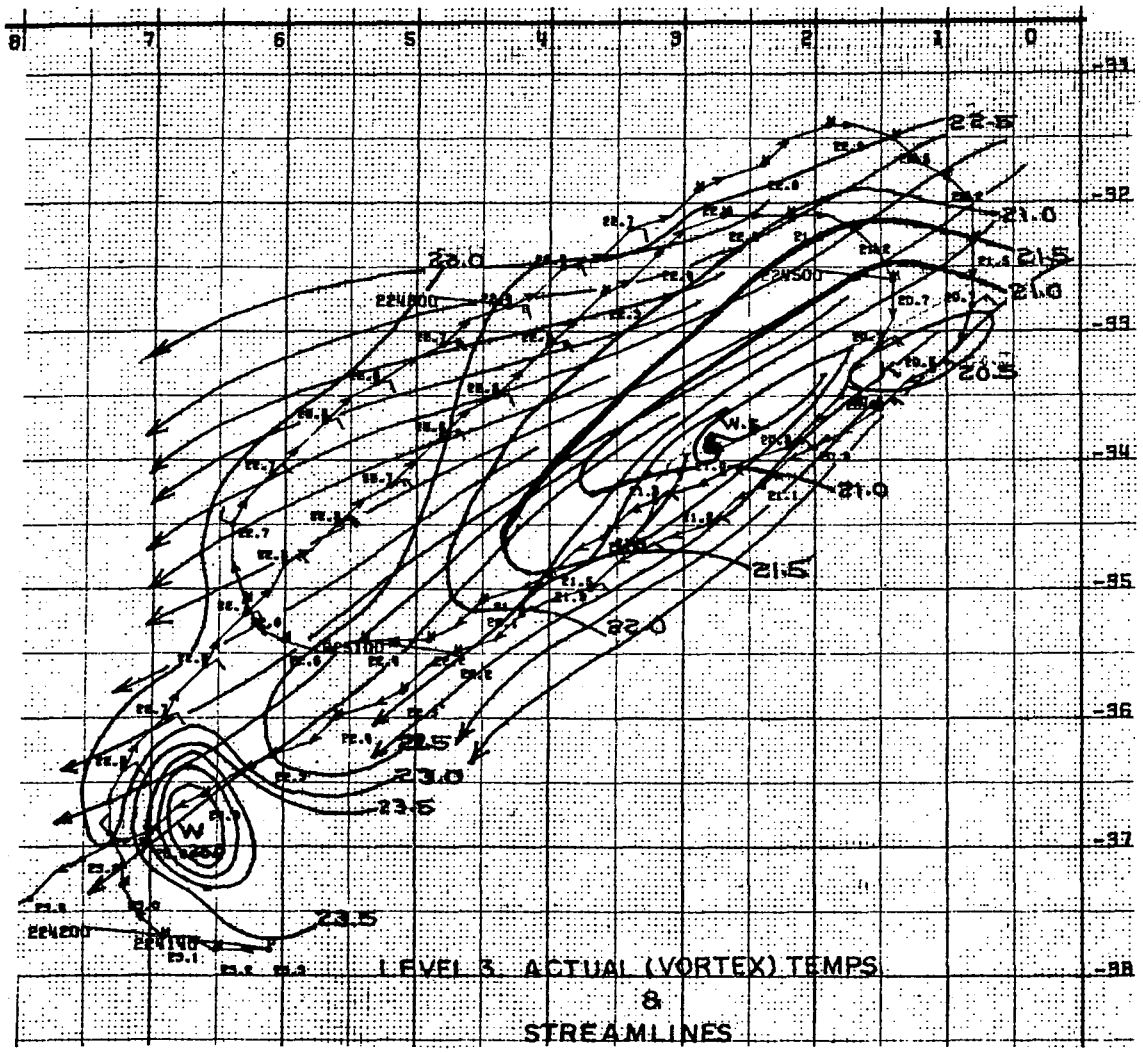

Figure B-14. Level-3 actual (Vortex) temperature isotherms (0.5°C interval) with streamlines superimposed.

NATIONAL SEVERE STORMS LABORATORY

The NSSL Technical Memoranda, beginning with No. 28, continue the sequence established by the U. S. Weather Bureau National Severe Storms Project, Kansas City, Missouri. Numbers 1-22 were designated NSSP Reports. Numbers 23-27 were NSSL Reports, and 24-27 appeared as subseries of Weather Bureau Technical Notes. These reports are available from the National Technical Information Service, Operations Division, Springfield, Virginia 22151, for $3.00, and a microfiche version for $0.95. NTIS numbers are given below in parentheses.

No. 1 National Severe Storms Project Objectives and Basic Design. Staff, NSSP. March 1961. (PB-168207)

No. 2 The Development of Aircraft Investigations of Squall Lines from 1956-1960. B. B. Goddard. (PB-168208)

No. 3 Instability Lines and Their Environments as Shown by Aircraft Soundings and Quasi-Horizontal Traverses. D. T. Williams. February 1962. (PB-168209)

No. 4 On the Mechanics of the Tornado. J. R. Fulks. February 1962. (PB-168210)

No. 5 A Summary of Field Operations and Data Collection by the National Severe Storms Project in Spring 1961. J. T. Lee. March 1962. (PB-165095)

No. 6 Index to the NSSP Surface Network. T. Fujita. April 1962. (PB-168212)

No. 7 The Vertical Structure of Three Dry Lines as Revealed by Aircraft Traverses. E. L. McGuire. April 1962. (PB-168213)

No. 8 Radar Observations of a Tornado Thunderstorm in Vertical Section. Ralph J. Donaldson, Jr. April 1962. (PB-174859)

No. 9 Dynamics of Severe Convective Storms. Chester W. Newton. July 1962. (PB-163319)

No. 10 Some Measured Characteristics of Severe Storms Turbulence. Roy Steiner and Richard H. Rhyne. July 1962. (N62-16401)

No. 11 A Study of the Kinematic Properties of Certain Small-Scale Systems. D. T. Williams. October 1962. (PB-168216)

No. 12 Analysis of the Severe Weather Factor in Automatic Control of Air Route Traffic. W. Boynton Beckwith. December 1962. (PB-168217)

No. 13 500-Kc./Sec. Sferics Studies in Severe Storms. Douglas A. Kohl and John E. Miller. April 1963. (PB-168218)

No. 14 Field Operations of the National Severe Storms Project in Spring 1962. L. D. Sanders. May 1963. (PB-168219)

No. 15 Penetrations of Thunderstorms by an Aircraft Flying at Supersonic Speeds. G. P. Roys. Radar Photographs and Gust Loads in Three Storms of 1961 Rough Rider. Paul W. J. Schumacher. May 1963. (PB-168220)

No. 16 Analysis of Selected Aircraft Data from NSSP Operations, 1962. T. Fujita. May 1963. (PB-168221)

No. 17 Analysis of Methods for Small-Scale Surface Network Data. D. T. Williams. August 1963. (PB-168222)

No. 18 The Thunderstorm Wake of May 4, 1961. D. T. Williams. August 1963. (PB-168223)

No. 19 Measurements by Aircraft of Condensed Water in Great Plains Thunderstorms. George P. Roys and Edwin Kessler. July 1966. (PB-173048)

No. 20 Field Operations of the National Severe Storms Project in Spring 1963. J. T. Lee, L. D. Sanders and D. T. Williams. January 1964. (PB-168224)

No. 21 On the Motion and Predictability of Convective Systems as Related to the Upper Winds in a Case of Small Turning of Wind with Height. James C. Fankhauser. January 1964. (PB168225)

No. 22 Movement and Development Patterns of Convective Storms and Forecasting the Probability of Storm Passage at a Given Location. Chester W. Newton and James C. Fankhauser. January 1964. (PB-168226)

No. 23 Purposes and Programs of the National Severe Storms Laboratory, Norman, Oklahoma. Edwin Kessler. December 1964. (PB-166675)

No. 24 Papers on Weather Radar, Atmospheric Turbulence, Sferics, and Data Processing. August 1965. (AD-621586)

No. 25 A Comparison of Kinematically Computed Precipitation with Observed Convective Rainfall. James C. Fankhauser. September 1965. (PB-168445).

No. 26 Probing Air Motion by Doppler Analysis of Radar Clear Air Returns. Roger M. Lhermitte. May 1966. (PB-170636)

No. 27 Statistical Properties of Radar Echo Patterns and the Radar Echo Process. Larry Armijo. May 1966. The Role of the Kutta-Joukowski Force in Cloud Systems with Circulation. J. L. Goldman. May 1966. (PB-170756)

No. 28 Movement and Predictablity of Radar Echoes. James Warren Wilson. November 1966. (PB-173972)

No. 29 Notes on Thunderstorm Motions, Heights, and Circulations. T. W. Harrold, W. T. Roach, and Kenneth E. Wilk. November 1966. (AD-644899)

No. 30 Turbulence in Clear Air Near Thunderstorms. Anne Burns, Terence W. Harrold, Jack Burnham, and Clifford S. Spavins. December 1966. (PB-173992)

No. 31 Study of a Left-Moving Thunderstorm of 23 April 1964. George R. Hammond. April 1967. (PB-174681)

No. 32 Thunderstorm Circulations and Turbulence from Aircraft and Radar Data. James C. Fankhauser and J. T. Lee. April 1967. (PB-174860)

No. 33 On the Continuity of Water Substance. Edwin Kessler. April 1967. (PB-175840)

No. 34 Note on the Probing Balloon Motion by Doppler Radar. Roger M. Lhermitte. July 1967. (PB-175930)

No. 35 A Theory for the Determination of Wind and Precipitation Velocities with Doppler Radars. Larry Armijo. August 1967. (PB-176376)

No. 36 A Preliminary Evaluation of the F-100 Rough Rider Turbulence Measurement System. U. O. Lappe. October 1967. (PB-177037)

No. 37 Preliminary Quantitative Analysis of Airborne Weather Radar. Lester P. Merritt. December 1967. (PB-177188)

No. 38 On the Source of Thunderstorm Rotation. Stanley L. Barnes. March 1968. (PB-178990)

No. 39 Thunderstorm - Environment Interactions Revealed by Chaff Trajectories in the Mid-Troposphere. James C. Fankhauser. June 1968. (PB-179659)

No. 40 Objective Detection and Correction of Errors in Radiosonde Data. Rex L. Inman. June 1968. (PB-180284)

No. 41 Structure and Movement of the Severe Thunderstorms of 3 April 1964 as Revealed from Radar and Surface Mesonetwork Data Analysis. Jess Charba and Yoshikazu Sasaki. October 1968. (PB-183310)

No. 42 A Rainfall Rate Sensor. Brian E. Morgan. November 1968. (PB-183979)

No. 43 Detection and Presentation of Severe Thunderstorms by Airborne and Ground-Based Radars: A Comparative Study. Kenneth E. Wilk, John K. Carter, and J. T. Dooley. February 1969. (PB-183572)

No. 44 A Study of a Severe Local Storm of 16 April 1967. George Thomas Haglund. May 1969. (PB-184-970)

No. 45 On the Relationship Between Horizontal Moisture Convergence and Convective Cloud Formation. Horace R. Hudson. March 1970. (PB-191720)

No. 46 Severe Thunderstorm Radar Echo Motion and Related Weather Events Hazardous to Aviation Operations. Peter A. Barclay and Kenneth E. Wilk. June 1970. (PB-192498)

No. 47 Evaluation of Roughness Lengths at the NSSL-WKY Meteorological Tower. Leslie D. Sanders and Allen H. Weber. August 1970. (PB-194587)

No. 48 Behavior of Winds in the Lowest 1500 ft in Central Oklahoma: June 1966 - May 1967. Kenneth C. Crawford and Horace R. Hudson. August 1970.

No. 49 Tornado Incidence Maps. Arnold Court. August 1970. (COM-71-00019)

No. 50 The Meteorologically Instrumented WKY-TV Tower Facility. John K. Carter. September 1970. (COM-71-00108)

No. 51 Papers on Operational Objective Analysis Schemes at the National Severe Storms Forecast Center. Rex L. Inman. November 1970. (COM-71-00136)

No. 52 The Exploration of Certain Features of Tornado Dynamics Using a Laboratory Model. Neil B. Ward. November 1970. (COM-71-00139)

No. 53 Rawinsonde Observation and Processing Techniques at the National Severe Storms Laboratory. Stanley L. Barnes, James H. Henderson and Robert J. Ketchum. April 1971. (COM-71-00707)

No. 54 Model of Precipitation and Vertical Air Currents. Edwin Kessler and William C. Bumgarner. June 1971. (COM-71-00911)

No. 55 The NSSL Surface Network and Observations of Hazardous Wind Gusts. Operations Staff. June 1971. (COM-71-00910)

No. 56 Pilot Chaff Project at the National Severe Storms Laboratory. Edward A. Jessup. November 1971. (COM-72-10106)

No. 57 Numerical Simulation of Convective Vortices. Robert P. Davies-Jones and Glenn T. Vickers. November 1971. (COM-72-10269)

No. 58 The Thermal Structure of the Lowest Half Kilometer in Central Oklahoma: December 9, 1966 - May 31, 1967. R. Craig Goff and Horace R. Hudson. July 1972. (COM-72-11281)

No. 59 Cloud-to-Ground Lightning Versus Radar Reflectivity in Oklahoma Thunderstorms. Gilbert D. Kinzer. September 1972. (COM-73-10050)

No. 60 Simulated Real Time Displays of Velocity Fields by Doppler Radar. L. D. Hennington and G. B. Walker. November 1972. (COM-73-10515)

No. 61 Gravity Current Model Applied to Analysis of Squall-Line Gust Front. Jess Charba. November 1972. (COM-73-10410)

No. 62 Mesoscale Objective Map Analysis Using Weighted Time-Series Observations. Stanley L. Barnes. March 1973. (COM-73-10781)

No. 63 Observations of Severe Storms on 26 and 28 April 1971. Charles L. Vlcek. April 1973. (COM-73-11200)

No. 64 Meteorological Radar Signal Intensity Estimation. Dale Sirmans and R. J. Doviak. September 1973. (COM-73-11923/2AS)

No. 65 Radiosonde Altitude Measurement Using Double Radiotheodolite Techniques. Stephan P. Nelson. September 1973. (COM-73-11934/9AS)

No. 66 The Motion and Morphology of the Dryline. Joseph T. Schaefer. September 1973. (COM-74-10043)

No. 67 Radar Rainfall Pattern Optimizing Technique. Edward A. Brandes. March 1974.

No. 68 The NSSL/WKY-TV Tower Data Collection Program: April - July 1972. R. Craig Goff and W. David Zittel. May 1974.

No. 69 Papers on Oklahoma Thunderstorms, April 29-30, 1970. Stanley L. Barnes, et al. May 1974

☆ U.S. GOVERNMENT PRINTING OFFICE: 1974 - 784-578 / 1280 REGION NO. 8